

# **Studies of Catalytic Materials with *In Situ* Transmission Electron Microscopy**

## **Studies van Katalytische Materialen met *in situ* Transmissie-elektronenmicroscopie**

*(met een samenvatting in het Nederlands)*

### **Proefschrift**

ter verkrijging van de graad van doctor aan de Universiteit Utrecht op gezag van de rector magnificus, prof.dr. H.R.B.M. Kummeling, ingevolge het besluit van het college voor promoties in het openbaar te verdedigen op woensdag 9 september 2020 des middags te 2.30 uur

*door*

**Mark Johan Meijerink**

geboren op 18 mei 1991 te Amstelveen

**Promotor:**

Prof. dr. ir. K.P. de Jong

**Copromotor:**

Dr. J. Zečević

This research was supported by the European Research Council (ERC) under the Seventh Framework Programme for Research and Technological Development of the European Union (ERC Advanced Grant no. 338846)

"Writing is easy. All you have to do is cross out the wrong words."

~~*A completely and utterly wrong*~~ Mark Twain

Author: M. J. Meijerink

Title: Studies of Catalytic Materials with In Situ Transmission Electron Microscopy

ISBN: 978-94-640-2443-2

Printed by: Gildeprint – The Netherlands

Cover by: Y. Meeuwsen & M. J. Meijerink

# Table of Contents

## Chapter 1

General Introduction on Heterogeneous Catalysis, catalyst deactivation and (in situ) Electron Microscopy p.1

## Chapter 2

Assessment of Oxide Nanoparticle Stability in Liquid Phase Transmission Electron Microscopy p.29

## Chapter 3

Nanoscale Imaging and Stabilization of Silica Nanospheres in Liquid Phase Transmission Electron Microscopy p.63

## Chapter 4

Growth of Supported Gold Nanoparticles in Aqueous Phase Studied by in Situ Transmission Electron Microscopy p.89

## Chapter 5

Advanced transmission electron microscopy study of structural changes in gold catalysts relevant for the oxidation of HMF p.127

## Chapter 6

Summary p.161

Outlook p.165

Nederlandse Samenvatting p.167

List of Abbreviations p.171

List of Publications and Presentations p.173

Acknowledgements p.175

Curriculum Vitae p.179



# **Chapter 1**

## **Introduction**

Since the dawn of humanity, the materials available have defined many aspects of people's lives, to the extent that we named entire eras of human (pre)history after their dominant material of choice.<sup>1</sup> Fortunately, this naming tradition has stopped after the Iron Age, otherwise learning history would be rather challenging with the plethora of important materials in use in modern times. Nevertheless, many scientific challenges are still due to the limitations of the currently available materials.<sup>2</sup> One field where this is abundantly clear, is that of heterogeneous catalysis, especially for pollution reduction, sustainable energy use and chemicals production.<sup>3-6</sup>

### 1.1 Heterogeneous Catalysts

A heterogeneous catalyst is a substance, usually a solid material, that is added to a system to increase the rate of a chemical reaction without being consumed itself and is in a different phase than the reactants and products.<sup>3</sup> This increase in rate, along with the ability of many catalysts to increase the rate of desired reactions more than the rate of undesired reactions, allows for massive increases in both atom and energy efficiency in chemical conversions.<sup>7</sup> As a result, catalysts are essential for the modern (petro)chemical industry and it is estimated that for approximately 85% of all chemical processes a catalyst is used, and for roughly 80% of industrial catalytic processes this is a solid catalyst.<sup>8</sup>

The performance of a catalyst is evaluated by three main aspects, namely activity, selectivity and stability. Activity is the rate at which the reactants are converted, usually expressed in amount of reactant converted per unit of time per gram of (active) material. Selectivity is the amount of desired product(s) obtained, usually as a percentage of the total amount of reactant converted or product formed. Although a catalyst is not consumed during the reaction, it nevertheless often slowly changes over time. When these changes result in a lower activity and/or selectivity, it is referred to as catalyst deactivation and the stability is an indication of resistance to this deactivation.<sup>9</sup>

In heterogeneous catalysts, the chemical reactions occur at the interface between the phases and because of this, it is preferable to maximize the interfacial area and obtain the highest activity possible. As we will only consider solid heterogeneous catalysts in this thesis, the chemical reactions therefore occur at the surface of the catalyst, which should therefore be maximized. In practice, this means producing catalysts with very small particles to obtain a high specific surface area (SSA, surface area per gram of material).<sup>3</sup> Therefore, most heterogeneous catalysts consist of metal or metal oxide nanoparticles, although many other compositions exist as well, with some examples being sulfides,<sup>10</sup> carbides<sup>11-12</sup> and hydroxides.<sup>13</sup> There are lower limits for the particle



size, first of all due to the fact that atoms themselves have a finite size.<sup>14</sup> In addition, the high fraction of surface atoms for particles below approximately 10 nm can change the material properties drastically. This is especially the case for the nanoparticle surface structure, which can be different from the surface structure of bulk materials, and the high fraction of low coordinated sites and surface defects can influence catalytic activity and selectivity, but particles also become very mobile.<sup>15</sup> Although the change in surface structure in very small particles is sometimes for the better, such as in CO oxidation over gold catalysts,<sup>16</sup> it is also sometimes for the worse, such as in Fischer-Tropsch catalysis with cobalt catalysts<sup>17</sup> and therefore, smaller is not always better.

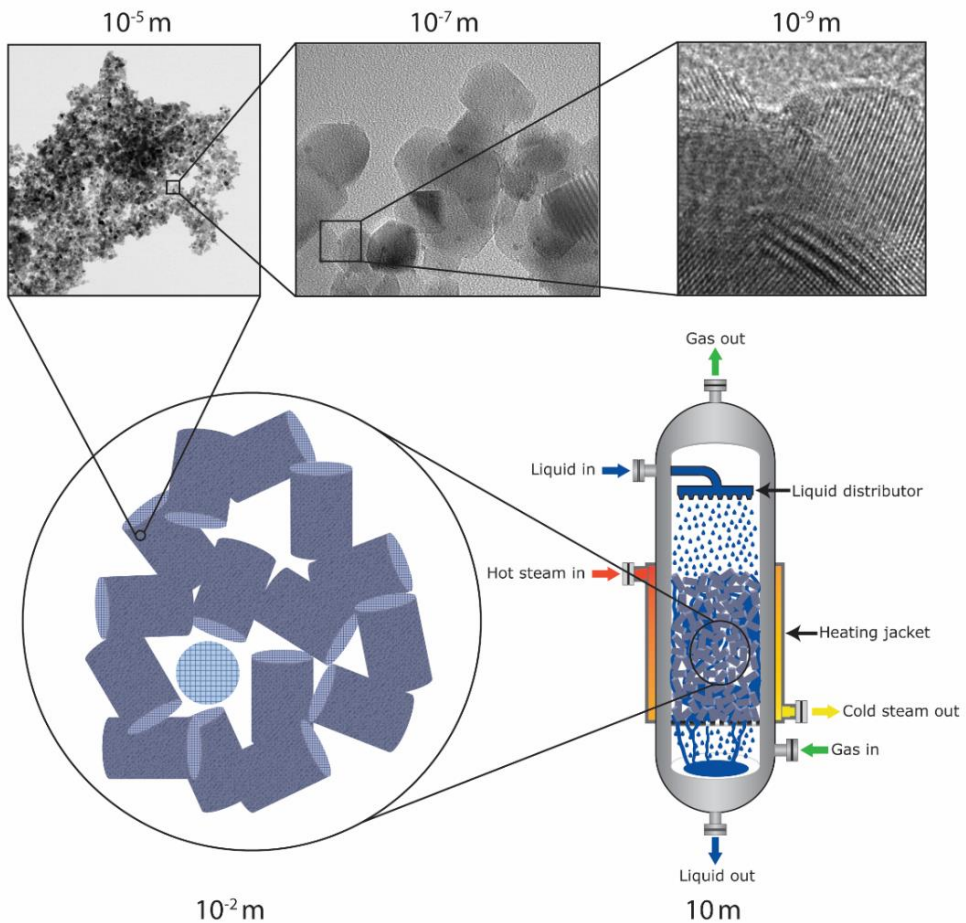


**Figure 1.1.** Different length scales of catalysis, from individual atoms (sub-nanometer scale) to entire chemical reactors.

The increased mobility also results in an increase in agglomeration, and to prevent it, nanoparticles are usually anchored on a material with a high specific surface area, which is the support.<sup>3</sup> Apart from stabilizing the catalytically active nanoparticles, in some cases the support can also actively participate in the reaction,<sup>18</sup> for example with a Mars-van Krevelen-type mechanism<sup>19-20</sup> or when using an acidic support (e.g. zeolite supports),<sup>21-22</sup> or have electronic effects changing the chemical properties of the nanoparticles (e.g. Pt supported on TiO<sub>2</sub>),<sup>23</sup> which is often observed with transition metal oxide supports.

High-surface area supports are usually a very fine powder (primary particle sizes of less than 1 μm), which cannot be used in a chemical reactor. Therefore, the support powder with the catalytic nanoparticles is shaped into a catalyst body, often together with many additives, such as binders and fillers, for improved mechanical and heat/mass transfer properties.<sup>24</sup> These bodies, ranging in size from ~0.1 mm to monoliths of more than a meter, are then placed in an industrial reactor to catalyze a chemical reaction (see Figure 1.1).

## 1.2 Gold Catalysis

One group of catalysts in which many of the above aspects can be seen, is that of heterogeneous gold catalysts. For millennia gold was revered for its inertness and seen as the divine metal by the ancient Egyptians for this very reason.<sup>25</sup> As a result of its inertness, gold itself was thought to be completely inactive as a catalyst in the past, but the discovery that very small gold nanoparticles of less than ~10 nm were highly active for multiple reactions sparked great interest in the possibilities of supported gold catalysts.<sup>26</sup> In particular the discovery of its high activity for hydrogenation by Bond et al.,<sup>27-28</sup> the hydrochlorination of ethyne by Hutchings et al.<sup>29</sup> and most famously, the ability of supported gold catalysts to oxidize CO to CO<sub>2</sub> at (sub) ambient temperature by Haruta et al.<sup>30</sup> were very important to this field.

Since then, many other reactions were found that could be catalyzed by supported gold catalysts.<sup>31-32</sup> It is for example possible to catalyze many selective oxidation<sup>33</sup> and hydrogenation<sup>34</sup> reactions under far milder conditions than many other catalysts and with high selectivity towards the desired products. For many of these reactions, the support also plays an important role beyond stabilizing the particles, but to which extent depends on the reaction being catalyzed and the catalyst preparation method.<sup>35</sup> Many supports have strong electronic interactions with gold nanoparticles, often also changing the surface plasmon resonance which results in striking color differences when using different supports (Figure 1.2).



**Figure 1.2.** Gold nanoparticles of ~2-5 nm supported on different oxides, displaying distinct differences in color (all three oxides without gold are white). Supports from left to right: TiO<sub>2</sub>, MgO, SiO<sub>2</sub>.

Due to their high selectivity towards the desired products in selective oxidation reactions, gold based catalysts are also very attractive for multiple steps during the production of platform chemicals from biomass.<sup>36</sup> Therefore these catalysts can aid significantly in reducing the need for fossil sources to produce many important chemicals. One example is the oxidation of (fructose derived) 5-hydroxymethyl furfural (HMF) to 2,5-furandicarboxylic acid (FDCA), a possible and renewable building block for many types of polymers, with air or pure O<sub>2</sub> in water.<sup>37</sup> It has been shown that gold is an excellent catalyst for this reaction, with high activity and good selectivity towards FDCA.<sup>38</sup>

This reaction unfortunately also showcases one of the major challenges in the actual application of gold catalysts in industrial processes: their rapid deactivation during catalysis.<sup>39</sup> Along with its relatively high price and large price fluctuations,<sup>40</sup> deactivation is one of the major concerns in the large scale application of gold catalysts.<sup>41</sup> This is seen in the very limited number of industrial processes (2 as of 2019, not including the use of gold as an alloying element for Pd catalysts<sup>42-43</sup>) in which gold catalysts are used, namely the oxidative esterification of methacrolein to methyl methacrylate<sup>44</sup> and the hydrochlorination of acetylene to vinyl chloride.<sup>45</sup> In the catalyst development for both of these processes, the low stability of the gold catalyst was the main challenge to overcome before they could be commercialized.<sup>41</sup>

## 1.3 Catalyst Deactivation

As mentioned before, catalysts can and do change over time and when these changes have a detrimental influence on the activity, selectivity or both, the catalyst is said to deactivate.<sup>9</sup> Many different mechanisms for this deactivation exist, as illustrated in Figure 1.3, namely attrition, poisoning, fouling, particle growth, leaching and chemical changes in the active nanoparticles.<sup>9, 46</sup> Which mechanism or combination causes the deactivation of a catalyst, depends on many aspects, such as the catalyst itself, the reaction it catalyzes and the reaction conditions.<sup>46</sup>

The attrition concerns macroscale physical changes, whereby the catalytic body suffers physical damage to the extent that it is no longer able to perform its function, i.e. it breaks or becomes a powder that is too fine. This type of deactivation is often a major consideration in fluidized bed reactors, such as during fluid catalytic cracking<sup>47</sup> or the synthesis of maleic anhydride.<sup>48</sup> This can result in loss of the catalytic material when it is crushed to such a fine powder that it cannot be retained in the reactor. Attrition can also result in collapse of the pores, reducing accessibility of the active phase of the catalytic component, which results in significant internal mass transfer limitations.<sup>49</sup>

In poisoning, strong chemisorption of certain species can block active sites and reduce overall catalytic activity. These species can be reactants, (side) products and/or impurities in the reactor feed. Well-known examples include sulphur and nitrogen-containing molecules ( $\text{H}_2\text{S}$ ,  $\text{NH}_3$ , various organic molecules) chemisorbing on noble metal nanoparticles, or organic bases chemisorbing on zeolite acid sites.<sup>50</sup> A special case is seen in catalysts with strong metal-support interactions (SMSI's), in which the support itself migrates over the metal particles and blocks (part of) the active sites by encapsulation.<sup>18</sup> A classic example is that of Pt supported on  $\text{TiO}_2$  in a reducing environment, in which the Pt nanoparticles are rapidly covered with a thin layer of  $\text{TiO}_x$ .<sup>51</sup> Poisoning is however not always problematic and in certain cases even desired. For example, the poison can block specific active sites that catalyze undesired side reactions while leaving the active sites for the desired reaction available.<sup>52</sup> Or in the case of properly tuned SMSI, more metal-oxide interface active sites can be generated, increasing activity<sup>53</sup> and selectivity,<sup>54</sup> or slowing down particle growth while retaining sufficient catalytic activity.<sup>55</sup>

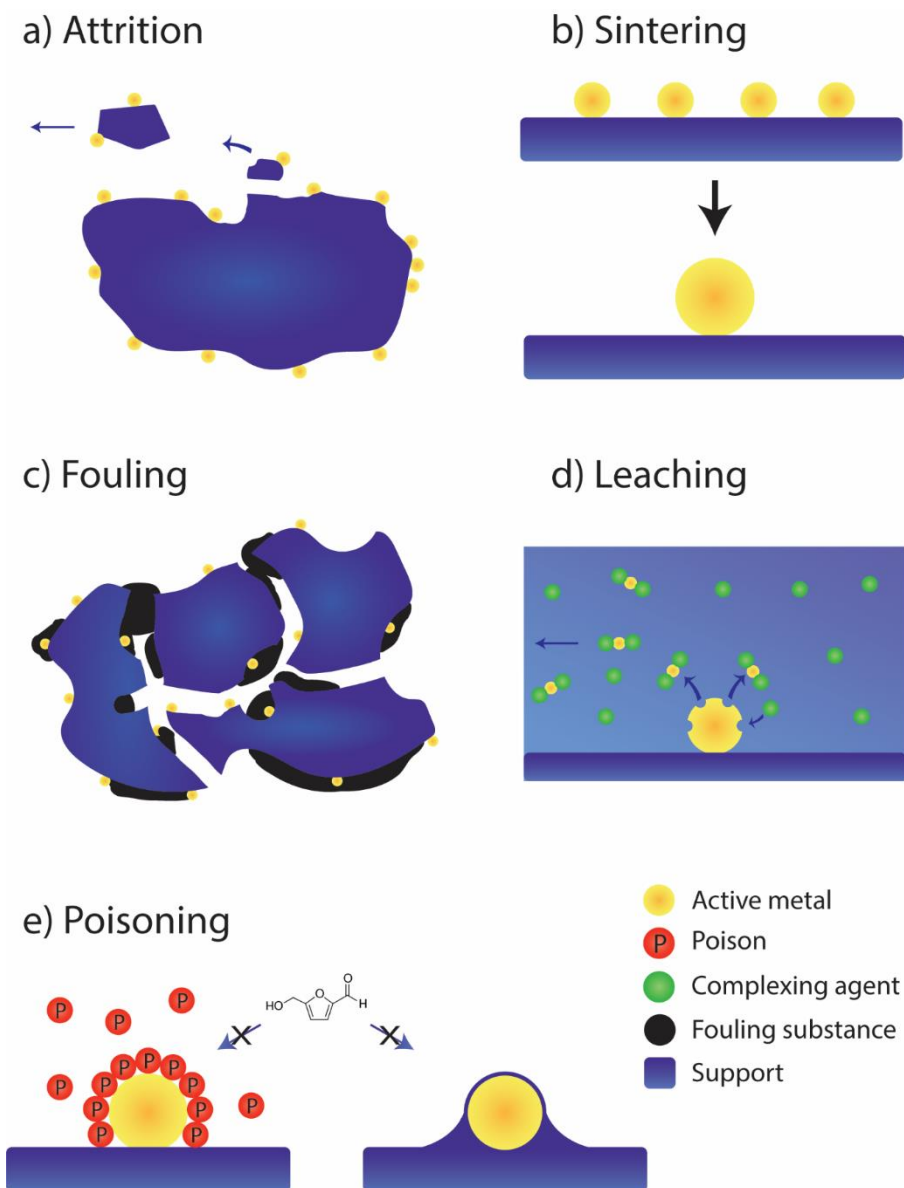


**Figure 1.3.** The most common deactivation mechanisms illustrated for a supported metal nanoparticle heterogeneous catalyst, with (a) attrition, in which the catalyst and support suffer mechanical damage. (b) Particle growth, where many small particles become a few large particles, decreasing the specific surface area. (c) Fouling, or physical blocking of the catalyst surface and pores. (d) Leaching, or dissolution of material in the fluid phase and (e) poisoning, illustrating both chemisorption of a poison on the metal nanoparticle (left) and strong metal-support interaction blocking (right).

In fouling, a species originating from the feed or reaction mixture deposits physically on the catalyst. This can cover the active sites of the catalyst and/or block pores, limiting accessibility and introducing significant mass transfer limitations, decreasing the overall activity significantly. One of the most well-known forms of fouling in catalysis is coking, in which a layer of carbonaceous species, referred to as coke, is formed and deposited on the catalyst during the reaction.<sup>56</sup> A similar phenomenon is also observed with other species in the feed, such as various metal (Fe, Ni, V etc.) impurities in oil that deposit on a fluid catalytic cracking (FCC) catalyst, again physically blocking the active sites and pores.<sup>57</sup>

Leaching usually refers to the active phase reacting with certain species in the reaction mixture to form volatile or soluble compounds that enter the fluid phase and are then transported out of the reactor, resulting in loss of catalytically active material. This can for example be seen in the formation of  $\text{PtO}_x$  species that can evaporate under the right conditions, causing loss of Pt<sup>58</sup> or dissolution of gold species during liquid phase biomass processing, such as in the selective oxidation of glucose.<sup>59</sup> In the case of chemical changes of the catalyst, the active material also reacts with other species, but then forms an inactive phase that remains on the support, such as metallic catalysts slowly being oxidized during the reaction, such as iron-based catalysts in  $\text{NH}_3$  synthesis<sup>60</sup> or Fischer-Tropsch synthesis<sup>61</sup> under the wrong conditions.

Finally, in particle growth, also known as sintering, the individual nanoparticles of the catalyst grow over time, resulting in a loss of specific surface area and active sites.<sup>62</sup> This growth is a result of the high surface energy contribution to the thermodynamic potential of the nanoparticles, which yields a large driving force for reduction of the specific surface area.

In the deactivation of gold catalysts, sintering is usually the main culprit, mostly because of the small gold particle size required for catalytic activity and gold's relatively low melting point (1064 °C)<sup>63</sup> compared to many other metals used in catalysis. A low melting temperature means the material also has a low Hüttig temperature, or the temperature at which surface atoms attain significant mobility (about 1/3 of the melting point in K, ~130 °C for Au). In addition, a low melting point yields a low Tamman temperature, which is the temperature at which atom bulk mobility becomes appreciable and movement of entire nanoparticles over the support starts to become important (approximately half of the melting temperature in K, for Au ~400 °C). The mechanism and extent of sintering also depends on many other factors, such as the support,<sup>64</sup> presence of chlorides<sup>65-66</sup> and the chemical environment (such as oxidizing versus reducing gas atmosphere<sup>67</sup> or liquid versus gas phase).

Sintering is commonly considered to take place by Ostwald ripening (OR), by particle diffusion and coalescence (PDC) or as a result of both mechanisms combined. A schematic representation of these two mechanisms and the difference between them can be found in Figure 1.4. In OR, it is assumed that the nanoparticles themselves are immobile and that growth is the result of atoms, complexes or other small and mobile species, called monomers, moving from smaller particles to larger particles. In particle diffusion and coalescence, the particles are mobile, move over the support and merge upon interaction.

Because of the importance of sintering for catalyst deactivation, several mathematical models have been developed for these mechanisms to understand and predict particle growth behavior. In the case of particle diffusion and coalescence, the kinetics are usually described using some form of the Smoluchowski coagulation equation.<sup>68</sup> In this type of sintering, the most important parameters for deactivation rate are the (size-dependent) diffusion coefficients of the particles and the interparticle distances. As a result, limiting deactivation when this mechanism is dominant, can be achieved by increasing the interparticle distance through lowering metal loading or by increasing the homogeneity of the particle distribution over the support. Decreasing the particle diffusion coefficient can be achieved through a change of the support surface that hinders particle movement, confining the particles in pores or by increasing the particle size, which decreases particle mobility.<sup>55,69</sup>

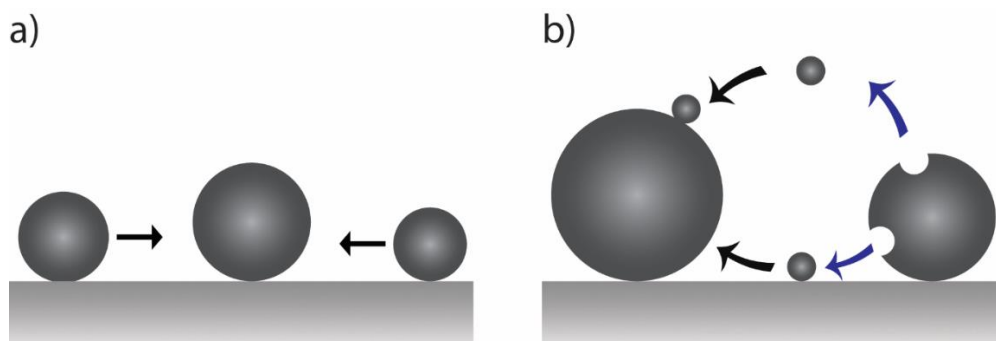


**Figure 1.4.** Illustration of the two main sintering mechanisms, with (a) particle diffusion and coalescence and (b) Ostwald ripening.

When Ostwald ripening is the dominant mechanism for sintering, kinetics are generally modelled using the Lifshitz-Slyozov-Wagner (LSW) model.<sup>70-72</sup> This model generally assumes static particles and a uniform background concentration (far away from the particles) of monomer, equal to the bulk solubility of that particular monomer in the fluid phase. As a consequence of the Kelvin effect, small particles have a higher solubility than the bulk material and the smaller the particle is, the

higher the solubility and local supersaturation.<sup>73</sup> This model then predicts that there is a critical particle diameter and any particle smaller than this diameter will shrink, while any particle larger than this diameter will grow, i.e. monomers move from the smaller to the larger particles. Particle growth rate then depends not only on the average size of the particles, but also on the width of the particle size distribution, with a wider distribution resulting in more rapid growth. Depending on whether diffusion or detachment/attachment of the monomer is the slowest step, the monomer diffusion coefficient or the surface reaction rate are also important for the sintering rate.<sup>74</sup>

Investigation of sintering behavior usually relies heavily on measuring particle sizes and their distribution before and after catalysis.<sup>75</sup> The validity of this approach has however been questioned due to the fact that it usually takes a very long time for a particle size distribution (PSD) to evolve to the PSD predicted by the model, if it happens at all.<sup>76</sup> Due to the small size of the nanoparticles present in catalysts, evaluating PSDs and PSD evolution usually requires transmission electron microscopy (TEM). However, despite the current availability of excellent TEMs that can image even the smallest particles, sintering behavior is still not very well understood and many discrepancies between models and experimental data are still seen when using PSDs before and after sintering.<sup>77</sup> This is especially noticeable in the case of Ostwald ripening, which will be discussed in more detail in Chapter 4, where OR is discussed in more detail and where in situ TEM is used to follow the OR of Au nanoparticles supported on TiO<sub>2</sub> in an aqueous phase.

## 1.4 Electron Microscopy

Despite the omnipresence of optical illusions, the old adage of ‘seeing is believing’ remains in widespread use, never more so than in electron microscopy. However, although it is indeed important to be careful with interpretation of electron microscopy (EM) data, as illustrated by Figure 1.5, it is an incredibly powerful tool in many fields of nanotechnology. Due to their short de Broglie wavelength, high-energy electrons do not suffer from diffraction limitations seen in optical microscopes when one is trying to observe nanomaterials. This allows for significantly higher spatial resolution and visualization of nanoscale morphology and even atomic structures with the right equipment.<sup>78</sup>



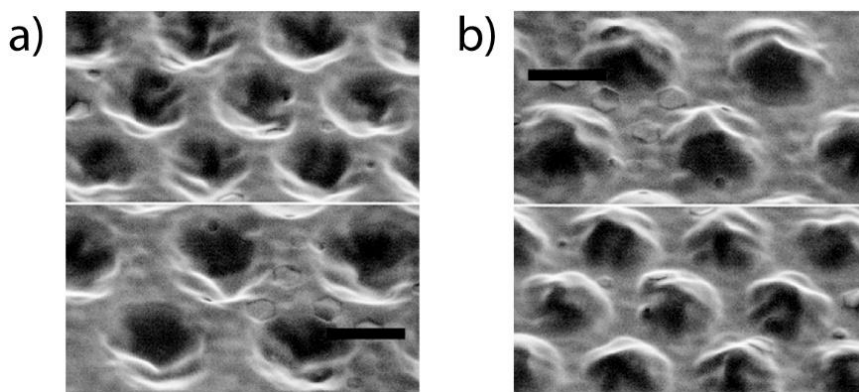


**Figure 1.5.** Example of an optical illusion in a Scanning Electron Microscope (SEM), with (a) a secondary electron image of small pits in an indium tin oxide layer. (b) Exactly the same image, but rotated 180°, with the pits now appearing to be bumps sticking out of the surface. The scale bar corresponds to 500 nm. The image in (a) was acquired by Liu et al. and reproduced with permission.<sup>79</sup>

In electron microscopy, the sample is illuminated with a beam of high energy electrons, which interact with the sample in many ways, as shown in Figure 1.6c. These interactions produce all kinds of signals that can be detected with the appropriate detectors and detector locations, each of which then provides different information about the specimen.<sup>78, 80-81</sup> In scanning electron microscopy (SEM), the electron beam is focused into a very small spot and scanned across the sample in a raster. Most commonly, signals originating from the surface, such as secondary and backscattered electrons, are used to construct an image. In transmission electron microscopy (TEM), illustrated in Figure 1.6a, the sample is illuminated by a parallel beam of electrons and images are constructed from electrons that went through (transmitted) the necessarily very thin sample. In addition, scanning transmission electron microscopy (STEM) exists as well, in which the electron beam is focused into a very small spot, raster-scanned across the thin sample and, but unlike SEM, the image is constructed from transmitted electrons, as illustrated in Figure 1.6b. (S)TEM images are therefore 2D projections of a 3D sample, which is important to keep in mind when analyzing the data.

Because (S)TEM techniques typically have a significantly higher resolution than SEM<sup>78</sup> and only the former can visualize most of the small nanoparticles (<10 nm) used in catalysis, the discussion here will only consider (S)TEM. In both TEM and STEM, image contrast is formed by differences in forward scattering of electrons over the field of view. This scattering can be either elastic (electrons in the beam do not lose energy) or inelastic (energy is lost). Scattering originates from interactions of the high

energy electrons from the beam with the electron cloud of the atoms in the sample or strong coulombic interactions between the electron beam and the nucleus (the latter usually referred to as Rutherford scattering). Although an electron can scatter many times, for (S)TEM it is generally assumed that each electron has at most one scattering event, which is usually a valid assumption for the thin samples encountered here.

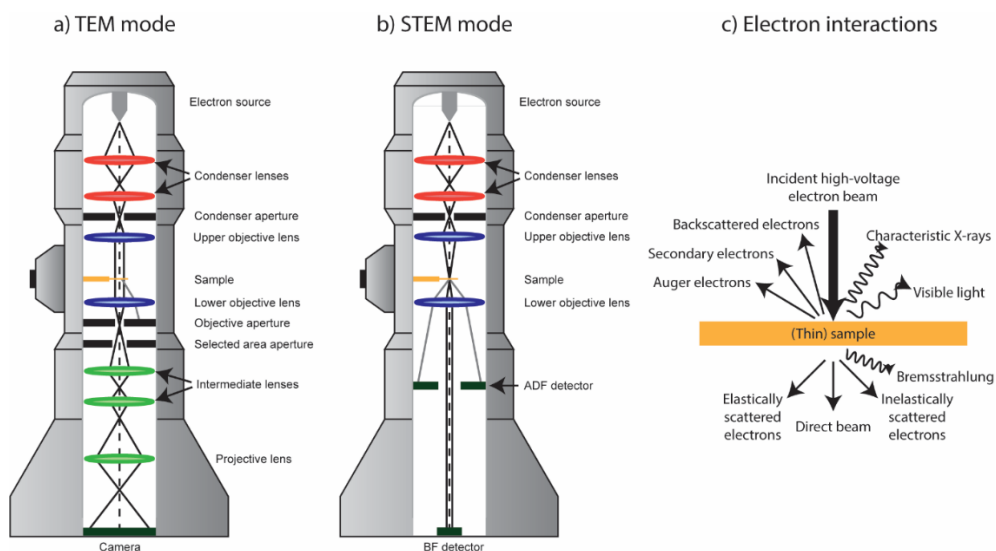


**Figure 1.6.** Overview of the two main modes of transmission electron microscopy, TEM (a) and STEM (b) and the possible interactions of electrons with a material (c).

In regular bright-field TEM (BF-TEM), the sample is illuminated with a parallel beam and the electrons are detected using a screen/camera below the sample, directly in the path of the beam. In this way, only electrons that have not been scattered or scattered with a very low angle compared to the optical axis will be detected. Therefore, contrast is mostly dependent on local electron density and parts that are thicker or have higher density, will scatter more electrons and appear darker in the image, essentially producing a shadow of the sample, which is also known as mass-thickness contrast.

In STEM, the electron beam is focused into a very small spot (typically 50-200 pm) and raster-scanned over the field of view. Depending on the electrons of interest, one or more electron detectors are placed below the sample. For bright-field STEM (BF-STEM), the detector is again located directly in the path of the unscattered beam, in the optical axis, and detects electrons that have not been scattered significantly. However, it is also possible to detect the scattered electrons only, using an annular detector located outside of the direct path. Because in this mode the parts that scatter most electrons are the brightest and the background is dark, this mode is called dark-field STEM (DF-STEM).

Depending on the angle relative to the optical axis, different types of scattering can be detected which can provide different information. In particular the higher angles ( $>5^\circ$ ) are of interest, as in this range, Rutherford scattering is dominant. Because the Coulomb interaction is proportional to the charge of the nucleus squared, scattering and therefore contrast is highly dependent on the atomic number ( $Z$ ) for these angles. It is therefore possible to distinguish small particles of heavy elements on larger particles of lighter elements significantly easier, which is particularly useful for catalysts with small metal nanoparticles on a low- $Z$  element support (most of them). Because scientists are so imaginative, using an annular detector at high angles is called high angle annular dark-field STEM (HAADF-STEM).

In addition to elastic scattering, there is also inelastic scattering of electrons, in which a significant amount of energy from the electron is deposited in the sample. This energy deposition can damage the sample, but also produces a lot of valuable information, in particular by emitting various types of X-rays and electrons. One of the most commonly used signals is characteristic X-rays, which is used in energy-dispersive X-ray spectroscopy (EDX).<sup>82</sup> When a high-energy electron from the beam transfers sufficient energy to one of the core electrons of an atom in the sample, that core electron can be ejected. One of the electrons from an outer shell can then fill the resulting hole, producing an X-ray photon in the process. This photon has a very specific energy equal to the difference in energy between the two shells. The exact energy depends on the element and the two shells the electron transitions between and can therefore be used to distinguish elements present in the specimen, providing very local information on the chemical composition.<sup>83</sup>

In addition, many other signals and both the wave-like and particle-like properties of electrons are used in a TEM, which can yield a tremendous amount of additional information. As entire books have been written on the possible information that can be obtained from (S)TEM and the techniques mentioned below are not used in this thesis, they will not be discussed in detail. Several well-known ones are electron tomography for obtaining 3D information,<sup>84-87</sup> electron diffraction<sup>88</sup> for information on the crystal structure and crystallinity and electron energy loss spectroscopy<sup>83, 89-90</sup> for additional elemental and chemical information. Furthermore, dark-field TEM, electron holography and secondary electron imaging are also commonly used, among many other techniques.<sup>78</sup>

## 1.5 In situ Transmission Electron Microscopy

Despite TEM being an incredibly powerful tool for investigating nanomaterials the strong interactions of electrons with matter also mean that a high vacuum is necessary to limit scattering by gas molecules in the path of the electrons and that samples have to be very thin. As a result, the samples under investigation must be dry and no liquid or gas can be present. This severely limits the possibilities of investigating dynamic nanoscale processes of samples in contact with a gas or liquid. Although many strategies have been devised to overcome these challenges, it remains difficult to image in the presence of a gas or liquid.

Over the years, new developments have been able to address these limitations. One important leap forward was the introduction of environmental TEM (ETEM) for investigating samples in contact with a gas.<sup>91-93</sup> This system consists of a dedicated microscope that has a small gas inlet close to the specimen holder to locally raise the gas pressure of the gas of interest, as can be seen in Figure 1.7. To prevent severe loss of resolution and damage to the electron gun, several additional diffusion limiting apertures and pumps are located close to the specimen holder to limit the gas pressure in the rest of the column as much as possible. With this ETEM system, it is then possible to investigate samples in contact with a gas atmosphere of several millibars (<approx. 20 mbar, depending on the gas and ETEM system).<sup>91</sup> In addition, almost any holder that can be used in a regular TEM, can be used in this system and especially heating holders<sup>94</sup> can complement this type of in situ research significantly.

For liquids on the other hand, such a strategy is unfortunately not possible since the liquids that are most commonly used (such as water, ethanol, toluene etc.), have a vapor pressure that is too high to be used in a TEM.<sup>63</sup> There are some liquids that do have a sufficiently low vapor pressure to be deposited on a grid and can be exposed to the TEM vacuum, mostly ionic liquids, which have been used as an in situ liquid cell to study several processes.<sup>95-97</sup> One problem that was often seen though, was the difficulty of controlling the liquid layer thickness, which was generally overcome by a combination of using very high acceleration voltages (>300 kV), looking for small (and thin) droplets on the grid and accepting lower resolution.<sup>98</sup>

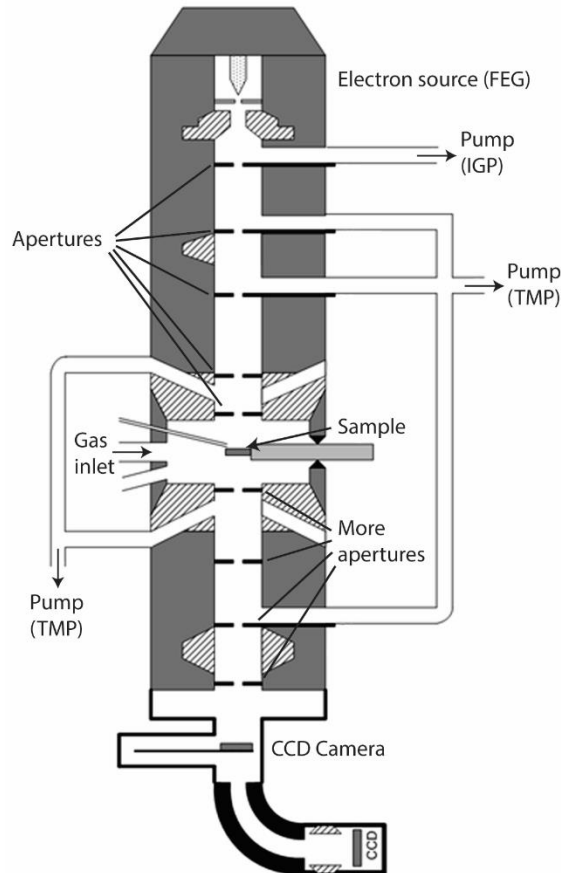


**Figure 1.7.** Schematic overview of an Environmental Transmission Electron Microscope (ETEM), showing the large number of diffusion limiting apertures and additional pumps. These ensure sufficiently low pressure in the rest of the column while the sample is in contact with a gas and prevent damage to the electron source. Adapted with permission from Wagner et al.<sup>91</sup>

A solution to this type of problem is to use an enclosed (thin) specimen chamber with an electron transparent thin film on each side, referred to as a window, in which the gas or liquid is kept separate from the vacuum of the TEM column. In such a system, the thickness can be controlled much easier, but it requires materials for the windows that can be made into very thin films and are strong and stiff enough to withstand the pressure difference. The first use of such a chamber was reported by Marton et al. in 1935,<sup>99</sup> only a few years after the first electron microscope was developed. In this work, 0.5 micrometer thick aluminum foil was used as a window material, which limited resolution quite a bit. Later developments used plastic films, often coated with

additional layers of SiO, SiO<sub>2</sub>, gold or silver,<sup>100</sup> which when combined with ultra-high voltage electron microscopes (1-3 MV acceleration voltage), could provide a good resolution of samples in contact with gas or liquid.<sup>101</sup>

With recent advances in microfabrication and microelectromechanical system (MEMS) technology, it is possible to obtain a better resolution and many new capabilities became available.<sup>102</sup> Enclosing small liquid droplets between graphene sheets (Figure 1.8c) has even resulted in atomic resolution studies of platinum nanocrystal growth<sup>103</sup> and oriented merging of gold nanoparticles<sup>104</sup> in a liquid. In addition, the use of silicon chips with very thin silicon nitride windows has also become very popular in recent years. This is mainly due to the ease of fabrication of chemically and mechanically robust, homogeneous Si<sub>x</sub>N<sub>y</sub> films and the ease with which micro-electrodes can be integrated on the chips.<sup>102</sup> Combined with improvements in holder design and fabrication, this allows for in situ investigation of many specimens in contact with a gas or liquid with the possibility of heating, biasing and gas or liquid flow and exchange during the experiment, with high spatial and temporal resolution (although still lower resolution than in vacuum). In addition, such enclosed systems can be used in a regular TEM without the need for a dedicated (and expensive) ETEM.

Several of the main types of in situ liquid cells for (S)TEM are illustrated in Figure 1.8. As can be seen in Figure 1.8a and b, slightly different configurations are needed when using TEM imaging mode versus STEM imaging mode if the liquid is too thick for the single scattering assumption to be valid for a significant fraction of electrons. In the case of graphene liquid cells (Figure 1.8c), the liquid is generally thin enough to use the same configuration for TEM and STEM mode, but for silicon chips, the liquid layer thickness is usually quite large. The location of the sample then becomes very important and in TEM mode, placing the sample at the bottom chip yields the highest resolution, while in STEM mode, placing the sample on the top chip is preferable.<sup>102</sup> This optimal sample position originates from the method of image acquisition and the inelastic scattering of the electrons by the liquid.

As mentioned previously, in (bright field) TEM, a camera detects electrons that have not been scattered to any significant extent and all pixels are measured at the same time. As a result, if electrons are scattered before interacting with the sample, they will only contribute to the background noise. On the other hand, if scattered after interaction, the electrons might hit the camera in a slightly different location, causing sample blurring. Therefore, minimizing scattering after interaction with the sample is crucial and achieved by placing the sample on the bottom chip.

In STEM mode, the image is constructed pixel by pixel and therefore scattering after interaction with the sample will mostly add to the background noise. However, the best resolution in STEM is achieved by having the smallest probe size (width of the electron beam at the sample surface) possible, as this confines the interaction to the smallest sample area. Scattering before interaction with the sample broadens the probe, which then results in blurring as well, decreasing the resolution. Therefore, in STEM it is most important to limit scattering before interaction with the sample and this can be achieved by placing the sample on the top chip.

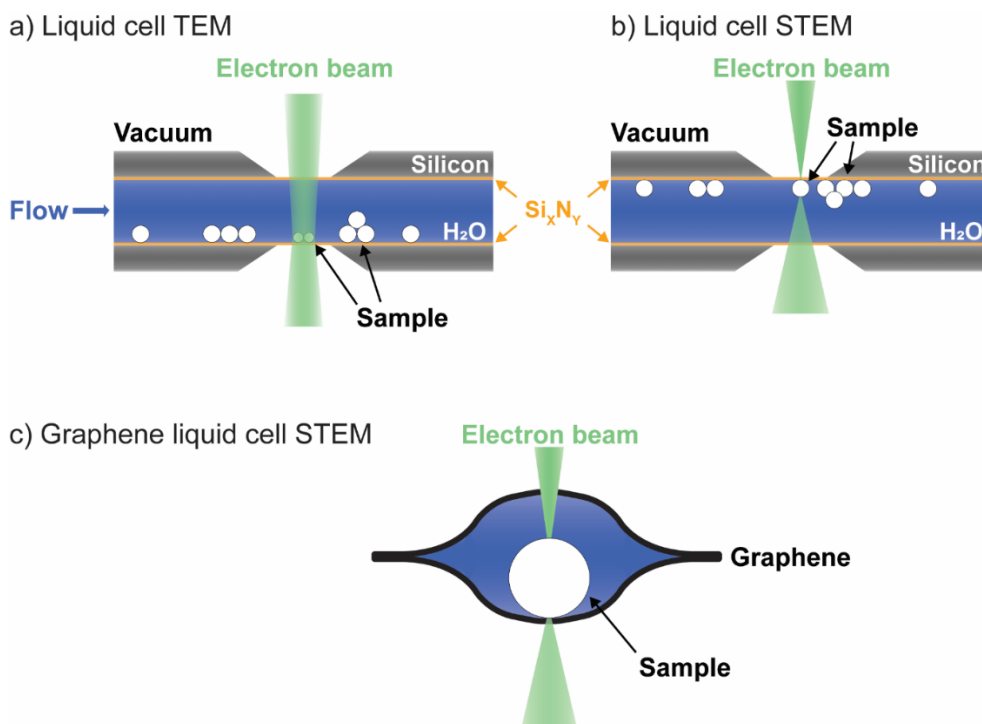


**Figure 1.8.** Different types of liquid cell (S)TEM illustrated, with a) Si chip based liquid cell configuration for transmission mode, b) Si chip based liquid cell configuration for scanning transmission mode and c) graphene sheet liquid cell for STEM.

ETEM and gas cell TEM have already provided many new insights into dynamic processes occurring in nanomaterials in contact with a gas, such as the influence of  $H_2$  on dislocation/defect mobility in stainless steel and aluminum,<sup>105</sup> following the oxidation of a niobium suboxide,<sup>106</sup> observing carbon nanofiber growth<sup>107</sup> and the phase transition of an Au-Si eutectic at the nanoscale,<sup>108</sup> among many others. This is also seen in the field of catalysis, where catalyst synthesis,<sup>93, 109</sup> evolution<sup>110-112</sup> and deactivation<sup>113-115</sup> have been studied in some detail using ETEM and gas cell TEM.

Liquid phase TEM (LP-TEM) work has also allowed visualization of many nanoscale processes occurring in materials in contact with a liquid phase. It has been successfully employed in studying processes such as biomineralization,<sup>116-117</sup> protein movement over a cell membrane,<sup>118</sup> metal nucleation and growth,<sup>119-120</sup> electrochemical deposition and growth,<sup>121-122</sup> oxide stability,<sup>123-126</sup>, chemical stability of gold nanoparticles in different environments,<sup>127</sup> and carbon nanotube degradation by macrophages,<sup>128</sup> among many other processes. Several applications are also emerging in the field of catalyst synthesis<sup>129</sup> and deactivation.

In addition, improvements in technology also allowed for many other types of holders for other in situ experiments. In particular holders for heating and cooling, mechanical testing and biasing are also becoming increasingly more common.<sup>130</sup>

## 1.6 Electron Beam Damage

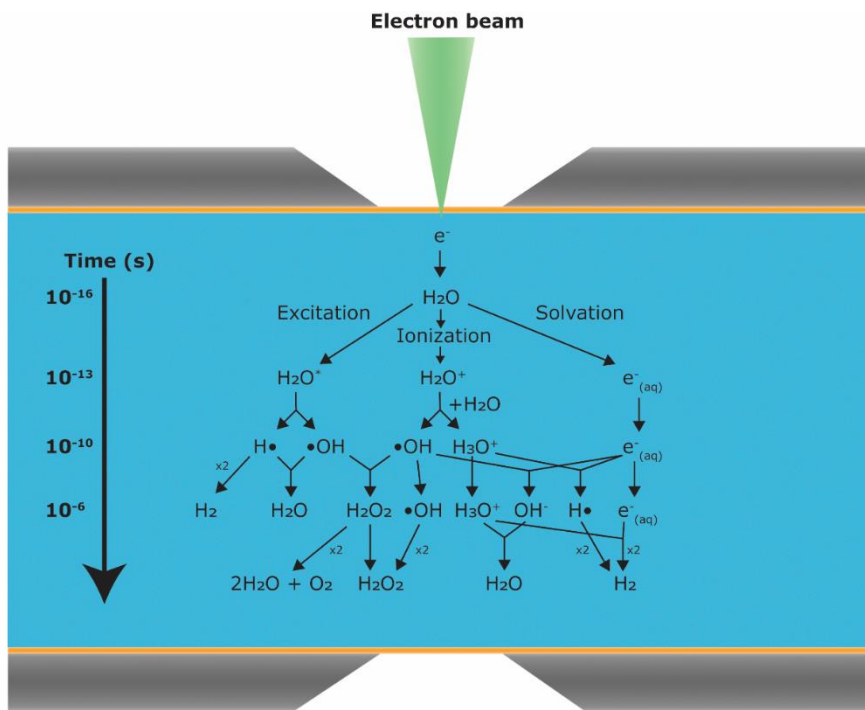
The short de Broglie wavelength and strong interactions of electrons with matter allow for the high resolution of the various electron microscopy techniques, but the electrons can also introduce significant damage in the sample.<sup>78, 131</sup> There are several effects the electron beam can have on the sample, such as charging of the sample, specimen heating, local carbon deposition in the irradiated area from contaminated samples, atomic displacement or knock-on damage, sputtering and radiolysis. These effects can often be reduced by selecting the right imaging conditions (in particular acceleration voltage and beam current used) and proper specimen preparation, but should be kept in mind.

For in situ experiments, especially in LP-TEM, radiolysis is a significantly more important consideration and is usually a limiting factor in the imaging.<sup>102</sup> Apart from direct electron beam induced radiolysis in solid samples in vacuum, often seen in polymers,<sup>132</sup> biological samples<sup>133</sup> and several alkali halides,<sup>134</sup> in the in situ experiments significant radiolysis of the fluid is also present.<sup>135</sup>

Radiolysis in fluids produces many radicals and other highly reactive species.<sup>135-136</sup> An example of this is shown in Figure 1.9, in which the effect of ionizing radiation (high-energy electrons in the case of LP-TEM) on the water molecules is displayed. Following various pathways, ionization or excitation of water molecules produces a number of both oxidizing and reducing radicals and species in the liquid, namely  $\bullet\text{OH}$ ,  $\bullet\text{H}$ ,  $e^{-}(\text{aq})$ ,  $\text{H}_2$ ,  $\text{OH}^{-}$ ,  $\text{H}_3\text{O}^{+}$  and  $\text{H}_2\text{O}_2$ . All of these species can interact with the sample and subsequently alter and/or degrade the material, as is seen in many instances.<sup>137</sup> Radicals also often interfere with the nanoscale processes under investigation, and although usually not desired, these radicals are sometimes used to drive or accelerate the process under investigation.<sup>122, 138</sup> In all cases, but especially when using the beam



to accelerate the process, it is crucial to perform sufficient control experiments – also outside of the electron microscope – to verify whether and to which extent the beam is altering the process.



Transient species yield (molecules/100 electronvolt deposited):

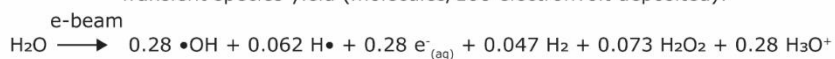


**Figure 1.9.** Scheme of reactions and transient species produced by the irradiation of water with high-energy electrons in a liquid cell. Below is the yield of transient species obtained from electron irradiation of water, in number of molecules produced per 100 electronvolts of energy deposited by the beam. Under typical STEM conditions, the electron beam deposits between  $10^{11} - 10^{12}$  eV/s.

## 1.7 Scope of the Thesis

The aim of this thesis is to explore the capabilities and limitations of liquid phase transmission electron microscopy (LP-TEM) for investigating dynamic processes taking place in solid catalysts in a liquid environment, such as catalyst synthesis and catalyst evolution during a chemical reaction. This involves a detailed exploration of the nanoscale behavior and stability of several important oxidic catalyst supports in LP-TEM, with a focus on the characterization of electron beam effects and strategies to mitigate these effects. Having identified sufficiently stable materials and conditions for LP-TEM studies, the second part of the thesis explores the application of LP-TEM to investigate nanoparticle growth phenomena that are highly relevant for heterogeneous catalysis. By applying this technique in conjunction with several other (S)TEM techniques, new insights could be obtained in the Ostwald ripening mechanisms of gold nanoparticles supported on titanium dioxide and in contact with an aqueous solution of NaCl. Moreover, the study of this Au/TiO<sub>2</sub> catalyst was extended to investigating the deactivation mechanisms during the selective oxidation of 5-(hydroxymethyl)furfural to 2,5-furandicarboxylic acid, demonstrating the promise of LP-TEM for in situ investigations of heterogeneous catalysts.

**Chapter 2** provides an assessment of the stability of 6 different oxides that are commonly used as a catalyst support, when they are in contact with water and being irradiated by the beam. Through the use of commercially available catalyst supports, significant differences in oxide stability were observed that were correlated with the Gibbs free energy of hydration of the oxide. Other properties that might be considered important, such as specific surface area, crystallinity and solubility were found to have negligible influence. Several highly stable oxides have also been identified.

**Chapter 3** reports the origin of the degradation of one of the oxides studied in Chapter 2, namely SiO<sub>2</sub>, in more detail. By using SiO<sub>2</sub> with different degrees of hydroxylation and by changing the chemical environment the SiO<sub>2</sub> is in contact with through varying the liquids and solutes, a mechanism for the silica degradation in LP-TEM was identified. It was found that the formation of reducing radicals, such as •H and e<sup>-</sup><sub>(aq)</sub> by the beam was likely responsible for opening Si-O-Si bonds and the subsequent silica hydroxylation and dissolution. Environmental TEM (ETEM) demonstrated that the presence of even small amounts of water vapor has a significant detrimental effect on silica stability during in situ TEM. Scavenging these reducing radicals in the liquid did however stabilize the silica significantly.

**Chapter 4** focuses on the fundamentals of Ostwald ripening of catalysts in a liquid phase. Having identified TiO<sub>2</sub> as a very stable oxide in Chapter 2, this material was

used as a support for gold nanoparticles, to obtain a model system for Ostwald ripening. This catalyst is quite stable but sinters rapidly in the presence of  $\text{Cl}^-$  ions. When bringing this catalyst in contact with an aqueous solution of NaCl in LP-TEM to follow the process at the individual nanoparticle level, the particle ensemble behavior conformed very well to Ostwald ripening model predictions. At the individual nanoparticle level, the process was found to be remarkably different from model predictions.

**Chapter 5** investigates the mechanisms behind deactivation of Au/TiO<sub>2</sub> catalysts during the selective oxidation of 5-(hydroxymethyl)furfural (HMF) to 2,5-furandicarboxylic acid (FDCA). This was done through systematic variation of the reaction conditions and extracting TEM samples directly from the reaction mixture. It was found that the main cause for deactivation was gold nanoparticle detachment from the support most likely caused by negative charging of both the Au nanoparticles and the support in an alkaline environment. Several strategies to mitigate this deactivation are discussed and tested.

Finally, a summary in both English and Dutch, along with several concluding remarks and future prospects are presented in Chapter 6.

## 1.8 References

- (1). Rowley-Conwy, P., *From Genesis to Prehistory: The Archaeological Three Age System and Its Contested Reception in Denmark, Britain, and Ireland*. Oxford University Press: 2007.
- (2). Callister, W. D.; Rethwisch, D. G., *Materials Science and Engineering: An Introduction*. John Wiley & Sons New York: 2007; Vol. 7.
- (3). Hanefeld, U.; Lefferts, L., *Catalysis: An Integrated Textbook for Students*. John Wiley & Sons: 2018.
- (4). Descorme, C.; Gallezot, P.; Geantet, C.; George, C., Heterogeneous Catalysis: A Key Tool toward Sustainability. *ChemCatChem* **2012**, *4* (12), 1897-1906.
- (5). Centi, G.; Perathoner, S., Catalysis, a Driver for Sustainability and Societal Challenges. *Catal. Today* **2008**, *138* (1-2), 69-76.
- (6). Armstrong, R. C.; Wolfram, C.; De Jong, K. P.; Gross, R.; Lewis, N. S.; Boardman, B.; Ragauskas, A. J.; Ehrhardt-Martinez, K.; Crabtree, G.; Ramana, M., The Frontiers of Energy. *Nature Energy* **2016**, *1*, 15020.
- (7). Rothenberg, G., *Catalysis: Concepts and Green Applications*. John Wiley & Sons: 2017.
- (8). De Jong, K. P., *Synthesis of Solid Catalysts*. John Wiley & Sons: 2013.
- (9). Bartholomew, C. H., Mechanisms of Catalyst Deactivation. *Appl. Catal., A* **2001**, *212* (1-2), 17-60.
- (10). Furimsky, E.; Massoth, F. E., Deactivation of Hydroprocessing Catalysts. *Catal. Today* **1999**, *52* (4), 381-495.
- (11). López, C.; Corma, A., Supported Iron Nanoparticles as Catalysts for Sustainable Production of Lower Olefins. *ChemCatChem* **2012**, *4* (6), 751-752.

- (12). Shroff, M. D.; Kalakkad, D. S.; Coulter, K. E.; Kohler, S. D.; Harrington, M. S.; Jackson, N. B.; Sault, A. G.; Datye, A. K., Activation of Precipitated Iron Fischer-Tropsch Synthesis Catalysts. *J. Catal.* **1995**, *156* (2), 185-207.
- (13). Gong, M.; Li, Y.; Wang, H.; Liang, Y.; Wu, J. Z.; Zhou, J.; Wang, J.; Regier, T.; Wei, F.; Dai, H., An Advanced Ni-Fe Layered Double Hydroxide Electrocatalyst for Water Oxidation. *J. Am. Chem. Soc.* **2013**, *135* (23), 8452-8455.
- (14). Weller, M.; Overton, T.; Rourke, J.; Armstrong, F., *Inorganic Chemistry, 7th Edition*. Oxford University Press, UK: 2018.
- (15). Roduner, E., Size Matters: Why Nanomaterials Are Different. *Chem. Soc. Rev.* **2006**, *35* (7), 583-592.
- (16). Lopez, N.; Janssens, T.; Clausen, B.; Xu, Y.; Mavrikakis, M.; Bligaard, T.; Nørskov, J. K., On the Origin of the Catalytic Activity of Gold Nanoparticles for Low-Temperature CO Oxidation. *J. Catal.* **2004**, *223* (1), 232-235.
- (17). Bezemer, G. L.; Bitter, J. H.; Kuipers, H. P.; Oosterbeek, H.; Holewijn, J. E.; Xu, X.; Kapteijn, F.; van Dillen, A. J.; de Jong, K. P., Cobalt Particle Size Effects in the Fischer-Tropsch Reaction Studied with Carbon Nanofiber Supported Catalysts. *J. Am. Chem. Soc.* **2006**, *128* (12), 3956-3964.
- (18). van Deelen, T. W.; Mejía, C. H.; de Jong, K. P., Control of Metal-Support Interactions in Heterogeneous Catalysts to Enhance Activity and Selectivity. *Nature Catalysis* **2019**, 1-16.
- (19). Doornkamp, C.; Ponec, V., The Universal Character of the Mars and Van Krevelen Mechanism. *J. Mol. Catal. A: Chem.* **2000**, *162* (1-2), 19-32.
- (20). Mars, P.; Van Krevelen, D. W., Oxidations Carried out by Means of Vanadium Oxide Catalysts. *Chem. Eng. Sci.* **1954**, *3*, 41-59.
- (21). Zečević, J.; Vanbutsele, G.; De Jong, K. P.; Martens, J. A., Nanoscale Intimacy in Bifunctional Catalysts for Selective Conversion of Hydrocarbons. *Nature* **2015**, *528* (7581), 245-248.
- (22). Francis, J.; Guillon, E.; Bats, N.; Pichon, C.; Corma, A.; Simon, L., Design of Improved Hydrocracking Catalysts by Increasing the Proximity between Acid and Metallic Sites. *Appl. Catal., A* **2011**, *409*, 140-147.
- (23). Hervier, A.; Renzas, J. R.; Park, J. Y.; Somorjai, G. A., Hydrogen Oxidation-Driven Hot Electron Flow Detected by Catalytic Nanodiodes. *Nano Lett.* **2009**, *9* (11), 3930-3933.
- (24). Whiting, G. T.; Chung, S.-H.; Stosic, D.; Chowdhury, A. D.; van der Wal, L. I.; Fu, D.; Zecevic, J.; Travert, A.; Houben, K.; Baldus, M., Multiscale Mechanistic Insights of Shaped Catalyst Body Formulations and Their Impact on Catalytic Properties. *ACS Catal.* **2019**, *9*, 4792-4803.
- (25). Klemm, R.; Klemm, D., *Gold and Gold Mining in Ancient Egypt and Nubia: Geoarchaeology of the Ancient Gold Mining Sites in the Egyptian and Sudanese Eastern Deserts*. Springer Science & Business Media: 2012.
- (26). Haruta, M., When Gold Is Not Noble: Catalysis by Nanoparticles. *The chemical record* **2003**, *3* (2), 75-87.
- (27). Bond, G.; Sermon, P., Gold Catalysts for Olefin Hydrogenation. *Gold Bulletin* **1973**, *6* (4), 102-105.
- (28). Bond, G. C.; Sermon, P. A.; Webb, G.; Buchanan, D. A.; Wells, P. B., Hydrogenation over Supported Gold Catalysts. *J. Chem. Soc., Chem. Commun.* **1973**, (13), 444b-445.
- (29). Nkosi, B.; Coville, N. J.; Hutchings, G. J., Reactivation of a Supported Gold Catalyst for Acetylene Hydrochlorination. *J. Chem. Soc., Chem. Commun.* **1988**, (1), 71-72.
- (30). Haruta, M.; Kobayashi, T.; Sano, H.; Yamada, N., Novel Gold Catalysts for the Oxidation of Carbon Monoxide at a Temperature Far Below 0 C. *Chem. Lett.* **1987**, *16* (2), 405-408.
- (31). Stratakis, M.; Garcia, H., Catalysis by Supported Gold Nanoparticles: Beyond Aerobic Oxidative Processes. *Chem. Rev.* **2012**, *112* (8), 4469-4506.

- (32). Zhang, Y.; Cui, X.; Shi, F.; Deng, Y., Nano-Gold Catalysis in Fine Chemical Synthesis. *Chem. Rev.* **2011**, *112* (4), 2467-2505.
- (33). Della Pina, C.; Falletta, E.; Prati, L.; Rossi, M., Selective Oxidation Using Gold. *Chem. Soc. Rev.* **2008**, *37* (9), 2077-2095.
- (34). McEwan, L.; Julius, M.; Roberts, S.; Fletcher, J. C., A Review of the Use of Gold Catalysts in Selective Hydrogenation Reactions. *Gold Bull* **2010**, *43* (4), 298-306.
- (35). Haruta, M., Size-and Support-Dependency in the Catalysis of Gold. *Catal. Today* **1997**, *36* (1), 153-166.
- (36). Chheda, J. N.; Huber, G. W.; Dumesic, J. A., Liquid-Phase Catalytic Processing of Biomass-Derived Oxygenated Hydrocarbons to Fuels and Chemicals. *Angew. Chem. Int. Ed.* **2007**, *46* (38), 7164-7183.
- (37). Zhang, Z.; Deng, K., Recent Advances in the Catalytic Synthesis of 2, 5-Furandicarboxylic Acid and Its Derivatives. *ACS Catal.* **2015**, *5* (11), 6529-6544.
- (38). Davis, S. E.; Houk, L. R.; Tamargo, E. C.; Datye, A. K.; Davis, R. J., Oxidation of 5-Hydroxymethylfurfural over Supported Pt, Pd and Au Catalysts. *Catal. Today* **2011**, *160* (1), 55-60.
- (39). Masoud, N.; Donoeva, B.; de Jongh, P. E., Stability of Gold Nanocatalysts Supported on Mesoporous Silica for the Oxidation of 5-Hydroxymethyl Furfural to Furan-2, 5-Dicarboxylic Acid. *Appl. Catal., A* **2018**, *561*, 150-157.
- (40). Nasdaq Gold Price. <https://www.nasdaq.com/market-activity/commodities/gc%3Acmx> (accessed 11-11-2019).
- (41). Ciriminna, R.; Falletta, E.; Della Pina, C.; Teles, J. H.; Pagliaro, M., Industrial Applications of Gold Catalysis. *Angew. Chem. Int. Ed.* **2016**, *55* (46), 14210-14217.
- (42). Nicolau, I.; Colling, P. M.; Johnson, L. R., Palladium-Gold Catalyst for Vinyl Acetate Production. Google Patents: 1997.
- (43). Gao, F.; Goodman, D. W., Pd-Au Bimetallic Catalysts: Understanding Alloy Effects from Planar Models and (Supported) Nanoparticles. *Chem. Soc. Rev.* **2012**, *41* (24), 8009-8020.
- (44). Suzuki, K.; Yamaguchi, T.; Matsushita, K.; Iitsuka, C.; Miura, J.; Akaogi, T.; Ishida, H., Aerobic Oxidative Esterification of Aldehydes with Alcohols by Gold-Nickel Oxide Nanoparticle Catalysts with a Core-Shell Structure. *ACS Catal.* **2013**, *3* (8), 1845-1849.
- (45). Johnston, P.; Carthey, N.; Hutchings, G. J., Discovery, Development, and Commercialization of Gold Catalysts for Acetylene Hydrochlorination. *J. Am. Chem. Soc.* **2015**, *137* (46), 14548-14557.
- (46). Moulijn, J. A.; Van Diepen, A.; Kapteijn, F., Catalyst Deactivation: Is It Predictable?: What to Do? *Appl. Catal., A* **2001**, *212* (1-2), 3-16.
- (47). Boerefijn, R.; Gudde, N.; Ghadiri, M., A Review of Attrition of Fluid Cracking Catalyst Particles. *Adv. Powder Technol.* **2000**, *11* (2), 145-174.
- (48). Contractor, R.; Bergna, H.; Horowitz, H.; Blackstone, C.; Malone, B.; Torardi, C.; Griffiths, B.; Chowdhry, U.; Sleight, A., Butane Oxidation to Maleic Anhydride over Vanadium Phosphate Catalysts. *Catal. Today* **1987**, *1* (1-2), 49-58.
- (49). Wu, D.; Zhou, J.; Li, Y., Mechanical Strength of Solid Catalysts: Recent Developments and Future Prospects. *AIChE J.* **2007**, *53* (10), 2618-2629.
- (50). Oudar, J., *Deactivation and Poisoning of Catalysts*. CRC Press: 1985; Vol. 20.
- (51). Tauster, S., Strong Metal-Support Interactions. *Acc. Chem. Res.* **1987**, *20* (11), 389-394.

- (52). Campisi, S.; Ferri, D.; Villa, A.; Wang, W.; Wang, D.; Kröcher, O.; Prati, L., Selectivity Control in Palladium-Catalyzed Alcohol Oxidation through Selective Blocking of Active Sites. *J. Phys. Chem. C* **2016**, *120* (26), 14027-14033.
- (53). Vannice, M. A.; Sudhakar, C., A Model for the Metal-Support Effect Enhancing Carbon Monoxide Hydrogenation Rates over Platinum-Titania Catalysts. *The Journal of Physical Chemistry* **1984**, *88* (12), 2429-2432.
- (54). Corma, A.; Serna, P.; Concepción, P.; Calvino, J. J., Transforming Nonselective into Chemoselective Metal Catalysts for the Hydrogenation of Substituted Nitroaromatics. *J. Am. Chem. Soc.* **2008**, *130* (27), 8748-8753.
- (55). Wang, L.; Zhang, J.; Zhu, Y.; Xu, S.; Wang, C.; Bian, C.; Meng, X.; Xiao, F.-S., Strong Metal-Support Interactions Achieved by Hydroxide-to-Oxide Support Transformation for Preparation of Sinter-Resistant Gold Nanoparticle Catalysts. *ACS Catal.* **2017**, *7* (11), 7461-7465.
- (56). Menon, P., Coke on Catalysts-Harmful, Harmless, Invisible and Beneficial Types. *J. Mol. Catal.* **1990**, *59* (2), 207-220.
- (57). Otterstedt, J.; Gevert, S.; Jäas, S.; Menon, P., Fluid Catalytic Cracking of Heavy (Residual) Oil Fractions: A Review. *Applied catalysis* **1986**, *22* (2), 159-179.
- (58). Lee, H. C.; Farrauto, R. J., Catalyst Deactivation Due to Transient Behavior in Nitric Acid Production. *Industrial & engineering chemistry research* **1989**, *28* (1), 1-5.
- (59). Biella, S.; Prati, L.; Rossi, M., Selective Oxidation of D-Glucose on Gold Catalyst. *J. Catal.* **2002**, *206* (2), 242-247.
- (60). Menon, P. G., Diagnosis of Industrial Catalyst Deactivation by Surface Characterization Techniques. *Chem. Rev.* **1994**, *94* (4), 1021-1046.
- (61). de Smit, E.; Weckhuysen, B. M., The Renaissance of Iron-Based Fischer-Tropsch Synthesis: On the Multifaceted Catalyst Deactivation Behaviour. *Chem. Soc. Rev.* **2008**, *37* (12), 2758-2781.
- (62). Dai, Y.; Lu, P.; Cao, Z.; Campbell, C. T.; Xia, Y., The Physical Chemistry and Materials Science Behind Sinter-Resistant Catalysts. *Chem. Soc. Rev.* **2018**, *47* (12), 4314-4331.
- (63). Haynes, W. M., *CRC Handbook of Chemistry and Physics*. CRC press: New York, 2014; Vol. 95.
- (64). Masoud, N.; Partsch, T.; de Jong, K. P.; de Jongh, P. E., Thermal Stability of Oxide-Supported Gold Nanoparticles. *Gold Bulletin* **2019**, *52* (2), 105-114.
- (65). Bond, G. C.; Louis, C.; Thompson, D. T., *Catalysis by Gold*. Imperial College Press: London, 2006; Vol. 6.
- (66). Carabineiro, S. A. C.; Silva, A. M. T.; Dražić, G.; Tavares, P. B.; Figueiredo, J. L., Effect of Chloride on the Sinterization of Au/CeO<sub>2</sub> Catalysts. *Catal. Today* **2010**, *154* (3-4), 293-302.
- (67). Yang, F.; Chen, M.; Goodman, D., Sintering of Au Particles Supported on TiO<sub>2</sub> (110) During CO Oxidation. *J. Phys. Chem. C* **2008**, *113* (1), 254-260.
- (68). Von Smoluchowski, M., Drei Vorträge Über Diffusion. Brownsche Bewegung Und Koagulation Von Kolloidteilchen. *Z. Phys.* **1916**, *17*, 557-585.
- (69). Ma, Z.; Brown, S.; Howe, J. Y.; Overbury, S. H.; Dai, S., Surface Modification of Au/TiO<sub>2</sub> Catalysts by SiO<sub>2</sub> Via Atomic Layer Deposition. *J. Phys. Chem. C* **2008**, *112* (25), 9448-9457.
- (70). Lifshitz, I. M.; Slyozov, V. V., The Kinetics of Precipitation from Supersaturated Solid Solutions. *J. Phys. Chem. Solids* **1961**, *19* (1-2), 35-50.
- (71). Wagner, C., Theorie Der Alterung Von Niederschlägen Durch Umlösen (Ostwald-Reifung). *Zeitschrift für Elektrochemie, Berichte der Bunsengesellschaft für physikalische Chemie* **1961**, *65* (7-8), 581-591.

- (72). Kahlweit, M., Ostwald Ripening of Precipitates. *Adv. Colloid Interface Sci.* **1975**, 5 (1), 1-35.
- (73). Finsky, R., On the Critical Radius in Ostwald Ripening. *Langmuir* **2004**, 20 (7), 2975-2976.
- (74). Wynblatt, P.; Gjostein, N. A., Supported Metal Crystallites. *Prog. Solid State Chem.* **1975**, 9, 21-58.
- (75). Granqvist, C. G.; Buhrman, R. A., Size Distributions for Supported Metal Catalysts: Coalescence Growth Versus Ostwald Ripening. *J. Catal.* **1976**, 42 (3), 477-479.
- (76). Wanke, S. E., Comments on the Sintering Mechanism of Supported Metal Catalysts. *J. Catal.* **1977**, 46 (2), 234-237.
- (77). Datye, A. K.; Xu, Q.; Kharas, K. C.; McCarty, J. M., Particle Size Distributions in Heterogeneous Catalysts: What Do They Tell Us About the Sintering Mechanism? *Catal. Today* **2006**, 111 (1-2), 59-67.
- (78). Carter, C. B.; Williams, D. B., *Transmission Electron Microscopy*. Springer-Verlag US: 2009.
- (79). Liu, Z.; Wang, Y.; Yang, H.; Yin, H.; Quan, B.; Xia, X.; Li, W.; Gu, C., Fabrication of Indium Tin Oxide Bump/Pit Structures on GaN-Based Light Emitting Diodes. *Journal of Vacuum Science & Technology B*, **2013**, 31 (1), 011804.
- (80). Chapman, J.; Craven, A.; Scott, C., Electron Detection in the Analytical Electron Microscope. *Ultramicroscopy* **1989**, 28 (1-4), 108-117.
- (81). Goldstein, J. I.; Newbury, D. E.; Michael, J. R.; Ritchie, N. W.; Scott, J. H. J.; Joy, D. C., *Scanning Electron Microscopy and X-Ray Microanalysis*. Springer: 2017.
- (82). Zaluzec, N. J., Theoretical and Experimental X-Ray Peak/Background Ratios and Implications for Energy-Dispersive Spectrometry in the Next-Generation Analytical Electron Microscope. *Microsc. Microanal.* **2016**, 22 (1), 230-236.
- (83). Hren, J., *Introduction to Analytical Electron Microscopy*. Springer Science & Business Media: 2013.
- (84). Koster, A.; Ziese, U.; Verkleij, A.; Janssen, A.; De Jong, K., Three-Dimensional Transmission Electron Microscopy: A Novel Imaging and Characterization Technique with Nanometer Scale Resolution for Materials Science. *The Journal of Physical Chemistry B* **2000**, 104 (40), 9368-9370.
- (85). Zecevic, J.; van der Eerden, A. M. J.; Friedrich, H.; de Jongh, P. E.; de Jong, K. P., Heterogeneities of the Nanostructure of Platinum/Zeolite Y Catalysts Revealed by Electron Tomography. *ACS Nano* **2013**, 7 (4), 3698-3705.
- (86). Midgley, P. A.; Dunin-Borkowski, R. E., Electron Tomography and Holography in Materials Science. *Nat. Mater.* **2009**, 8 (4), 271.
- (87). Frank, J., *Electron Tomography*. Springer: 1992.
- (88). Wang, Z.-L., *Elastic and Inelastic Scattering in Electron Diffraction and Imaging*. Springer Science & Business Media: 2013.
- (89). Egerton, R. F., *Electron Energy-Loss Spectroscopy in the Electron Microscope*. Springer Science & Business Media: 2011.
- (90). Ahn, C. C., *Transmission Electron Energy Loss Spectrometry in Materials Science and the EELS Atlas*. John Wiley & Sons: 2006.
- (91). Wagner, J. B.; Cavalca, F.; Damsgaard, C. D.; Duchstein, L. D. L.; Hansen, T. W., Exploring the Environmental Transmission Electron Microscope. *Micron* **2012**, 43 (11), 1169-1175.
- (92). Hansen, T. W.; Wagner, J. B.; Hansen, P. L.; Dahl, S.; Topsøe, H.; Jacobsen, C. J. H., Atomic-Resolution in Situ Transmission Electron Microscopy of a Promoter of a Heterogeneous Catalyst. *Science* **2001**, 294 (5546), 1508-1510.

- (93). Van den Berg, R.; Elkjaer, C. F.; Gommel, C. J.; Chorkendorff, I.; Sehested, J.; De Jongh, P. E.; De Jong, K. P.; Helveg, S., Revealing the Formation of Copper Nanoparticles from a Homogeneous Solid Precursor by Electron Microscopy. *J. Am. Chem. Soc.* **2016**, *138* (10), 3433-3442.
- (94). Saka, H.; Kamino, T.; Ara, S.; Sasaki, K., In Situ Heating Transmission Electron Microscopy. *MRS Bull.* **2008**, *33* (2), 93-100.
- (95). Huang, J. Y.; Zhong, L.; Wang, C. M.; Sullivan, J. P.; Xu, W.; Zhang, L. Q.; Mao, S. X.; Hudak, N. S.; Liu, X. H.; Subramanian, A., In Situ Observation of the Electrochemical Lithiation of a Single SnO<sub>2</sub> Nanowire Electrode. *Science* **2010**, *330* (6010), 1515-1520.
- (96). Yoshida, K.; Nozaki, T.; Hirayama, T.; Tanaka, N., In Situ High-Resolution Transmission Electron Microscopy of Photocatalytic Reactions by Excited Electrons in Ionic Liquid. *J. Electron Microsc.* **2007**, *56* (5), 177-180.
- (97). Miyata, T.; Fukuyama, M.; Hibara, A.; Okunishi, E.; Mukai, M.; Mizoguchi, T., Measurement of Vibrational Spectrum of Liquid Using Monochromated Scanning Transmission Electron Microscopy-Electron Energy Loss Spectroscopy. *J. Electron Microsc.* **2014**, *63* (5), 377-382.
- (98). Parsons, D.; Matricardi, V.; Moretz, R.; Turner, J., Electron Microscopy and Diffraction of Wet Unstained and Unfixed Biological Objects. In *Advances in Biological and Medical Physics*, Elsevier: 1974; Vol. 15, pp 161-270.
- (99). Marton, L., La Microscopie Electronique Des Objets Biologiques. *Bull. Acad. Roy. Med. Belg* **1935**, *21*, 600-617.
- (100). Heide, H. G., Electron Microscopic Observation of Specimens under Controlled Gas Pressure. *The Journal of cell biology* **1962**, *13* (1), 147-152.
- (101). Parsons, D., Structure of Wet Specimens in Electron Microscopy. *Science* **1974**, *186* (4162), 407-414.
- (102). De Jonge, N.; Ross, F. M., Electron Microscopy of Specimens in Liquid. *Nat. Nanotechnol.* **2011**, *6* (11), 695-704.
- (103). Yuk, J. M.; Park, J.; Ercius, P.; Kim, K.; Hellebusch, D. J.; Crommie, M. F.; Lee, J. Y.; Zettl, A.; Alivisatos, A. P., High-Resolution EM of Colloidal Nanocrystal Growth Using Graphene Liquid Cells. *Science* **2012**, *336* (6077), 61-64.
- (104). Zhu, C.; Liang, S.; Song, E.; Zhou, Y.; Wang, W.; Shan, F.; Shi, Y.; Hao, C.; Yin, K.; Zhang, T., In-Situ Liquid Cell Transmission Electron Microscopy Investigation on Oriented Attachment of Gold Nanoparticles. *Nature communications* **2018**, *9* (1), 421.
- (105). Ferreira, P. J.; Robertson, I.; Birnbaum, H., Hydrogen Effects on the Interaction between Dislocations. *Acta Mater.* **1998**, *46* (5), 1749-1757.
- (106). Sayagués, M.; Hutchison, J., From Nb<sub>12</sub>O<sub>29</sub> to Nb<sub>22</sub>O<sub>54</sub> in a Controlled Environment High-Resolution Microscope. *J. Solid State Chem.* **1999**, *146* (1), 202-210.
- (107). Helveg, S.; López-Cartes, C.; Sehested, J.; Hansen, P. L.; Clausen, B. S.; Rostrup-Nielsen, J. R.; Abild-Pedersen, F.; Nørskov, J. K., Atomic-Scale Imaging of Carbon Nanofibre Growth. *Nature* **2004**, *427* (6973), 426.
- (108). Kim, B.; Tersoff, J.; Wen, C.-Y.; Reuter, M.; Stach, E.; Ross, F., Determination of Size Effects During the Phase Transition of a Nanoscale Au-Si Eutectic. *Phys. Rev. Lett.* **2009**, *103* (15), 155701.
- (109). Creemer, J.; Helveg, S.; Hoveling, G.; Ullmann, S.; Molenbroek, A.; Sarro, P.; Zandbergen, H., Atomic-Scale Electron Microscopy at Ambient Pressure. *Ultramicroscopy* **2008**, *108* (9), 993-998.
- (110). Vendelbo, S.; Elkjær, C. F.; Falsig, H.; Puspitasari, I.; Dona, P.; Mele, L.; Morana, B.; Nelissen, B.; Van Rijn, R.; Creemer, J., Visualization of Oscillatory Behaviour of Pt Nanoparticles Catalysing CO Oxidation. *Nat. Mater.* **2014**, *13* (9), 884.



- (111). Crozier, P. A.; Wang, R.; Sharma, R., In Situ Environmental TEM Studies of Dynamic Changes in Cerium-Based Oxides Nanoparticles During Redox Processes. *Ultramicroscopy* **2008**, *108* (11), 1432-1440.
- (112). Hansen, P. L.; Wagner, J. B.; Helveg, S.; Rostrup-Nielsen, J. R.; Clausen, B. S.; Topsøe, H., Atom-Resolved Imaging of Dynamic Shape Changes in Supported Copper Nanocrystals. *Science* **2002**, *295* (5562), 2053-2055.
- (113). Van den Berg, R.; Parmentier, T. E.; Elkjær, C. F.; Gommès, C. J.; Sehested, J.; Helveg, S.; De Jongh, P. E.; De Jong, K. P., Support Functionalization to Retard Ostwald Ripening in Copper Methanol Synthesis Catalysts. *ACS Catal.* **2015**, *5* (7), 4439-4448.
- (114). Challa, S. R.; Delariva, A. T.; Hansen, T. W.; Helveg, S.; Sehested, J.; Hansen, P. L.; Garzon, F.; Datye, A. K., Relating Rates of Catalyst Sintering to the Disappearance of Individual Nanoparticles During Ostwald Ripening. *J. Am. Chem. Soc.* **2011**, *133* (51), 20672-20675.
- (115). Rodriguez, N.; Kim, M.; Fortin, F.; Mochida, I.; Baker, R., Carbon Deposition on Iron-Nickel Alloy Particles. *Appl. Catal., A* **1997**, *148* (2), 265-282.
- (116). Hendley, C. T.; Tao, J.; Kunitake, J. A. M. R.; De Yoreo, J. J.; Estroff, L. A., Microscopy Techniques for Investigating the Control of Organic Constituents on Biomineralization. *MRS Bull.* **2015**, *40* (06), 480-489.
- (117). Smeets, P. J. M.; Cho, K. R.; Kempen, R. G. E.; Sommerdijk, N. A. J. M.; De Yoreo, J. J., Calcium Carbonate Nucleation Driven by Ion Binding in a Biomimetic Matrix Revealed by in Situ Electron Microscopy. *Nat. Mater.* **2015**, *14* (4), 394-399.
- (118). De Jonge, N.; Peckys, D. B.; Kremers, G. J.; Piston, D. W., Electron Microscopy of Whole Cells in Liquid with Nanometer Resolution. *Proc. Natl. Acad. Sci. U. S. A.* **2009**, *106* (7), 2159-2164.
- (119). Zheng, H.; Smith, R. K.; Jun, Y.-w.; Kisielowski, C.; Dahmen, U.; Alivisatos, A. P., Observation of Single Colloidal Platinum Nanocrystal Growth Trajectories. *Science* **2009**, *324* (5932), 1309-1312.
- (120). Alloyeau, D.; Dachraoui, W.; Javed, Y.; Belkahla, H.; Wang, G.; Lecoq, H.; Ammar, S.; Ersen, O.; Wisnet, A.; Gazeau, F.; Ricolleau, C., Unravelling Kinetic and Thermodynamic Effects on the Growth of Gold Nanoplates by Liquid Transmission Electron Microscopy. *Nano Lett.* **2015**, *15* (4), 2574-2581.
- (121). Sacci, R. L.; Dudney, N. J.; More, K. L.; Parent, L. R.; Arslan, I.; Browning, N. D.; Unocic, R. R., Direct Visualization of Initial SEI Morphology and Growth Kinetics During Lithium Deposition by In Situ Electrochemical Transmission Electron Microscopy. *Chem. Commun.* **2014**, *50* (17), 2104-2107.
- (122). Radisic, A.; Vereecken, P. M.; Hannon, J. B.; Searson, P. C.; Ross, F. M., Quantifying Electrochemical Nucleation and Growth of Nanoscale Clusters Using Real-Time Kinetic Data. *Nano Lett.* **2006**, *6* (2), 238-242.
- (123). Meijerink, M. J.; De Jong, K. P.; Zečević, J., Assessment of Oxide Nanoparticle Stability in Liquid Phase Transmission Electron Microscopy. *Nano Res.* **2019**, *12* (9), 2355-2363.
- (124). Meijerink, M. J.; Spiga, C.; Hansen, T. W.; Damsgaard, C. D.; De Jong, K. P.; Zečević, J., Nanoscale Imaging and Stabilization of Silica Nanospheres in Liquid Phase Transmission Electron Microscopy. *Part. Part. Syst. Charact.* **2019**, *36* (1), 1800374.
- (125). Lu, Y.; Geng, J.; Wang, K.; Zhang, W.; Ding, W.; Zhang, Z.; Xie, S.; Dai, H.; Chen, F.-R.; Sui, M., Modifying Surface Chemistry of Metal Oxides for Boosting Dissolution Kinetics in Water by Liquid Cell Electron Microscopy. *ACS Nano* **2017**, *11* (8), 8018-8025.
- (126). Zečević, J.; Hermannsdörfer, J.; Schuh, T.; De Jong, K. P.; De Jonge, N., Anisotropic Shape Changes of Silica Nanoparticles Induced in Liquid with Scanning Transmission Electron Microscopy. *Small* **2017**, *13* (1), 1602466.
- (127). Hermannsdörfer, J.; de Jonge, N.; Verch, A., Electron Beam Induced Chemistry of Gold Nanoparticles in Saline Solution. *Chem. Commun.* **2015**, *51* (91), 16393-16396.

- (128). Elgrabli, D.; Dachraoui, W.; Ménard-Moyon, C.; Liu, X. J.; Bégin, D.; Bégin-Colin, S.; Bianco, A.; Gazeau, F.; Alloyeau, D., Carbon Nanotube Degradation in Macrophages: Live Nanoscale Monitoring and Understanding of Biological Pathway. *ACS Nano* **2015**, *9* (10), 10113-10124.
- (129). Krans, N. A.; Ahmad, N.; Alloyeau, D.; de Jong, K.; Zečević, J., Attachment of Iron Oxide Nanoparticles to Carbon Nanofibers Studied by in-Situ Liquid Phase Transmission Electron Microscopy. *Micron* **2019**, *117*, 40-46.
- (130). Ferreira, P.; Mitsuishi, K.; Stach, E., In Situ Transmission Electron Microscopy. *MRS Bull.* **2008**, *33* (2), 83-90.
- (131). Egerton, R. F.; Li, P.; Malac, M., Radiation Damage in the TEM and SEM. *Micron* **2004**, *35* (6), 399-409.
- (132). Libera, M. R.; Egerton, R. F., Advances in the Transmission Electron Microscopy of Polymers. *Polymer Reviews* **2010**, *50* (3), 321-339.
- (133). Glaeser, R. M., Limitations to Significant Information in Biological Electron Microscopy as a Result of Radiation Damage. *Journal of ultrastructure research* **1971**, *36* (3-4), 466-482.
- (134). Itoh, N., Mechanism of Electron-Excitation-Induced Defect Creation in Alkali Halides. *Radiation Effects* **1982**, *64* (1-4), 161-169.
- (135). Schneider, N. M.; Norton, M. M.; Mendel, B. J.; Grogan, J. M.; Ross, F. M.; Bau, H. H., Electron-Water Interactions and Implications for Liquid Cell Electron Microscopy. *J. Phys. Chem. C* **2014**, *118* (38), 22373-22382.
- (136). Spothem-Maurizot, M.; Mostafavi, M.; Douki, T., *Radiation Chemistry: From Basics to Applications in Material and Life Sciences*. EDP Sciences: 2008.
- (137). Woehl, T.; Abellan, P., Defining the Radiation Chemistry During Liquid Cell Electron Microscopy to Enable Visualization of Nanomaterial Growth and Degradation Dynamics. *Journal of microscopy* **2017**, *265* (2), 135-147.
- (138). Evans, J. E.; Jungjohann, K. L.; Browning, N. D.; Arslan, I., Controlled Growth of Nanoparticles from Solution with in Situ Liquid Transmission Electron Microscopy. *Nano Lett.* **2011**, *11* (7), 2809-2813.

## Chapter 2

# Assessment of Oxide Nanoparticle Stability in Liquid Phase Transmission Electron Microscopy

### Abstract

Studying liquid phase nanoscale dynamic processes of oxide nanoparticles is of considerable interest to a wide variety of fields. Recently developed liquid phase transmission electron microscopy (LP-TEM) is a promising technique, but destabilization of oxides by solid-liquid-electron interactions remains an important challenge. In this chapter we present a methodology to assess LP-TEM oxide stability in an aqueous phase, by subjecting several oxides of technological importance to a controlled electron dose in water. We show a correlation based on the Gibbs free energy of oxide hydration that can be used to assess the stability of oxides and demonstrate the existence of several remarkably stable oxides, with no observable structural changes after one hour of electron beam irradiation in LP-TEM. Rationalizing such destabilization phenomena combined with the identification of stable oxides allows for designing LP-TEM experiments free from adverse beam effects and thus investigations of numerous relevant nanoscale processes in water.

This chapter is based on: Meijerink, M. J.; De Jong, K. P.; Zečević, J., Assessment of oxide nanoparticle stability in liquid phase transmission electron microscopy. *Nano Res.* **2019**, *12* (9), 2355-2363.

## 2.1 Introduction

Since time immemorial, oxides have been incredibly important materials in a wide variety of applications, from ancient pottery to modern superconductors. Industrial applications include heterogeneous catalysts, where nanoparticle oxides are often used as support or catalyst,<sup>1-4</sup> structural and refractory ceramics such as bricks or concrete,<sup>5</sup> or semiconductors,<sup>6-7</sup> adsorbents,<sup>8</sup> superconductors,<sup>9</sup> and protective coatings.<sup>10</sup>

Properties and performance of oxides in many of these applications are dictated by nanometer scale structural features. Influence of the catalyst nanoparticle size,<sup>11</sup> morphology<sup>12</sup> and nanoparticle support interactions<sup>4, 13</sup> on catalyst activity, selectivity and stability, the morphology and nature of nanoscale defects on corrosion,<sup>14-15</sup> or the presence of nanometer-sized defects in oxide boundary layers on semiconductor performance<sup>16</sup> are all important examples of how nanoscale features can influence overall oxide behavior.

Transmission electron microscopy (TEM) has been an indispensable tool to this end, allowing visualization of nanoscale morphology and atomic structure of a variety of oxide materials.<sup>17-19</sup> However, due to the high vacuum conditions under which TEM is operated, studies were limited to dry samples, which excludes the option to investigate the material during its formation or subsequent application. In recent years, the development of technologies for in situ heating,<sup>20</sup> gas<sup>21-25</sup> and in particular liquid<sup>26-28</sup> TEM measurements has expanded the possibilities for characterization of nanomaterials and nanoscale processes dramatically.

Liquid phase TEM (LP-TEM) is particularly relevant to studying the formation of nanoscale oxide systems, such as nanoparticle nucleation and growth, as many of these processes take place in a liquid. Furthermore, LP-TEM also allows the study of the liquid-based processes involving oxide materials. For example, in catalyst synthesis,<sup>29</sup> often small metal or metal oxide nanoparticles are deposited on a thermally stable and high surface area oxide, such as  $\text{Al}_2\text{O}_3$  or  $\text{SiO}_2$ , in a liquid phase. Knowledge of the nanoscale processes involved in such syntheses is incomplete, thus limiting our ability to control the catalyst structure.<sup>4</sup> Despite the massive body of work on catalyst synthesis and a large variety of preparation methods, this lack of fundamental knowledge results in catalyst preparation often being considered more of an art rather than a science.<sup>30</sup> Furthermore, stability of catalysts in liquid phase reactions, in particular for biomass conversion,<sup>31-32</sup> is highly important, but still poorly understood. Other processes of significant interest are metal corrosion<sup>33</sup> and battery

assembly and operation.<sup>34</sup> These fields, among many others, could therefore greatly benefit from the application of LP-TEM.

The most popular method to perform LP-TEM experiments is by utilizing the closed cell design,<sup>35</sup> which encloses the sample and liquid between two silicon chips with silicon nitride windows in a dedicated holder, although enclosing liquids between two graphene layers<sup>36-37</sup> or differential aperture pumping techniques have also been reported.<sup>38</sup> The closed cell technique has already been employed to study nanoscale dynamic processes such as biomineralization,<sup>39-40</sup> carbon nanotube degradation by macrophages,<sup>41</sup> nanoparticle movement and interactions,<sup>42-43</sup> and electrochemical deposition and growth.<sup>44-45</sup>

The majority of the published articles still highlight an important challenge in LP-TEM though, which is distinguishing electron beam induced effects from the phenomena under investigation. Along with the beam damage mechanisms already known from conventional TEM imaging in a vacuum, LP-TEM additionally suffers effects originating from interactions of the electron beam with the liquid. The main result of these interactions is radiolysis of the liquid and the subsequent formation of radicals and other reactive chemical species which can locally alter liquid chemistry.<sup>46</sup> This beam-induced effect can be and has been used to initiate and drive nanoscale processes, such as nucleation and growth of nanoparticles.<sup>47-48</sup> However, it is mostly considered detrimental to the process under investigation, as it was shown to significantly alter the structure or even lead to dissolution of the materials under investigation.<sup>49</sup>

Although this effect is well-known for biological and carbonaceous samples,<sup>50</sup> most LP-TEM studies so far have focused on metal nanoparticles, while the understanding of oxide degradation behavior is still limited. Recent investigations on iron (hydr)oxide<sup>51</sup> and silicon dioxide<sup>52-54</sup> (see also Chapter 3 of this thesis) have shown that oxide materials can also suffer from electron beam induced destabilization in a liquid environment. In addition, Lu et al.<sup>55</sup> investigated dissolution behavior of several oxides in LP-TEM. They observed a significant increase in dissolution rate of the oxides in the presence of the electron beam, which was attributed to the electron beam induced formation of oxygen vacancies. However, they also observed significant variations in stability and dissolution rate between the oxides, which could not be fully explained by this mechanism.

In view of growing interest in using LP-TEM to study oxide materials, it is of vital importance to improve our understanding of these degradation phenomena and to devise methodologies to suppress them. The goal of our study was to systematically investigate the factors contributing to oxide destabilization in LP-TEM, for which we

selected six technologically important and widely used oxides, namely silica, alumina, magnesia, titania, niobia and zirconia. The stability of oxides imaged in an LP-TEM environment ranged from fully stable ones to those that dissolve within minutes of exposure to the electron beam. We discovered that the oxide stability directly correlates with the extent to which the formation of the respective hydroxide is thermodynamically favored. This correlation is an excellent requisite that will aid in predicting the behavior of oxides during LP-TEM experiments. Furthermore, it can be used to select suitable oxides, i.e. those not affected by the combination of an electron beam and water, for LP-TEM studies of nanoscale processes in water.

## **2.2 Results**

### **2.2.1 Materials Characterization**

For this study we have selected SiO<sub>2</sub>, Al<sub>2</sub>O<sub>3</sub>, MgO, TiO<sub>2</sub>, ZrO<sub>2</sub> and Nb<sub>2</sub>O<sub>5</sub>. Before introducing them to liquid phase transmission electron microscopy and studying their stability and behavior, we performed a study of their bulk physicochemical properties. Table 2.1 summarizes the main properties of the oxides used in this work.

In nitrogen physisorption the MgO and calcined Nb<sub>2</sub>O<sub>5</sub> (c-Nb<sub>2</sub>O<sub>5</sub>) samples exhibited a type II N<sub>2</sub> sorption isotherm (Supporting Figure S2.1(c) and S2.1(h) in the appendix), indicating a macroporous (pores > 50 nm) morphology. For the other oxides, a type IV isotherm was observed, indicating the presence of mesoporosity (2–50 nm pores) (Figure S2.1). For all mesoporous oxides, a H<sub>3</sub> type of hysteresis was observed, usually associated with non-rigid aggregates of primary particles<sup>56</sup> and often indicative of non-spherical particles. Except for the case of the amorphous TiO<sub>2</sub>, the oxides did not display significant microporosity (pores < 2 nm). Specific surface areas varied significantly between the oxides, from 9 m<sup>2</sup>·g<sup>-1</sup> for c-Nb<sub>2</sub>O<sub>5</sub> to almost 300 m<sup>2</sup>·g<sup>-1</sup> for the amorphous TiO<sub>2</sub> sample. Pore volumes also varied, from < 0.1 mL·g<sup>-1</sup> for the MgO and c-Nb<sub>2</sub>O<sub>5</sub> to 0.44 mL·g<sup>-1</sup> for the Al<sub>2</sub>O<sub>3</sub>.

TEM supported these observations, as can be observed in Figure 2.1, with all of the materials consisting of agglomerates of nanoparticles, albeit with different primary particle size. In the case of MgO and c-Nb<sub>2</sub>O<sub>5</sub> (Figure 2.1(c) and 2.1(h)), the primary particles were too large for any significant capillary condensation to take place in the interparticle space during N<sub>2</sub> physisorption, explaining the lack of hysteresis in the isotherm and lack of mesoporosity observed. The other oxides had significantly smaller primary particle sizes, often non-spherical, leading to the presence of interparticle mesoporosity, and thus occurrence of capillary condensation. In the case of niobic acid, intraparticle mesopores of about 5 nm were present next to the interparticle mesoporosity, as highlighted in the magnified part of Figure 2.1(g) and

reported before.<sup>57</sup> In the case of amorphous TiO<sub>2</sub> the primary particle size was only a few nm, giving rise to micropores in addition to the mesopores, as can be observed in the magnified part of Figure 2.1(e). Furthermore, the oxides with the smaller primary particle size, as expected, displayed larger Brunauer–Emmett–Teller (BET) specific surface area.

**Table 2.1.** Summary of the characterization results for all oxides used in this research.

Oxide	BET surface area (m <sup>2</sup> ·g <sup>-1</sup> )	Total pore volume* (cm <sup>3</sup> ·g <sup>-1</sup> )	TGA total mass loss (% of initial)	MS species detected (-)	XRD crystal structures (-)
Stöber SiO <sub>2</sub>	49	0.38	0.4	—	Amorphous
Puralox Al <sub>2</sub> O <sub>3</sub>	145	0.44	5.0	H <sub>2</sub> O, CO <sub>2</sub>	<i>Fd<math>\bar{3}m</math></i> ( $\gamma$ -Al <sub>2</sub> O <sub>3</sub> )
MgO	22	0.01	3.1	CO <sub>2</sub>	<i>Fm<math>\bar{3}m</math></i> (periclase)
ZrO <sub>2</sub>	97	0.25	2.7	H <sub>2</sub> O, CO <sub>2</sub>	<i>P2<sub>1</sub>/c</i> (Baddeleyite)
P25 TiO <sub>2</sub>	45	0.16	-1.3	—	<i>P42/mnm</i> (rutile) <i>I 4<sub>1</sub>/amd</i> (anatase)
Amorphous TiO <sub>2</sub>	292	0.28	16.0	H <sub>2</sub> O	Amorphous
Niobic acid	155	0.18	12.5	H <sub>2</sub> O	Amorphous
Calcined Nb <sub>2</sub> O <sub>5</sub>	9	0.04	-0.1	—	<i>P2/m</i> (H-Nb <sub>2</sub> O <sub>5</sub> )

\*From nitrogen physisorption at  $p/p_0 = 0.9$

X-ray diffractograms of the oxides (summarized in Table 2.1 and Supporting Figure S2.2) confirmed that the oxides are present in the expected crystal structures and that the amorphous TiO<sub>2</sub>, Stöber SiO<sub>2</sub> and niobic acid are indeed non-crystalline.

Finally, thermogravimetric analysis (TGA) coupled with mass spectrometry (MS) in an O<sub>2</sub>/Ar atmosphere (summarized in Table 2.1 and Supporting Figure S2.3) showed that several oxides still contained water, which was expected and poses no problem for the LP-TEM experiments which take place in H<sub>2</sub>O. The commercial MgO, Al<sub>2</sub>O<sub>3</sub> and ZrO<sub>2</sub> powders released also significant amounts of CO<sub>2</sub>. In the case of MgO, this can be attributed to adsorption of carbon dioxide from air leading to formation of a surface carbonate, which is a well-known phenomenon for this oxide.<sup>58</sup> The most significant mass loss and CO<sub>2</sub> MS signal was also observed at the expected

decomposition temperature for  $\text{MgCO}_3$  at approximately  $350^\circ\text{C}$ , indicating that the origin of the observed  $\text{CO}_2$  is likely from a  $\text{MgCO}_3$  surface carbonate. For the  $\text{ZrO}_2$  and  $\text{Al}_2\text{O}_3$ , this  $\text{CO}_2$  probably originated from the preparation method that might have involved the use of metal alkoxides.

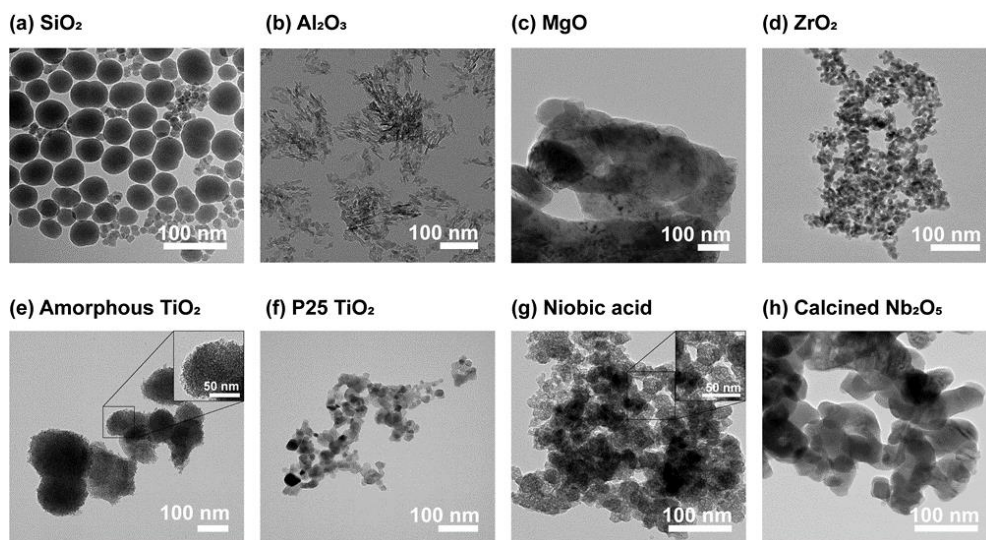


**Figure 2.1.** Bright-field transmission electron microscopy images in vacuum of the oxides used in this research: (a) Stöber  $\text{SiO}_2$ , (b) Puralox  $\gamma\text{-Al}_2\text{O}_3$ , (c)  $\text{MgO}$ , (d)  $\text{ZrO}_2$ , (e) amorphous  $\text{TiO}_2$ , with the primary particles visible in the inset, (f) P25  $\text{TiO}_2$  with some dark regions due to diffraction contrast, (g) niobic acid, with  $\sim 5$  nm mesopores visible in the inset, (h) calcined  $\text{Nb}_2\text{O}_5$ .

### 2.2.2 Liquid Phase Transmission Electron Microscopy

The stability and behavior of all aforementioned oxides in LP-TEM was investigated. While detailed explanation of preparation and imaging conditions can be found in the Materials & Methods section, it is important to note that oxides as received or synthesized were placed in an LP-TEM cell containing water and that imaging was performed in scanning TEM (STEM) mode whereby a focused beam of electrons is raster scanned across the field of view.

Imaging metal and metal oxide nanoparticles in liquid environment with the spread parallel (TEM) electron beam has been shown to lead to dissolution and degradation of the material under investigation, while imaging with a scanning electron beam (STEM) also introduced shape changes associated with the scanning direction of the beam.<sup>52</sup> As a control experiment, a sample of each oxide was also subjected to continuous electron beam scanning in high vacuum, using a comparable or slightly higher cumulative electron dose and electron dose rate ( $1.9 \cdot 10^7 \text{ e}^- \cdot \text{nm}^{-2}$  and  $5.2 \cdot 10^3$



$e^- \cdot \text{nm}^{-2} \cdot \text{s}^{-1}$ , respectively, for the vacuum experiments). Apart from carbon contamination depositing during scanning of some samples, in particular the  $\text{SiO}_2$  and P25  $\text{TiO}_2$  samples, no changes in particle morphology were observed for any of the oxides during these experiments (Supporting Figure S2.4 in the appendix).

In LP-TEM however, shape and size changes were apparent and occurred to varying degrees, indicating that the overall stability was markedly different between the studied oxides, as illustrated in Figure 2.2 and Supporting Figure S2.5, with the latter containing several frames of the supporting Movies MI-M4 (available online,<sup>59</sup> details in the appendix). As reported previously,<sup>52</sup> spherical  $\text{SiO}_2$  nanoparticles significantly elongated along the scanning direction of the electron beam and lost material during this process; when changing the scanning direction, the particle elongation changed accordingly (Figure 2.2(a) and 2.2(b), Movie MI and Supporting Figure S2.5(a)).

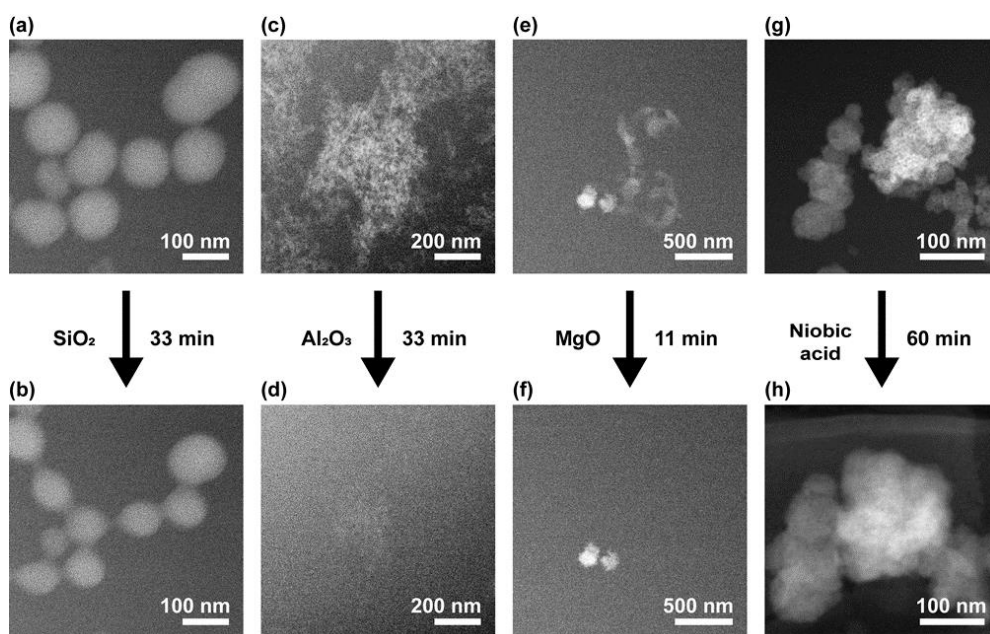


**Figure 2.2.** Overview of LP-TEM behavior of the studied oxides with low stability. (a) and (b) Stöber  $\text{SiO}_2$  before and after 33 min. of imaging (dose rate:  $5.2 \cdot 10^3 e^- \cdot \text{nm}^{-2} \cdot \text{s}^{-1}$ ), (c) and (d)  $\gamma\text{-Al}_2\text{O}_3$  before and after 33 min. of imaging (dose rate:  $1.3 \cdot 10^3 e^- \cdot \text{nm}^{-2} \cdot \text{s}^{-1}$ ), (e) and (f)  $\text{MgO}$  before and after 11 min. of imaging, with some  $\text{ZrO}_2$  contamination (two bright particles in the lower left corner of the agglomerate) (dose rate:  $3.3 \cdot 10^3 e^- \cdot \text{nm}^{-2} \cdot \text{s}^{-1}$ ), (g) and (h) niobic acid before and after 60 min. of imaging (dose rate:  $1.0 \cdot 10^4 e^- \cdot \text{nm}^{-2} \cdot \text{s}^{-1}$ ).

$\text{Al}_2\text{O}_3$  and  $\text{MgO}$  on the other hand did not show this elongation behavior (Figure 2.2(c)-2.2(f), Movies M1 and M2, Supporting Figures S2.5(b) and S2.5(c)), but did dissolve significantly faster than the silica. Although reduced in size,  $\text{SiO}_2$  particles were still present after 33 min of scanning, while for both  $\text{Al}_2\text{O}_3$  and  $\text{MgO}$  no material could be detected after 12 and 2 minutes respectively, for the highest dose rates used. This despite the fact that the dose rate for the  $\text{Al}_2\text{O}_3$  was comparable to that of the  $\text{SiO}_2$  experiments and was significantly lower for the  $\text{MgO}$  experiments (details on dose rates are available in the methods and Supporting Tables S2.1–S2.3 in the appendix for the  $\text{SiO}_2$ ,  $\text{Al}_2\text{O}_3$  and  $\text{MgO}$ , respectively).

In the case of  $\text{Al}_2\text{O}_3$ , two stages can be distinguished (see Movie M2 and Supporting Figure S2.5(b)). In the initial stage the contrast between particle and liquid decreased a lot, indicating thinning in the direction of the beam, as contrast in these experiments is mainly governed by the atomic number of the elements and the aluminum oxide particle thickness. During the second stage, the particles decreased in size, but interestingly, the shape remained unchanged. For  $\text{MgO}$ , particles tended to move during imaging despite initially being fixed to the window of the LP-TEM cell, and they dissolved even more quickly than the alumina (Figure 2.2(e) and 2.2(f), Supporting Figure S2.5(c) and Movie M3). It was therefore challenging to evaluate contrast differences. Both shape changes and reduction in size were observed but appeared not to be correlated with the electron beam scanning direction.

A semi-quantification of the oxide volume at different times during the experiment has also been performed based on the respective TEM images. The volume of the material in the field of view was estimated by measuring particle length and width of all particles present in the image and assuming perfectly spheroidal particles in the case of  $\text{SiO}_2$  and  $\text{MgO}$ . In the case of  $\text{Al}_2\text{O}_3$ , volume was determined by assuming a linear relationship between pixel intensity and alumina thickness and subsequently integrating over the entire image. Volume loss for the individual experiments has been summarized in Supporting Tables S2.1–S2.3.

For each of these three oxides, the volume as a function of time of a representative experiment has also been plotted in Figure 2.3. This clearly illustrates the large differences in stability between these oxides, with  $\text{MgO}$  losing far more volume than  $\text{Al}_2\text{O}_3$  or  $\text{SiO}_2$ , even though the electron beam current was the same in all experiments.

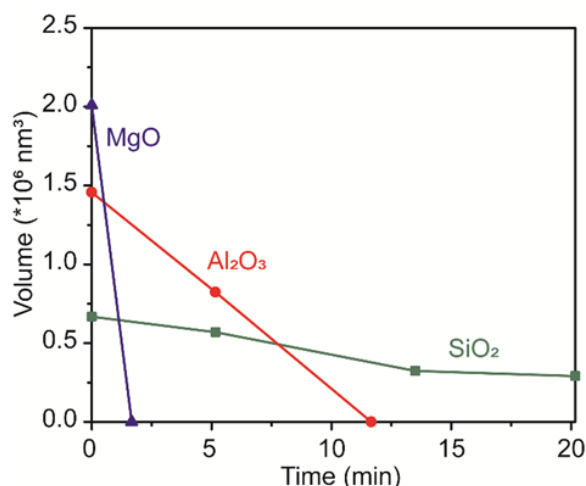


**Figure 2.3.** A representative experiment of each oxide of low stability, except niobic acid, following their volume in  $\text{nm}^3$  over time, all with an electron beam current of  $0.21 \text{ nA}$  ( $1.3 \cdot 10^9 \text{ e}^- \cdot \text{s}^{-1}$ ).

For niobic acid, the behavior in LP-TEM was very different from the previous three oxides (Figure 2.2(g) and 2.2(h), Supporting Figure S2.5(d) and Movie M4). Instead of reducing in size, the particles seemed to grow or swell and became more rounded, while the mesopores of  $\sim 5 \text{ nm}$  disappeared over time. The contrast also decreased, indicating thinning in the direction of the electron beam. This could originate from the oxide particles slowly collapsing and spreading on the surface of the  $\text{Si}_x\text{N}_y$  window. All of the observed effects occurred much slower than in the previous three oxides, with imaging time reaching 60 minutes without niobic acid dissolving and disappearing, using a dose rate of  $5.2 \cdot 10^3 \text{ e}^- \cdot \text{nm}^{-2} \cdot \text{s}^{-1}$ .

Surprisingly, the  $\text{c-Nb}_2\text{O}_5$ ,  $\text{ZrO}_2$ , amorphous  $\text{TiO}_2$  and P25  $\text{TiO}_2$  oxides appeared to be highly stable under these LP-TEM imaging conditions, as illustrated in Figure 2.4, Supporting Figure S2.6 and Movies M5–M8. Apart from some movement during imaging, no significant changes in shape, size or contrast were observed for any of these oxides, even after 60 minutes of imaging with a dose rate of  $5.2 \cdot 10^3 \text{ e}^- \cdot \text{nm}^{-2} \cdot \text{s}^{-1}$ . However, the P25  $\text{TiO}_2$ ,  $\text{ZrO}_2$  and  $\text{c-Nb}_2\text{O}_5$  showed an interesting “flashing” phenomenon involving the occasional formation, growth and disappearance of very bright spots at the surface of the oxide, as can be observed in the Movies M5, M6 and M8 and a still-frame depicting one such bright spot in Figure 2.4(g). Such a phenomenon was not observed in the case of the amorphous  $\text{TiO}_2$  or any of the less stable oxides from Figure 2.2. Although not fully understood yet, this “flashing” is tentatively ascribed to a local charging of the sample, which can result in changes in the deflection angle of electrons passing through the sample.<sup>17, 60</sup>

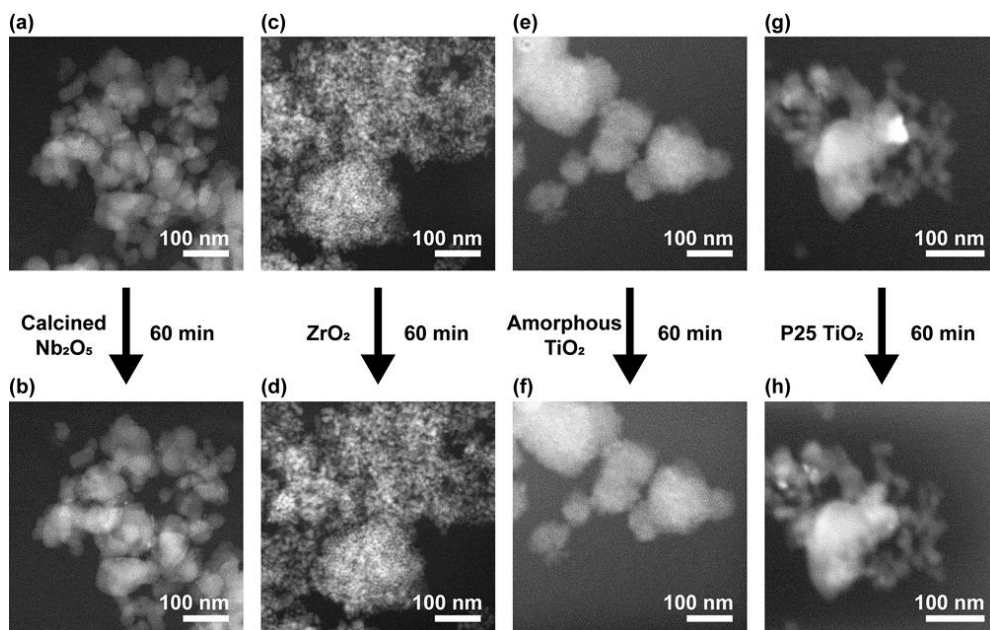


**Figure 2.4.** Overview of LP-TEM behavior for the stable oxides. (a) and (b) Calcined  $\text{Nb}_2\text{O}_5$  before and after 60 min. of imaging. (c) and (d)  $\text{ZrO}_2$  before and after 60 min. of imaging. (e) and (f) Amorphous  $\text{TiO}_2$  before and after 60 min. of imaging. (g) and (h) P25  $\text{TiO}_2$  before and after 60 min. of imaging. The dose rate in each experiment was  $5.2 \cdot 10^3 \text{ e}^- \cdot \text{nm}^{-2} \cdot \text{s}^{-1}$ , except for the P25  $\text{TiO}_2$ , in which the dose rate was  $1.0 \cdot 10^4 \text{ e}^- \cdot \text{nm}^{-2} \cdot \text{s}^{-1}$ .

## 2.3 Discussion

As demonstrated with LP-TEM, oxides which are generally stable in aqueous environments at neutral or mildly acidic pH<sup>61</sup> can exhibit large differences in stability when irradiated with electrons in an aqueous environment. Some oxides degraded rapidly, while others remained stable during one hour of continuous imaging. Furthermore, all oxides were proven to be stable when either the electron beam or the water is absent, highlighting the detrimental effect of combining electron beam and water.

To understand the origin of these differences in stability in LP-TEM, we first consider some of the major physicochemical properties that are known to influence oxide stability in water (Tables 2.1 and 2.2). First such is solubility at neutral or mildly acidic pH, as calculations indicate that electron beam induced water radiolysis produces, among other species, a significant number of hydronium ions ( $\text{H}_3\text{O}^+_{(\text{aq})}$ ) and solvated electrons ( $\text{e}^-_{(\text{aq})}$ ). This results in a local decrease in pH to approximately 4-5, depending

on the intensity of the ionizing radiation.<sup>62</sup> The solubility under these conditions varies between the oxides studied here and ranges from  $2.5 \cdot 10^{-12} \text{ mol} \cdot \text{L}^{-1}$  for zirconia to  $1.6 \cdot 10^{-3} \text{ mol} \cdot \text{L}^{-1}$  for silica, as summarized in Table 2.2. Although the oxides that appeared stable in LP-TEM also have a very low solubility, the oxide with the highest solubility of all is  $\text{SiO}_2$ , which proved to be much more stable than either  $\text{Al}_2\text{O}_3$  or  $\text{MgO}$ , both of which exhibit lower solubility than  $\text{SiO}_2$ . Furthermore, it has been argued that in aqueous environments subjected to intense ionizing radiation, local supersaturation could be present,<sup>55</sup> suggesting that solubility is not the major cause for the observed differences in stability.

**Table 2.2.** Solubility and standard Gibbs free energy for reaction 2.1 per mole of metal for various oxides.

Oxide	Solubility in $\text{H}_2\text{O}$ ( $\text{mol}_{\text{metal}} \cdot \text{L}^{-1}$ )	$\Delta G^0_{\text{Hydration}}$ ( $\text{kJ} \cdot \text{mol}_{\text{metal}}^{-1}$ )	References
Amorphous $\text{SiO}_2$	1.6E-03	-8.0	61, 63-64
$\gamma\text{-Al}_2\text{O}_3$	1.6E-08	-18	63-65
$\text{MgO}$	1.8E-04	-27	63-65
$\text{Nb}_2\text{O}_5$	2.5E-08	52	61, 66
$\text{TiO}_2$	1.0E-09	46	63, 67
$\text{Ti}_2\text{O}_3$	—	16	63-65
$\text{TiO}$	—	34	63-65
$\text{ZrO}_2$	2.5E-12	30	63-65
$\text{CeO}_2$	—	110	61
$\text{Ce}_2\text{O}_3$	1.6E-06	-59	61, 64, 68
$\text{CuO}$	2.0E-10	13	63-65
$\text{Cu}_2\text{O}$	—	-63	61, 63-65
$\text{Fe}_2\text{O}_3$	4.0E-12	12	63-65
$\text{FeO}$	3.2E-10	-6.6	63-65

Second, morphological differences, including surface area, porosity and particle morphology vary widely between the studied oxides (Table 2.1). Specific surface area in particular could be considered as a potential cause of difference in the stability, since it relates to the contact area between liquid and oxide, allowing for more

interaction. However, no clear correlation was found between any of the textural properties and oxide stability either. Comparing for example SiO<sub>2</sub>, Al<sub>2</sub>O<sub>3</sub> and MgO, with MgO having the lowest specific surface area of these oxides and Al<sub>2</sub>O<sub>3</sub> the highest, both were less stable than SiO<sub>2</sub>, demonstrating that surface area does not seem to dominate stability.

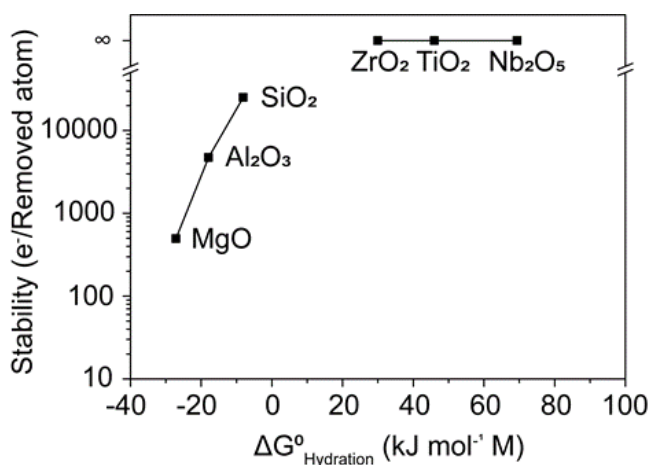
Third, crystallinity and residual water content does not seem to affect the stability of TiO<sub>2</sub>, but interestingly, it did relate to an effect on the stability of niobia, with the amorphous and hydrated niobic acid not being completely stable, as opposed to the crystalline Nb<sub>2</sub>O<sub>5</sub>. The main difference between niobic acid and calcined niobia is that water forms significantly stronger bonds in the former than in the latter,<sup>69</sup> to the extent that niobic acid is a highly acidic oxide. In the completely stable amorphous TiO<sub>2</sub> on the other hand, even though it is also a precipitated form of a relatively ill-defined and non-calcined oxide, the water does not form similar strong bonds. This indicates that chemical bond formation of water with the oxide is of significant importance to the stability of the oxides. To confirm this hypothesis, we compared the thermodynamic driving force for the formation of the hydroxide from the oxide in water (Reaction 2.1), that is, the Gibbs free energy for the hydration reaction ( $\Delta G^0_{\text{H}}$ ) of the investigated oxides.



Figure 2.5 clearly illustrates the correlation between oxide stability and the  $\Delta G^0_{\text{H}}$  (values listed in Table 2.2), with all stable oxides having a positive  $\Delta G^0_{\text{H}}$ , favoring the oxide over the hydroxide. On the other hand, the  $\Delta G^0_{\text{H}}$  is negative for the unstable oxides, favoring the hydroxide. As a semi-quantitative measure of (in)stability of the SiO<sub>2</sub>, Al<sub>2</sub>O<sub>3</sub> and MgO, the number of electrons required to remove a single atom from the oxide was calculated by determining the number of removed atoms based on the volume that has been removed from the oxide, approximating particle geometry and assuming bulk densities, and the number of electrons the area has been exposed to. The dose rate, volume reduction and values for the electrons required to remove a single atom for each of the individual experiments are listed in Supporting Tables S2.1–S2.3 in the appendix for SiO<sub>2</sub>, Al<sub>2</sub>O<sub>3</sub> and MgO, respectively. Due to the difficulty of assessing the instability of the niobic acid and the lack of thermodynamic data, quantification was not possible for this sample. The semi-quantification shows that the severity of electron beam induced oxide degradation correlates with the favorability of hydroxide formation. For oxides with a more negative value of  $\Delta G^0_{\text{H}}$  (e.g. MgO vs. SiO<sub>2</sub>), far fewer electrons are required to remove an atom from the oxide.

Although dose rate ( $\text{e}^- \cdot \text{nm}^{-2} \cdot \text{s}^{-1}$ ) has been shown to sometimes influence the observed phenomena in liquid cell,<sup>70</sup> variation thereof in these experiments did not show any

significant differences in the amount of electrons required to remove an atom. This is also observed when comparing the resulting values for electrons required per removed atom for the  $\text{Al}_2\text{O}_3$  and  $\text{MgO}$  experiments performed at different magnifications, as listed in Supporting Tables S2.2 and S2.3. Therefore, the required lower magnifications and hence lower dose rates in the case of  $\text{Al}_2\text{O}_3$  and  $\text{MgO}$ , necessary to image long enough to observe the degradation in sufficient detail, did not influence the comparison to any significant extent.



**Figure 2.5.** Comparison of the stability of the oxides used in this research under the prevailing conditions of LP-TEM experiments as a function of the Gibbs free energy of formation of the solid hydroxide from the respective oxide (hydration energy), with stability defined as the number of electrons required to remove a single atom (both the oxygen and metal atoms) from the material.

Another difference between the stable and unstable oxides in this study is that the stable oxides are all reducible, relatively easily releasing oxygen atoms, which could also be used to explain these observations. However, a recent study showed that  $\text{Fe}_2\text{O}_3$ ,  $\text{CeO}_2$  and  $\text{CuO}$ , which are also reducible oxides, were unstable under electron beam irradiation in the presence of water.<sup>55</sup> Seeing that these three oxides also have a positive  $\Delta G^{\circ}_{\text{H}}$ , according to our hypothesis they should be stable. However, because they are easily reducible, it is important to also consider their sub-oxides such as  $\text{Cu}_2\text{O}$ ,  $\text{FeO}$  and  $\text{Ce}_2\text{O}_3$ . As can be seen in Table 2.2, these sub-oxides actually have a negative  $\Delta G^{\circ}_{\text{H}}$ . This is also in agreement with the observations of Lu et al.,<sup>55</sup> in which they report that electron beam induced dissolution of cerium oxide becomes extremely fast only after the  $\text{Ce}_2\text{O}_3$  phase is observed. The sub-oxides of  $\text{TiO}_2$  ( $\text{Ti}_2\text{O}_3$  and  $\text{TiO}$ ) on the other hand have a positive  $\Delta G^{\circ}_{\text{H}}$ , indicating  $\text{TiO}_2$  should be stable according to this correlation, which is indeed the case. This clearly demonstrates that

while reducibility should be taken into account for the possible suboxide formation, the main driving force for oxide destabilization is its affinity to form hydroxides.

It is worth mentioning that two modes of performing LP-TEM can be used, namely TEM and STEM mode. In TEM mode, the electron beam is spread and illuminates the region of interest uniformly, which results in a uniform distribution of electrons and a constant concentration of radiolysis products. In our work, STEM mode was used, in which a sub-nanometer probe is scanned across the region of interest. The dwell time (time the probe spends at a single point in the raster) is usually in the same order of magnitude as the lifetime of the radiolysis products. This means that not all regions of the scanned particle are exposed to the radiolysis products at the same time. Considering that the scanning is always in 1 direction, this could lead to directionality in electron beam induced effects. In fact, the previously mentioned selective etching that was observed for silica is a result of this effect.<sup>52, 54</sup> The higher electron dose rates of the STEM probe could also allow effects that only occur above a certain threshold of electron dose rate to take place easier in STEM than in TEM, such as nucleation.<sup>70</sup> However, as liquid radiolysis plays a pivotal role in the oxide dissolution and occurs in both TEM and STEM, apart from potential directionality of the dissolution process the end result should be similar.

The exact mechanism through which the electron beam causes the oxides to degrade in the presence of H<sub>2</sub>O, is likely very complex and oxide-dependent. Based on first-principle calculations, it has been suggested that the formation of oxygen vacancies by the electron beam, followed by rapid dissolution of neighboring metal atoms is the main mechanism.<sup>55</sup> This would however suggest that reducible oxides, in which oxygen vacancies form more easily, should be less stable, while the opposite is observed in our experiments. As stated above and demonstrated in this study, reducibility should be considered to account for the formation of suboxides, but the stability is clearly correlated to hydroxide formation from respective (sub)oxides.

For amorphous silica, it has recently been found that the mechanism likely involves the acceleration of silica hydroxylation and subsequent dissolution through the electron beam induced formation of reducing radicals capable of breaking the Si–O–Si bonds (chapter 3 of this thesis).<sup>54</sup> Suppressing the formation of these radicals by using a 1:1 acetic acid/sodium acetate buffer as radical scavenger, resulted in a more stable silica. In the same study, a test with a 1:1 H<sub>3</sub>PO<sub>4</sub>/NaH<sub>2</sub>PO<sub>4</sub> buffer did not change the silica stability compared to pure water, indicating that pH change or buffering did not influence the stability of silica significantly. However, when employing the same strategy of adding a 0.2 mol·L<sup>-1</sup> acetic acid/sodium acetate buffer to suppress radical formation and stabilize Al<sub>2</sub>O<sub>3</sub>, no significant improvement in stability was observed



(Supporting Figure S2.7), which suggests a different mechanism, but again likely not influenced by pH changes or buffering.

Based on previous work<sup>54-55</sup> and this study, we can conclude that while the proposed formation of oxygen vacancies can still take place, especially at high electron beam dose rates,<sup>55</sup> it is likely not a universal mechanism of oxide dissolution, nor the driving force. Oxide (and suboxide) hydration seems to be a key factor in determining their stability, but the exact mechanism of oxide dissolution in LP-TEM is clearly a very complex process and likely unique for each oxide. Therefore, further experimental work as well as theoretical modeling that will take the Gibbs free energy of hydration into account, is needed to unravel the mechanism of these processes.

## **2.4 Conclusion**

In view of the growing popularity of LP-TEM in academic and industrial research, in particular for studying metal (oxide) systems in an aqueous environment, this study represents a critical step towards deepening our understanding of the diverse behaviors of metal oxides in LP-TEM. The origin of the varying stability of the oxide materials in LP-TEM environment is shown to correlate strongly with the oxide's Gibbs free energy of hydration. Other physio-chemical properties such as porosity, surface area or crystallinity of the oxide material are shown to be of limited importance in LP-TEM experiments. Furthermore, these results point to the need of redesigning the LP-TEM experiments such that hydration is suppressed when oxides with thermodynamic affinity towards forming hydroxides are studied.

Most importantly, the correlation found in this study can aid in predicting the stability of oxides without performing elaborate and time-consuming LP-TEM experiments. Several oxides which were identified in our study as very stable are also excellent candidates for studying important dynamic nanoscale processes for which high electron doses would be required. For instance, LP-TEM provides an excellent platform for studying the diffusion behavior and movement of nanometer size particles. Next to this, using LP-TEM to study catalyst evolution during synthesis and its structural changes during catalysis, has a tremendous potential to unravel phenomena that have never been observed or only indirectly investigated until now. Considering that heterogeneous catalysts typically consist of metal nanoparticles supported on an oxide, and that high electron doses are required for their visualization, using oxides that are stable in LP-TEM is a prerequisite for further studies in this field.

## 2.5 Materials & Methods

### 2.5.1 Oxides

The oxides used in this investigation were commercially available oxides, except for the amorphous Stöber silica spheres and the amorphous titania, which were prepared according to the procedures outlined below. The other oxides were P25 TiO<sub>2</sub> (Evonik Degussa), Puralox  $\gamma$ -Al<sub>2</sub>O<sub>3</sub> SCCa-5/170 (Sasol), ZrO<sub>2</sub> XZ catalyst support (Saint-Gobain), niobic acid (CBMM) and MgO nanopowder (Sigma-Aldrich). All oxides were used as received without additional treatment. Additionally, part of the niobic acid was calcined at 600 °C for 4 h with a heating and cooling rate of 5 °C·min<sup>-1</sup> to obtain a water-free crystalline Nb<sub>2</sub>O<sub>5</sub> nanopowder.

Spherical silica nanoparticles were prepared adapting the procedure from Stöber et al.<sup>71</sup> In a typical experiment, a mixture of 11.25 mL of NH<sub>3</sub> solution (30 wt.%, Merck) and 230 mL ethanol was heated to 35 °C in an oil bath. 17.3 mL of tetraethyl orthosilicate (TEOS, 98%, Sigma-Aldrich) was subsequently added to this mixture and then left to stir (250 rpm) at 35 °C for 16 h. The solution was then neutralized with nitric acid (65%, Sigma-Aldrich) and the liquid removed by rotary evaporation. The remaining solid was dried overnight at 120 °C, followed by calcination in air at 200 °C for 2 h, 400 °C for 1 h and subsequently 3 h at 800 °C, all with a heating and cooling rate of 1.7 °C·min<sup>-1</sup>. The resulting silica particles were spherical with a bimodal size distribution in the range of 20–30 and 60–120 nm.

Amorphous titania was prepared according to the procedure of Wang et al.<sup>72</sup> from a sol-gel hydrolysis precipitation of titanium isopropoxide Ti(OC<sub>3</sub>H<sub>7</sub>)<sub>4</sub>, (Sigma-Aldrich,  $\geq 97\%$ ). 2.0 g of titanium isopropoxide was dissolved in 4.2 mL of anhydrous ethanol in a glovebox. Then the solution was taken out of the glovebox and added dropwise with rigorous stirring at 500 rpm to 4.5 mL of a 16.5 wt.% water in ethanol solution for a final water:alkoxide molar ratio of 5:1. White precipitates of hydrous oxide formed immediately. After the solutions were completely mixed, the mixture was left stirring for 2 h and subsequently transferred to an autoclave to gelate at 80 °C for one day. Then the precipitate was separated from the mother liquor by centrifugation at 5000 RPM and washed with demineralized water 3 times. The sample was subsequently dried at room temperature for one week.

### 2.5.2 Characterization

All oxides were characterized by powder X-ray diffraction (XRD) using a Brücker D2 Phaser with a Co K $\alpha$  source for phase identification. Samples were evaluated for  $2\theta$  between 25° and 90°, except for the amorphous TiO<sub>2</sub> which was evaluated up to 75°.

To determine morphology, the oxides were examined with TEM using a Talos F200X (Thermo Fischer Scientific), operated at 200 kV acceleration voltage in both TEM and HAADF-STEM mode. The samples were dispersed in isopropanol (Honeywell, Chromasolv™ 99.9%) and deposited on a 200 mesh copper-formvar grid. Vacuum control experiments were performed by continuous STEM scanning for 1 h using a beam current of 0.21 nA, as determined by the fluscreen current measured without a holder present. For the control experiments in vacuum, imaging was performed at 225,000× magnification, corresponding to a 500 nm × 500 nm image size, resulting in an average dose rate of  $5.2 \cdot 10^3 \text{ e}^- \cdot \text{nm}^{-2} \cdot \text{s}^{-1}$ . Images were collected with a pixel dwell time of 9.5 μs, with 1024 × 1024 pixel images, for a total of 10 s/frame.

TGA was performed using a PerkinElmer Pyris1 TGA instrument. Samples were heated from room temperature to 50 °C and held there for 10 min to stabilize the sample. Then the sample was heated to 600 °C at a rate of 2 °C·min<sup>-1</sup> in a gas mixture of 20% O<sub>2</sub> in Ar. Exhaust gases were analyzed by mass spectrometry (MS) using an Omnistar MS instrument from Pfeiffer Vacuum.

N<sub>2</sub> physisorption measurements were performed at -196 °C (77K) using a Micromeritics Tristar 3000 instrument. Before the isotherm measurements, samples were dried between 150 and 250 °C under vacuum. The appropriate drying temperature was selected based on TGA results and kept as low as possible to prevent sample transformation. Specific surface areas were calculated using the multipoint BET method ( $0.05 < p/p_0 < 0.25$ ). Pore volume was determined at  $p/p_0 = 0.9$  from the adsorption branches of the isotherms using the Barrett–Joyner–Halenda (BJH) method. Microporosity was evaluated using the t-plot method.

### **2.5.3 LP-TEM experiments**

A small amount of the oxide was dispersed in 2 mL of high-purity isopropanol (Honeywell, Chromasolv™ 99.9%) and sonicated for at least 15 min to disperse agglomerates. A 0.5 μL droplet of this suspension was placed and left for 5 min to evaporate on the silicon nitride (Si<sub>x</sub>N<sub>y</sub>) layer of the large silicon liquid cell chip with a nominally 50 nm thick Si<sub>x</sub>N<sub>y</sub> window with dimensions of 20 μm × 550 μm (Protochips Inc., USA). In this manner the oxide particles are attached to the window, allowing them to be imaged and studied for a sufficient amount of time under electron beam irradiation in an aqueous environment.

A small silicon chip also containing a 20 μm × 550 μm Si<sub>x</sub>N<sub>y</sub> window and 150 nm gold spacers to separate the two chips, was then placed in the dedicated liquid cell TEM holder (Protochips Inc., USA), a 1 μL drop of water (sterile-filtered, Bioreagent, ≤1 Eu·mL<sup>-1</sup>, ≤ 5 ppm metal impurities, Sigma-Aldrich) was added on top of it and the

cell was subsequently assembled by placing the large silicon chip containing the oxide sample on top. In this configuration, the sample is dispersed on the top chip when the holder is inserted in the microscope for optimal spatial resolution in STEM mode.<sup>26</sup> Both the large and small chip were plasma cleaned in an 80%Ar/20%O<sub>2</sub> plasma for two minutes before the sample was dispersed to render the chip surface hydrophilic.

Imaging was performed using a Talos F200X (Thermo Fischer Scientific), operated in scanning transmission mode (STEM) mode at 200 kV acceleration voltage and using an HAADF detector for imaging. The imaging was performed with a beam current of 0.21 nA, as determined by the screen current without a holder present in the electron microscope and with a camera length of 125 mm. Images were collected with a pixel dwell time of 9.5  $\mu$ s, with 1024  $\times$  1024 pixel images, for a total of 10 s/frame. Experiments were performed at multiple magnifications between 57,000 $\times$  and 320,000 $\times$ , resulting in an image size of 2000 nm  $\times$  2000 nm and 360 nm  $\times$  360 nm, respectively, which also corresponds to the area exposed to the scanning electron beam and allows control of the dose rate and total dose the sample receives. The applied current in combination with these window sizes correspond to dose rates between  $3.3 \times 10^2$  and  $1.0 \cdot 10^4$  e<sup>-</sup>·nm<sup>-2</sup>·s<sup>-1</sup>.

Each liquid cell experiment was performed in flow mode using a flow of 2  $\mu$ L·min<sup>-1</sup> to prevent the buildup of gases and bubble formation due to electron beam induced water decomposition. Before the start of each experiment, the presence of water was verified by checking for contrast differences between the corners of the liquid cell and the middle at low magnification, which is evidence for significant differences in thickness of the water layer as a result of bowing of the Si<sub>x</sub>N<sub>y</sub> membrane. An example of such contrast gradient is presented in Supporting Figure S2.8 in the appendix. For the oxides that degraded appreciably (MgO, Al<sub>2</sub>O<sub>3</sub> and SiO<sub>2</sub>), at most 200 images were acquired, corresponding to approximately 33 min of continuous electron beam scanning. In the case the sample already completely disappeared beforehand, at least 10 additional images were acquired. For the other, more stable oxides, a total of 360 images were acquired, corresponding to exactly 1 h of continuous electron beam scanning. For all stable oxides and for SiO<sub>2</sub>, the magnification used was the same as in the vacuum experiments, namely 225,000 $\times$ , corresponding to a dose rate of  $5.2 \times 10^3$  e<sup>-</sup>·nm<sup>-2</sup>·s<sup>-1</sup>. For Al<sub>2</sub>O<sub>3</sub> and MgO, different experiments with different magnifications were performed, with the image sizes and corresponding electron dose rates listed in Supporting Tables S2.2 and S2.3.

Due to the very local nature of the electron beam induced degradation and dissolution, the overall amount of material dissolving is too low to be detectable in the liquid coming from the outlet of the liquid cell system (a concentration of less

than 1 ng metal per liter in the MgO experiments and even lower for the Al<sub>2</sub>O<sub>3</sub> and SiO<sub>2</sub> experiments), hence analysis of the liquid was not performed. To obtain a semi-quantitative assessment of the stability of the SiO<sub>2</sub>, Al<sub>2</sub>O<sub>3</sub> and MgO, the number of electrons required to remove a single atom was calculated. First the total number of electrons received by the sample during the experiment was calculated from the current, the total irradiation time and surface area of the STEM image. The number of atoms lost was determined from the lost volume by using bulk density and molecular weight for each oxide. Volumes lost, electron dose rates, duration of scanning and the resulting number of electrons required per removed atom are listed in Supporting Tables S2.1–S2.3 for each experiment of SiO<sub>2</sub>, Al<sub>2</sub>O<sub>3</sub> and MgO, respectively.

The volume of the material that has disappeared, was calculated by, in the case of SiO<sub>2</sub> and MgO, measuring length and width of all individual particles and calculating the total volume present before and after the experiment, assuming particles to be perfect ellipsoids with the third axis being equal to the shortest axis of the projected ellipse.

In the case of Al<sub>2</sub>O<sub>3</sub>, image analysis was performed using ImageJ. First, background was subtracted from the image and subsequently noise was reduced by using the despeckle function, which replaces each pixel with the median value of the 3 × 3 grid around it. Then, assuming a linear relationship between intensity and thickness, an intensity of 0 was assumed to correspond to no Al<sub>2</sub>O<sub>3</sub> being present and the maximum intensity observed was assumed to correspond to the width of the associated particle. Then the total Al<sub>2</sub>O<sub>3</sub> volume was determined by integrating over the entire image.

## 2.6 Acknowledgements

The authors gratefully acknowledge J. D. Meeldijk for technical assistance with the electron microscope, R. Dalebout, L. Weber and P. Paalanen for the N<sub>2</sub> physisorption measurements, M. Versluijs-Helder for the TGA-MS measurements, S. M. C. de Jong for help with the synthesis of the amorphous TiO<sub>2</sub> and C. Hernandez Meija for providing the Nb<sub>2</sub>O<sub>5</sub> samples. K. P. de Jong and M. J. Meijerink acknowledge funding from the European Research Council, an EU FP7 ERC Advanced Grant no. 338846. J. Zečević acknowledges financial support by Netherlands Organization for Scientific Research (NWO), Veni Grant No. 722.015.010.

## 2.7 References

- (1). Casavola, M.; Hermannsdörfer, J.; de Jonge, N.; Dugulan, A. I.; de Jong, K. P., Fabrication of Fischer–Tropsch Catalysts by Deposition of Iron Nanocrystals on Carbon Nanotubes. *Adv. Funct. Mater.* **2015**, *25* (33), 5309-5319.
- (2). Prieto, G.; Zečević, J.; Friedrich, H.; De Jong, K. P.; De Jongh, P. E., Towards Stable Catalysts by Controlling Collective Properties of Supported Metal Nanoparticles. *Nat. Mater.* **2013**, *12* (1), 34-39.
- (3). Zečević, J.; Vanbutsele, G.; De Jong, K. P.; Martens, J. A., Nanoscale Intimacy in Bifunctional Catalysts for Selective Conversion of Hydrocarbons. *Nature* **2015**, *528* (7581), 245-248.
- (4). Soled, S., Silica-Supported Catalysts Get a New Breath of Life. *Science* **2015**, *350* (6265), 1171-1172.
- (5). Sanchez, F.; Sobolev, K., Nanotechnology in Concrete—a Review. *Constr. Build. Mater.* **2010**, *24* (11), 2060-2071.
- (6). Fortunato, E.; Barquinha, P.; Martins, R., Oxide Semiconductor Thin-Film Transistors: A Review of Recent Advances. *Adv. Mater.* **2012**, *24* (22), 2945-2986.
- (7). Wang, Z. L.; Kong, X. Y.; Ding, Y.; Gao, P.; Hughes, W. L.; Yang, R.; Zhang, Y., Semiconducting and Piezoelectric Oxide Nanostructures Induced by Polar Surfaces. *Adv. Funct. Mater.* **2004**, *14* (10), 943-956.
- (8). Wang, S.; Peng, Y., Natural Zeolites as Effective Adsorbents in Water and Wastewater Treatment. *Chem. Eng. J.* **2010**, *156* (1), 11-24.
- (9). Müller, K. A.; Bednorz, J. G., The Discovery of a Class of High-Temperature Superconductors. *Science* **1987**, *237* (4819), 1133-1139.
- (10). Cao, X. Q.; Vassen, R.; Stoeber, D., Ceramic Materials for Thermal Barrier Coatings. *J. Eur. Ceram. Soc.* **2004**, *24* (1), 1-10.
- (11). Zhang, Z.; Wang, C.-C.; Zakaria, R.; Ying, J. Y., Role of Particle Size in Nanocrystalline TiO<sub>2</sub>-Based Photocatalysts. *J. Phys. Chem. B* **1998**, *102* (52), 10871-10878.
- (12). Csicsery, S. M., Shape-Selective Catalysis in Zeolites. *Zeolites* **1984**, *4* (3), 202-213.
- (13). Haruta, M., Size-and Support-Dependency in the Catalysis of Gold. *Catal. Today* **1997**, *36* (1), 153-166.
- (14). Kruska, K.; Lozano-Perez, S.; Saxey, D. W.; Terachi, T.; Yamada, T.; Smith, G. D. W., Nanoscale Characterisation of Grain Boundary Oxidation in Cold-Worked Stainless Steels. *Corros. Sci.* **2012**, *63*, 225-233.
- (15). Zeng, R.-C.; Zhang, J.; Huang, W.-J.; Dietzel, W.; Kainer, K. U.; Blawert, C.; Ke, W., Review of Studies on Corrosion of Magnesium Alloys. *Trans. Nonferrous Met. Soc. China* **2006**, *16*, s763-s771.
- (16). Mannhart, J.; Schlom, D. G., Oxide Interfaces—an Opportunity for Electronics. *Science* **2010**, *327* (5973), 1607-1611.
- (17). Carter, C. B.; Williams, D. B., *Transmission Electron Microscopy*. Springer-Verlag US: 2009.

- (18). Gramm, F.; Baerlocher, C.; McCusker, L. B.; Warrender, S. J.; Wright, P. A.; Han, B.; Hong, S. B.; Liu, Z.; Ohsuna, T.; Terasaki, O., Complex Zeolite Structure Solved by Combining Powder Diffraction and Electron Microscopy. *Nature* **2006**, *444* (7115), 79-81.
- (19). Yuan, C.; Li, J.; Hou, L.; Zhang, X.; Shen, L.; Lou, X. W. D., Ultrathin Mesoporous NiCo<sub>2</sub>O<sub>4</sub> Nanosheets Supported on Ni Foam as Advanced Electrodes for Supercapacitors. *Adv. Funct. Mater.* **2012**, *22* (21), 4592-4597.
- (20). Saka, H.; Kamino, T.; Ara, S.; Sasaki, K., In Situ Heating Transmission Electron Microscopy. *MRS Bull.* **2008**, *33* (2), 93-100.
- (21). Mehraeen, S.; McKeown, J. T.; Deshmukh, P. V.; Evans, J. E.; Abellan, P.; Xu, P.; Reed, B. W.; Taheri, M. L.; Fischione, P. E.; Browning, N. D., A (S)TEM Gas Cell Holder with Localized Laser Heating for in Situ Experiments. *Microsc. Microanal.* **2013**, *19* (2), 470-478.
- (22). Tao, F.; Crozier, P. A., Atomic-Scale Observations of Catalyst Structures under Reaction Conditions and During Catalysis. *Chem. Rev.* **2016**, *116* (6), 3487-3539.
- (23). Wagner, J. B.; Cavalca, F.; Damsgaard, C. D.; Duchstein, L. D. L.; Hansen, T. W., Exploring the Environmental Transmission Electron Microscope. *Micron* **2012**, *43* (11), 1169-1175.
- (24). Van den Berg, R.; Elkjaer, C. F.; Gommès, C. J.; Chorkendorff, I.; Sehested, J.; De Jongh, P. E.; De Jong, K. P.; Helveg, S., Revealing the Formation of Copper Nanoparticles from a Homogeneous Solid Precursor by Electron Microscopy. *J. Am. Chem. Soc.* **2016**, *138* (10), 3433-3442.
- (25). Feng, X.; Chee, S. W.; Sharma, R.; Liu, K.; Xie, X.; Li, Q.; Fan, S.; Jiang, K., In Situ TEM Observation of the Gasification and Growth of Carbon Nanotubes Using Iron Catalysts. *Nano Res.* **2011**, *4* (8), 767-779.
- (26). De Jonge, N.; Ross, F. M., Electron Microscopy of Specimens in Liquid. *Nat. Nanotechnol.* **2011**, *6* (11), 695-704.
- (27). Chen, X.; Li, C.; Cao, H., Recent Developments of the in Situ Wet Cell Technology for Transmission Electron Microscopies. *Nanoscale* **2015**, *7* (11), 4811-4819.
- (28). Li, C.; Chen, X.; Liu, H.; Fang, J.; Zhou, X., In-Situ Liquid-Cell TEM Study of Radial Flow-Guided Motion of Octahedral Au Nanoparticles and Nanoparticle Clusters. *Nano Res.* **2018**, *11* (9), 4697-4707.
- (29). Munnik, P.; De Jongh, P. E.; De Jong, K. P., Recent Developments in the Synthesis of Supported Catalysts. *Chem. Rev.* **2015**, *115* (14), 6687-6718.
- (30). Mehrabadi, B. A. T.; Eskandari, S.; Khan, U.; White, R. D.; Regalbuto, J. R., A Review of Preparation Methods for Supported Metal Catalysts. In *Advances in Catalysis*, Elsevier: 2017; Vol. 61, pp 1-35.
- (31). Xiong, H.; Pham, H. N.; Datye, A. K., Hydrothermally Stable Heterogeneous Catalysts for Conversion of Biorenewables. *Green Chem.* **2014**, *16* (11), 4627-4643.
- (32). Ravenelle, R. M.; Copeland, J. R.; Kim, W.-G.; Crittenden, J. C.; Sievers, C., Structural Changes of  $\gamma$ -Al<sub>2</sub>O<sub>3</sub>-Supported Catalysts in Hot Liquid Water. *ACS Catal.* **2011**, *1* (5), 552-561.
- (33). Chee, S. W.; Pratt, S. H.; Hattar, K.; Duquette, D.; Ross, F. M.; Hull, R., Studying Localized Corrosion Using Liquid Cell Transmission Electron Microscopy. *Chem. Commun.* **2015**, *51* (1), 168-171.

- (34). Gu, M.; Parent, L. R.; Mehdi, B. L.; Unocic, R. R.; McDowell, M. T.; Sacci, R. L.; Xu, W.; Connell, J. G.; Xu, P.; Abellan, P.; Chen, X.; Zhang, Y.; Perea, D. E.; Evans, J. E.; Lauhon, L. J.; Zhang, J.-G.; Liu, J.; Browning, N. D.; Cui, Y.; Arslan, I.; Wang, C.-M., Demonstration of an Electrochemical Liquid Cell for Operando Transmission Electron Microscopy Observation of the Lithiation/Delithiation Behavior of Si Nanowire Battery Anodes. *Nano Lett.* **2013**, *13* (12), 6106-6112.
- (35). Williamson, M. J.; Tromp, R. M.; Vereecken, P. M.; Hull, R.; Ross, F. M., Dynamic Microscopy of Nanoscale Cluster Growth at the Solid-Liquid Interface. *Nat. Mater.* **2003**, *2* (8), 532-536.
- (36). Yuk, J. M.; Park, J.; Ercius, P.; Kim, K.; Hellebusch, D. J.; Crommie, M. F.; Lee, J. Y.; Zettl, A.; Alivisatos, A. P., High-Resolution EM of Colloidal Nanocrystal Growth Using Graphene Liquid Cells. *Science* **2012**, *336* (6077), 61-64.
- (37). Ye, X.; Jones, M. R.; Frechette, L. B.; Chen, Q.; Powers, A. S.; Ercius, P.; Dunn, G.; Rotskoff, G. M.; Nguyen, S. C.; Adiga, V. P.; Zettl, A.; Rabani, E.; Geissler, P. L.; Alivisatos, A. P., Single-Particle Mapping of Nonequilibrium Nanocrystal Transformations. *Science* **2016**, *354* (6314), 874-877.
- (38). Dai, L. L.; Sharma, R.; Wu, C.-Y., Self-Assembled Structure of Nanoparticles at a Liquid-Liquid Interface. *Langmuir* **2005**, *21* (7), 2641-2643.
- (39). Hendley, C. T.; Tao, J.; Kunitake, J. A. M. R.; De Yoreo, J. J.; Estroff, L. A., Microscopy Techniques for Investigating the Control of Organic Constituents on Biomineralization. *MRS Bull.* **2015**, *40* (06), 480-489.
- (40). Smeets, P. J. M.; Cho, K. R.; Kempen, R. G. E.; Sommerdijk, N. A. J. M.; De Yoreo, J. J., Calcium Carbonate Nucleation Driven by Ion Binding in a Biomimetic Matrix Revealed by in Situ Electron Microscopy. *Nat. Mater.* **2015**, *14* (4), 394-399.
- (41). Elgrabli, D.; Dachraoui, W.; Ménard-Moyon, C.; Liu, X. J.; Bégin, D.; Bégin-Colin, S.; Bianco, A.; Gazeau, F.; Alloyeau, D., Carbon Nanotube Degradation in Macrophages: Live Nanoscale Monitoring and Understanding of Biological Pathway. *ACS Nano* **2015**, *9* (10), 10113-10124.
- (42). Zheng, H.; Claridge, S. A.; Minor, A. M.; Alivisatos, A. P.; Dahmen, U., Nanocrystal Diffusion in a Liquid Thin Film Observed by in Situ Transmission Electron Microscopy. *Nano Lett.* **2009**, *9* (6), 2460-2465.
- (43). Pohlmann, E. S.; Patel, K.; Guo, S.; Dukes, M. J.; Sheng, Z.; Kelly, D. F., Real-Time Visualization of Nanoparticles Interacting with Glioblastoma Stem Cells. *Nano Lett.* **2015**, *15* (4), 2329-2335.
- (44). Radisic, A.; Vereecken, P. M.; Hannon, J. B.; Searson, P. C.; Ross, F. M., Quantifying Electrochemical Nucleation and Growth of Nanoscale Clusters Using Real-Time Kinetic Data. *Nano Lett.* **2006**, *6* (2), 238-242.
- (45). Sacci, R. L.; Dudney, N. J.; More, K. L.; Parent, L. R.; Arslan, I.; Browning, N. D.; Unocic, R. R., Direct Visualization of Initial SEI Morphology and Growth Kinetics During Lithium Deposition by in Situ Electrochemical Transmission Electron Microscopy. *Chem. Commun.* **2014**, *50* (17), 2104-2107.
- (46). Woehl, T.; Abellan, P., Defining the Radiation Chemistry During Liquid Cell Electron Microscopy to Enable Visualization of Nanomaterial Growth and Degradation Dynamics. *Journal of microscopy* **2017**, *265* (2), 135-147.



- (47). Kraus, T.; De Jonge, N., Dendritic Gold Nanowire Growth Observed in Liquid with Transmission Electron Microscopy. *Langmuir* **2013**, *29* (26), 8427-8432.
- (48). Jungjohann, K. L.; Bliznakov, S.; Sutter, P. W.; Stach, E. A.; Sutter, E. A., In Situ Liquid Cell Electron Microscopy of the Solution Growth of Au-Pd Core-Shell Nanostructures. *Nano Lett.* **2013**, *13* (6), 2964-2970.
- (49). Abellan, P.; Mehdi, B. L.; Parent, L. R.; Gu, M.; Park, C.; Xu, W.; Zhang, Y.; Arslan, I.; Zhang, J.-G.; Wang, C.-M.; Evans, J. E.; Browning, N. D., Probing the Degradation Mechanisms in Electrolyte Solutions for Li-Ion Batteries by in Situ Transmission Electron Microscopy. *Nano Lett.* **2014**, *14* (3), 1293-1299.
- (50). Park, J.; Park, H.; Ercius, P.; Pegoraro, A. F.; Xu, C.; Kim, J. W.; Han, S. H.; Weitz, D. A., Direct Observation of Wet Biological Samples by Graphene Liquid Cell Transmission Electron Microscopy. *Nano Lett.* **2015**, *15* (7), 4737-4744.
- (51). Nielsen, M. H.; Li, D.; Zhang, H.; Aloni, S.; Han, T. Y.-J.; Frandsen, C.; Seto, J.; Banfield, J. F.; Cölfen, H.; De Yoreo, J. J., Investigating Processes of Nanocrystal Formation and Transformation Via Liquid Cell TEM. *Microsc. Microanal.* **2014**, *20* (2), 425-436.
- (52). Zečević, J.; Hermannsdörfer, J.; Schuh, T.; De Jong, K. P.; De Jonge, N., Anisotropic Shape Changes of Silica Nanoparticles Induced in Liquid with Scanning Transmission Electron Microscopy. *Small* **2017**, *13* (1), 1602466.
- (53). Van de Put, M. W. P.; Carcouët, C. C. M. C.; Bomans, P. H. H.; Friedrich, H.; de Jonge, N.; Sommerdijk, N. A. J. M., Writing Silica Structures in Liquid with Scanning Transmission Electron Microscopy. *Small* **2015**, *11* (5), 585-590.
- (54). Meijerink, M. J.; Spiga, C.; Hansen, T. W.; Damsgaard, C. D.; De Jong, K. P.; Zečević, J., Nanoscale Imaging and Stabilization of Silica Nanospheres in Liquid Phase Transmission Electron Microscopy. *Part. Part. Syst. Charact.* **2019**, *36* (1), 1800374.
- (55). Lu, Y.; Geng, J.; Wang, K.; Zhang, W.; Ding, W.; Zhang, Z.; Xie, S.; Dai, H.; Chen, F.-R.; Sui, M., Modifying Surface Chemistry of Metal Oxides for Boosting Dissolution Kinetics in Water by Liquid Cell Electron Microscopy. *ACS Nano* **2017**, *11* (8), 8018-8025.
- (56). Thommes, M.; Kaneko, K.; Neimark, A. V.; Olivier, J. P.; Rodriguez-Reinoso, F.; Rouquerol, J.; Sing, K. S. W., Physisorption of Gases, with Special Reference to the Evaluation of Surface Area and Pore Size Distribution (IUPAC Technical Report). *Pure Appl. Chem.* **2015**, *87* (9-10), 1051-1069.
- (57). Hernández-Mejía, C.; den Otter, J. H.; Weber, J. L.; de Jong, K. P., Crystalline Niobia with Tailored Porosity as Support for Cobalt Catalysts for the Fischer-Tropsch Synthesis. *Appl. Catal., A* **2017**, *548*, 143-149.
- (58). Ropp, R. C., *Encyclopedia of the Alkaline Earth Compounds*. Elsevier: The Netherlands, 2012.
- (59). Meijerink, M. J.; De Jong, K. P.; Zečević, J., Assessment of Oxide Nanoparticle Stability in Liquid Phase Transmission Electron Microscopy. *Nano Res.* **2019**, *12* (9), 2355-2363.
- (60). Koh, A. L.; Gidcumb, E.; Zhou, O.; Sinclair, R., The Dissipation of Field Emitting Carbon Nanotubes in an Oxygen Environment as Revealed by in Situ Transmission Electron Microscopy. *Nanoscale* **2016**, *8* (36), 16405-16415.

- (61). Schweitzer, G. K.; Pesterfield, L. L., *The Aqueous Chemistry of the Elements*. Oxford University Press: USA, 2010.
- (62). Schneider, N. M.; Norton, M. M.; Mendel, B. J.; Grogan, J. M.; Ross, F. M.; Bau, H. H., Electron-Water Interactions and Implications for Liquid Cell Electron Microscopy. *J. Phys. Chem. C* **2014**, *118* (38), 22373-22382.
- (63). Robie, R. A.; Hemingway, B. S.; Fisher, J. R. *Thermodynamic Properties of Minerals and Related Substances at 298.15 K and 1 Bar (10<sup>5</sup> Pascals) Pressure and at Higher Temperatures*; Geological Survey, Washington, DC (USA): 1978.
- (64). Green, D. W.; Perry, R. H., *Perry's Chemical Engineers' Handbook, Eighth Edition*. McGraw-Hill: New York, 2008.
- (65). Wesolowski, D. J.; Ziemniak, S. E.; Anovitz, L. M.; Machesky, M. L.; Bénézeth, P.; Palmer, D. A., Solubility and Surface Adsorption Characteristics of Metal Oxides. In *Aqueous Systems at Elevated Temperatures and Pressures*, Elsevier: The Netherlands, 2004; pp 493-595.
- (66). Peiffert, C.; Nguyen-Trung, C.; Palmer, D. A.; Laval, J.-P.; Giffaut, E., Solubility of B-Nb<sub>2</sub>O<sub>5</sub> and the Hydrolysis of Niobium (V) in Aqueous Solution as a Function of Temperature and Ionic Strength. *J. Solution Chem.* **2010**, *39* (2), 197-218.
- (67). Lencka, M. M.; Anderko, A.; Riman, R. E., Hydrothermal Precipitation of Lead Zirconate Titanate Solid Solutions: Thermodynamic Modeling and Experimental Synthesis. *J. Am. Ceram. Soc.* **1995**, *78* (10), 2609-2618.
- (68). Söhnel, O.; Garside, J., *Precipitation: Basic Principles and Industrial Applications*. Butterworth-Heinemann: 1992.
- (69). Tanabe, K., Niobic Acid as an Unusual Acidic Solid Material. *Mater. Chem. Phys.* **1987**, *17* (1-2), 217-225.
- (70). Abellan, P.; Woehl, T. J.; Parent, L. R.; Browning, N. D.; Evans, J. E.; Arslan, I., Factors Influencing Quantitative Liquid (Scanning) Transmission Electron Microscopy. *Chem. Commun.* **2014**, *50* (38), 4873-4880.
- (71). Stöber, W.; Fink, A.; Bohn, E., Controlled Growth of Monodisperse Silica Spheres in the Micron Size Range. *J. Colloid Interface Sci.* **1968**, *26* (1), 62-69.
- (72). Wang, C.-C.; Ying, J. Y., Sol-Gel Synthesis and Hydrothermal Processing of Anatase and Rutile Titania Nanocrystals. *Chem. Mater.* **1999**, *11* (11), 3113-3120.

## **Supporting Information**

### **Supporting Movies description**

- 1) Movie M1: Stöber SiO<sub>2</sub> under continuous STEM scanning in pure water.
- 2) Movie M2: Puralox Al<sub>2</sub>O<sub>3</sub> under continuous STEM scanning in pure water.
- 3) Movie M3: MgO under continuous STEM scanning in pure water.
- 4) Movie M4: Niobic acid under continuous STEM scanning in pure water.
- 5) Movie M5: Calcined Nb<sub>2</sub>O<sub>5</sub> under continuous STEM scanning in pure water.
- 6) Movie M6: ZrO<sub>2</sub> under continuous STEM scanning in pure water.
- 7) Movie M7: Amorphous TiO<sub>2</sub> under continuous STEM scanning in pure water.
- 8) Movie M8: P25 TiO<sub>2</sub> under continuous STEM scanning in pure water

(Movies available online at <https://doi.org/10.1007/s12274-019-2419-3>)

**Table S2.1.** Volumes lost for the SiO<sub>2</sub> particles after 33 minutes of continuous scanning and electrons required\* per removed atom (both Si and O included).

Particle	Total volume start (nm <sup>3</sup> )	Volume after 2000s (nm <sup>3</sup> )	Volume disappeared (nm <sup>3</sup> )	Electrons per removed atom (e <sup>-</sup> /atom)
1	5.7E+05	1.6E+05	4.1E+05	2.1E+04
2	3.6E+05	9.3E+04	2.6E+05	2.4E+04
3	3.9E+05	1.2E+05	2.7E+05	2.5E+04
4	6.7E+05	1.3E+05	5.3E+05	1.7E+04
5	5.7E+05	2.4E+05	3.3E+05	2.6E+04
6	5.7E+05	2.5E+05	3.2E+05	2.7E+04
7	7.1E+05	2.7E+05	4.4E+05	2.1E+04
8	3.9E+05	1.6E+05	2.3E+05	3.0E+04
9	6.4E+05	1.5E+05	5.0E+05	1.8E+04
10	5.8E+05	1.3E+05	4.6E+05	1.8E+04
11	3.1E+05	1.5E+05	1.6E+05	3.6E+04
12	4.7E+05	2.9E+05	1.9E+05	4.0E+04
13	5.1E+05	2.1E+05	3.0E+05	2.6E+04
14	4.7E+05	1.4E+05	3.3E+05	2.3E+04
15	5.7E+05	1.9E+05	3.8E+05	2.3E+04
16	5.4E+05	1.7E+05	3.7E+05	2.2E+04
17	2.4E+05	8.7E+04	1.5E+05	3.2E+04
18	6.5E+05	1.6E+05	4.8E+05	1.9E+04
			Average	2.5E+04

\*The same magnification (225 kx, or a scanned area size of 500x500 nm) was used in all experiments, resulting in a dose rate of  $5.2 \cdot 10^3 \text{ e}^- \cdot \text{nm}^{-2} \cdot \text{s}^{-1}$  and a cumulative dose of  $1.0 \cdot 10^7 \text{ e}^- \cdot \text{nm}^{-2}$  after 33 minutes.

**Table S2.2.** Volumes lost for the Al<sub>2</sub>O<sub>3</sub> experiments and electrons required per removed atom (both Al and O included).

Area	Size scanned area (nm $\times$ nm)	Electron dose rate (e $\cdot$ nm <sup>-2</sup> $\cdot$ s <sup>-1</sup> )	Total volume start (nm <sup>3</sup> )	Time disappearance (s)	Electrons per removed atom (e-/atom)
1	500 $\times$ 500	5.2E+03	2.9E+06	1550	6.5E+03
2	360 $\times$ 360	1.0E+04	1.2E+06	680	6.7E+03
3	1000 $\times$ 1000	1.3E+03	1.8E+07	1550	1.0E+03
4	500 $\times$ 500	5.2E+03	2.3E+06	1500	7.9E+03
5	1000 $\times$ 1000	1.3E+03	1.1E+07	2000	2.2E+03
6	500 $\times$ 500	5.2E+03	2.4E+06	610	3.1E+03
7	500 $\times$ 500	5.2E+03	1.5E+06	700	5.8E+03
Average					4.7E+03

**Table S2.3.** Volumes lost for the MgO experiments and electrons required\* per removed atom (both Mg and O included).

Area	Size scanned area (nm $\times$ nm)	Electron dose rate (e $\cdot$ nm <sup>-2</sup> $\cdot$ s <sup>-1</sup> )	Total volume start (nm <sup>3</sup> )	Time disappearance (s)	Electrons per removed atom (e-/atom)
1	2000 $\times$ 2000	3.3E+02	8.9E+06	360	5.0E+02
2	1000 $\times$ 1000	1.3E+03	7.8E+06	270	4.2E+02
3	1000 $\times$ 1000	1.3E+03	2.0E+06	100	6.1E+02
4	2000 $\times$ 2000	3.3E+02	3.8E+06	220	7.1E+02
Average					5.6E+02

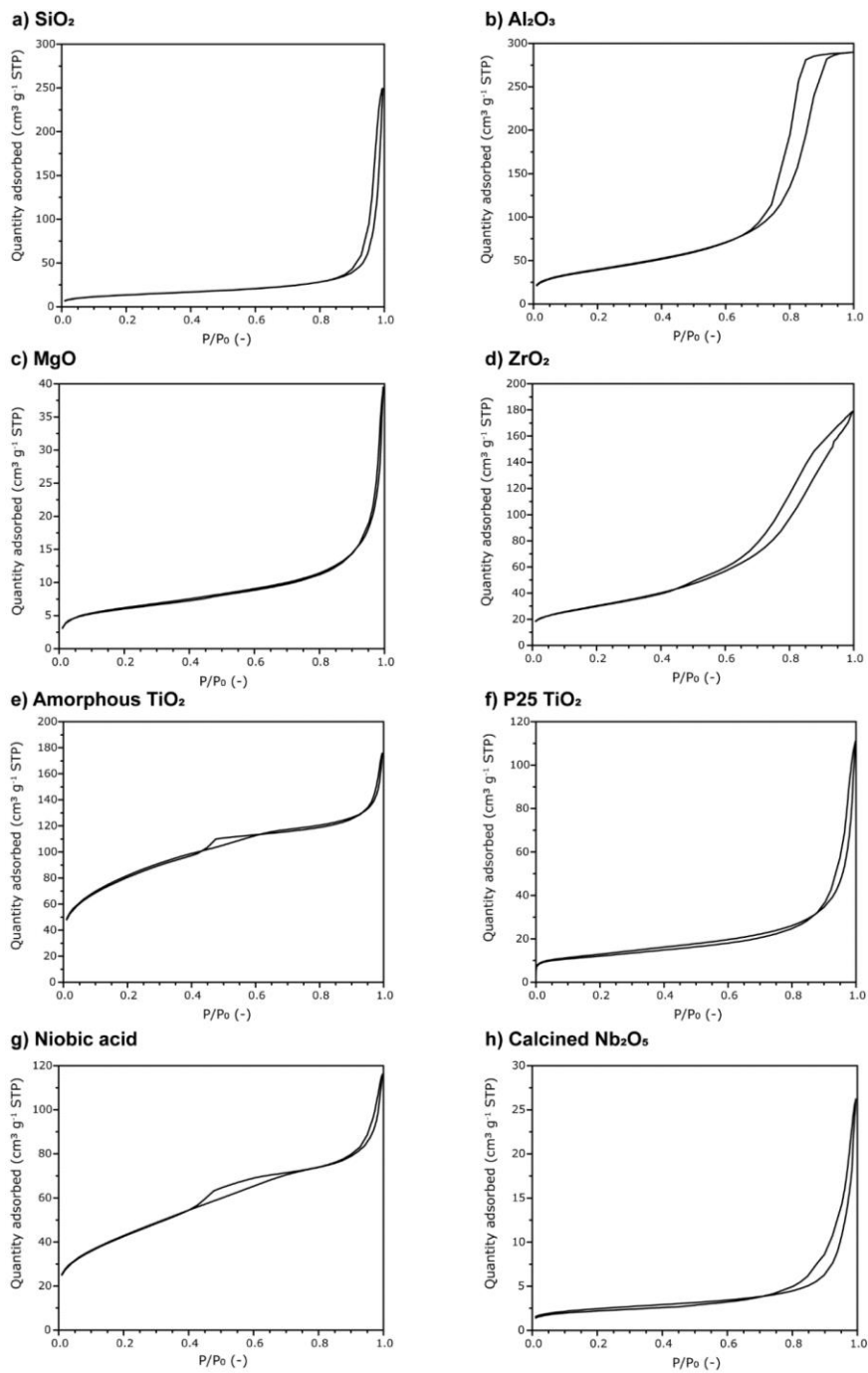


**Figure S2.1.**  $N_2$  physisorption isotherms of (a) Stöber  $\text{SiO}_2$ , (b) Puralox  $\gamma\text{-Al}_2\text{O}_3$ , (c)  $\text{MgO}$ , (d)  $\text{ZrO}_2$ , (e) amorphous  $\text{TiO}_2$ , (f) P25  $\text{TiO}_2$ , (g) Niobic acid, (h) Calcined  $\text{Nb}_2\text{O}_5$ .

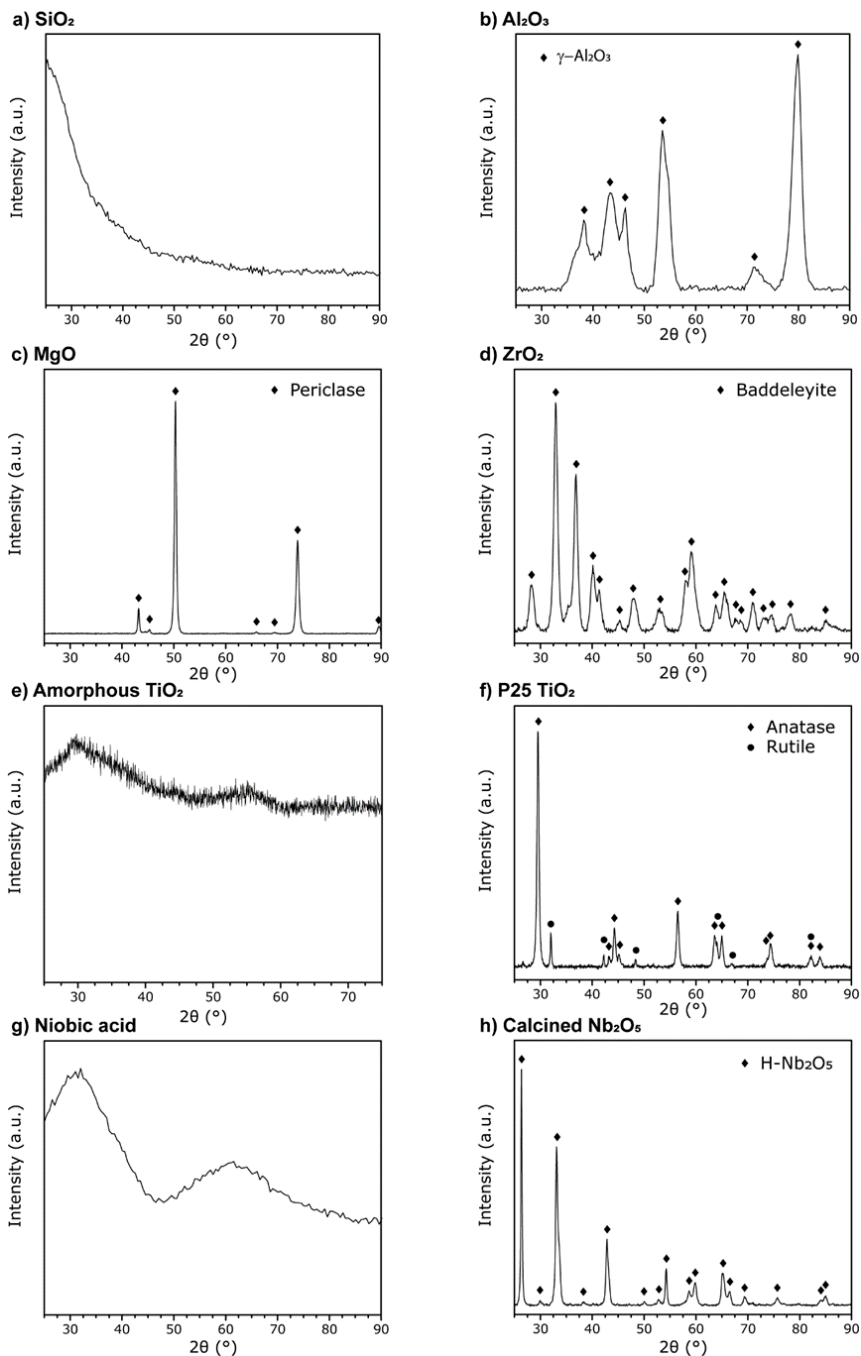


**Figure S2.2.** X-ray diffraction patterns of (a) Stöber  $\text{SiO}_2$ , (b) Puralox  $\gamma\text{-Al}_2\text{O}_3$ , (c)  $\text{MgO}$ , (d)  $\text{ZrO}_2$ , (e) amorphous  $\text{TiO}_2$ , (f) P25  $\text{TiO}_2$ , (g) Niobic acid, (h) Calcined  $\text{Nb}_2\text{O}_5$ . The amorphous oxides  $\text{SiO}_2$  (a),  $\text{TiO}_2$  (e) and niobic acid (g), all contain a characteristic broad band at approx.  $30^\circ$ .

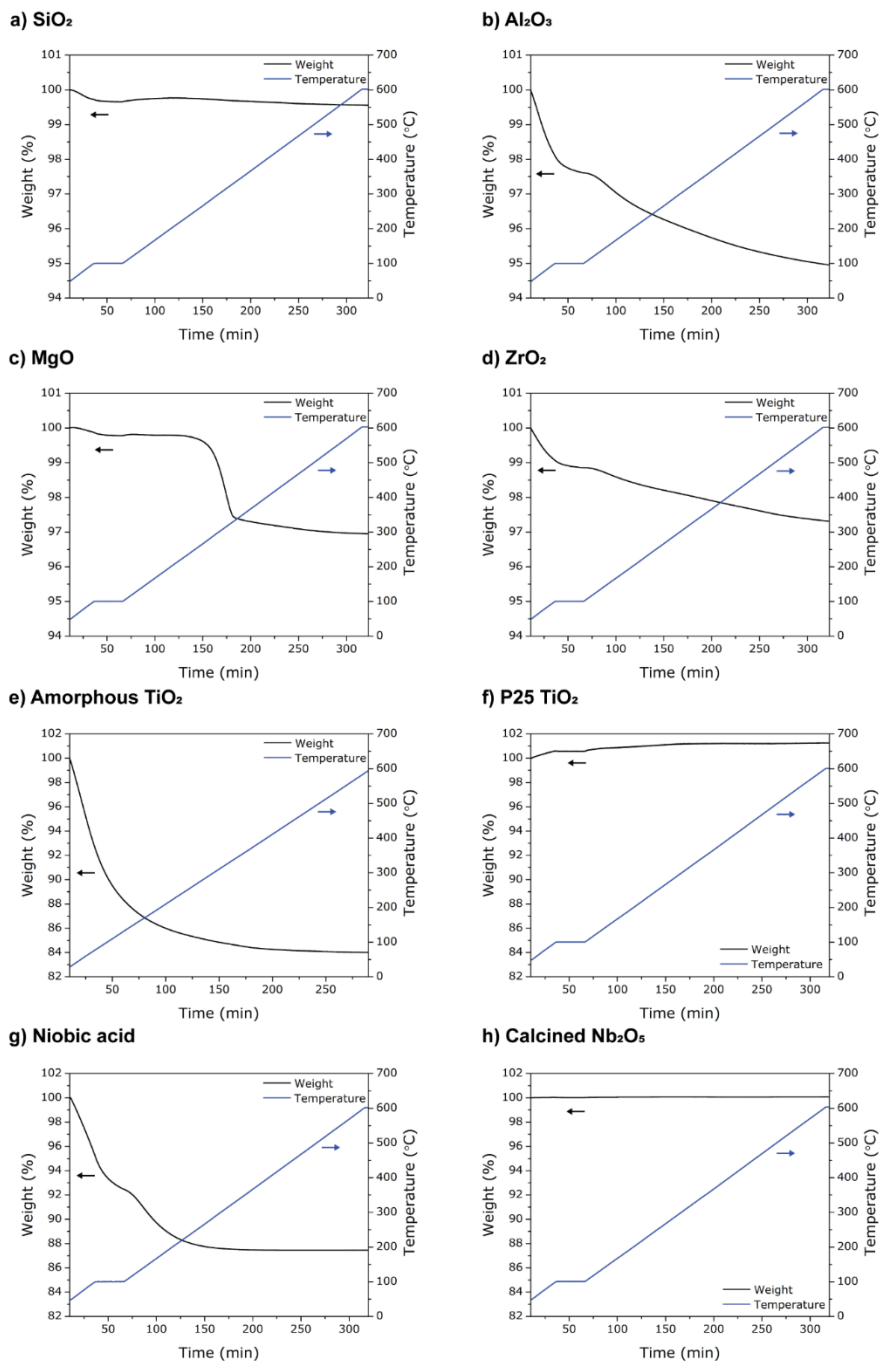


**Figure S2.3.** Thermogravimetric profiles of (a) Stöber  $\text{SiO}_2$ , (b) Puralox  $\gamma\text{-Al}_2\text{O}_3$ , (c)  $\text{MgO}$ , (d)  $\text{ZrO}_2$ , (e) amorphous  $\text{TiO}_2$ , (f) P25  $\text{TiO}_2$ , (g) Niobic acid, (h) Calcined  $\text{Nb}_2\text{O}_5$  in a 20 V%  $\text{O}_2$ /80 V% Ar gas mixture.



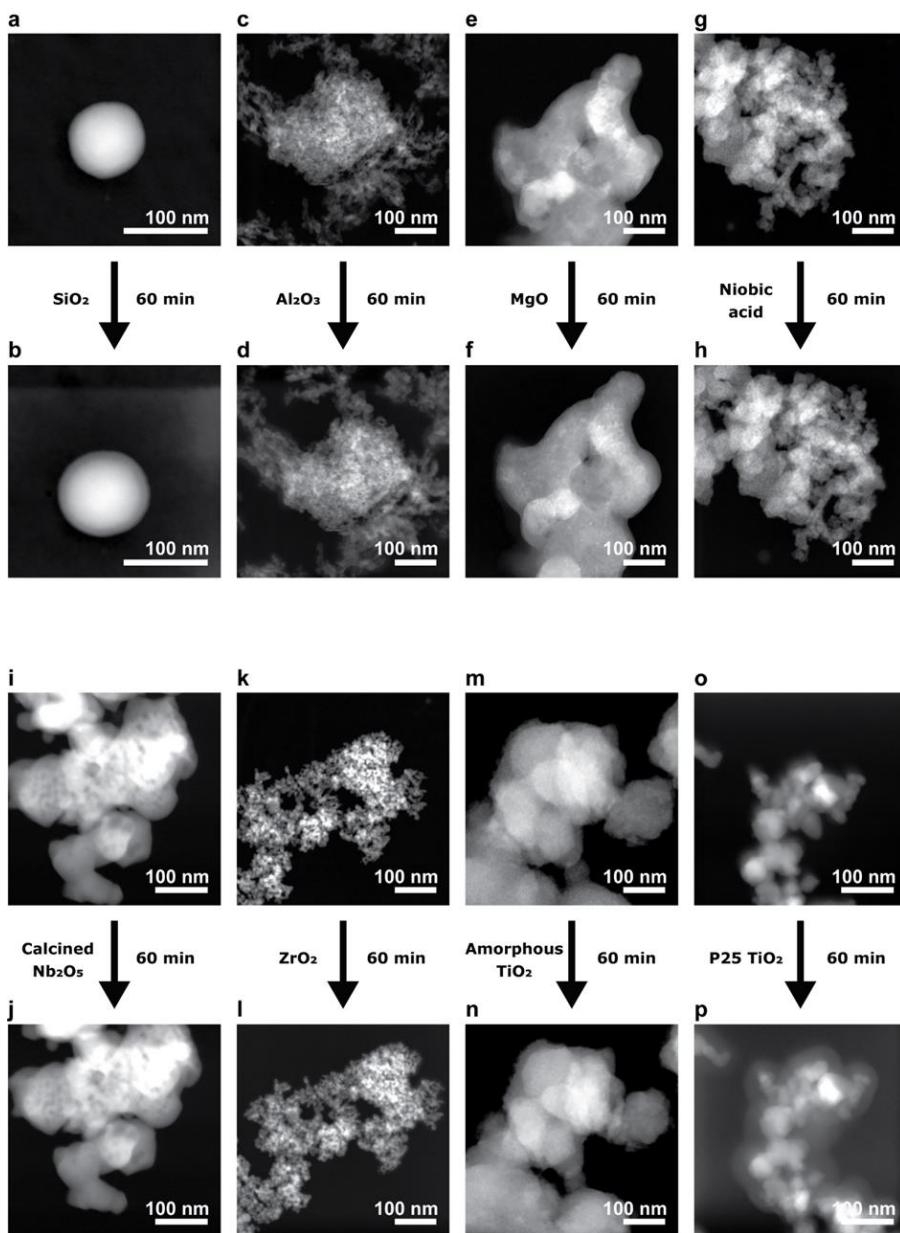


**Figure S2.4.** Images before and after the control experiments of 60 minutes of continuous scanning in vacuum for  $\text{SiO}_2$  (a and b),  $\text{Al}_2\text{O}_3$  (c and d),  $\text{MgO}$  (e and f), Niobic acid (g and h), calcined  $\text{Nb}_2\text{O}_5$  (i and j),  $\text{ZrO}_2$  (k and l), amorphous  $\text{TiO}_2$  (m and n) and P25  $\text{TiO}_2$  (o and p). Some carbon deposition around the oxides from hydrocarbons in the column of the microscope can be observed, in particular for  $\text{SiO}_2$  and P25  $\text{TiO}_2$ , but otherwise the oxides remain unchanged. The dose rate was  $5.2 \cdot 10^3 \text{ e}^- \cdot \text{nm}^{-2} \cdot \text{s}^{-1}$  in all cases, except for the  $\text{SiO}_2$ , in which case the dose rate was  $1.0 \cdot 10^4 \text{ e}^- \cdot \text{nm}^{-2} \cdot \text{s}^{-1}$ .

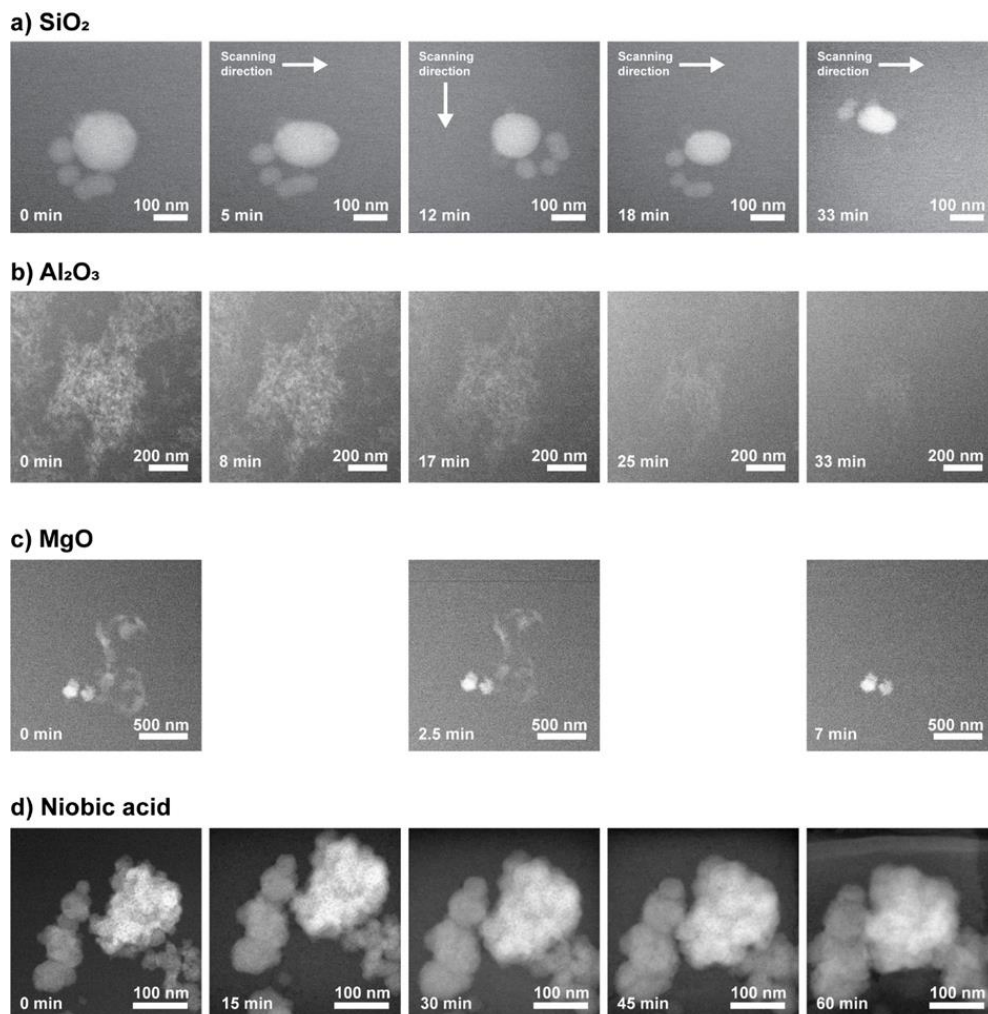
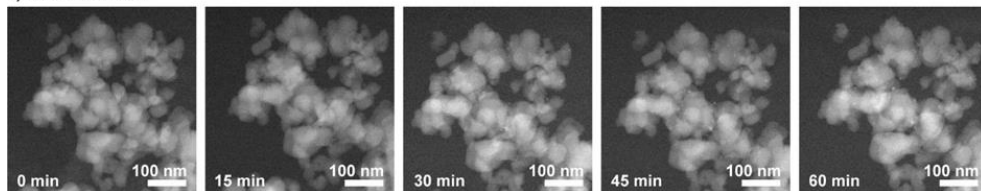
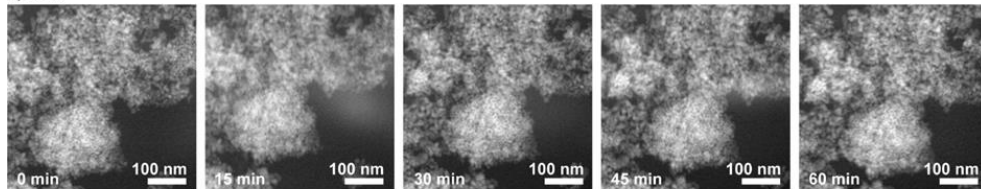


**Figure S2.5.** HAADF-STEM images of the oxides with limited stability in the liquid cell in pure water at different times indicated in the lower left of the images, during the continuous electron beam scanning. (a) Stöber  $\text{SiO}_2$  (dose rate:  $5.2 \cdot 10^3 \text{ e}^- \cdot \text{nm}^{-2} \cdot \text{s}^{-1}$ ), (b) Puralox  $\gamma\text{-Al}_2\text{O}_3$  (dose rate:  $1.3 \cdot 10^3 \text{ e}^- \cdot \text{nm}^{-2} \cdot \text{s}^{-1}$ ), (c)  $\text{MgO}$  with two  $\text{ZrO}_2$  particles in the lower left (confirmed by EDX), in which only 3 images are presented due to the rapid disappearance of the  $\text{MgO}$  (dose rate:  $3.3 \cdot 10^2 \text{ e}^- \cdot \text{nm}^{-2} \cdot \text{s}^{-1}$ ) and (d) niobic acid (dose rate:  $1.0 \cdot 10^4 \text{ e}^- \cdot \text{nm}^{-2} \cdot \text{s}^{-1}$ ).

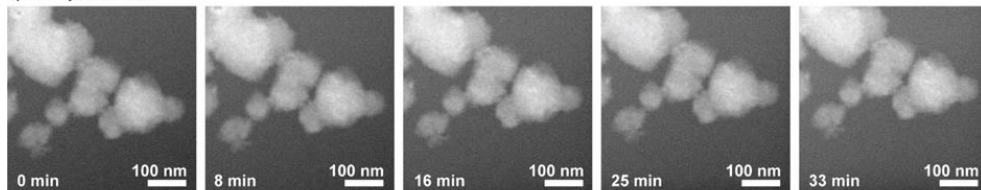
a) Calcined Nb<sub>2</sub>O<sub>5</sub>



b) ZrO<sub>2</sub>



c) Amorphous TiO<sub>2</sub>



d) P25 TiO<sub>2</sub>

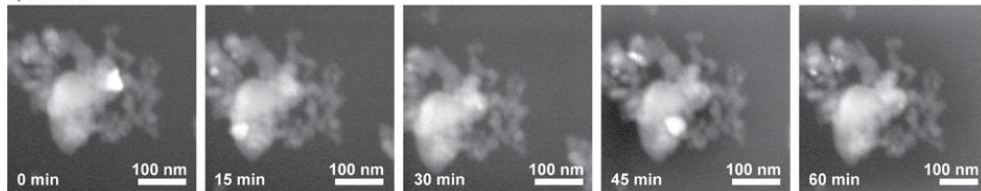


**Figure S2.6.** HAADF-STEM images for each of the oxides stable in the liquid cell in water at different times, indicated in the lower left of the images, during the continuous electron beam scanning, with (a) Calcined Nb<sub>2</sub>O<sub>5</sub>, (b) ZrO<sub>2</sub>, (c) Amorphous TiO<sub>2</sub> and (d) P25 TiO<sub>2</sub>. The dose rate in each experiment was  $5.2 \cdot 10^3 \text{ e}^- \cdot \text{nm}^{-2} \cdot \text{s}^{-1}$ , except for the P25 TiO<sub>2</sub>, in which the dose rate was  $1.0 \cdot 10^4 \text{ e}^- \cdot \text{nm}^{-2} \cdot \text{s}^{-1}$ .

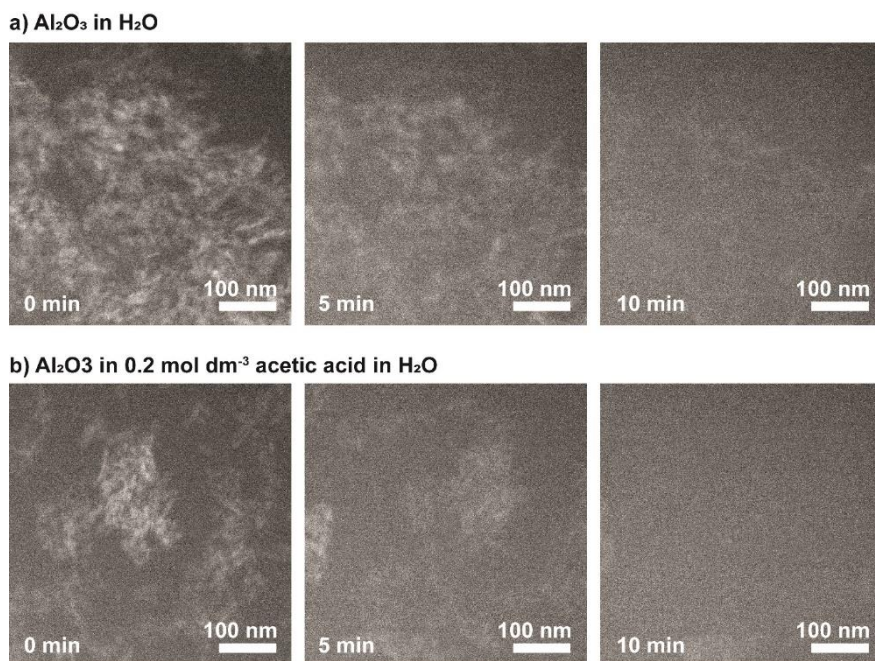


**Figure S2.7.** HAADF-STEM images in the liquid cell comparing the stability of Puralox  $\text{Al}_2\text{O}_3$  in pure  $\text{H}_2\text{O}$  (a) and in a  $0.2 \text{ mol}\cdot\text{L}^{-1}$  1:1 acetic acid/sodium acetate in  $\text{H}_2\text{O}$  buffer (b). In both cases the dose rate was  $5.2 \cdot 10^3 \text{ e}^- \cdot \text{nm}^{-2} \cdot \text{s}^{-1}$ . The calculated number of electrons per removed atom is  $7.9 \cdot 10^3 \text{ e}^-/\text{atom}$  for (a) and  $5.8 \cdot 10^3 \text{ e}^-/\text{atom}$  for (b).

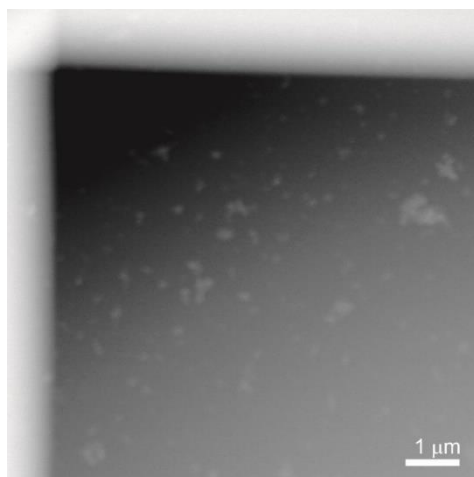


**Figure S2.8.** HAADF-STEM image displaying a clear background contrast difference between the corner (upper left), where the liquid cell is thinnest and a thicker part closer to the middle (lower right corner). This displays a clear difference in liquid layer thickness as a result of bowing of the thin  $\text{Si}_x\text{N}_y$  membrane due to a pressure difference between the inside of the cell and the TEM vacuum.

## Chapter 3

# Nanoscale Imaging and Stabilization of Silica Nanospheres in Liquid Phase Transmission Electron Microscopy

### Abstract

Liquid phase transmission electron microscopy (LP-TEM) is a novel and highly promising technique for the in situ study of important nanoscale processes, in particular the synthesis and modification of various nanostructures in a liquid. Destabilization of the samples, including reduction, oxidation, or dissolution by interactions between electron beam, liquid, and sample, is still one of the main challenges of this technique. This work focuses on amorphous silica nanospheres and the phenomena behind their reshaping and dissolution in LP-TEM. It is proposed that silica degradation is primarily the result of reducing radical formation in the liquid phase and the subsequent accelerated hydroxylation of the silica, while alterations in silica solid structure, pH, and oxidizing species formation had limited influence. Furthermore, the presence of water vapor instead of liquid water also results in degradation of silica. Most importantly however, it is shown that the addition of scavengers for reducing radicals significantly improved amorphous silica stability during LP-TEM imaging. Devising such methods to overcome adverse effects in LP-TEM is of the utmost importance for further development and implementation of this technique in studies of nanoscale processes in liquid.

This chapter is based on: Meijerink, M. J.; Spiga, C.; Hansen, T. W.; Damsgaard, C. D.; De Jong, K. P.; Zečević, J., Nanoscale Imaging and Stabilization of Silica Nanospheres in Liquid Phase Transmission Electron Microscopy. *Part. Part. Syst. Charact.* **2019**, *36* (1), 1800374

## 3.1 Introduction

For millennia, philosophers have speculated about the nature of matter and one of the most important ideas for modern science was the philosophy of ‘atomism’. The word itself originating from the Greek *ατομος* (uncuttable), the theory proposes that the world consists of a large number of indivisible components called atoms.<sup>1</sup> In the 19th century, scientists found that many chemical compounds and materials could be divided in a small number of elements, which they thought were indivisible and were therefore named atoms. Although it was later discovered that these elements could actually be split, the name stuck. Nevertheless, the concept of atoms forms the basis of chemistry, but actually observing individual atoms has been very challenging for a long time.

One of the main modern techniques that is actually capable of visualizing atoms, is transmission electron microscopy (TEM), which is also a leading technique for investigations of nanoscale morphology of a variety of materials.<sup>2-5</sup> However, one of the main limitations of conventional TEM is that the sample can only be imaged in a vacuum. Although the electron beam can be utilized to drive nanoscale dynamic processes in this environment,<sup>6</sup> the possibilities to study such processes taking place in gaseous or liquid environment, such as fabrication of microelectromechanical systems (MEMS) and microsupercapacitors (MSC),<sup>7</sup> nanoparticle formation, and catalyst synthesis,<sup>8-9</sup> are severely limited.

Recently developed liquid phase TEM (LP-TEM) offers a means to overcome this challenge, allowing samples to be imaged in a liquid with nanoscale spatial resolution and high temporal resolution.<sup>10-12</sup> The most popular method to perform these experiments is by utilizing the closed cell design,<sup>13</sup> which encloses the sample and liquid between two silicon nitride windows in a dedicated holder, although enclosing liquids between two graphene layers<sup>14-15</sup> or differential aperture pumping techniques has also been utilized.<sup>16</sup> The closed cell technique has already been employed to study nanoscale dynamic processes such as biomineralization,<sup>17-18</sup> carbon nanotube degradation by macrophages,<sup>19</sup> nanoparticle movement and interactions,<sup>20-21</sup> electrochemical deposition and growth,<sup>22-24</sup> and in particular nucleation and growth induced by the electron beam.<sup>25-28</sup>

The majority of the published articles highlight an important challenge in liquid phase TEM, which is to distinguish electron beam induced effects from the phenomena under investigation, and ultimately to suppress these effects. Along with the beam damage already known from TEM imaging in vacuum,<sup>29</sup> liquid phase TEM suffers from additional beam induced effects,<sup>30</sup> the most prominent challenge being the formation

of radicals and other reactive species in the liquid upon electron beam irradiation, which significantly changes local chemistry.<sup>31</sup> It was recently found that such a change in chemistry also affects oxides, materials usually considered quite stable under electron beam irradiation.<sup>32-33</sup> This destabilizing effect is also seen for amorphous SiO<sub>2</sub>, an important oxide in many nanoscale applications,<sup>34-36</sup> which although stable in vacuum, is severely destabilized by electron beam induced chemistry in water.<sup>37-38</sup> Specifically, it was shown that upon imaging with a scanning electron beam, silica nanospheres tended to elongate in the scanning direction of the beam and shrink significantly over time, as described in chapter 2. To date however, most studies in LP-TEM focused on metallic nanoparticles, resulting in a limited understanding of oxide behavior under these conditions.

To enable LP-TEM studies free from adverse electron beam effects, on not only amorphous silica, but also other metals and oxides, or possibly even to utilize such beam-induced chemistry changes,<sup>39</sup> it is vital to improve our understanding of these degradation phenomena. In this article, we investigate the factors contributing to the degradation of amorphous silica in LP-TEM, focusing on the oxide structure and the beam-induced chemistry changes of the environment and demonstrate that the main route of degradation is related to the formation of reducing radicals in the liquid phase. In addition, using Environmental TEM (ETEM), we demonstrate that a similar electron beam induced degradation phenomenon takes place when water vapor instead of liquid water is present, with a strong dependence on water partial pressure. Identifying this degradation route allowed us to develop a method to mitigate electron beam induced effects by scavenging these radicals. The accomplished stabilization of amorphous silica is an important and promising step toward establishing controlled conditions for imaging nanomaterials in in situ TEM experiments.

## **3.2 Results and Discussion**

In this study, amorphous silica spheres prepared using the Stöber method<sup>40</sup> were used as a model system to establish the impact of the electron beam during the LP-TEM imaging and ETEM imaging in the presence of water. The spherical shape of the particles allows to accurately track and analyze their reshaping and resizing. Three representative high angle annular dark field (HAADF)-STEM images of the silica sample, one image in vacuum and two images of the sample in liquid water, prior to and after 5 min of continuous electron beam scanning are shown in Figure 3.1a, 3.1b, and 3.1c, respectively.

As seen in Figure 3.1, silica particles vary in size, and the majority of the particles have a diameter between 60 and 100 nm, but with a fraction of 20–30 nm diameter particles

(see also Supporting Figure S3.1 in the appendix). As was previously reported<sup>37</sup> and also visible in Figure 3.1c, the scanning of the electron beam introduced elongation in the scanning direction and shrinkage of particles.

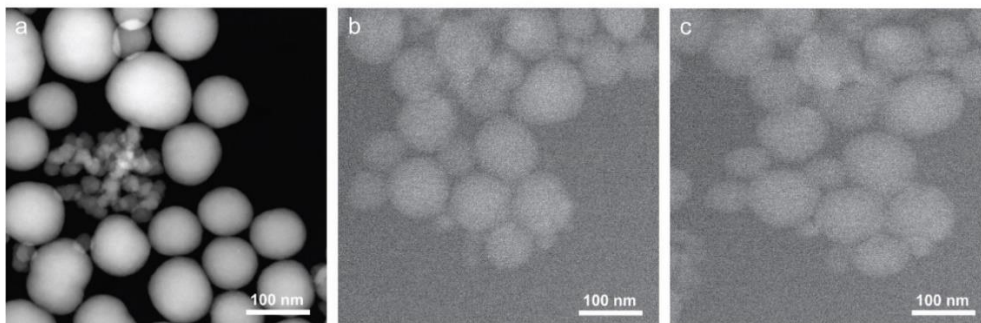


**Figure 3.1.** Representative images of the amorphous silica spheres calcined at 800 °C. (a) HAADF-STEM image in vacuum, (b-c) HAADF-STEM images of amorphous silica spheres in water before (b) and after (c) 5 minutes of exposure to scanning with the electron beam from left to right.

### 3.2.1 Influence of Silica Solid Structure

One of the possible parameters relevant for silica degradation observed in Figure 3.1c is the solid structure of the silica itself, in particular the porosity and the degree of hydroxylation of both the surface and bulk of the particles.<sup>37</sup> Lowering the degree of silica condensation could result in increasing susceptibility toward excitation and destabilization by the electron beam. This would facilitate reactions with water, leading to the formation of soluble  $\text{Si}(\text{OH})_4$  species thought to be responsible for the deformation and dissolution of the particles. To investigate the potential influence of the silica structure, the silica nanospheres were submitted to a heat treatment in stagnant air at temperatures ranging from 400 to 1000 °C. By varying the temperature of the calcination step, the structural properties of the silica nanospheres were altered, with higher calcination temperatures resulting in a decrease of both porosity and number of hydroxyl groups according to literature.<sup>41-43</sup>

Nitrogen physisorption was performed to investigate the change in porosity and surface area of these samples (Table 3.1). As can be observed, upon increasing calcination temperature a significant decrease in surface area occurred, which can be partly attributed to the collapse of pores, as a reduction in pore volume is also observed. Another likely contribution to the decrease in surface area is the sintering of the small 20–30 nm silica particles observed in Figure 3.1a. These small particles underwent considerable sintering with each other, but not with the larger spherical particles, which did not sinter or grow at all, as can be observed in the images and



histograms in Supporting Figure S3.1 in the appendix. Although present, these smaller particles were not studied in the LP-TEM experiments as their visibility was impaired by the micron thick liquid layer.

**Table 3.1.** N<sub>2</sub> physisorption measurements of pore volume and external surface area for the silica samples calcined at different temperatures.

Sample	BET total surface area (m <sup>2</sup> ·g <sup>-1</sup> )	Total pore volume (cm <sup>3</sup> ·g <sup>-1</sup> )	t-plot external surface area (m <sup>2</sup> ·g <sup>-1</sup> )	Surface area based average particle diameter (nm)
400 °C	81	0.44	60	23
600 °C	63	0.41	53	26
800 °C	49	0.38	45	30
1000 °C	33	0.31	31	43

Figure 3.2a and b show representative images of samples that were calcined at the lowest (400 °C) and highest (1000 °C) temperatures, before and after 33 min of electron beam scanning in STEM with alternating horizontal and vertical scanning direction in H<sub>2</sub>O (≤5 ppm impurities, Sigma-Aldrich) at 225,000x magnification and with a dose rate of 5.2 ·10<sup>3</sup> e<sup>-</sup>·nm<sup>-2</sup>·s<sup>-1</sup>. Images showing silica particles before each change in scanning direction are available in Supporting Figure S3.2, with the corresponding movies (M1 and M2) of the entire experiment available online<sup>44</sup> (details in the appendix). In accordance with previous research,<sup>37</sup> the particles tended to elongate in the scanning direction of the beam, while shrinking in the direction perpendicular to that (Supporting Figure S3.2). The material removal rate in the perpendicular direction was found to be higher than the growth of the particles in the scanning direction, resulting in a net loss of volume.

The quantification of the size change of the silica particles was performed by determining the total surface area of the TEM projection of the particles assuming a perfect ellipse. Deformation in the z-axis perpendicular to the image plane was considered negligible, since previous work demonstrated no size change in the z-axis by imaging of the deformed particles at different tilt angles.<sup>37</sup> The quantitative analysis of the particle size change averaged over 10–20 silica particles before and after each change in scanning direction is shown in Figure 3.2c. After 5 min of exposure, samples calcined at higher calcination temperatures seem more stable, with even an expansion observed for the silica spheres calcined at 1000 °C. This might indicate the initial hydroxylation of silica is more extensive for samples that have been largely dehydroxylated. However, no statistically significant difference or trend can be

observed after 5–15 min between silica samples calcined at different temperatures, indicating that the initial silica structure and porosity seem to be of limited influence. We tentatively propose that independent of the initial structure, the silica–water system is quickly “equilibrated” to the same reactive state after which silica dissolves at similar rates.

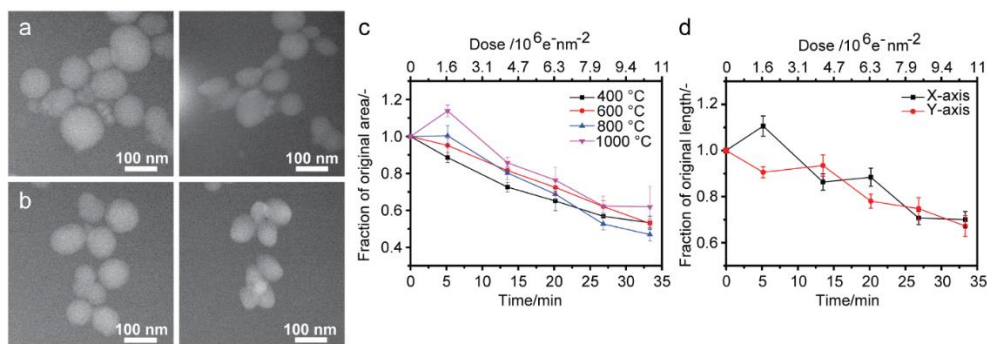


**Figure 3.2.** (a–b) HAADF-STEM images of silica nanospheres calcined at 400 °C (a) and 1000 °C (b) in water in the liquid cell before (left) and after (right) 33 minutes of electron beam scanning, changing the scanning direction between horizontal and vertical after 5, 13, 20 and 27 minutes. (c) Projected surface area relative to the initial projected surface area, averaged over 10–20 silica particles per sample as a function of time/dose. (d) Length of the x-axis and y-axis relative to the initial lengths, averaged over 10–20 silica particles of the sample calcined at 800 °C as a function of time/dose.

In previous work, the apparent elongation was reported to proceed through both shrinkage via dissolution of the particles parallel to the electron beam scanning direction and growth via redeposition of silica species at the sides of the particles. However, a closer look at the particles studied here indicates that dissolution is likely the prevailing cause for this shape change. As is shown in Figure 3.2d, growth of the particle axis in the scanning direction is limited, except for the time before the first change in scanning direction. The shrinkage of the axis perpendicular to the scanning direction on the other hand is far more significant. This indicates that material was preferentially removed from the sides of the particle aligned with the scanning direction, with only limited redeposition at the ends of the particle.

A possible explanation for this preferential removal could be that at the sides of particles aligned with the scanning direction, the beam–liquid–particle surface interface is the largest, resulting in accumulation of reactive species along that surface. For the rest of the particle, as the beam scans across it, this interface is smaller resulting in less radical accumulation and a diminished effect on the silica particles, as the lifetime of the formed radicals is just a few microseconds.<sup>45</sup>

### 3.2.2 Influence of Organic Liquids

Another possible explanation for the observed silica degradation involves the changes in local chemistry of the liquid induced by the beam. In water, this chemistry is relatively complex with many species being formed upon ionization or excitation of water molecules by the electron beam and the consequent reaction network.<sup>45-46</sup> According to literature, the most important species to consider in water are the  $\text{OH}^-$ ,  $\text{H}^+$ ,  $\text{H}_2$ , and  $\text{H}_2\text{O}_2$  species and the  $\text{e}^-_{(\text{aq})}$ ,  $\text{OH}\cdot$ ,  $\text{H}\cdot$ , and  $\text{HO}_2\cdot$  radicals. All of these species could possibly interact with and destabilize the amorphous silica. In particular, the formed  $\text{OH}^-$  and the radicals are likely to aid in the degradation of the particles, by breaking silicon-oxygen bonds and forming soluble silica species.

To reduce the number of reactive species brought about by water radiolysis, LP-TEM imaging of silica spheres was also performed in toluene and in octane, which both have a very different radical chemistry. In these experiments, the same scanning conditions as in Figure 3.2 were applied with the sample of silica calcined at 800 °C. In these nonpolar organic systems, the formation of ionic species is much more limited due to the significantly lower relative permittivity compared to water. This results in a much higher chance of recombination of ions formed by the electron beam and ensures that the beam-induced radical chemistry in these liquids is dominated by excitations and associated homolytic bond cleavage.<sup>45, 47</sup> Due to this and the preference for C-H bond cleavage over C-C bond cleavage, the main species produced by the electron beam are  $\text{H}\cdot$  and  $\text{C}_x\text{H}_y\cdot$ , both strongly reducing radicals.

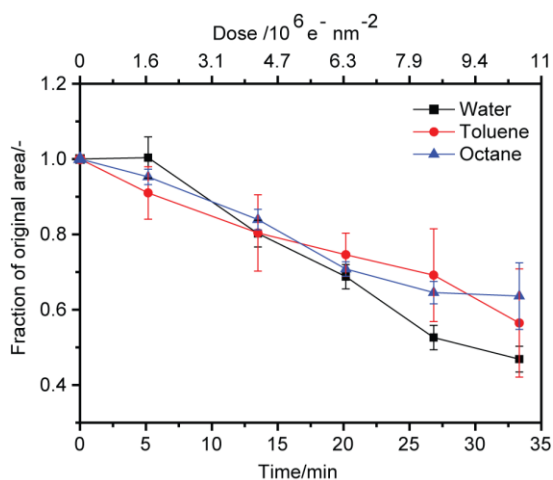
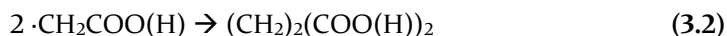


**Figure 3.3.** Projected surface area relative to the initial projected surface area, averaged over 10-20 silica particles (calcined at 800 °C) in water, toluene and octane as a function of time/dose for continuous electron beam scanning, with the scanning direction alternated between horizontal and vertical after 5, 13, 20 and 27 minutes.

The results of these experiments are shown in Figure 3.3 and Supporting Figure S3.3. The degradation of silica in both toluene and octane is remarkably similar when compared to that of water. For toluene, no statistically significant difference is found, while for the octane a minor difference in degradation at highest accumulated dose can be observed. Considering that silica nanoparticles do not deform and degrade when imaged in vacuum, it is probable that degradation observed in water, toluene, and octane is due to beam-induced liquid chemistry. The most likely explanation would be that the degradation is caused by reducing radicals, namely  $e^-_{(aq)}$ ,  $C_xH_y\cdot$ , and  $H\cdot$ , the last one being the only produced species all three liquids have in common.

### 3.2.3 Radical Scavenging Solutes

To investigate the hypothesis that reducing radicals contribute to the observed degradation of silica, an additional series of experiments was performed with solutes added to water, namely acetic acid buffer, phosphoric acid buffer, and potassium persulfate. Although the high dose rates encountered in LP-TEM generally result in a significantly higher number of radicals compared to radiation chemistry studies and rapid consumption of scavengers, only a very small part of the liquid is irradiated. Diffusion from outside the irradiated area can likely compensate for this loss up to very high dose rates, even with low concentrations. According to calculations, typical steady state concentrations of reducing radicals are  $<10 \mu\text{mol}\cdot\text{L}^{-1}$  in deaerated water,<sup>46</sup> indicating that concentrations of  $0.1 \text{ mol}\cdot\text{L}^{-1}$  should be sufficient to significantly decrease steady state radical concentrations. As direct detection of radical species and their reactions is as yet not possible in TEM, only indirect evidence in the form of changing silica behavior upon the addition of radical scavengers is available. Acetic acid, along with other organic acids, is one such radical scavenger and is capable of scavenging radicals through reactions 3.1 and 3.2, which results in the elimination of  $e^-_{(aq)}$ ,  $OH\cdot$ , and  $H\cdot$  and the formation of the  $\cdot\text{CH}_2\text{COO}(\text{H})$  radical, which is known to rapidly dimerize to succinate.<sup>45, 48</sup>



As can be observed in Figure 3.4a–c, and Supporting Figure S3.4 in the appendix, along with Movies M3 and M4 (available online, details in the appendix), the acetic acid buffer was capable of substantially stabilizing the amorphous silica nanoparticles calcined at 800 °C, with a clear dose–response relation for lower concentrations. When using a concentration of  $0.2 \text{ mol}\cdot\text{L}^{-1}$  of acetic acid buffer, surface area of the silica particles decreased by less than 10% even after 33 min of intense radiation, which is significantly less compared to more than 50% loss in the case of pure water. At

concentrations higher than  $0.2 \text{ mol}\cdot\text{L}^{-1}$ , this stability decreased again, although it still surpassed that of pure water. This effect is likely a result of the direct radiolysis of the acetate itself, which produces significant numbers of  $\text{H}\cdot$  radicals. The effects of direct radiolysis for solutes are usually not observed at low concentrations ( $<0.1 \text{ mol}\cdot\text{L}^{-1}$ ), but at higher concentrations become increasingly prevalent, resulting in an optimum between scavenging and additional radical production.<sup>45</sup>

Besides being a scavenger for most of the radicals produced by electron beam radiolysis of water, the acetic acid buffer could also have a buffering effect, which could mitigate the influence of protons and hydroxide ions also produced upon water radiolysis, although previous work on other oxides seems to indicate that increased acidity is of limited influence on dissolution kinetics.<sup>33</sup> Calculations do indicate that electron beam  $\text{H}^+$  yield is higher than the hydroxide yield in most aqueous liquids, which would result in a mildly acidic solution, but the local activity of the  $\text{OH}^-$  ion is also higher than in pure water.<sup>46</sup> As silica solubility increases with higher  $\text{OH}^-$  activity, this could indicate that an acidic buffer is capable of stabilizing the particle as well.

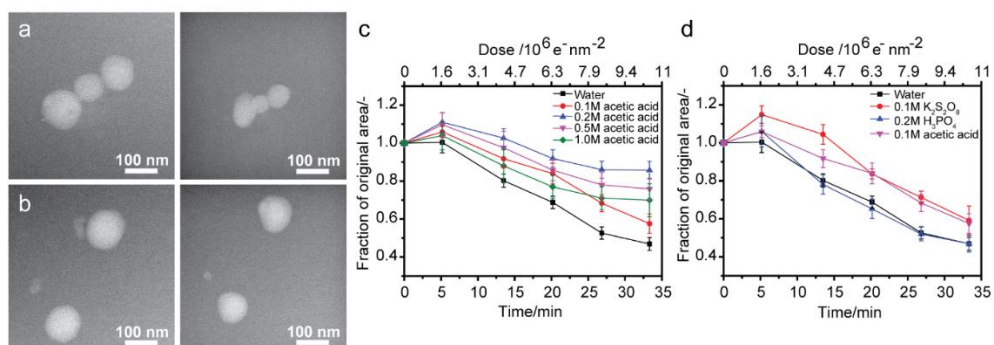


**Figure 3.4.** (a-b) HAADF-STEM images of silica nanoparticles calcined at  $800 \text{ }^\circ\text{C}$  in water (a) and in  $0.2 \text{ mol}\cdot\text{L}^{-1}$  acetic acid buffer solution (b) in the liquid cell before (left) and after (right) 33 minutes of electron beam scanning at  $225,000 \times$  magnification, changing the scanning direction between horizontal and vertical after 5, 13, 20 and 27 minutes. (c) Projected surface area relative to the initial projected surface area, averaged over 10-20 silica particles in solutions with different concentrations of acetic acid buffer as a function of time/electron dose. (d) Projected surface area relative to the initial projected surface area, averaged over 10-20 silica particles in solutions with various solutes as a function of time/electron dose.

To ensure that the observed stabilizing effect is due to the reducing  $\text{H}\cdot$  radicals and not due to a buffering effect of the acetate solution, the same experiment was performed with a  $0.2 \text{ mol}\cdot\text{L}^{-1}$  phosphoric acid buffer. The results presented in Figure 3.4d and Supporting Figure S3.5 clearly show that there was no observable difference between the phosphoric acid buffer and pure water. Furthermore, considering very

similar degradation observed in aprotic organic liquids (toluene, octane), it is clear that the presence or absence of  $H^+$  and  $OH^-$  had no impact on silica stability.

Finally, oxidizing  $\cdot OH$  radicals formed upon electron beam induced water radiolysis might also have an influence on the degradation of  $SiO_2$ . To investigate the influence of  $\cdot OH$  radicals, an additional experiment with a solution containing  $0.1 \text{ mol}\cdot\text{L}^{-1}$  of potassium persulfate ( $K_2S_2O_8$ ) was also performed. The persulfate anion reacts as illustrated in reaction 3.3, selectively scavenging  $e^-_{(aq)}$  and  $H\cdot$  and producing the strongly oxidizing  $\cdot SO_4^-$  radical. As the  $\cdot OH$  radicals are not scavenged, this results in a highly oxidizing environment with similar concentrations of  $\cdot OH$ , but a lower concentration of reducing radicals.



Figure 3.4d and Supporting Figure S3.5 clearly illustrate that the addition of potassium persulfate was also able to stabilize the silica, with a very comparable effect to that of the same concentration of acetic acid buffer. This indicates that  $\cdot OH$  seems to have a limited influence on the  $SiO_2$  degradation.

Another interesting observation is that the particles investigated in experiments with radical scavengers remained much more spherical than their counterparts in water. Although this can be explained partially by the shrinkage being more limited, the effect is even observed for particles still losing a significant amount of surface area, such as those in the experiments with  $0.1 \text{ mol}\cdot\text{L}^{-1} K_2S_2O_8$ .

### **3.2.4 Environmental TEM Using Gaseous $H_2O$**

To further investigate the extent to which presence of water influences silica degradation during in situ STEM imaging, a series of electron beam scanning experiments was performed with the silica in vacuum and in contact with water vapor partial pressures between 0.01 and 1 mbar in a dedicated ETEM. Based on the LP-TEM study, deformation of silica was expected to some extent due to the presence of water, while shrinkage, which occurs mainly through dissolution, was not expected due to the absence of a water layer in which dissolved silica species would diffuse.

As can be observed in Figure 3.5 and Supporting Figure S3.6 in the appendix, a single particle (Supporting Figure S3.6) did not change to any significant extent after 30 min of continuous electron beam scanning, even at 1 mbar of water vapor. However, when close together particles started to sinter quite rapidly when they were in contact with water vapor, as can be seen in Movie M5 (available online, details in the appendix). The rate of sintering seemed to be dependent on the  $H_2O$  partial pressure as well, whereby an increase of water partial pressure from 0.01 to 0.1 and 1 mbar clearly

resulted in an acceleration of sintering, as can be observed from Supporting Figure S3.6. The effect of water on the mobility of the  $\text{SiO}_2$  was quite pronounced, especially when comparing the experiments with and without silica drying at  $600\text{ }^\circ\text{C}$  for 2 h in the TEM vacuum (Figure 3.5). Drying clearly led to an appreciable difference in sintering rate, indicating that even the small amount of adsorbed water from the air can significantly influence silica behavior during electron beam scanning.

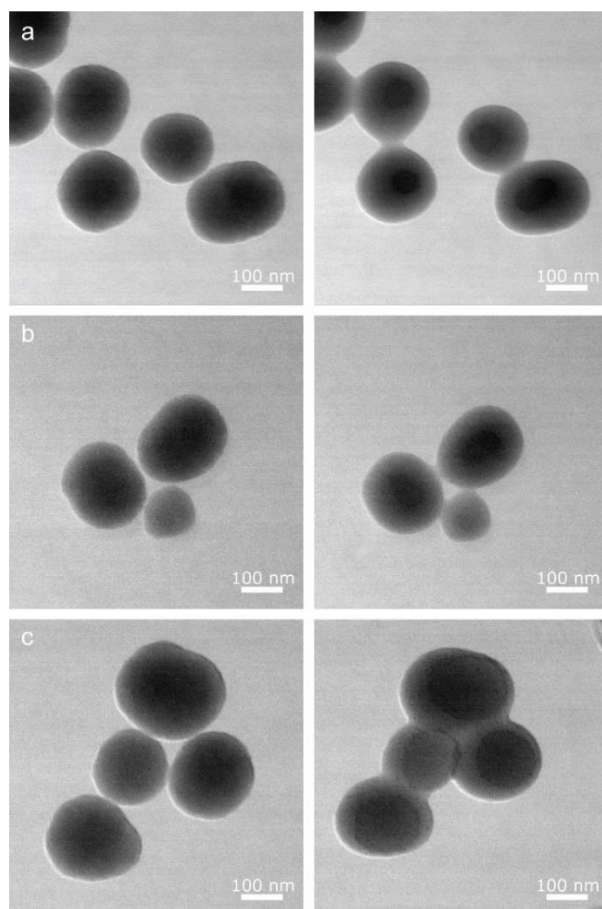
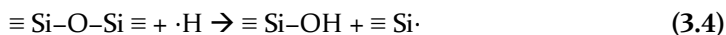


**Figure 3.5.** Bright-Field (BF)-STEM images of silica nanospheres calcined at  $800\text{ }^\circ\text{C}$ , before (left) and after (right) 30 minutes of electron beam scanning at  $225,000\times$  magnification. (a) Silica sample as prepared imaged in vacuum, (b) Silica sample dried in the ETEM vacuum for 2 hours at  $600\text{ }^\circ\text{C}$  prior to imaging in vacuum and (c) Silica sample dried in the ETEM for 2 hours at  $600\text{ }^\circ\text{C}$  prior to imaging in 1 mbar of  $\text{H}_2\text{O}$  during scanning.

### 3.2.5 Model of Silica Deformation and Degradation

To understand the mechanism of silica degradation under LP-TEM conditions, two important phenomena observed in this study will be considered: detrimental influence of reducing radicals formed by the electron beam induced water radiolysis and the stabilizing effect of radical scavengers. As suggested previously,<sup>37</sup> mass loss occurs primarily as a result of dissolution of silica, which in water is predominantly through formation of silicic acid or  $\text{Si}(\text{OH})_4$  species. The formation of silicic acid requires hydroxylation of the silica, which usually proceeds through the opening/hydrolysis of siloxane bonds by  $\text{H}_2\text{O}$ .<sup>49</sup> Earlier study showed that breaking silicon-oxygen bonds can be facilitated by low-energy electrons (300–500 eV) in combination with a thin layer of amorphous ice, although the mechanism was not entirely clear.<sup>50</sup>

Based on the results of this study, we argue that the cleavage of the siloxane bonds is likely accelerated through a reaction with reducing radicals. A possible mechanism for this is through the partial reduction of silica by a hydrogen radical through reaction 3.4, which leads to the formation of a dangling bond. This dangling bond is highly reactive and can subsequently react with water according to reaction 5, forming another hydroxyl group and hydrogen radical.



A similar process is expected to occur in toluene and octane, with reaction 3.5 involving the hydrocarbon species or a hydrocarbon radical instead of water. This would result in the formation of organosilicon compounds with a mixture of silanol, alkoxide, and organosilicon groups. These compounds are known to be kinetically stable<sup>51</sup> and expected to be quite soluble as the groups attached to the silicon atom are derived from the solvent. As a result, a similar shrinkage and degradation of silica particles is expected, considering that the process proceeds via dissolution of soluble silica species. In the absence of surrounding liquid, as demonstrated in ETEM studies with water vapor, dissolved silica species are prevented from diffusing away from the particles, limiting thus the degradation to sintering and moderate shape change, which is likely the result of the increase in mobility of silica species.

Although it is possible for the electron beam to cleave the silicon-oxygen bond,<sup>52</sup> it is unlikely that it would be the main mechanism, as the altering of the liquid chemistry would have far less influence than observed. Furthermore, the observed anisotropy in the shape change could not be explained since there was no difference in electron beam exposure across the particle.



### **3.3 Conclusion**

Identifying the cause and mitigating degradation of amorphous silica and other oxide and metal particles during liquid phase TEM is crucial for enabling application of this technique in studies of dynamic nanoscale processes in liquid. As shown here, the main process responsible for silica degradation is an electron beam induced local change in chemistry, both in liquid and gas phase water in contact with the silica. We propose that reducing radicals produced by the electron beam are the species responsible for this degradation, while oxidizing species, local changes in pH, and the nature of the solid silica do not have a pronounced influence. The addition of species capable of scavenging reducing radicals remarkably lessened the degradation, to the extent that amorphous silica can be more easily used for LP-TEM investigations. Devising such a method for mitigating silica degradation is an important step for the LP-TEM technique, as it allows not only the study of SiO<sub>2</sub> and silica-based materials in a liquid phase, but also demonstrates that a higher degree of control in LP-TEM experiments is feasible.

### **3.4 Materials & Methods**

#### **3.4.1 Silica Preparation**

Spherical silica nanoparticles were prepared adapting the procedure from Stöber et al.<sup>40</sup> In a typical experiment, a mixture of NH<sub>3</sub> solution (11.25 mL, 30%, Merck) and ethanol (230 mL) was heated to 35 °C in an oil bath. Tetraethyl orthosilicate (17.3 mL, TEOS, 98%, Sigma-Aldrich) was subsequently added to this mixture and then left to stir (250 RPM) at 35 °C for 16 h. The solution was then neutralized with nitric acid (65%, Sigma-Aldrich) and the liquid removed by rotary evaporation. The remaining solid was dried overnight at 120 °C, followed by calcination in air at 200 °C for 2 h, then at 400 °C for 1 h, and subsequently 3 h at the final calcination temperature, either 400, 600, 800 or 1000 °C, all with a heating and cooling rate of 1.7 °C·min<sup>-1</sup>. The resulting silica particles were spherical with diameters in the range of 20-30 nm and 60-120 nm.

#### **3.4.2 Liquid Cell Preparation**

A small amount of the prepared silica was dispersed in isopropanol (2 mL, 99.9%, Sigma-Aldrich) and sonicated for at least 15 min. to disperse agglomerates. A droplet of this suspension (0.5 μL) was placed and left for 5 min. to evaporate on the silicon nitride (Si<sub>x</sub>N<sub>y</sub>) layer of the large silicon liquid cell chip with a 50 nm thick Si<sub>x</sub>N<sub>y</sub> window with dimensions of 20 x 550 μm (Protochips Inc., USA). A small silicon chip also containing a 20 x 550 μm Si<sub>x</sub>N<sub>y</sub> window and 150 nm gold spacers to separate the

two chips was then placed in the dedicated liquid cell TEM holder (Protochips Inc., USA), a drop of pure water (1  $\mu\text{L}$ , sterile-filtered, Bioreagent,  $\leq 1$  Eu mL,  $\leq 5$  ppm metal impurities, Sigma-Aldrich) was added on top of it, and the cell was subsequently assembled by placing the large silicon chip on top. In this configuration, the sample is dispersed on the top chip when the holder is inserted in the microscope for optimal spatial resolution in STEM mode.<sup>10</sup> Both the large and small chips were plasma cleaned in an 80%Ar/20%O<sub>2</sub> plasma for 2 min. before the sample was dispersed to render the chip surface hydrophilic.

### **3.4.3 Liquid Cell TEM Experiments**

Liquid cell experiments were performed using a Talos F200X (Thermo Fisher Scientific, Netherlands), operated in STEM mode at 200 kV acceleration voltage and using an HAADF detector for imaging. The imaging was performed with a beam current of 0.21 nA, as determined by the screen current without a holder present in the electron microscope and with a camera length of 125 mm. Images were collected with a pixel dwell time of 9.5  $\mu\text{s}$ , with 1024 pixel x 1024 pixel images, for a total of 10 s per frame. All experiments were performed at 225,000x magnification, corresponding to an image size of 500 nm x 500 nm, which results in a dose rate of  $5.2 \cdot 10^3 \text{ e}^- \cdot \text{nm}^{-2} \cdot \text{s}^{-1}$ .

Each liquid cell experiment was performed in flow mode using a flow of 2  $\mu\text{L} \cdot \text{min}^{-1}$  to prevent the buildup of gases and bubble formation. For each individual measurement, a group of particles was selected and 200 images were acquired, for a total time of approximately 33 min. The scanning direction was rotated by 90° after image number 30, 80, 120, and 160. The particles were assumed to be perfect ellipses throughout the entire experiment and to determine the area, the length of the long and short axis of each ellipse was measured at these image numbers, as well as in the first and last image. Only particles that were sufficiently large to be observable and remained in the field of view during the entire measurement were measured. For each experiment, at least two different locations were chosen for measurements that contained at least five suitable particles each. In total, between 10 and 20 particles were measured and results were averaged for each different condition investigated.

All experiments were performed with the silica particles prepared at a final calcination temperature of 800 °C, except for the experiments in which the effect of silica calcination temperature was studied, in which case the silica samples selected were calcined at 400, 600, 800, and 1000 °C. The experiments were performed in ultrapure water ( $\leq 5$  ppm metal impurities, Sigma-Aldrich), toluene ( $\geq 99.7\%$ , Sigma-Aldrich), or octane ( $\geq 99\%$ , Sigma-Aldrich). All solutions used were prepared using ultrapure water. Solutions containing 0.1, 0.2, 0.5, or 1.0 mol·L<sup>-1</sup> of acetic acid were prepared by

addition of the corresponding amount of acetic acid ( $\geq 99.5\%$ , Sigma-Aldrich) and half of the corresponding molar ratio of NaOH ( $\geq 99\%$ , Sigma-Aldrich) to ultrapure water to obtain a 1:1 buffer of approximately pH 4.5. The  $0.2 \text{ mol}\cdot\text{L}^{-1}$  phosphoric acid ( $\geq 99.9\%$ , Sigma-Aldrich) solution was prepared with the same method, resulting in a pH of approximately 2. The  $0.1 \text{ mol}\cdot\text{L}^{-1} \text{ S}_2\text{O}_8^{2-}$  solution was prepared by dissolving solid  $\text{K}_2\text{S}_2\text{O}_8$  ( $\geq 99\%$ , Sigma-Aldrich) in ultrapure water and care was taken to prepare the solution no more than 1 day in advance to prevent significant decomposition of the persulfate.

### **3.4.3 Environmental TEM Experiments**

The ETEM experiments were performed using a Wildfire heating holder (DENSsolutions, Netherlands) and a heating chip with silicon nitride windows. The heating chip was plasma cleaned for 2 min in a 20 vol%  $\text{O}_2$ /80 vol% Ar plasma prior to loading. A drop of a suspension ( $1.5 \mu\text{L}$ ) of the silica nanospheres calcined at  $800^\circ\text{C}$  in isopropanol was then placed on the heating chip and left to evaporate for 5 min.

The ETEM experiments were performed in a dedicated Titan (Thermo Fisher Scientific, Netherlands) microscope modified for ETEM studies. All experiments were performed in STEM mode at 300 kV acceleration voltage, with a beam current of 0.21 nA. Both the bright field (BF) and HAADF detectors were used. For the HAADF detector, a camera length of either 115 or 165 mm was used to optimize resolution. Images were collected with a pixel dwell time of  $9.5 \mu\text{s}$ , with 1024 pixel x 1024 pixel images, for a total of 10 s per frame. All experiments were also performed at 225,000x magnification, corresponding to an image size of 500 nm x 500 nm, which results in a dose rate of  $5.2 \cdot 10^3 \text{ e}^- \cdot \text{nm}^{-2} \cdot \text{s}^{-1}$ .

For all ETEM experiments, a suitable particle or group of particles was selected and then subjected to continuous scanning for 180 images, corresponding to 30 min, or until all particles disappeared from the field of view as a result of electrostatic charging. Samples were scanned in vacuum ( $\approx 10^{-7}$  mbar) at room temperature both before and after being heated at  $600^\circ\text{C}$  for 2 h inside the column to remove any adsorbed moisture. Afterward, the water vapor pressure was increased in steps up to 1 mbar and scanning experiments were performed at 0.01, 0.1, and 1 mbar of water partial pressure at room temperature.

## 3.5 Acknowledgements

The authors gratefully acknowledge J. D. Meeldijk for technical assistance with the electron microscope, L. Weber for the N<sub>2</sub> physisorption measurements, and R. van den Berg for providing help with synthesis of silica samples. Furthermore, the authors thank D. M. Bartels for the discussions regarding the radical chemistry of all species involved in this work. K. P. de Jong and M. J. Meijerink acknowledge funding from the European Research Council, an EU FP7 ERC Advanced Grant no. 338846. J. Zečević acknowledges financial support by the Netherlands Organization for Scientific Research (NWO), Veni Grant no. 722.015.010. C. Spiga and C.D. Damsgaard acknowledge funding from the Danish Research Council for Technology and Production (FTP), Grant no. 4005-00293.

## 3.6 References

- (1). Kenny, A., *Ancient Philosophy: A New History of Western Philosophy*. OUP Oxford: 2004; Vol. 1.
- (2). Carter, C. B.; Williams, D. B., *Transmission Electron Microscopy*. Springer-Verlag US: 2009.
- (3). Gómez-Navarro, C.; Meyer, J. C.; Sundaram, R. S.; Chuvilin, A.; Kurasch, S.; Burghard, M.; Kern, K.; Kaiser, U., Atomic Structure of Reduced Graphene Oxide. *Nano Lett.* **2010**, *10* (4), 1144-1148.
- (4). Gramm, F.; Baerlocher, C.; McCusker, L. B.; Warrender, S. J.; Wright, P. A.; Han, B.; Hong, S. B.; Liu, Z.; Ohsuna, T.; Terasaki, O., Complex Zeolite Structure Solved by Combining Powder Diffraction and Electron Microscopy. *Nature* **2006**, *444* (7115), 79-81.
- (5). Wang, C.; Van der Vliet, D.; More, K. L.; Zaluzec, N. J.; Peng, S.; Sun, S.; Daimon, H.; Wang, G.; Greeley, J.; Pearson, J.; Paulikas, A. P.; Karapetrov, G.; Strmcnik, D.; Markovic, N. M.; Stamenkovic, V. R., Multimetallic Au/FePt<sub>3</sub> Nanoparticles as Highly Durable Electrocatalyst. *Nano Lett.* **2010**, *11* (3), 919-926.
- (6). Li, J.; Chen, J.; Wang, H.; Chen, N.; Wang, Z.; Guo, L.; Deepak, F. L., In Situ Atomic-Scale Study of Particle-Mediated Nucleation and Growth in Amorphous Bismuth to Nanocrystal Phase Transformation. *Advanced Science* **2018**, *5* (6), 1700992.
- (7). Han, J.; Lin, Y. C.; Chen, L.; Tsai, Y. C.; Ito, Y.; Guo, X.; Hirata, A.; Fujita, T.; Esashi, M.; Gessner, T.; Chen, M., On-Chip Micro-Pseudocapacitors for Ultrahigh Energy and Power Delivery. *Advanced Science* **2015**, *2* (5), 1500067.
- (8). Munnik, P.; De Jongh, P. E.; De Jong, K. P., Recent Developments in the Synthesis of Supported Catalysts. *Chem. Rev.* **2015**, *115* (14), 6687-6718.
- (9). Zečević, J.; Vanbutsele, G.; De Jong, K. P.; Martens, J. A., Nanoscale Intimacy in Bifunctional Catalysts for Selective Conversion of Hydrocarbons. *Nature* **2015**, *528* (7581), 245-248.
- (10). De Jonge, N.; Ross, F. M., Electron Microscopy of Specimens in Liquid. *Nat. Nanotechnol.* **2011**, *6* (11), 695-704.

- (11). Li, D.; Nielsen, M. H.; De Yoreo, J. J., Chapter Seven - Design, Fabrication, and Applications of in Situ Fluid Cell Tem. In *Methods Enzymol.*, James, J. D. Y., Ed. Academic Press: 2013; Vol. Volume 532, pp 147-164.
- (12). Grogan, J. M.; Schneider, N. M.; Ross, F. M.; Bau, H. H., The Nanoaquarium: A New Paradigm in Electron Microscopy. *J. Indian Inst. Sci.* **2012**, *92* (2), 295-308.
- (13). Williamson, M. J.; Tromp, R. M.; Vereecken, P. M.; Hull, R.; Ross, F. M., Dynamic Microscopy of Nanoscale Cluster Growth at the Solid-Liquid Interface. *Nat. Mater.* **2003**, *2* (8), 532-536.
- (14). Yuk, J. M.; Park, J.; Ercius, P.; Kim, K.; Hellebusch, D. J.; Crommie, M. F.; Lee, J. Y.; Zettl, A.; Alivisatos, A. P., High-Resolution Em of Colloidal Nanocrystal Growth Using Graphene Liquid Cells. *Science* **2012**, *336* (6077), 61-64.
- (15). Ye, X.; Jones, M. R.; Frechette, L. B.; Chen, Q.; Powers, A. S.; Ercius, P.; Dunn, G.; Rotskoff, G. M.; Nguyen, S. C.; Adiga, V. P.; Zettl, A.; Rabani, E.; Geissler, P. L.; Alivisatos, A. P., Single-Particle Mapping of Nonequilibrium Nanocrystal Transformations. *Science* **2016**, *354* (6314), 874-877.
- (16). Dai, L. L.; Sharma, R.; Wu, C.-Y., Self-Assembled Structure of Nanoparticles at a Liquid-Liquid Interface. *Langmuir* **2005**, *21* (7), 2641-2643.
- (17). Hendley, C. T.; Tao, J.; Kunitake, J. A. M. R.; De Yoreo, J. J.; Estroff, L. A., Microscopy Techniques for Investigating the Control of Organic Constituents on Biomineralization. *MRS Bull.* **2015**, *40* (06), 480-489.
- (18). Smeets, P. J. M.; Cho, K. R.; Kempen, R. G. E.; Sommerdijk, N. A. J. M.; De Yoreo, J. J., Calcium Carbonate Nucleation Driven by Ion Binding in a Biomimetic Matrix Revealed by in Situ Electron Microscopy. *Nat. Mater.* **2015**, *14* (4), 394-399.
- (19). Elgrabli, D.; Dachraoui, W.; Ménard-Moyon, C.; Liu, X. J.; Bégin, D.; Bégin-Colin, S.; Bianco, A.; Gazeau, F.; Alloyeau, D., Carbon Nanotube Degradation in Macrophages: Live Nanoscale Monitoring and Understanding of Biological Pathway. *ACS Nano* **2015**, *9* (10), 10113-10124.
- (20). Zheng, H.; Claridge, S. A.; Minor, A. M.; Alivisatos, A. P.; Dahmen, U., Nanocrystal Diffusion in a Liquid Thin Film Observed by in Situ Transmission Electron Microscopy. *Nano Lett.* **2009**, *9* (6), 2460-2465.
- (21). Pohlmann, E. S.; Patel, K.; Guo, S.; Dukes, M. J.; Sheng, Z.; Kelly, D. F., Real-Time Visualization of Nanoparticles Interacting with Glioblastoma Stem Cells. *Nano Lett.* **2015**, *15* (4), 2329-2335.
- (22). Radisic, A.; Vereecken, P. M.; Hannon, J. B.; Searson, P. C.; Ross, F. M., Quantifying Electrochemical Nucleation and Growth of Nanoscale Clusters Using Real-Time Kinetic Data. *Nano Lett.* **2006**, *6* (2), 238-242.
- (23). Sacci, R. L.; Dudney, N. J.; More, K. L.; Parent, L. R.; Arslan, I.; Browning, N. D.; Unocic, R. R., Direct Visualization of Initial SEI Morphology and Growth Kinetics During Lithium Deposition by in Situ Electrochemical Transmission Electron Microscopy. *Chem. Commun.* **2014**, *50* (17), 2104-2107.
- (24). Abellan, P.; Mehdi, B. L.; Parent, L. R.; Gu, M.; Park, C.; Xu, W.; Zhang, Y.; Arslan, I.; Zhang, J.-G.; Wang, C.-M.; Evans, J. E.; Browning, N. D., Probing the Degradation Mechanisms in Electrolyte Solutions for Li-Ion Batteries by in Situ Transmission Electron Microscopy. *Nano Lett.* **2014**, *14* (3), 1293-1299.

- (25). Kraus, T.; De Jonge, N., Dendritic Gold Nanowire Growth Observed in Liquid with Transmission Electron Microscopy. *Langmuir* **2013**, *29* (26), 8427-8432.
- (26). Jungjohann, K. L.; Bliznakov, S.; Sutter, P. W.; Stach, E. A.; Sutter, E. A., In Situ Liquid Cell Electron Microscopy of the Solution Growth of Au-Pd Core-Shell Nanostructures. *Nano Lett.* **2013**, *13* (6), 2964-2970.
- (27). Liang, W.-I.; Zhang, X.; Bustillo, K.; Chiu, C.-H.; Wu, W.-W.; Xu, J.; Chu, Y.-H.; Zheng, H., In Situ Study of Spinel Ferrite Nanocrystal Growth Using Liquid Cell Transmission Electron Microscopy. *Chem. Mater.* **2015**, *27* (23), 8146-8152.
- (28). Zhang, Y.; Keller, D.; Rossell, M. D.; Erni, R., Formation of Au Nanoparticles in Liquid Cell Transmission Electron Microscopy: From a Systematic Study to Engineered Nanostructures. *Chem. Mater.* **2017**, *29* (24), 10518-10525.
- (29). Egerton, R. F.; Li, P.; Malac, M., Radiation Damage in the TEM and SEM. *Micron* **2004**, *35* (6), 399-409.
- (30). Woehl, T. J.; Jungjohann, K. L.; Evans, J. E.; Arslan, I.; Ristenpart, W. D.; Browning, N. D., Experimental Procedures to Mitigate Electron Beam Induced Artifacts During in Situ Fluid Imaging of Nanomaterials. *Ultramicroscopy* **2013**, *127*, 53-63.
- (31). Woehl, T.; Abellan, P., Defining the Radiation Chemistry During Liquid Cell Electron Microscopy to Enable Visualization of Nanomaterial Growth and Degradation Dynamics. *Journal of microscopy* **2017**, *265* (2), 135-147.
- (32). Meijerink, M. J.; De Jong, K. P.; Zečević, J., Assessment of Oxide Nanoparticle Stability in Liquid Phase Transmission Electron Microscopy. *Nano Res.* **2019**, *12* (9), 2355-2363.
- (33). Lu, Y.; Geng, J.; Wang, K.; Zhang, W.; Ding, W.; Zhang, Z.; Xie, S.; Dai, H.; Chen, F.-R.; Sui, M., Modifying Surface Chemistry of Metal Oxides for Boosting Dissolution Kinetics in Water by Liquid Cell Electron Microscopy. *ACS Nano* **2017**, *11* (8), 8018-8025.
- (34). Liong, M.; Lu, J.; Kovoichich, M.; Xia, T.; Ruehm, S. G.; Nel, A. E.; Tamanoi, F.; Zink, J. I., Multifunctional Inorganic Nanoparticles for Imaging, Targeting, and Drug Delivery. *ACS Nano* **2008**, *2* (5), 889.
- (35). Ding, H. L.; Zhang, Y. X.; Wang, S.; Xu, J. M.; Xu, S. C.; Li, G. H., Fe<sub>3</sub>O<sub>4</sub>@ SiO<sub>2</sub> Core/Shell Nanoparticles: The Silica Coating Regulations with a Single Core for Different Core Sizes and Shell Thicknesses. *Chem. Mater.* **2012**, *24* (23), 4572-4580.
- (36). Archer, R. J.; Parnell, A. J.; Campbell, A. I.; Howse, J. R.; Ebbens, S. J., A Pickering Emulsion Route to Swimming Active Janus Colloids. *Advanced Science* **2018**, *5* (2), 1700528.
- (37). Zečević, J.; Hermansdörfer, J.; Schuh, T.; De Jong, K. P.; De Jonge, N., Anisotropic Shape Changes of Silica Nanoparticles Induced in Liquid with Scanning Transmission Electron Microscopy. *Small* **2017**, *13* (1), 1602466.
- (38). Van de Put, M. W. P.; Carcouët, C. C. M. C.; Bomans, P. H. H.; Friedrich, H.; de Jonge, N.; Sommerdijk, N. A. J. M., Writing Silica Structures in Liquid with Scanning Transmission Electron Microscopy. *Small* **2015**, *11* (5), 585-590.

- (39). Rehn, S. M.; Jones, M. R., New Strategies for Probing Energy Systems with in Situ Liquid-Phase Transmission Electron Microscopy. *ACS Energy Lett.* **2018**, *3* (6), 1269-1278.
- (40). Stöber, W.; Fink, A.; Bohn, E., Controlled Growth of Monodisperse Silica Spheres in the Micron Size Range. *J. Colloid Interface Sci.* **1968**, *26* (1), 62-69.
- (41). Zhuravlev, L. T., The Surface Chemistry of Amorphous Silica. Zhuravlev Model. *Colloids Surf., A* **2000**, *173* (1), 1-38.
- (42). Romeis, S.; Paul, J.; Hanisch, M.; Reddy Marthala, V. R.; Hartmann, M.; Taylor, R. N. K.; Schmidt, J.; Peukert, W., Correlation of Enhanced Strength and Internal Structure for Heat-Treated Submicron Stöber Silica Particles. *Part. Part. Syst. Charact.* **2014**, *31* (6), 664-674.
- (43). Zhang, L.; D'Acunzi, M.; Kappl, M.; Imhof, A.; van Blaaderen, A.; Butt, H.-J.; Graf, R.; Vollmer, D., Tuning the Mechanical Properties of Silica Microcapsules. *Phys. Chem. Chem. Phys.* **2010**, *12* (47), 15392-15398.
- (44). Meijerink, M. J.; Spiga, C.; Hansen, T. W.; Damsgaard, C. D.; De Jong, K. P.; Zečević, J., Nanoscale Imaging and Stabilization of Silica Nanospheres in Liquid Phase Transmission Electron Microscopy. *Part. Part. Syst. Charact.* **2019**, *36* (1), 1800374.
- (45). Spothem-Maurizot, M.; Mostafavi, M.; Douki, T., *Radiation Chemistry: From Basics to Applications in Material and Life Sciences*. EDP Sciences: 2008.
- (46). Schneider, N. M.; Norton, M. M.; Mendel, B. J.; Grogan, J. M.; Ross, F. M.; Bau, H. H., Electron-Water Interactions and Implications for Liquid Cell Electron Microscopy. *J. Phys. Chem. C* **2014**, *118* (38), 22373-22382.
- (47). Calvert, J. G. P., James N., Jr., *Photochemistry*. Wiley: New York, 1966; Vol. 43, p 564.
- (48). Ross A.B., M. W. G., Helman W.P., Buxton G.V., Huie R.E., Neta P., NDRL-NIST Solution Kinetics Database Version 3.0. 1998.
- (49). Rimola, A.; Costa, D.; Sodupe, M.; Lambert, J.-F.; Ugliengo, P., Silica Surface Features and Their Role in the Adsorption of Biomolecules: Computational Modeling and Experiments. *Chem. Rev.* **2013**, *113* (6), 4216-4313.
- (50). Yu, X.; Emmez, E.; Pan, Q.; Yang, B.; Pomp, S.; Kaden, W. E.; Sterrer, M.; Shaikhutdinov, S.; Freund, H.-J.; Goikoetxea, I.; Włodarczyk, R.; Sauer, J., Electron Stimulated Hydroxylation of a Metal Supported Silicate Film. *Phys. Chem. Chem. Phys.* **2016**, *18* (5), 3755-3764.
- (51). Pawlenko, S., *Organosilicon Chemistry*. Walter de Gruyter: 1986.
- (52). Zheng, K.; Wang, C.; Cheng, Y.-Q.; Yue, Y.; Han, X.; Zhang, Z.; Shan, Z.; Mao, S. X.; Ye, M.; Yin, Y.; Ma, E., Electron-Beam-Assisted Superplastic Shaping of Nanoscale Amorphous Silica. *Nature Communications* **2010**, *1*, 24.

## **Supporting Information**

### **Supporting Movies description**

- 1) Movie M1: Degradation of silica nanospheres calcined at 400 °C under continuous STEM scanning in pure water.
- 2) Movie M2: Degradation of silica nanospheres calcined at 1000 °C under continuous STEM scanning in pure water.
- 3) Movie M3: Degradation of silica nanospheres calcined at 800 °C under continuous STEM scanning in pure water.
- 4) Movie M4: Degradation of silica nanospheres calcined at 800 °C under continuous STEM scanning in a 0.2M acetic acid solution.
- 5) Movie M5: Sintering of silica nanospheres calcined at 800 °C under continuous STEM scanning in contact with 1 mbar H<sub>2</sub>O vapor in the ETEM.

(Movies available online at <https://doi.org/10.1002/ppsc.201800374>)



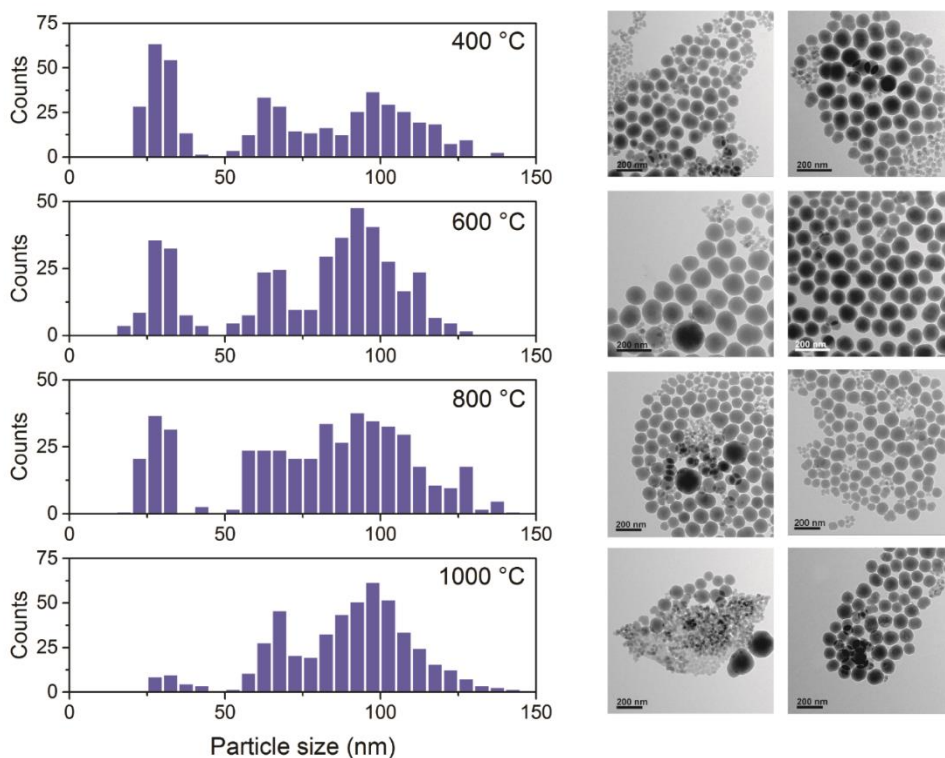
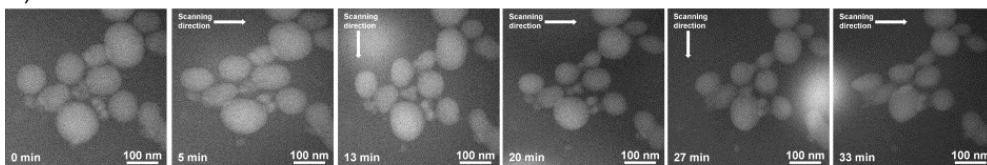
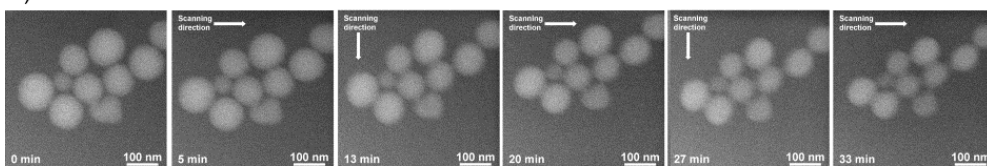


**Figure S3.1.** Histogram and representative TEM images of silica nanospheres calcined at different temperatures. On the left, the histograms of the particle size distribution are presented and indicated the temperature used to calcine the silica samples. At least 400 individual particles were measured for each sample to obtain the histogram. To the right of each histogram are two representative bright-field TEM images of the sample calcined at the indicated temperature. The histograms show only limited difference in particle size distribution between the samples in the size region of 60 - 100 nm. For the sample calcined at 1000 °C, small particles of about 30 nm (not used for LP-TEM imaging and analysis) disappear, likely as a result of sintering at such a high temperature.

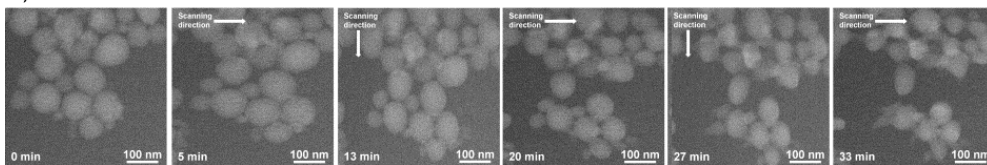
## a) Stöber silica calcined at 400 °C



## b) Stöber silica calcined at 600 °C



## c) Stöber silica calcined at 800 °C



## d) Stöber silica calcined at 1000 °C

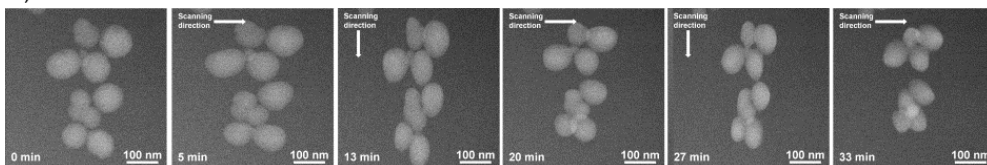
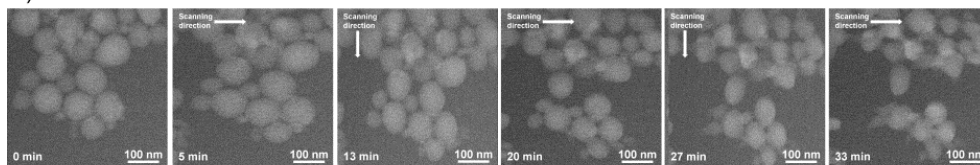
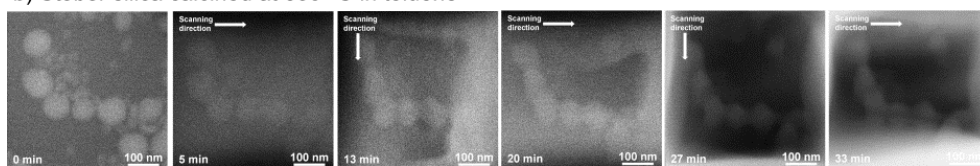


**Figure S3.2.** Liquid cell images of silica nanospheres calcined at different temperatures. HAADF-STEM images of silica samples in the liquid cell showing one of the areas used for determining the particle shrinkage during continuous electron beam scanning. Each row corresponds to a sample prepared at different calcination temperature, with (a) 400 °C, (b) 600 °C, (c) 800 °C and (d) 1000 °C respectively. Each image corresponds to the point in time indicated in the lower left corner at which measurements presented in Figure 3.2 were performed. Furthermore, each image represents the last frame before the change in scanning direction indicated by the arrow. The dose rate was  $5.2 \cdot 10^3 \text{ e}^- \cdot \text{nm}^{-2} \cdot \text{s}^{-1}$  in all cases.

a) Stöber silica calcined at 800 °C in water



b) Stöber silica calcined at 800 °C in toluene



c) Stöber silica calcined at 800 °C in octane

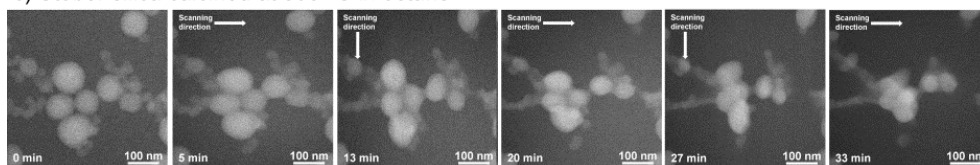
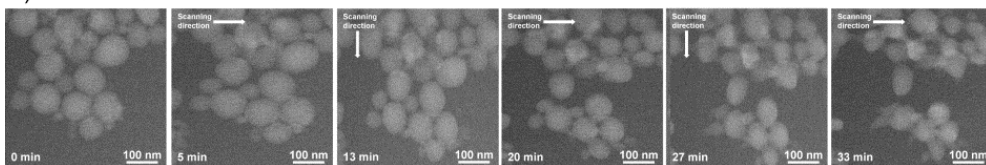
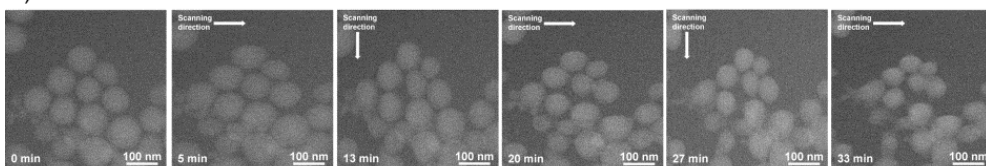


**Figure S3.3.** Liquid cell images of silica nanospheres in organic liquids. HAADF-STEM images of silica samples in the liquid cell showing one of the areas used for determining the particle shrinkage during continuous electron beam scanning. Each row corresponds to a sample in a different liquid, namely (a) pure water, (b) pure toluene and (c) pure octane. Each image corresponds to the point in time indicated in the lower left corner at which measurements presented in Figure 3.3 were performed. Furthermore, each image represents the last frame before the change in scanning direction indicated by the arrow. The dose rate was  $5.2 \cdot 10^3 \text{ e}^- \cdot \text{nm}^{-2} \cdot \text{s}^{-1}$  in all cases.

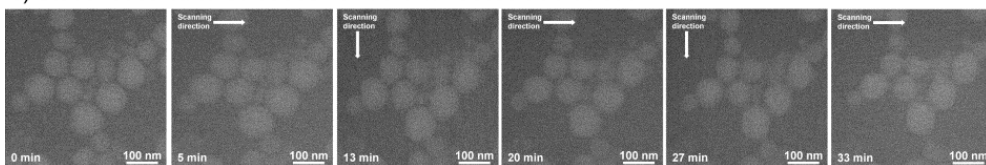
a) Stöber silica calcined at 800 °C in water



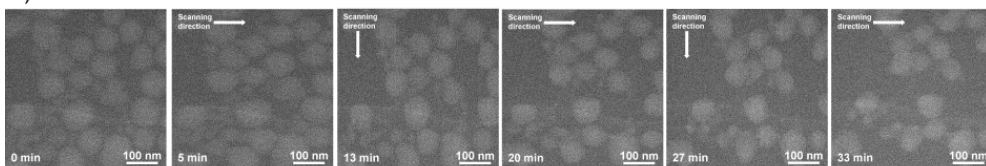
b) Stöber silica calcined at 800 °C in a 0.1M acetic acid solution



c) Stöber silica calcined at 800 °C in a 0.2M acetic acid solution



d) Stöber silica calcined at 800 °C in a 0.5M acetic acid solution



e) Stöber silica calcined at 800 °C in a 1.0M acetic acid solution

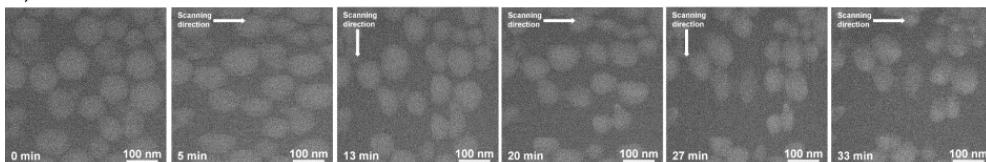
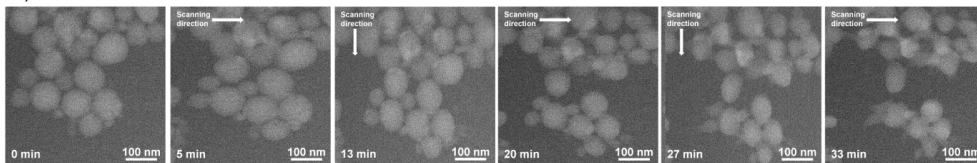
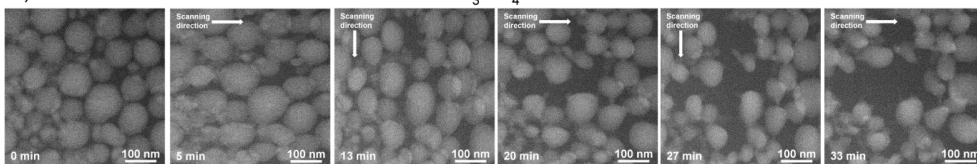


**Figure S3.4.** Liquid cell images of silica nanospheres in acetic acid solutions of different concentrations. HAADF-STEM images of silica samples in the liquid cell showing one of the areas used for determining the particle shrinkage during continuous electron beam scanning. Each row corresponds to a sample with a different concentration of acetic acid/sodium acetate buffer, with (a) pure water for comparison, (b) 0.1M of acetic acid buffer, (c) 0.2M of acetic acid buffer, (d) 0.5M of acetic acid buffer, (e) 1.0M of acetic acid buffer, respectively. Each image corresponds to the point in time indicated in the lower left corner at which measurements presented in Figure 3.4c were performed. Furthermore, each image represents the last frame before the change in scanning direction indicated by the arrow. The dose rate was  $5.2 \cdot 10^3 \text{ e}^- \cdot \text{nm}^{-2} \cdot \text{s}^{-1}$  in all cases.

a) Stöber silica calcined at 800 °C in water



b) Stöber silica calcined at 800 °C in a 0.2M H<sub>3</sub>PO<sub>4</sub> solution



c) Stöber silica calcined at 800 °C in a 0.1M K<sub>2</sub>S<sub>2</sub>O<sub>8</sub> solution

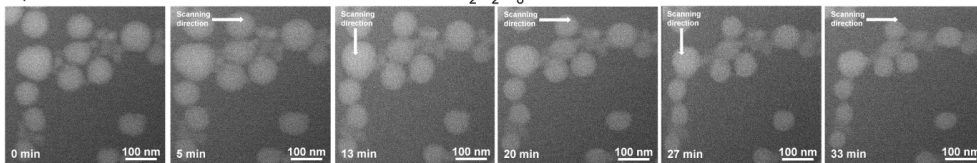


**Figure S3.5.** Liquid cell images of Stöber silica samples in 0.1M K<sub>2</sub>S<sub>2</sub>O<sub>8</sub> and 0.2M H<sub>3</sub>PO<sub>4</sub> solutions. HAADF-STEM images of silica samples in the liquid cell showing one of the areas used for determining the particle shrinkage during continuous electron beam scanning. Each row corresponds to a sample with different solutes, with (a) pure water for comparison, (b) 0.1M K<sub>2</sub>S<sub>2</sub>O<sub>8</sub> solution and (c) 0.2M H<sub>3</sub>PO<sub>4</sub> buffer solution respectively. Each image corresponds to the point in time indicated in the lower left corner at which measurements presented in Figure 3.4d were performed. Furthermore, each image represents the last frame before the change in scanning direction indicated by the arrow. The dose rate was  $5.2 \cdot 10^3 \text{ e}^- \cdot \text{nm}^{-2} \cdot \text{s}^{-1}$  in all cases.

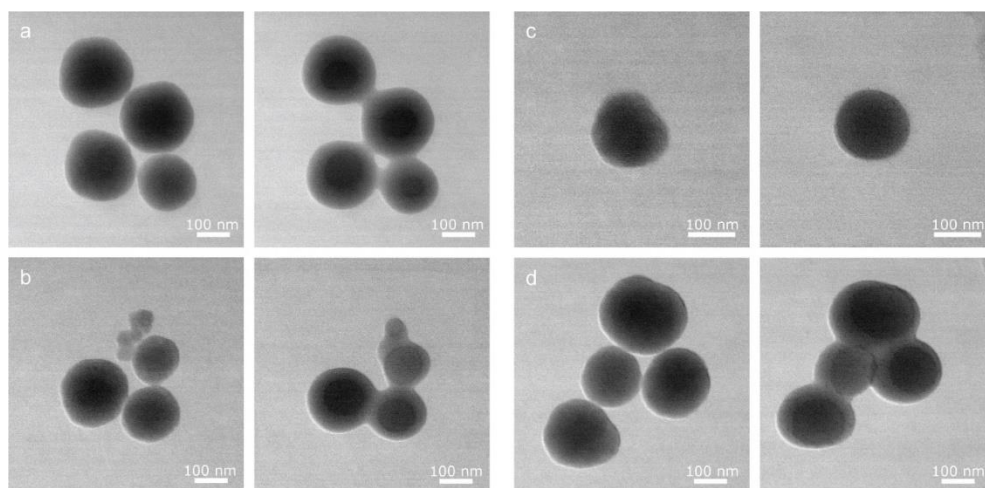


**Figure S3.6.** Environmental TEM images of silica nanoparticles in contact with different  $H_2O$  vapor partial pressures. BF-STEM images of silica sample calcined at  $800\text{ }^\circ\text{C}$  before (left) and after (right) 30 minutes of continuous electron beam scanning at  $225,000\times$  magnification for (a), (b) and (d), and  $320,000\times$  magnification for (c). (a) the silica sample scanned at  $0.01\text{ mbar}$   $H_2O$  vapor partial pressure, (b) the silica sample scanned at  $0.1\text{ mbar}$   $H_2O$  vapor partial pressure, (c) a single silica particle scanned in  $1\text{ mbar}$   $H_2O$  vapor partial pressure and (d) a group of silica particles at  $1\text{ mbar}$   $H_2O$  vapor partial pressure. The dose rate was  $5.2 \cdot 10^3\text{ e}^- \cdot \text{nm}^{-2} \cdot \text{s}^{-1}$  in (a), (b) and (d) and  $1.0 \cdot 10^4\text{ e}^- \cdot \text{nm}^{-2} \cdot \text{s}^{-1}$  for (c).

## Chapter 4

# Growth of Supported Gold Nanoparticles in Aqueous Phase Studied by in Situ Transmission Electron Microscopy

### Abstract

Nanoparticle growth has long been a significant challenge in nanotechnology and catalysis, but the lack of knowledge on the fundamental nanoscale aspects of this process has made its understanding and prediction difficult, especially in a liquid phase. In this work, we successfully used liquid-phase transmission electron microscopy (LP-TEM) to image this process in real time at the nanometer scale, using an Au/TiO<sub>2</sub> catalyst in the presence of NaCl<sub>(aq)</sub> as a case study. In situ LP-TEM clearly showed that the growth of Au nanoparticles occurred through a form of Ostwald ripening, whereby particles grew or disappeared, probably via monomer transfer, without clear correlation to particle size in contrast to predictions of classical Ostwald ripening models. In addition, the existence of a significant fraction of inert particles that neither grew nor shrank was observed. Furthermore, in situ transmission electron microscopy (TEM) showed that particle shrinkage was sudden and seemed a stochastic process, while particle growth by monomer attachment was slow and likely the rate-determining step for sintering in this system. Identification and understanding of these individual nanoparticle events are critical for extending the accuracy and predictive power of Ostwald ripening models for nanomaterials.

This chapter is based on: Meijerink, M. J.; de Jong, K. P.; Zečević, J., Growth of Supported Gold Nanoparticles in Aqueous Phase Studied by In Situ Transmission Electron Microscopy. *J. Phys. Chem. C* **2020**, *124* (3), 2202-2212.

## 4.1 Introduction

Almost 60 years ago, it was said that there is plenty of room at the bottom.<sup>1</sup> Nowadays, we are however getting very close to that bottom, with many new inventions in nanotechnology based on the unique properties originating from quantum mechanical effects. Many of these physicochemical properties are highly size dependent and it is therefore crucial not only to obtain, but also to preserve nanoparticles of this size.<sup>2-3</sup>

Unfortunately, due to their small size and thus a high surface energy contribution to the thermodynamic potential, a large driving force for nanoparticle growth exists. As a result, nanoparticles grow (sinter) rapidly, often losing the desirable size-dependent properties in the process. This sintering is especially problematic in the field of heterogeneous catalysis, where chemical reactions are catalyzed at the particle surface. To maximize the available surface area and thus catalyst activity, particles should be and remain small (often <10 nm).<sup>4</sup>

Particle growth is therefore a significant challenge for heterogeneous catalysts, and for decades, researchers have been trying to understand underlying mechanisms and build kinetic models that explain and predict the sintering behavior.<sup>5</sup> This sintering is commonly considered to take place by Ostwald ripening (OR), by particle migration and coalescence, or as a result of a combination of both mechanisms. In OR, it is assumed that particles themselves are immobile and growth is the result of monomer transfer from particles smaller than a certain critical radius to particles larger than this radius. In the case of particle migration and coalescence, the particles are mobile, move across a support, and merge together upon interaction.

To understand and model sintering behavior and kinetics, most studies follow the behavior of an ensemble of particles. This is often done through the analysis of Transmission Electron Microscopy (TEM)-derived average particle sizes and particle size distributions (PSDs) prior to and after sintering, resulting in several models. In the case of Ostwald ripening, sintering is usually described using the Lifshitz–Slyozov–Wagner (LSW) model, which predicts that the PSD is self-similar (the shape does not change with time) with a long tail toward smaller particle sizes, while the volume average particle size increases linearly with time.<sup>6-8</sup> For particle migration and coalescence, the process is usually described by some form of the Von Smoluchowski coagulation model, where the PSD displays a tail toward larger particles and typically fits a lognormal distribution.<sup>9-10</sup>

However, using PSDs before and after catalyst sintering often led to discrepancies between model predictions and experimental data. This is particularly noticeable in



the case of Ostwald ripening, where the predicted small nanoparticles are almost never found in practice, and the reason why this was the case is unclear.<sup>11</sup> After OR, this then also results in a PSD that fits a lognormal distribution, which makes it impossible to infer the sintering mechanism from the PSDs alone.

A leap forward in solving these challenges has been made with the introduction of environmental TEM (ETEM), which allows direct in situ observation of catalyst nanoparticle sintering in a gas phase and at elevated temperature.<sup>12-15</sup> However, ETEM limits the studies of catalyst sintering processes to only those that take place in a gaseous environment and has a limited range of gas partial pressure (typically <5 mbar) due to the high vacuum requirements.<sup>16</sup> More recent developments in microfabrication allowed for cell-type holders and resulted in a wider range of gas pressures and gas types becoming available for in situ TEM.<sup>17</sup> However, these technologies still do not allow study of liquid phase sintering, which is a major issue in important systems such as catalysts for (H<sub>2</sub>) polymer-electrolyte membrane fuel cells<sup>18-19</sup> or several biomass-to-chemical processes.<sup>20-22</sup>

It is not until recently that TEM imaging can also be performed in a liquid environment.<sup>23-25</sup> The so-called liquid-phase transmission electron microscopy (LP-TEM) is a powerful tool that allows visualization of materials in a liquid at a nanometer scale and has been, so far, successfully employed in studying, e.g., biomineralization,<sup>26</sup> protein movement over a cell membrane,<sup>27</sup> metal nucleation and growth,<sup>28-29</sup> electrochemical deposition and growth,<sup>25, 30</sup> and oxide stability, as also discussed in more detail in chapter 2 and 3.<sup>31-34</sup> LP-TEM has also been used by Hermannsdörfer et al. to study the chemical stability of gold colloids in different aqueous environments.<sup>35</sup> In addition, Woehl et al. followed the aggregation of silver particles in situ.<sup>36</sup> These studies, although performed on unsupported and relatively large particles, do indicate that LP-TEM can have a great potential for studying catalyst sintering processes taking place in a liquid.

Studying sintering behavior in a liquid phase is particularly important for Au-based catalysts, highly attractive catalysts for a variety of industrial applications<sup>37</sup> such as the conversion of biomass to platform chemicals, which often takes place in a harsh aqueous environment.<sup>20, 22, 38-39</sup> Even when immobilized on a support, small gold nanoparticles invariably sinter rapidly in a liquid phase, especially in the presence of chloride ions, a common contaminant in biomass-derived feedstock.<sup>40-41</sup> This yields a lower specific surface area (SSA) and hence lower activity of the catalyst over time. Despite extensive work on the characterization of gold catalysts, our understanding of the processes underlying this sintering is limited.<sup>37</sup>

This work therefore employs the LP-TEM technique for the first time to study sintering of a titania-supported gold catalyst in a liquid environment. LP-TEM provided direct evidence that for gold nanoparticles of 3 nm number-average diameter Ostwald ripening is the main sintering mechanism, as predicted in a number of earlier studies; however, it also revealed that there is only a limited particle size dependence, as opposed to predictions and assumptions of the classical Ostwald ripening model.<sup>42-43</sup> Furthermore, it appears that this shrinkage is likely an activated process in which particles of all sizes investigated (1–5 nm) may shrink rapidly once destabilized. Particle growth, probably via monomer reattachment, on the other hand, was slow and likely the rate-limiting step, while a significant fraction of particles did not change size at all. In the presence of large (~20 nm) gold particles, the growth of ~3 nm particles does not occur, but a similar fraction of particles still disappears and the mobile gold species are deposited on the large particles.

## **4.2 Results and Discussion**

### **4.2.1 Au/TiO<sub>2</sub> catalyst**

To study the liquid phase growth of gold nanoparticles supported on TiO<sub>2</sub>, two samples were prepared, one with a unimodal and one with a bimodal particle size distribution (PSD). The unimodal Au/TiO<sub>2</sub> catalyst sample was synthesized using a gold–ethylene diamine complex and titanium dioxide nanopowder (P25, Evonik) by adapting the procedure of Zhu et al.<sup>44</sup> The bimodal Au/TiO<sub>2</sub> sample was prepared by depositing 20 nm gold colloidal particles on the previously prepared unimodal Au/TiO<sub>2</sub> sample, resulting in the desired bimodal particle size distribution.

Scanning transmission electron microscopy (STEM) images showed that Au nanoparticles with a number-average diameter of 3 nm, relatively narrow size distribution, and uniform distribution across the TiO<sub>2</sub> support were present in both the unimodal (Figure 4.1a,b) and bimodal (Figure 4.1c,d) samples. Next to 3 nm Au particles, the bimodal sample also contained well-dispersed 20 nm colloidal Au particles (Figure 4.1d). X-ray diffraction and N<sub>2</sub> physisorption analyses of the pristine TiO<sub>2</sub> support and the unimodal catalyst (Figure S4.1) indicated that the TiO<sub>2</sub> support structure of the unimodal sample was not altered during gold deposition. The TiO<sub>2</sub> powder still consisted of a mixture of anatase and rutile crystallites in the same ratio and the BET specific surface area remained 45 m<sup>2</sup>·g<sup>-1</sup>. Gold loading was 0.9 wt% for the unimodal sample, as determined by inductively coupled plasma atomic emission spectrometry (ICP-AES).

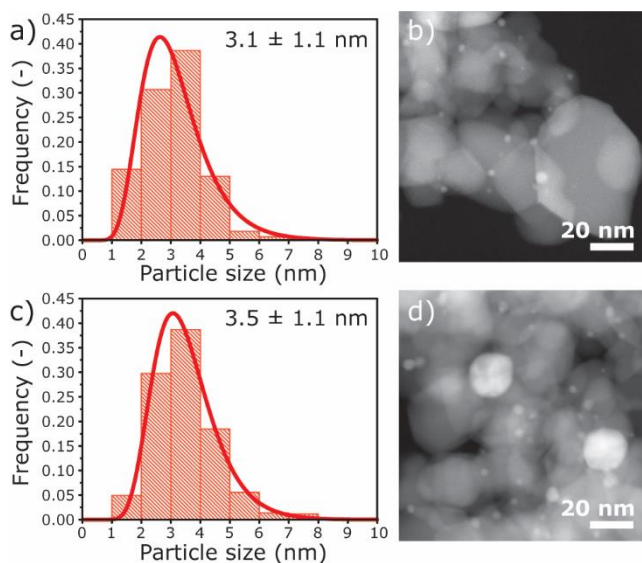


**Figure 4.1.** Particle size distributions (PSDs) with a lognormal fit and representative high-angle annular dark-field scanning transmission electron microscopy (HAADF-STEM) images of the unimodal (a, b) and the bimodal (c, d) Au/TiO<sub>2</sub> samples, respectively. Only the small particles (<10 nm) are included in the PSD of the bimodal sample.

#### 4.2.2 Sintering Behavior of the Unimodal Sample

Sintering of the individual Au nanoparticles in a liquid environment was investigated in situ using a specialized liquid-phase (LP) TEM holder (Poseidon Select, Protochips Inc.). This system consists of two chips with electron-transparent Si<sub>x</sub>N<sub>y</sub> windows, between which a thin layer of liquid and the sample are sandwiched to allow imaging while keeping the liquid separate from the high vacuum inside the TEM column, as illustrated in Figure S4.2. Using this system, it was possible to observe sintering behavior directly at the nanoscale with high spatial and temporal resolution.

Considering the inertness of gold in an aerated aqueous environment, no or limited sintering and other structural changes would be expected in the presence of water and dissolved oxygen alone.<sup>45</sup> However, the presence of chloride ions is detrimental to the stability of gold nanoparticles. It promotes sintering, both in gas and liquid phases and/or when present on the support, due to the ability of chloride to form a complex with gold ions, which results in the stabilization of mobile ionic gold species.<sup>46-47</sup> Therefore, sintering was investigated with LP-TEM in both water and a 10 mmol·L<sup>-1</sup> solution of NaCl in H<sub>2</sub>O. In addition to these in situ experiments, ex situ laboratory studies were performed to ensure that in situ observations accurately represent the

actual sintering behavior in this system. For ex situ studies, 30–50 mg of catalyst was exposed to the same water or 10 mmol·L<sup>-1</sup> NaCl in water environment used in situ, and the dispersion was heated to 80 °C to accelerate sintering.

Figure 4.2a,b displays the resulting PSDs of the unimodal sample based on 200–300 particles at different times in an NaCl environment for the in situ and ex situ experiments, respectively. Furthermore, a representative STEM image associated with each moment in time, for which the PSD was determined, is displayed as well. In addition, Movie M2, which is available online<sup>48</sup> (details in the appendix), also shows the real-time nanoparticle behavior during an entire in situ experiment. As can also be observed in Figure 4.2, the liquid layer limits the attainable resolution in LP-TEM to an extent and bright-field (BF) STEM imaging mode has been found to yield better resolution and contrast compared to high-angle annular dark-field (HAADF) STEM.<sup>49</sup> For imaging thin samples in vacuum (the ex situ samples) on the other hand, HAADF-STEM showed better contrast.

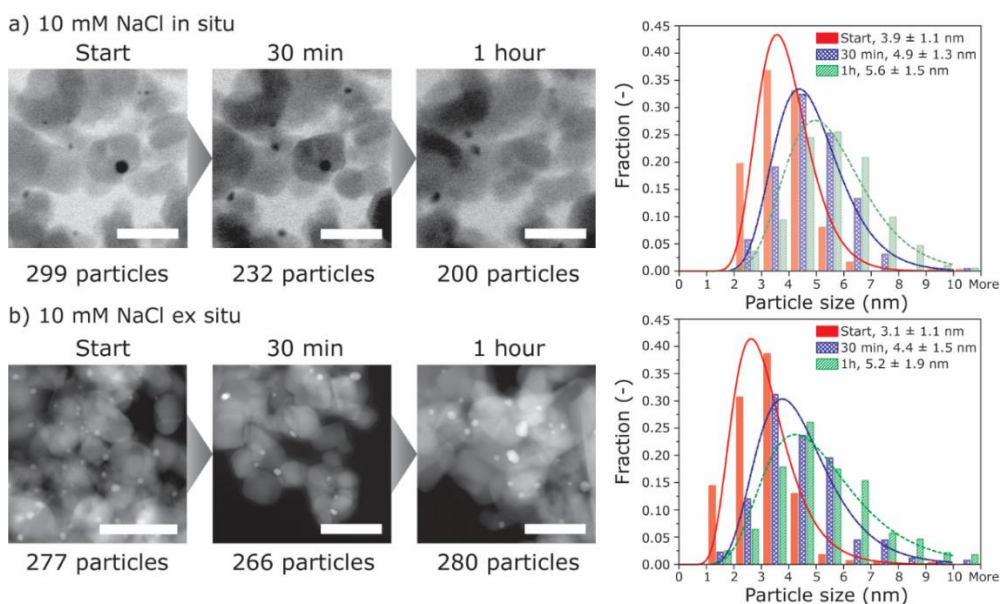


**Figure 4.2.** In situ and ex situ (a and b, respectively) comparison of the evolution of the particle size distributions for the Au/TiO<sub>2</sub> sample with unimodal particle size distribution in a 10 mmol·L<sup>-1</sup> NaCl aqueous solution. A representative scanning transmission electron microscopy image in a bright-field (BF) (a) or a high-angle annular dark-field (HAADF) (b) mode is shown for three different times, corresponding to the particle size distributions displayed in the graph on the right side of the images. For in situ experiments, images were taken at the same position. The scale bar in each image corresponds to 50 nm.

In both the in situ and ex situ experiments, growth of the Au nanoparticles in NaCl was observed after 1 h. In situ LP-TEM unambiguously showed that particle growth proceeded through Ostwald ripening, where particles did hardly move but changed in size, most likely through monomer transfer via the liquid phase. Particle migration and coalescence, as the other possible sintering mechanism, could be excluded noting that only two merging events within several hundred particles were observed and, overall, Au particles displayed a very low mobility on the TiO<sub>2</sub> surface. The presence of NaCl was shown to be crucial for sintering, since in both the in situ and ex situ experiments in water, very limited growth of Au particles was observed (Figure S4.3 and Movie M1, the latter also available online).

To exclude the possibility of primary damage by the electron beam influencing the observed particle growth, the samples were exposed to the same electron beam treatment in the vacuum of the electron microscope (Figure S4.4). No sintering or other alteration of the catalyst was observed, which confirms that the presence of a liquid medium was crucial for sintering. The support was not affected in the experiments, as the LPTEM experiments with the pristine P25 TiO<sub>2</sub> in H<sub>2</sub>O or a 10 mmol·L<sup>-1</sup> NaCl solution under the same imaging conditions showed no changes of the TiO<sub>2</sub> structure (Figure S4.5).

It was found however that the sintering rate did depend on the NaCl concentration. This is illustrated in Figure S4.6, where two in situ experiments in a solution of 10 and 100 mmol·L<sup>-1</sup> NaCl in H<sub>2</sub>O are compared, with sintering being significantly faster in the latter. As 10 mmol·L<sup>-1</sup> NaCl yielded a more suitable time scale to observe sintering, this concentration was used throughout further experiments.

Importantly, PSDs derived from the in situ experiments in 10 mmol·L<sup>-1</sup> NaCl (Figure 4.2a) do display the self-similar evolution characteristic for Ostwald ripening. However, they also show a tail toward the right, which is in disagreement with classical OR models and more akin to migration and coalescence. The evolution of the PSD does however correspond well to Ostwald ripening behavior observed in practice.<sup>6-7</sup> Clearly, direct in situ observation was crucial to determine the growth mechanism, as PSD analysis before and after growth could have led to the incorrect conclusion that this is either a mix of two mechanisms or even migration and coalescence only.

Furthermore, the PSDs derived from the in situ experiments are in good agreement with the PSDs obtained from the laboratory ex situ experiments (Figure 4.2b), although the beam did accelerate sintering somewhat. Because of this, in situ sintering experiments were performed at room temperature while ex situ the sample was heated to 80 °C to accelerate particle growth to similar time scales. The acceleration during

the in situ LP-TEM measurements likely originates from the oxidizing  $\bullet\text{OH}$  radical and  $\text{H}_2\text{O}_2$  and reducing hydrated electron ( $e_{(\text{aq})}^-$ ) produced by the beam, as it has been observed before that these radicals are able to accelerate growth of gold colloids.<sup>35</sup> Particle size measurements of nanoparticles well outside the reach of the radicals ( $>5 \times 0.2 \mu\text{m}$ , the latter of which is the Fick diffusion length in water for the lifetime of these radicals) were also performed after an in situ experiment. These particles were found to have the same PSD as the initial PSD of the irradiated area, confirming that the electron beam was indeed accelerating sintering somewhat but that the overall beam effects were minor.

However, to ensure that our in situ observations were indeed representative for ex situ behavior, an additional control experiment was performed using liquid cell heating chips to perform an in situ experiment at  $80^\circ\text{C}$  in the presence of  $10 \text{ mmol}\cdot\text{L}^{-1}$  NaCl in  $\text{H}_2\text{O}$ . Due to the electron beam and heating combination resulting in significant acceleration of growth, imaging of the region of interest was performed every 5 minutes, with the beam being blanked in between. Even then, significant acceleration of sintering compared to only heating or only using the electron beam was observed. Nevertheless, as can be observed in Figure S4.8, the behavior was qualitatively similar to both the in situ and ex situ observations and the rate was quite similar to that in the in situ experiment at room temperature with  $100 \text{ mmol}\cdot\text{L}^{-1}$  NaCl.

### 4.2.3 Individual Au Nanoparticle Study

Although the behavior of the assembly of particles seems to match Ostwald ripening observations for catalysts very well,<sup>11</sup> LP-TEM revealed that the dynamic behavior of individual nanoparticles is remarkably different from expectations. This is illustrated in Figure 4.3, wherein the size evolution of several individual particles over time is displayed. In most Ostwald ripening models, it is assumed that larger particles will grow at the expense of smaller particles, as a result of the higher specific surface energy of particles with a more convex surface. Models then typically predict a time-dependent critical particle diameter  $d$ , where particles smaller than  $d$  shrink, while all particles with a diameter larger than  $d$  are expected to grow.<sup>50</sup>

Strikingly, Figure 4.3 and Movie M2 actually reveal that the size of a nanoparticle does not seem to have a large influence on the type of behavior it displays. In our experiments, many of the larger (3–5 nm) particles were also found to shrink, while part of the smaller (1–3 nm) particles were seen to grow (Movie M2) and particles of all sizes could remain stable. The limited effect of particle size on the probability that it disappeared is also illustrated in Figure 4.4. Here, each point corresponds to the diameter of an individual particle at the moment it starts disappearing along with the time at which it disappears and the solid line showing the number-average particle

size over time. This figure highlights that although the majority of particles disappearing have a size below average, there is also a significant fraction above average size.

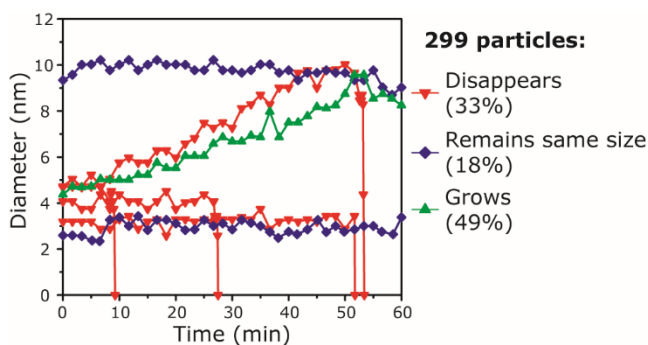


**Figure 4.3.** Diameter evolution over time of several particles during the in situ study of unimodal Au/TiO<sub>2</sub> in a solution of 10 mmol·L<sup>-1</sup> NaCl in H<sub>2</sub>O. Different evolution paths were observed, including shrinking/ disappearing particles (solid, red inverted triangle), particles that remain approximately the same size (solid, blue diamond), and particles that grow (solid, green upright triangle), with the percentage of particles displaying each type of behavior shown in the legend.

Besides an indifference to size, in situ data related to Figure 4.3 also revealed that although nanoparticles grew slowly over time, nanoparticle shrinkage was a fast process. From Movie 2 and Figure S4.7, in which a few consecutive frames of a disappearing nanoparticle are displayed, it is also clear that nanoparticles did not detach from the support, as they remained spherical and attached to TiO<sub>2</sub>. This, combined with the lack of nanoparticle mobility observed and the absence of reattaching/appearing nanoparticles, suggests that they dissolve as monomeric ionic gold species in line with an Ostwald ripening mechanism. This fast disappearance could also cause discrepancies between the LSW model predictions, which predict an asymmetric PSD skewed to smaller particles, and experimentally determined PSDs, where these smaller particles are almost never observed. These results indicate that nanoparticles in this size range disappear too fast to be observed at any given time. Another important observation is that a meaningful fraction of approximately 18% of nanoparticles does not seem to change size to any significant extent, while models predict nanoparticles to either grow or shrink.

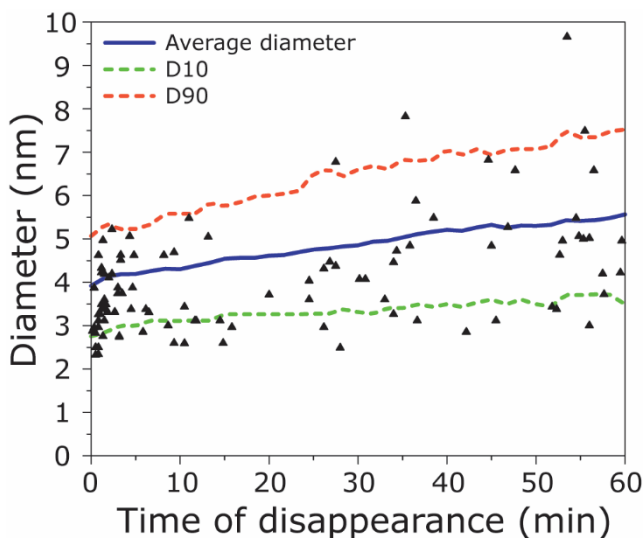


**Figure 4.4.** Overview of the diameter of each measured particle at the moment it starts disappearing, along with the corresponding time of disappearance for the in situ experiment in 10 mmol·L<sup>-1</sup> NaCl dissolved in H<sub>2</sub>O. Each point in the graph corresponds to a single particle. The solid line corresponds to the number-average particle diameter, and the lower and upper dashed lines correspond to D10 and D90, the size below which 10 and 90% of the particle population lies, respectively.

To understand the origin of the fast disappearance and limited influence of particle size, it is helpful to first consider the thermodynamic properties of this system. As previously mentioned, the formation of mobile Au<sup>3+</sup> species from metallic gold under standard conditions is highly unfavorable, but the addition of chloride ions results in the formation of an [AuCl<sub>4</sub>]<sup>-</sup> complex, which has a significantly lower reduction potential:<sup>51</sup>



As these are standard potentials, low gold ion concentrations and high concentrations of oxygen, chloride ions, and hydronium ions have to be present for the oxidation of gold to be thermodynamically favorable. In the conditions used in this work (pH = 7, PO<sub>2</sub> = 0.2 bar), the reduction potential of reaction 4.3 is only 0.81 V though, indicating that the chemical equilibrium should still be toward bulk metallic gold. Although theoretical calculations indicate that water irradiated with electrons has a small drop in pH to approximately 4.5 within the irradiated area for the irradiation conditions



used in this work,<sup>45</sup> this pH would still have an equilibrium toward bulk metallic gold. However, it is well known that the reduction potential of gold ions rapidly decreases with gold particle size, especially for nanoparticles smaller than approximately 10 nm, as a result of the higher fraction of low-coordinated surface atoms present.<sup>42, 52</sup> Work by Ivanova et al.<sup>53</sup> indicates that this shift can be in excess of 0.2 V for ~4 nm particles, which indicates that dissolution can actually be favorable for all particles present in these samples when the concentration of chloride ions is sufficiently high.

Some calculations on the equilibrium concentrations of the  $[\text{AuCl}_4]^-$  complex for different pH values,  $\text{Cl}^-$  concentrations, and  $\text{O}_2$  partial pressures are listed in Table S4.1. These values indicate that concentrations of the complex are low but significant for particles in this size range. The previously mentioned in situ experiment with 100  $\text{mmol}\cdot\text{L}^{-1}$  NaCl in  $\text{H}_2\text{O}$  (Figure S4.6) also demonstrates that the concentration of chloride ions is indeed important. Additionally, to investigate the influence of oxygen on Ostwald ripening, we have also performed a laboratory sintering experiment in a 10  $\text{mmol}\cdot\text{L}^{-1}$  NaCl solution under an inert  $\text{N}_2$  atmosphere instead of air. The results presented in Figure S4.9 clearly showed that the absence of  $\text{O}_2$  significantly slowed down sintering, indicating that oxidation of gold by oxygen is crucial and  $[\text{AuCl}_4]^-$  complexes are likely the mobile species.

Next to these thermodynamic aspects, we expect that the rate of the oxidation process is affected by kinetics too. It is likely that this dissolution occurs preferentially at defects/low-coordinated Au atoms and is able to proceed rapidly once such a site is available in a nanoparticle through thermal fluctuations in the experiments. It has been shown previously that such single events can indeed destabilize small silver nanoparticles and likely explain the observed rapid dissolution observed in these experiments.<sup>54-55</sup> This would also explain why particles of all sizes are dissolving, although with a bias toward smaller particles. The preference for smaller particles is likely a combination of their being more prone to oxidation (thermodynamics) and the faster formation of defects (kinetics), increasing their chances of being destabilized.

The slow growth of particles of all sizes indicates that reattachment of gold monomers to particles is a kinetically limited process and likely requires sites of high coordination for attaching gold atoms. This suggests that thermodynamic constraints are not prevailing once particles start growing and that growth requires a surface configuration containing such high coordination sites. In addition, Figure 4.3 shows a delay of roughly 10 min. before particle growth started, and according to Figure 4.4, significantly more particles disappeared during those first 10 min., indicating that a

certain concentration of the  $[\text{AuCl}_4]^-$  complex is necessary before growth proceeds at measurable rates.

Another possible explanation that should be considered is that the surface of gold is not always completely accessible as a result of ligand coverage. However, the synthesis procedure includes a high-temperature calcination step that should be sufficient to remove all of the remaining ethylene diamine ligands and any other organic contamination. It is therefore likely that almost all of the gold nanoparticles are completely accessible. The limited divergence in nanoparticle shape, also at the interface with the  $\text{TiO}_2$  support, indicates that the interaction of gold with the  $\text{TiO}_2$  support is very similar for all particles. Consequently, we expect that local differences in nanoparticle surface chemistry and accessibility do not play a significant role in the differences observed between the individual nanoparticles in these Ostwald ripening experiments.

The previously mentioned kinetic limitations might also explain why a significant fraction of particles do not change size during the experiments. Certain gold-support interactions or facets being exposed might result in slower kinetics for either gold oxidation or gold-ion reduction and attachment, resulting in very limited or no change in size. Although difficult to observe as a result of the small size, some facet formation during growth seems to take place for part of the particles. In the experiments with in situ heating with  $10 \text{ mmol}\cdot\text{L}^{-1}$  NaCl in water (Figure S4.8) and in the in situ experiments with  $100 \text{ mmol}\cdot\text{L}^{-1}$  NaCl at room temperature (Figure S4.6), several particles do have clear facets upon growth. The facet growth is likely more visible as a result of the larger final particle size obtained in these experiments. This facet formation during growth is another strong indication of reattachment taking place at specific surface structures.<sup>29, 56</sup> It could also be argued that some of these particles are inside support pores and their size is limited by the pore size.<sup>57</sup> However, several particles that are clearly not inside a pore were also found to remain the same size, as illustrated in Figure S4.10, and therefore this explanation is not satisfactory for all particles.

### 4.2.4 Bimodal Au Particle Size Distribution

To study the effect of the presence of significantly larger particles on sintering, we also prepared a sample with a bimodal particle size distribution by depositing 20 nm Au colloids on the unimodal sample with  $\sim 3$  nm Au particles. Due to their larger size, these particles should be significantly more stable and attachment kinetics should be more favorable.<sup>53</sup> When subjecting this sample to the same conditions as those used for the unimodal sample, in situ and ex situ experiments with only water present again showed only limited changes in Au particle size (Figure S4.11 and Movie M3).

In the presence of  $10 \text{ mmol}\cdot\text{L}^{-1}$  NaCl, the same fraction of small (1–5 nm) particles compared to the unimodal sample in NaCl disappeared in the same manner (33% in both cases), by shrinking and disappearing in less than 1 min. Although more stable than the small particles, the 20 nm particles are still significantly less stable than bulk gold and could therefore be expected to dissolve as well, albeit with lower probability.<sup>53</sup> It was indeed observed that one of the 21 observed large particles dissolved, which again indicates that dissolution is a stochastic process with only a limited influence of nanoparticle size for particles in this size range.

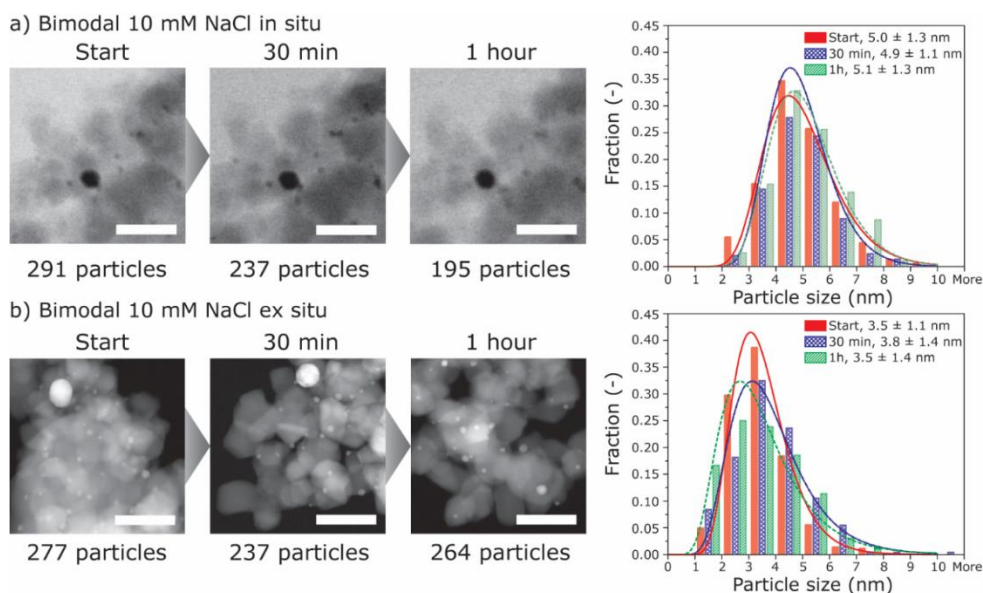


**Figure 4.5.** *In situ* and *ex situ* (a and b, respectively) comparison of the evolution of the particle size distributions for the small particles (<10 nm) of the Au/TiO<sub>2</sub> sample with bimodal particle size distribution in a  $10 \text{ mmol}\cdot\text{L}^{-1}$  NaCl in water solution. Due to the limited number of large particles (20 nm) and the uncertainty in the bulk ratio of smaller to larger particles, the large particles were not included in these PSDs. A representative scanning transmission electron microscopy image in bright-field (BF) (a) or high-angle annular dark-field (HAADF) (b) mode is shown for three different times, corresponding to the particle size distributions displayed in the graph on the right side of the images. For the *in situ* experiments, each image is taken at the same position. The scale bar in each image corresponds to 50 nm.

Surprisingly, although the same fraction of particles disappeared, the remaining small (~3 nm) particles did not change in size significantly in both the *in situ* and *ex situ* experiments, as Figure 4.5 and Movie M4 demonstrate. The 20 nm particles seemed to grow somewhat, but due to their large volume, the change in diameter is much harder to accurately determine compared to small particles. Assuming conservation

of gold in the field of view, the diameter of the large particles would increase by approximately 2 nm at most when all of the gold is deposited on these particles. In addition, the large size also results in a more gradual change in contrast at the edges of the particles, making it more difficult to exactly determine the diameter of the particle. An example of this measured size evolution of two of these larger particles is presented in Figure S4.12.

Still, the lack of growth of the small particles in the bimodal system suggests that  $[\text{AuCl}_4]^-$  monomer reattachment is predominantly happening on the larger particles. It is therefore likely that monomer reattachment is rate-limiting for Ostwald ripening in this system, as the thermodynamic driving force is larger for gold reattachment on the larger particles.<sup>53</sup> Diffusion limitations are unlikely, as in the case of the in situ experiments, typical ion diffusion lengths ( $\sim 30 \mu\text{m}$  for 1 s in water) are significantly larger than the area being irradiated by the electron beam used to drive sintering ( $0.5 \mu\text{m} \times 0.5 \mu\text{m}$ ). In the case of the ex situ experiments, vigorous stirring ensured a homogeneous dispersion of catalyst and fast mixing through convection. Furthermore, in the presence of diffusion limitations, one would generally expect the formation of at least some dendritic structures, whereas none were observed.<sup>58</sup>

#### **4.2.4 Sintering Kinetics**

For catalysis, the specific surface area (SSA) or the surface area per gram of the active material, in this case, the gold nanoparticles, is an important factor for the activity of the catalyst, as it determines the amount of active sites available to catalyze a chemical reaction. Using the obtained PSDs from the in situ experiments, this gold SSA was determined over time for the unimodal sample in  $10 \text{ mmol}\cdot\text{L}^{-1}$  NaCl and compared to the values obtained from the ex situ experiments acquired at 10 minute intervals. This comparison, presented in Figure 4.6, shows that this specific surface area decreases significantly over time, both in situ and ex situ, which would result in significant deactivation of the catalyst.

The rate of decrease in SSA through sintering is often fitted using a power-law fit, with an experimentally observed third-order dependence for Ostwald ripening.<sup>2</sup> Realizing the short time scale, fitting our in situ data with a third-order power law shows quite good agreement with the measured data for the in situ results. As can be observed, there is a large scatter in the ex situ results, as it was not possible to sample the same areas of the catalyst multiple times. This results in a larger error in the acquired particle size distribution and therefore a larger error in the rate constants obtained from short time experiments. Owing to this larger error, long-term, expensive catalyst sintering experiments are often required to accurately predict sintering behavior.<sup>42</sup> In situ observations could therefore aid significantly in building more accurate Ostwald

ripening models and with great potential as a quantitative method for predicting long-term Ostwald ripening.

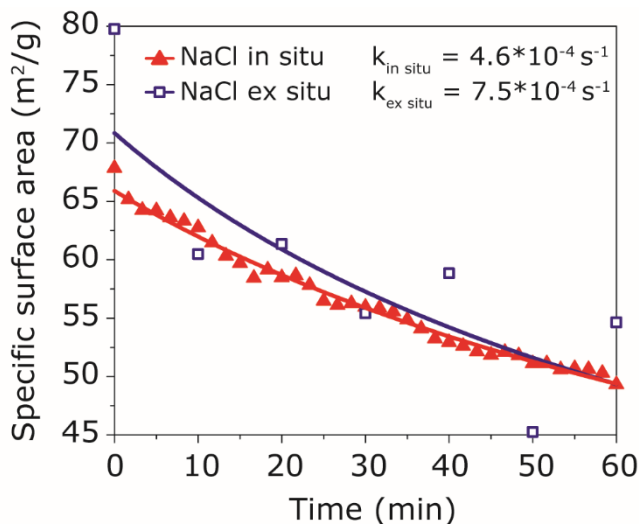


**Figure 4.6.** Gold specific surface area in  $\text{m}^2\cdot\text{g}^{-1}$  with measured values (symbols) and the fit (lines) for both the in situ and ex situ experiments on the unimodal sample in a solution of  $10 \text{ mmol}\cdot\text{L}^{-1}$  NaCl in  $\text{H}_2\text{O}$ .

The same kinetic analysis was performed for sintering of the sample with bimodal PSD as well, but as previously mentioned, it is challenging to observe the change in diameter of the large particles ( $\sim 20 \text{ nm}$ ). As a result, the gold mass balance in the field of view is significantly harder to determine and therefore, so is the specific surface area. In addition, it is very difficult to obtain the same ratio of gold mass between small particles and large particles in the in situ experiments as compared to the bulk sample. In our case, approximately 30% of the gold mass consisted of large particles at the start of the in situ experiments, while in the bulk, this is  $\leq 10\%$ . Due to this, in our analysis, only the surface area of the small particles was taken into account, which does however correspond to  $>95\%$  of the overall surface area in the bulk sample. It was assumed that the total volume of gold in the field of view was constant and that all of the gold from the disappeared particles was deposited on the large particles.

The result of this analysis for the decrease in SSA, normalized with respect to the initial SSA, is displayed in Figure 4.7, along with the normalized SSA of the unimodal sample. It can be seen that the gold SSA decreased faster for the bimodal sample than for the unimodal sample, although the difference becomes smaller after longer times. A likely explanation for this observation is that in the case of the unimodal sample the amount of gold in the field of view was found to increase with time, which yields a net

faster decrease in SSA. This increase could partially result from the fact that some of the smallest particles could be hard to observe in the liquid cell, resulting in more gold present at the start than actually measured, but it is possible that some gold is transported into the field of view from the surrounding area in all experiments.

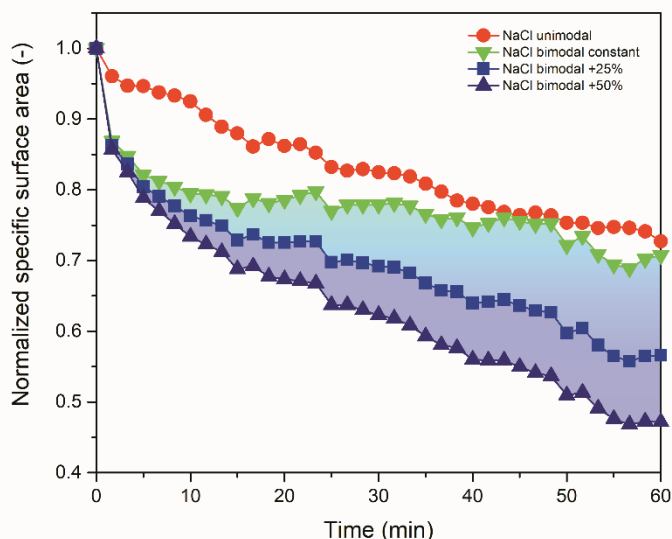


**Figure 4.7.** Gold specific surface area change over time derived from in situ experiments for the unimodal and bimodal sample in a solution of  $10 \text{ mmol}\cdot\text{L}^{-1}$  NaCl in  $\text{H}_2\text{O}$ , normalized with respect to the initial specific surface area. For the bimodal sample, three different lines are plotted, assuming an influx of gold in the field of view of 0, 25, and 50% of the initial amount of gold. The highlighted area in between indicates that the range of possible SSA decreases for the bimodal sample.

When comparing the areas close to the imaged area before and after each experiment, it also seems that a few particles just outside of the irradiated area have disappeared, indicating that there is indeed some gold entering the field of view, as can be seen in Figure S4.13. This net transport could be the result of the reducing radicals present in the field of view, which are a stronger and more reactive reducing agent than water. Reduction of the ionic gold complex in the field of view might then be slightly easier than outside of the field of view, resulting in a slightly lower gold concentration in the field of view and therefore net diffusive transport. It is however not possible to determine the exact amount of gold coming into the field of view for the in situ experiments with the bimodal sample.

However, when assuming that an amount of gold comparable to that in the unimodal in situ experiments is entering the field of view and also depositing on the large particles during the bimodal experiment, the SSA decreases a lot faster during the

bimodal experiments and the fitted Ostwald ripening rate constant is significantly higher. This is illustrated by the shaded area in Figure 4.7, where it was assumed that an additional amount of gold entered the field of view ranging from 0 to 50% of the initial amount of gold. This 50% increase of gold represents the maximum increase found for all except one of the in situ experiments with the unimodal sample.

These results do however clearly show that the specific surface area decreases significantly faster in the sample with bimodal particle size distribution, despite the almost nonexistent growth of most particles. This can be explained by the fact that a very similar fraction (~33%) of particles disappears in both samples but that in the bimodal sample, gold mostly redeposits on the large particles, with a negligible contribution to the overall SSA. In the unimodal sample, gold redeposits on other small particles, which then still have a significant SSA to which the redeposited gold can contribute. Hence, almost no gold is incorporated in very large particles in the unimodal sample, resulting in a significantly slower decrease in SSA.

These observations also provide a good explanation for a puzzling phenomenon often observed in catalytic experiments. It is often seen that a catalyst with a few large clusters deactivates faster than a similar catalyst without those clusters as a result of a decreasing specific surface area. Surprisingly though, investigation of the deactivated catalyst usually shows that the individual particles in the catalyst with the large clusters have grown significantly less than in the other catalyst, and one would expect this catalyst to have a higher specific surface area and therefore a higher activity.<sup>59</sup> If a significant fraction of the particles disappears and the metal is incorporated in very large clusters with a negligible SSA, the overall SSA of the catalyst is significantly lower than when all particles grow just a little bit, which results in faster catalyst deactivation.

### **4.3 Conclusions**

In conclusion, the present work offers new fundamental insights into the mechanism of Ostwald ripening of supported metal nanoparticles in a liquid phase and highlights the power of liquid-phase electron microscopy for investigating such processes in situ. An Au/TiO<sub>2</sub> catalyst was used as a case study and dissolved Cl<sup>-</sup> ions as sintering promoters. We found that although the behavior of the ensemble of particles agrees well with previous work in the literature and our ex situ results, the nanoscale mechanisms differ significantly from expectations. Particle dissolution was sudden and seemed a stochastic process, while particle growth, that is, monomer attachment, was slow and likely the rate-determining step for sintering in this system. We also observed the existence of a significant fraction of inert particles that neither grew nor

shrank. Furthermore, gold particle size has been shown to matter significantly less than predicted in classical Ostwald ripening models. Clearly, investigations of sintering processes at the individual nanoparticle level opposed to nanoparticle ensemble are instrumental for gaining new insights into the mechanisms involved and improving predictive power of sintering models.

## **4.4 Materials & Methods**

### **4.4.1 Catalyst Synthesis**

The gold–ethylene diamine complex salt  $\text{Au}(\text{H}_2\text{N}-\text{C}_2\text{H}_4-\text{NH}_2)_2\text{Cl}_3$  was prepared following a modified method of Block and Bailar.<sup>60</sup> In a typical synthesis, 0.25 g of  $\text{HAuCl}_4 \cdot 3\text{H}_2\text{O}$  ( $\geq 99.9\%$ , Sigma-Aldrich) was dissolved in 2.5 mL of demineralized water in a glass beaker, while stirring the liquid at 400 RPM. After 10 min. of stirring, 0.15 mL of pure ethylene diamine was added dropwise to the solution. The solution was then left to react for another 30 min. at room temperature while stirring, after which the gold complex was precipitated by adding 30 mL of ethanol (99.8%, Sigma-Aldrich). The suspension was subsequently left to settle overnight, after which the liquid was removed and the precursor was further dried under vacuum to remove the ethanol. The powder was finally redissolved in 50 mL of Milli-Q water, resulting in a  $11 \text{ mmol}\cdot\text{L}^{-1}$  solution of  $\text{Au}(\text{H}_2\text{N}-\text{C}_2\text{H}_4-\text{NH}_2)_2\text{Cl}_3$  in  $\text{H}_2\text{O}$ .

A 1 wt % gold supported on a titania catalyst with unimodal Au particle size distribution (3 nm number-average diameter) was prepared adapting the procedure of Zhu et al.<sup>44</sup> In a typical synthesis, 12 mL of the prepared  $11 \text{ mmol}\cdot\text{L}^{-1}$  solution of  $\text{Au}(\text{H}_2\text{N}-\text{C}_2\text{H}_4-\text{NH}_2)_2\text{Cl}_3$  in  $\text{H}_2\text{O}$  was added to 18 mL of Milli-Q water, followed by addition of 0.5 mL of a  $1.0 \text{ mol}\cdot\text{L}^{-1}$  solution of NaOH (99%, Sigma-Aldrich) in Milli-Q water. After 5 min. of vigorous stirring at 700 RPM, 3 g of commercial fumed  $\text{TiO}_2$  powder (P25, Evonik Degussa) was dispersed in the solution while stirring. The dispersion was then left for 2 h at room temperature for the ionic gold precursor to adsorb on the  $\text{TiO}_2$  surface. The solid was subsequently separated by centrifugation (10 min., 4000 RPM) and washed with 30 mL of demineralized water thrice.

The resulting powder was then dried overnight in an oven at  $60^\circ\text{C}$ , followed by 24 h of vacuum-drying at room temperature. The resulting powder was subsequently heated in a fluidized bed reactor for 2 h at  $300^\circ\text{C}$  in  $\text{N}_2$ , followed by 2 h at  $400^\circ\text{C}$  in  $20\%\text{O}_2/80\%\text{N}_2$ , using a flow of  $150 \text{ mL}\cdot\text{min}^{-1}$  and a heating and cooling rate of  $5^\circ\text{C}\cdot\text{min}^{-1}$  to reduce gold and remove the remaining ligands.

The bimodal sample was prepared by taking a part of the previously prepared unimodal sample followed by addition of a Au colloidal dispersion using the following



procedure: 0.1 g of the original unimodal sample was dispersed in 10 mL of demineralized H<sub>2</sub>O while stirring at 400 RPM. To this suspension, 3  $\mu$ L of a 1.0 mol·L<sup>-1</sup> HNO<sub>3</sub> in H<sub>2</sub>O solution was added, followed by addition of 2 mL of a commercial citrate-stabilized colloidal suspension of 20 nm gold nanoparticles (53 mg Au·L<sup>-1</sup>, 99% reactant free, Cytodiagnostics) for an additional colloid loading of maximum 0.1 wt % (resulting in a 1.1 wt % total gold loading on a titania catalyst).

After stirring for 2 h at 400 RPM, the solid was separated from the suspension by centrifugation (5 min, 4000 RPM), followed by washing thrice with 10 mL of demineralized water to remove the remaining ligands. The solid was subsequently dried overnight in an oven at 60 °C, followed by drying in vacuum for 24 h to obtain a powder.

In all of the synthesis steps, care was taken to limit the exposure of the gold (precursor) and catalyst to light as much as possible by covering the glassware with parafilm and aluminum foil to prevent light-induced reduction of gold ions. Care was also taken to prevent any contact of gold with metal by using poly(tetrafluoroethylene) (PTFE) and glass equipment.

#### **4.4.2 Characterization**

All samples were characterized by powder X-ray diffraction (XRD) using a Bruker D2 Phaser with a Co K $\alpha$  source for phase identification. Samples were evaluated for 2 $\theta$  between 25 and 90°. N<sub>2</sub> physisorption measurements were performed at -196 °C (77 K) using a Micromeritics TriStar 3000 instrument. Before the isotherm measurements, samples were dried at 250 °C in air. Specific surface areas were calculated using the multipoint Brunauer–Emmett–Teller (BET) method (0.05 < P/P<sub>0</sub> < 0.25).

Catalyst morphology, gold particle size, and particle dispersion were examined with TEM using a Talos F200X (Thermo Fischer Scientific), operated at 200 kV acceleration voltage in both TEM and high-angle annular dark-field (HAADF)-scanning transmission electron microscopy (STEM) modes. The samples were dispersed in isopropanol (Honeywell, Chromasolv™, 99.9%) and deposited on a 200 mesh copper-formvar grid. Gold particle sizes were subsequently determined by counting at least 250 particles manually using ImageJ.

Vacuum control experiments were performed by continuous STEM scanning for 1 h using a beam current of 0.21 nA, as determined by the electron current reaching the fluorescent screen without a holder present. For the control experiments in vacuum, imaging was performed using only the HAADF detector and at a magnification of 225,000 x, corresponding to a 500 × 500 nm<sup>2</sup> image size, resulting in an average dose

rate of  $5.2 \cdot 10^3 \text{ e}^- \cdot \text{nm}^{-2} \cdot \text{s}^{-1}$ . Images were collected with a pixel dwell time of 2.4  $\mu\text{s}$ , with 2048 x 2048 pixel images, and for a total of 10 s/frame.

Ex situ sintering experiments were performed using a glass beaker with either 20 mL of Milli-Q water or 2 mL of a  $0.1 \text{ mol} \cdot \text{L}^{-1}$  NaCl in  $\text{H}_2\text{O}$  solution added to 18 mL of Milli-Q water. The liquid was subsequently stirred and heated to 80 °C while in contact with air. When the liquid temperature reached 80 °C, as measured by a stainless steel thermocouple in a separate vial of water to prevent any contact between gold and stainless steel, 30–50 mg of the catalyst was added and the glass beaker was covered with parafilm to prevent evaporation. A drop of the suspension was deposited on a TEM grid at regular time intervals (30 min, 1 h, 1.5 h, 2 h, 3 h, 4 h, 6 h, 8 h, 24 h) to be analyzed in TEM. In the case of the sintering experiment under  $\text{N}_2$ , a round-bottom flask in an oil bath and connected to a  $\text{N}_2$  gas supply was used instead.  $\text{N}_2$  was then bubbled through the solution starting 10 min. before heating.

### 4.4.3 LP-TEM experiments

To prepare the liquid cell, a small and a large silicon chip with a nominally 50 nm thick silicon nitride ( $\text{Si}_x\text{N}_y$ ) window of  $20 \times 550 \mu\text{m}^2$  (Protochips Inc.) were cleaned in acetone and methanol according to manufacturer instructions. Subsequently, both the large and small chips were plasma-cleaned in an 80%Ar/20% $\text{O}_2$  plasma for 2 min. to render the chip surface hydrophilic.

A small amount of either the unimodal or bimodal Au on  $\text{TiO}_2$  catalyst was then dispersed in 2 mL of high-purity isopropanol (Honeywell, Chromasolv, 99.9%) and sonicated for at least 15 min. to disperse agglomerates. A 0.5  $\mu\text{L}$  droplet of this suspension was placed on the silicon nitride layer of the large silicon liquid cell chip and left to dry for 5 min. This resulted in a sufficient amount of catalyst particles being attached to the window of a chip and thus available for imaging.

A small silicon chip, also containing a  $20 \times 550 \mu\text{m}^2$   $\text{Si}_x\text{N}_y$  window and 150 nm gold spacers to separate the two chips, was then placed in the dedicated liquid cell TEM holder (Protochips Inc.), a 1  $\mu\text{L}$  drop of water (sterile-filtered, Bioreagent,  $\leq 1 \text{ Eu} \cdot \text{mL}^{-1}$ ,  $\leq 5$  ppm metal impurities, Sigma-Aldrich) was added on top of it, and the cell was subsequently assembled by placing the large silicon chip containing the sample on top. In this configuration, the sample was dispersed on the top chip when the holder was inserted in the microscope for optimal spatial resolution in STEM mode.<sup>23</sup>

Imaging was performed using Talos F200X (Thermo Fischer Scientific), operated in scanning transmission electron microscopy (STEM) mode at 200 kV acceleration voltage and using both a bright-field (BF) and a high-angle annular dark-field (HAADF) detector for imaging. The imaging was performed with a beam current of

0.21 nA, as determined by the screen current without a holder present in the electron microscope and with a camera length of 125 mm. Images were collected with a pixel dwell time of 2.4  $\mu\text{s}$ , with 2048 x 2048 pixel images, and for a total of 10 s/frame. Experiments were performed at a magnification of 225,000 x, corresponding to a field of view of  $500 \times 500 \text{ nm}^2$ , which results in an electron dose rate of  $5.2 \cdot 10^3 \text{ e}^- \cdot \text{nm}^{-2} \cdot \text{s}^{-1}$ .

Each liquid cell experiment was performed in flow mode using a flow of  $4 \mu\text{L} \cdot \text{min}^{-1}$  to prevent the buildup of gases and bubble formation due to electron-beam-induced water decomposition. Before an in situ experiment was started, either the  $\text{H}_2\text{O}$  or the  $10 \text{ mmol} \cdot \text{L}^{-1}$  NaCl solution was flushed through the holder for at least 30 min. to ensure the liquid around the sample had the desired composition. In each experiment, the sample was continuously imaged in scanning (S)TEM mode with a total of 360 images being acquired, corresponding to exactly 1 h of electron beam scanning. The  $10 \text{ mmol} \cdot \text{L}^{-1}$  NaCl solution was prepared diluting a  $100 \text{ mmol} \cdot \text{L}^{-1}$  solution by adding 2 g of the latter to 18 g of ultrapure water. The  $100 \text{ mmol} \cdot \text{L}^{-1}$  solution was in turn prepared by dissolving 95 mg of NaCl (>99%, AkzoNobel) in 15 g of ultrapure  $\text{H}_2\text{O}$  in a clean glass vial.

#### **4.4.4 Data processing and analysis**

Particle size was determined manually in all experiments using ImageJ software. For the ex situ experiments, the particle diameter was measured from HAADF-STEM images at 640,000 x magnification (image size of  $175 \times 175 \text{ nm}^2$ ). For the in situ measurements, images were first processed to enhance particle visibility using a Gaussian blur filter with a sigma of 1.5, followed by using the Despeckle function from ImageJ, which replaces each pixel with the median value of the  $3 \times 3$  grid of pixels around it. Then, the images were aligned using the “linear stack alignment with SIFT” plugin. Ellipses were subsequently fitted manually to the particle projections in the BF-STEM images taken at 225,000 x magnification ( $500 \times 500 \text{ nm}^2$  image size), from which the particle diameter was calculated. Particles were measured every 10th image, corresponding to every 100 s. When a particle was close to disappearing (typically from 1 min. before disappearance but earlier if significant changes could be observed before), the size of that particle was measured every image until disappearance, corresponding to a measurement every 10 s. Further calculations of particle area and volume were performed assuming spherical particles. Particle size distributions were calculated from the diameter using a bin size of 1 nm, and the accompanying lognormal fit was calculated using the lognfit function in Matlab. The average diameters reported are all number-average diameters, calculated by summing all measured diameters and dividing by the number of particles.

Particles were classified as growing, shrinking, or remaining the same size by analyzing their size over time. Any particle that disappeared during the 1 h experiment was classified as shrinking, as no particles were found that decreased significantly in size (defined as getting smaller than 66.7% of the initial diameter) without disappearing. Particles that increased in diameter more than 33% of their initial diameter were classified as growing, while the other particles were deemed not to change size to any significant extent.

Specific surface area (SSA) was calculated from the particle size distribution by calculating the surface area and volume of each individual particle from its diameter, assuming spherical particles. These values were subsequently summed over all measured particles to obtain the total particle surface area and the total particle volume. Assuming the nanoparticles to have the density of bulk gold ( $19.3 \text{ g}\cdot\text{cm}^{-3}$ ), the total mass of all particles was calculated from their total volume and then the total surface area was divided by this total mass to obtain the specific surface area in  $\text{m}^2\cdot\text{g}^{-1}$ .

Fitting of the decrease in SSA was performed using the experimentally determined third-order power law for the rate of decrease of specific surface area (equation 4.1), in which  $a$  is the specific surface area normalized with respect to the initial specific surface area (on a scale from 0 to 1),  $t$  is the time in min., and  $k$  is the rate constant.

$$\frac{da}{dt} = -ka^3 \quad (4.1)$$

Solving this differential equation results in the description of  $a$  as a function of  $t$ , as shown in equation 4.2:

$$a = \sqrt{\frac{1}{(C + \frac{1}{2}kt)}} \quad (4.2)$$

in which  $C$  is the constant of integration. Assuming  $a$  to be 1 for  $t = 0$  (in other words, assuming that the specific surface area is equal to the initial specific surface area when  $t = 0$ ), this results in  $C$  being equal to 1. The rate constant  $k$  was subsequently determined by fitting the measured data points using the least-squares method in Matlab.

## 4.5 Acknowledgements

The authors acknowledge J. D. Meeldijk for technical assistance with the electron microscope, L. Weber for the N<sub>2</sub> physisorption measurements, and S. M. C. de Jong for help with the synthesis. K. P. de Jong and M. J. Meijerink acknowledge funding from the European Research Council, EU FP7 ERC Advanced Grant no. 338846. J. Zečević acknowledges financial support by Netherlands Organization for Scientific Research (NWO), Veni Grant no. 722.015.010.

## 4.6 References

- (1). Feynman, R. P., There's Plenty of Room at the Bottom. *Engineering and Science* **1960**, 23 (5), 22-36.
- (2). Prieto, G.; Zečević, J.; Friedrich, H.; De Jong, K. P.; De Jongh, P. E., Towards Stable Catalysts by Controlling Collective Properties of Supported Metal Nanoparticles. *Nat. Mater.* **2013**, 12 (1), 34-39.
- (3). Farokhzad, O. C.; Langer, R., Impact of Nanotechnology on Drug Delivery. *ACS Nano* **2009**, 3 (1), 16-20.
- (4). Valden, M.; Lai, X.; Goodman, D. W., Onset of Catalytic Activity of Gold Clusters on Titania with the Appearance of Nonmetallic Properties. *Science* **1998**, 281 (5383), 1647-1650.
- (5). Dai, Y.; Lu, P.; Cao, Z.; Campbell, C. T.; Xia, Y., The Physical Chemistry and Materials Science Behind Sinter-Resistant Catalysts. *Chem. Soc. Rev.* **2018**, 47 (12), 4314-4331.
- (6). Lifshitz, I. M.; Slyozov, V. V., The Kinetics of Precipitation from Supersaturated Solid Solutions. *J. Phys. Chem. Solids* **1961**, 19 (1-2), 35-50.
- (7). Wagner, C., Theorie Der Alterung Von Niederschlägen Durch Umlösen (Ostwald-Reifung). *Zeitschrift für Elektrochemie, Berichte der Bunsengesellschaft für physikalische Chemie* **1961**, 65 (7-8), 581-591.
- (8). Kahlweit, M., Ostwald Ripening of Precipitates. *Adv. Colloid Interface Sci.* **1975**, 5 (1), 1-35.
- (9). Von Smoluchowski, M., Drei Vorträge Über Diffusion. Brownsche Bewegung Und Koagulation Von Kolloidteilchen. *Z. Phys.* **1916**, 17, 557-585.
- (10). Granqvist, C. G.; Buhrman, R. A., Size Distributions for Supported Metal Catalysts: Coalescence Growth Versus Ostwald Ripening. *J. Catal.* **1976**, 42 (3), 477-479.
- (11). Datye, A. K.; Xu, Q.; Kharas, K. C.; McCarty, J. M., Particle Size Distributions in Heterogeneous Catalysts: What Do They Tell Us About the Sintering Mechanism? *Catal. Today* **2006**, 111 (1-2), 59-67.
- (12). Challa, S. R.; Delariva, A. T.; Hansen, T. W.; Helveg, S.; Sehested, J.; Hansen, P. L.; Garzon, F.; Datye, A. K., Relating Rates of Catalyst Sintering to the Disappearance of Individual Nanoparticles During Ostwald Ripening. *J. Am. Chem. Soc.* **2011**, 133 (51), 20672-20675.

- (13). Liu, R.-J.; Crozier, P. A.; Smith, C. M.; Hucul, D. A.; Blackson, J.; Salaita, G., Metal Sintering Mechanisms and Regeneration of Palladium/Alumina Hydrogenation Catalysts. *Appl. Catal., A* **2005**, *282* (1-2), 111-121.
- (14). Simonsen, S. B.; Chorkendorff, I.; Dahl, S.; Skoglundh, M.; Sehested, J.; Helveg, S., Direct Observations of Oxygen-Induced Platinum Nanoparticle Ripening Studied by in Situ Tem. *J. Am. Chem. Soc.* **2010**, *132* (23), 7968-7975.
- (15). Van den Berg, R.; Elkjaer, C. F.; Gommers, C. J.; Chorkendorff, I.; Sehested, J.; De Jongh, P. E.; De Jong, K. P.; Helveg, S., Revealing the Formation of Copper Nanoparticles from a Homogeneous Solid Precursor by Electron Microscopy. *J. Am. Chem. Soc.* **2016**, *138* (10), 3433-3442.
- (16). Hansen, T. W.; Wagner, J. B.; Hansen, P. L.; Dahl, S.; Topsøe, H.; Jacobsen, C. J. H., Atomic-Resolution in Situ Transmission Electron Microscopy of a Promoter of a Heterogeneous Catalyst. *Science* **2001**, *294* (5546), 1508-1510.
- (17). Kawasaki, T.; Ueda, K.; Ichihashi, M.; Tanji, T., Improvement of Windowed Type Environmental-Cell Transmission Electron Microscope for in Situ Observation of Gas-Solid Interactions. *Rev. Sci. Instrum.* **2009**, *80* (11), 113701.
- (18). Borup, R.; Meyers, J.; Pivovar, B.; Kim, Y. S.; Mukundan, R.; Garland, N.; Myers, D.; Wilson, M.; Garzon, F.; Wood, D.; Zelenay, P.; More, K.; Stroh, K.; Zawodzinski, T.; Boncella, J.; McGrath, J. E.; Inaba, M.; Miyatake, K.; Hori, M.; Ota, K.; Ogumi, Z.; Miyata, S.; Nishikata, A.; Siroma, Z.; Uchimoto, Y.; Yasuda, K.; Kimijima, K.-i.; Iwashita, N., Scientific Aspects of Polymer Electrolyte Fuel Cell Durability and Degradation. *Chem. Rev.* **2007**, *107* (10), 3904-3951.
- (19). Hodnik, N.; Zorko, M.; Jozinović, B.; Bele, M.; Dražič, G.; Hočevar, S.; Gaberšček, M., Severe Accelerated Degradation of PEMFC Platinum Catalyst: A Thin Film IL-SEM Study. *Electrochem. Commun.* **2013**, *30*, 75-78.
- (20). Chheda, J. N.; Huber, G. W.; Dumesic, J. A., Liquid-Phase Catalytic Processing of Biomass-Derived Oxygenated Hydrocarbons to Fuels and Chemicals. *Angew. Chem. Int. Ed.* **2007**, *46* (38), 7164-7183.
- (21). Jin, X.; Dang, L.; Lohrman, J.; Subramaniam, B.; Ren, S.; Chaudhari, R. V., Lattice-Matched Bimetallic CuPd-Graphene Nanocatalysts for Facile Conversion of Biomass-Derived Polyols to Chemicals. *ACS Nano* **2013**, *7* (2), 1309-1316.
- (22). Zhang, Z.; Deng, K., Recent Advances in the Catalytic Synthesis of 2, 5-Furandicarboxylic Acid and Its Derivatives. *ACS Catal.* **2015**, *5* (11), 6529-6544.
- (23). De Jonge, N.; Ross, F. M., Electron Microscopy of Specimens in Liquid. *Nat. Nanotechnol.* **2011**, *6* (11), 695-704.
- (24). Yuk, J. M.; Park, J.; Ercius, P.; Kim, K.; Hellebusch, D. J.; Crommie, M. F.; Lee, J. Y.; Zettl, A.; Alivisatos, A. P., High-Resolution EM of Colloidal Nanocrystal Growth Using Graphene Liquid Cells. *Science* **2012**, *336* (6077), 61-64.
- (25). Sacci, R. L.; Dudney, N. J.; More, K. L.; Parent, L. R.; Arslan, I.; Browning, N. D.; Unocic, R. R., Direct Visualization of Initial SEI Morphology and Growth Kinetics During Lithium Deposition by in Situ Electrochemical Transmission Electron Microscopy. *Chem. Commun.* **2014**, *50* (17), 2104-2107.

- (26). Smeets, P. J. M.; Cho, K. R.; Kempen, R. G. E.; Sommerdijk, N. A. J. M.; De Yoreo, J. J., Calcium Carbonate Nucleation Driven by Ion Binding in a Biomimetic Matrix Revealed by in Situ Electron Microscopy. *Nat. Mater.* **2015**, *14* (4), 394-399.
- (27). De Jonge, N.; Peckys, D. B.; Kremers, G. J.; Piston, D. W., Electron Microscopy of Whole Cells in Liquid with Nanometer Resolution. *Proc. Natl. Acad. Sci. U. S. A.* **2009**, *106* (7), 2159-2164.
- (28). Zheng, H.; Smith, R. K.; Jun, Y.-w.; Kisielowski, C.; Dahmen, U.; Alivisatos, A. P., Observation of Single Colloidal Platinum Nanocrystal Growth Trajectories. *Science* **2009**, *324* (5932), 1309-1312.
- (29). Alloyeau, D.; Dachraoui, W.; Javed, Y.; Belkahla, H.; Wang, G.; Lecoq, H.; Ammar, S.; Ersen, O.; Wisnet, A.; Gazeau, F.; Ricolleau, C., Unravelling Kinetic and Thermodynamic Effects on the Growth of Gold Nanoplates by Liquid Transmission Electron Microscopy. *Nano Lett.* **2015**, *15* (4), 2574-2581.
- (30). Radisic, A.; Vereecken, P. M.; Hannon, J. B.; Searson, P. C.; Ross, F. M., Quantifying Electrochemical Nucleation and Growth of Nanoscale Clusters Using Real-Time Kinetic Data. *Nano Lett.* **2006**, *6* (2), 238-242.
- (31). Lu, Y.; Geng, J.; Wang, K.; Zhang, W.; Ding, W.; Zhang, Z.; Xie, S.; Dai, H.; Chen, F.-R.; Sui, M., Modifying Surface Chemistry of Metal Oxides for Boosting Dissolution Kinetics in Water by Liquid Cell Electron Microscopy. *ACS Nano* **2017**, *11* (8), 8018-8025.
- (32). Meijerink, M. J.; De Jong, K. P.; Zečević, J., Assessment of Oxide Nanoparticle Stability in Liquid Phase Transmission Electron Microscopy. *Nano Res.* **2019**, *12* (9), 2355-2363.
- (33). Zečević, J.; Hermansdörfer, J.; Schuh, T.; De Jong, K. P.; De Jonge, N., Anisotropic Shape Changes of Silica Nanoparticles Induced in Liquid with Scanning Transmission Electron Microscopy. *Small* **2017**, *13* (1), 1602466.
- (34). Meijerink, M. J.; Spiga, C.; Hansen, T. W.; Damsgaard, C. D.; De Jong, K. P.; Zečević, J., Nanoscale Imaging and Stabilization of Silica Nanospheres in Liquid Phase Transmission Electron Microscopy. *Part. Part. Syst. Charact.* **2019**, *36* (1), 1800374.
- (35). Hermansdörfer, J.; de Jonge, N.; Verch, A., Electron Beam Induced Chemistry of Gold Nanoparticles in Saline Solution. *Chem. Commun.* **2015**, *51* (91), 16393-16396.
- (36). Woehl, T. J.; Park, C.; Evans, J. E.; Arslan, I.; Ristenpart, W. D.; Browning, N. D., Direct Observation of Aggregative Nanoparticle Growth: Kinetic Modeling of the Size Distribution and Growth Rate. *Nano Lett.* **2013**, *14* (1), 373-378.
- (37). Ciriminna, R.; Falletta, E.; Della Pina, C.; Teles, J. H.; Pagliaro, M., Industrial Applications of Gold Catalysis. *Angew. Chem. Int. Ed.* **2016**, *55* (46), 14210-14217.
- (38). Haruta, M., Chance and Necessity: My Encounter with Gold Catalysts. *Angew. Chem. Int. Ed.* **2014**, *53* (1), 52-56.
- (39). Davis, S. E.; Houk, L. R.; Tamargo, E. C.; Datye, A. K.; Davis, R. J., Oxidation of 5-Hydroxymethylfurfural over Supported Pt, Pd and Au Catalysts. *Catal. Today* **2011**, *160* (1), 55-60.
- (40). Donoeva, B.; Masoud, N.; De Jongh, P. E., Carbon Support Surface Effects in the Gold-Catalyzed Oxidation of 5-Hydroxymethylfurfural. *ACS Catal.* **2017**, *7* (7), 4581-4591.

- (41). Villa, A.; Dimitratos, N.; Chan-Thaw, C. E.; Hammond, C.; Veith, G. M.; Wang, D.; Manzoli, M.; Prati, L.; Hutchings, G. J., Characterisation of Gold Catalysts. *Chem. Soc. Rev.* **2016**, *45* (18), 4953-4994.
- (42). Campbell, C. T.; Parker, S. C.; Starr, D. E., The Effect of Size-Dependent Nanoparticle Energetics on Catalyst Sintering. *Science* **2002**, *298* (5594), 811-814.
- (43). Parker, S. C.; Campbell, C. T., Reactivity and Sintering Kinetics of Au/TiO<sub>2</sub> (110) Model Catalysts: Particle Size Effects. *Top. Catal.* **2007**, *44* (1-2), 3-13.
- (44). Zhu, H.; Ma, Z.; Clark, J. C.; Pan, Z.; Overbury, S. H.; Dai, S., Low-Temperature CO Oxidation on Au/Fumed SiO<sub>2</sub>-Based Catalysts Prepared from Au(en)<sub>2</sub>Cl<sub>3</sub> Precursor. *Appl. Catal., A* **2007**, *326* (1), 89-99.
- (45). Schneider, N. M.; Norton, M. M.; Mendel, B. J.; Grogan, J. M.; Ross, F. M.; Bau, H. H., Electron-Water Interactions and Implications for Liquid Cell Electron Microscopy. *J. Phys. Chem. C* **2014**, *118* (38), 22373-22382.
- (46). Bond, G. C.; Louis, C.; Thompson, D. T., *Catalysis by Gold*. Imperial College Press: London, 2006; Vol. 6.
- (47). Carabineiro, S. A. C.; Silva, A. M. T.; Dražić, G.; Tavares, P. B.; Figueiredo, J. L., Effect of Chloride on the Sinterization of Au/CeO<sub>2</sub> Catalysts. *Catal. Today* **2010**, *154* (3-4), 293-302.
- (48). Meijerink, M. J.; de Jong, K. P.; Zečević, J., Growth of Supported Gold Nanoparticles in Aqueous Phase Studied by in Situ Transmission Electron Microscopy. *J. Phys. Chem. C* **2020**, *124* (3), 2202-2212.
- (49). De Jonge, N., Theory of the Spatial Resolution of (Scanning) Transmission Electron Microscopy in Liquid Water or Ice Layers. *Ultramicroscopy* **2018**, *187*, 113-125.
- (50). Wynblatt, P.; Gjostein, N. A., Supported Metal Crystallites. *Prog. Solid State Chem.* **1975**, *9*, 21-58.
- (51). Haynes, W. M., *CRC Handbook of Chemistry and Physics*. CRC press: New York, 2014; Vol. 95.
- (52). Henglein, A., Small-Particle Research: Physicochemical Properties of Extremely Small Colloidal Metal and Semiconductor Particles. *Chem. Rev.* **1989**, *89* (8), 1861-1873.
- (53). Ivanova, O. S.; Zamborini, F. P., Electrochemical Size Discrimination of Gold Nanoparticles Attached to Glass/Indium-Tin-Oxide Electrodes by Oxidation in Bromide-Containing Electrolyte. *Anal. Chem.* **2010**, *82* (13), 5844-5850.
- (54). Henglein, A.; Linnert, T.; Mulvaney, P., Reduction of Ag<sup>+</sup> in Aqueous Polyanion Solution: Some Properties and Reactions of Long-Lived Oligomeric Silver Clusters and Metallic Silver Particles. *Berichte der Bunsengesellschaft für physikalische Chemie* **1990**, *94* (12), 1449-1457.
- (55). Mulvaney, P.; Linnert, T.; Henglein, A., Surface Chemistry of Colloidal Silver in Aqueous Solution: Observations on Chemisorption and Reactivity. *J. Phys. Chem.* **1991**, *95* (20), 7843-7846.
- (56). Woehl, T. J.; Evans, J. E.; Arslan, I.; Ristenpart, W. D.; Browning, N. D., Direct in Situ Determination of the Mechanisms Controlling Nanoparticle Nucleation and Growth. *ACS Nano* **2012**, *6* (10), 8599-8610.
- (57). Munnik, P.; Velthoen, M. E. Z.; De Jongh, P. E.; De Jong, K. P.; Gommers, C. J., Nanoparticle Growth in Supported Nickel Catalysts During Methanation Reaction—Larger Is Better. *Angew. Chem. Int. Ed.* **2014**, *53* (36), 9493-9497.



- (58). Ben-Jacob, E.; Garik, P., The Formation of Patterns in Non-Equilibrium Growth. *Nature* **1990**, *343* (6258), 523-530.
- (59). Van den Berg, R.; Parmentier, T. E.; Elkjær, C. F.; Gommès, C. J.; Sehested, J.; Helveg, S.; De Jongh, P. E.; De Jong, K. P., Support Functionalization to Retard Ostwald Ripening in Copper Methanol Synthesis Catalysts. *ACS Catal.* **2015**, *5* (7), 4439-4448.
- (60). Block, B. P.; Bailer Jr, J. C., The Reaction of Gold (III) with Some Bidentate Coördinating Groups. *J. Am. Chem. Soc.* **1951**, *73* (10), 4722-4725.

## Supporting Information

### Supporting Movies description

1) Movie M1 (M1\_unimodal\_Au\_TiO<sub>2</sub>\_H<sub>2</sub>O): The unimodal sample being scanned for 1 hour in H<sub>2</sub>O, with only a limited number of particles disappearing and most other particles hardly growing. During the movie, some very dark spots appear, seem to grow to quite large proportions (typically >25 nm) and then disappear quickly. These are likely partially the result of some form of TiO<sub>2</sub> charging from the electron beam and partially from overlapping TiO<sub>2</sub> crystals, but not Au particles since they also appear in the pristine TiO<sub>2</sub> in H<sub>2</sub>O and are very rare if NaCl is present in solution. Furthermore, the gold particles are somewhat mobile, moving small distances, more so than in NaCl (see Movie M2). This also suggests that charging of the support might take place when the conductivity of the liquid is insufficient to dissipate the charging, weakening the Au-TiO<sub>2</sub> interactions.

2) Movie M2 (M2\_unimodal\_Au\_TiO<sub>2</sub>\_NaCl): The unimodal sample being scanned for 1 hour in 10 mmol·L<sup>-1</sup> NaCl in H<sub>2</sub>O. As can be seen, more particles disappear (and most do so rapidly) than in movie M1, while many others grow significantly. The only large dark spots observed are the result of overlapping crystals and Au particles are far less mobile. This movie also illustrates the limited influence of Au size on their sintering, with one of the larger particles disappearing during the experiment.

3) Movie M3 (M3\_bimodal\_Au\_TiO<sub>2</sub>\_H<sub>2</sub>O): The bimodal sample being scanned for 1 hour in H<sub>2</sub>O. Again, large dark spots appearing, growing and disappearing quickly and higher Au particle mobility can be observed, likely for the same reason as discussed above (see description of movie M1). But again, only few Au particles disappear and the other particles show very limited growth.

4) Movie M4 (M4\_bimodal\_Au\_TiO<sub>2</sub>\_NaCl): The bimodal sample being scanned for 1 hour in 10 mmol·L<sup>-1</sup> NaCl in H<sub>2</sub>O. As with the unimodal sample in movie M2, a significant portion of the particles disappears, but this time growth of the other particles is far more limited. Furthermore, one of the ~20 nm Au particles in the field of view disappears as well. There seem to be a few small dark spots that appear and disappear quickly in this movie as well (upper left and lower right), which seem to behave the same as the dark spots in the H<sub>2</sub>O samples and are unlikely to be particles.

Movies are available online at <https://doi.org/10.1021/acs.jpcc.9b10237>

**Table S4.1.** Calculations of equilibrium concentrations of the  $[\text{AuCl}_4]^-$  complex in water for various concentrations/pressures at 25 °C.

	pH	Concentration $\text{Cl}^-$ ( $\text{mol}\cdot\text{L}^{-1}$ )	$\text{O}_2$ partial pressure (bar)	Resulting equilibrium concentration $[\text{AuCl}_4]^-$ ( $\text{mol}\cdot\text{L}^{-1}$ )
Bulk Au	7	0.01	0.2	9.9E-19
Nanoparticles*	7	0.01	0.2	1.4E-08
Bulk Au	4	0.01	0.2	9.9E-10
Nanoparticles	4	0.01	0.2	1.4E+01**
Bulk Au	7	0.01	0.001	1.9E-20
Nanoparticles	7	0.01	0.001	2.6E-10
Bulk Au	7	0.001	0.2	9.9E-23
	7	0.01	0.2	9.9E-19
	7	0.1	0.2	9.9E-15
Nanoparticles	7	0.001	0.2	1.4E-12
	7	0.01	0.2	1.4E-08
	7	0.1	0.2	1.4E-04

\*Considered to have a reduction potential shift of -200 mV

\*\*Not considering solubility limits of the complex

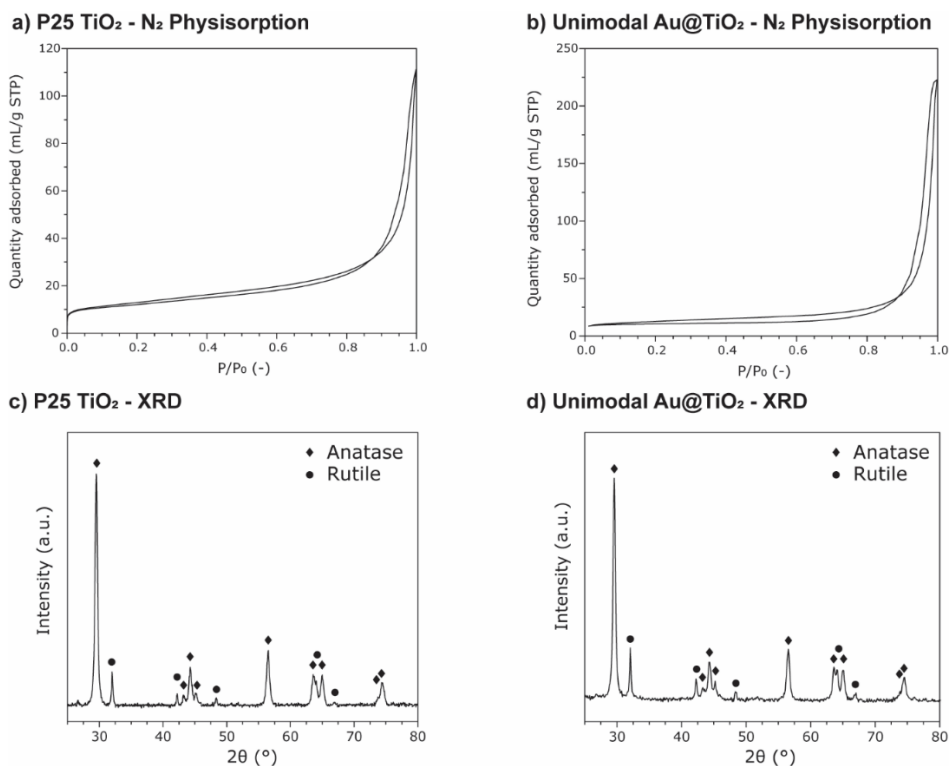


**Figure S4.1.** Nitrogen physisorption isotherms and X-ray diffraction patterns of P25 TiO<sub>2</sub> (a and c respectively) and the Au/TiO<sub>2</sub> catalyst with a unimodal particle size distribution (b and d respectively). For the nitrogen physisorption, a significantly finer powder was used for the Au/TiO<sub>2</sub> sample, resulting in the higher adsorption at high P/P<sub>0</sub>. The BET surface area was very similar for the two samples (45 m<sup>2</sup>·g<sup>-1</sup>).

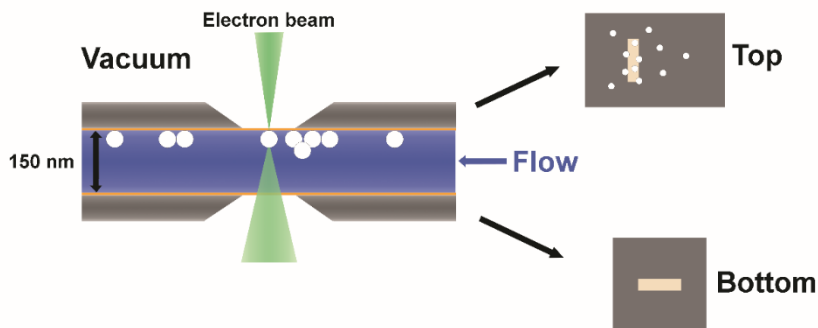


**Figure S4.2.** Schematic overview of a liquid cell for liquid phase transmission electron microscopy.

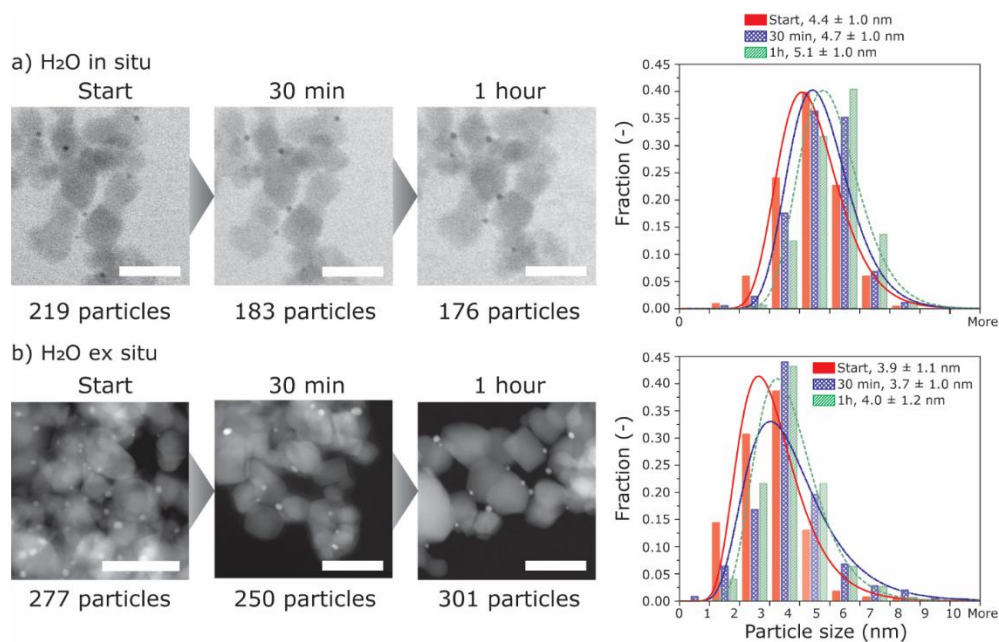


**Figure S4.3.** In situ and ex situ (a and b respectively) comparison of the evolution of the particle size distributions for the Au/TiO<sub>2</sub> sample with unimodal particle size distribution in water. A representative scanning transmission electron microscopy image in Bright Field (BF) (a) or High Angle Annular Dark Field (HAADF) (b) mode is shown for three different times, corresponding to the particle size distributions displayed in the graph to the right of the images. For the in situ experiments, each image is taken at the same position. The scale bar in each image corresponds to 50 nm.

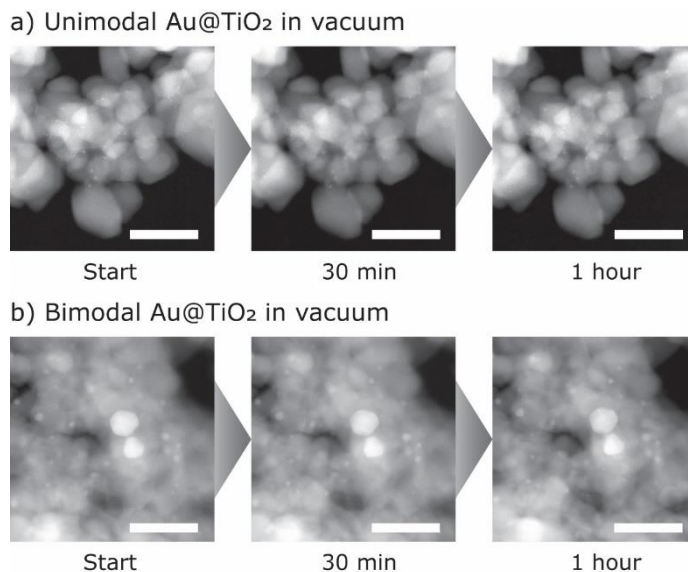


**Figure S4.4.** HAADF images before, halfway and after the control experiment of 60 minutes of continuous electron beam scanning in vacuum for the unimodal PSD Au/TiO<sub>2</sub> catalyst (a) and the bimodal PSD Au/TiO<sub>2</sub> catalyst (b). The scale bar in each image corresponds to 50 nm. The samples remained unchanged throughout the scanning.

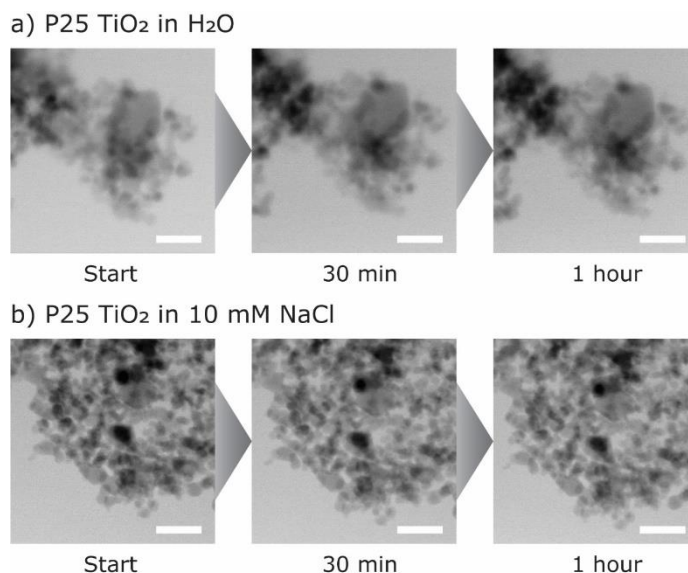
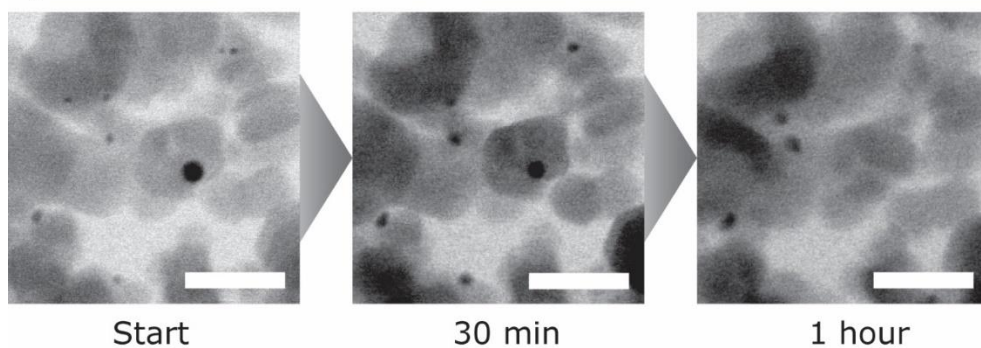


**Figure S4.5.** STEM images before, halfway and after the control experiment of 60 minutes of continuous electron beam scanning of the P25 TiO<sub>2</sub> support in H<sub>2</sub>O (a) and 10 mmol·L<sup>-1</sup> NaCl dissolved in H<sub>2</sub>O (b). The scale bar in each image corresponds to 100 nm. Apart from some minor rotation of the TiO<sub>2</sub> particles, the support structure remained unchanged.

a) 10 mM NaCl in situ



b) 100 mM NaCl in situ

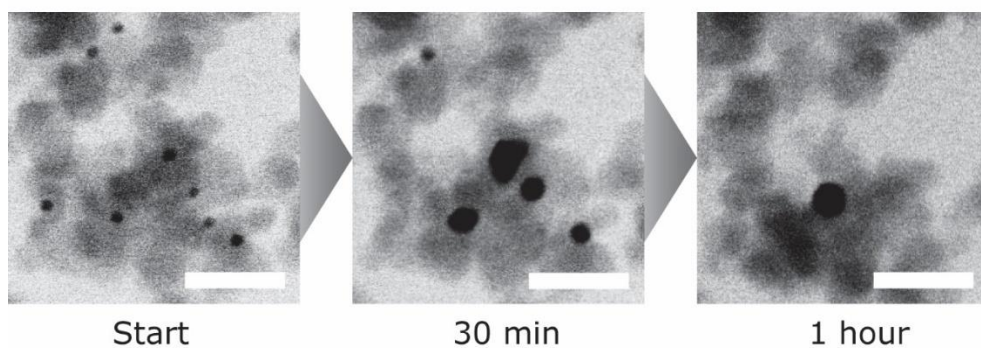


**Figure S4.6.** STEM images before, halfway and after sintering of the unimodal PSD Au/TiO<sub>2</sub> catalyst for 60 minutes in 10 mmol·L<sup>-1</sup> NaCl dissolved in H<sub>2</sub>O (a) and 100 mmol·L<sup>-1</sup> NaCl dissolved in H<sub>2</sub>O (b). The scale bar in each image corresponds to 50 nm.

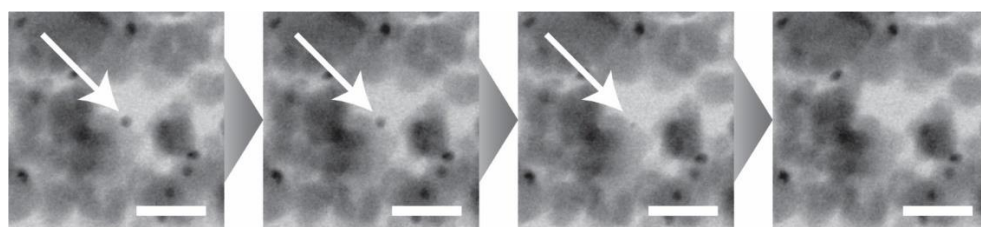


**Figure S4.7.** Consecutive STEM images of an individual particle disappearing during an in situ experiment with the unimodal PSD Au/TiO<sub>2</sub> sample in a 10 mmol·L<sup>-1</sup> NaCl in H<sub>2</sub>O solution. The scale bar in each image corresponds to 50 nm.

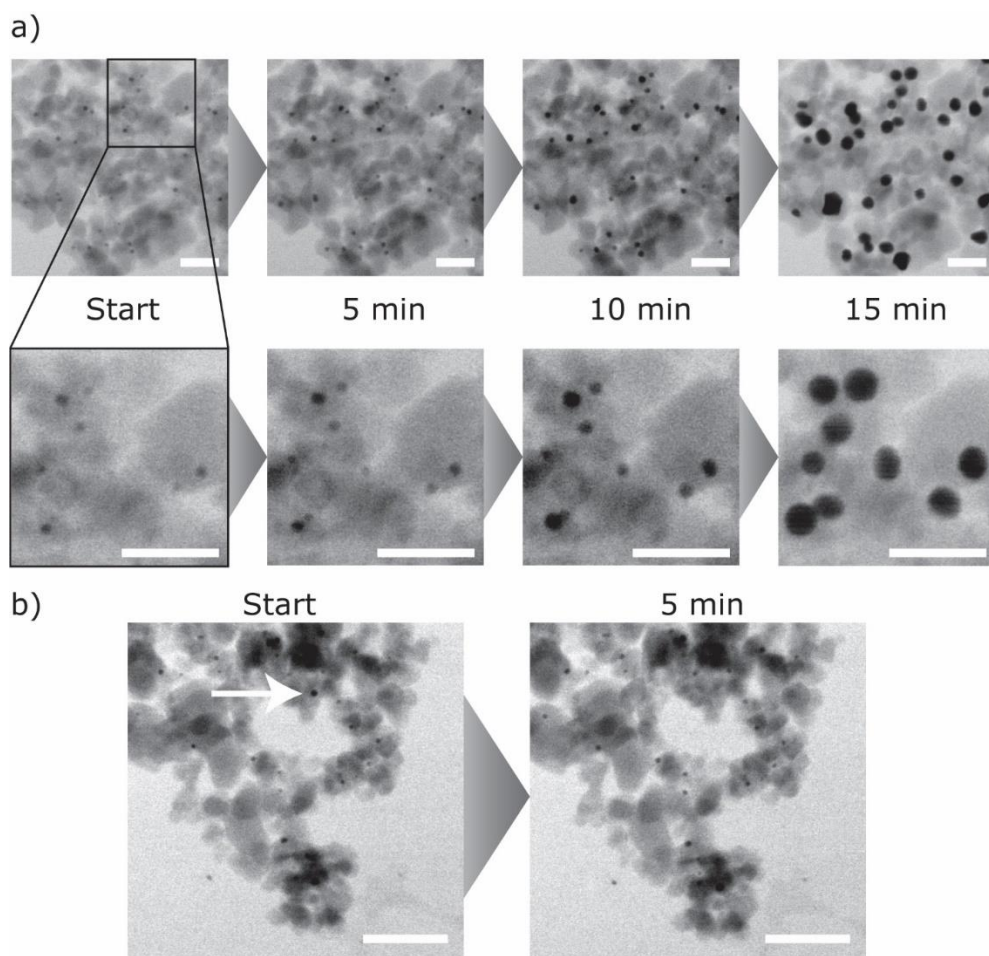


**Figure S4.8.** STEM images of 2 different areas during the heating LP-TEM experiment acquired after every 5 minutes of heating of the unimodal PSD Au/TiO<sub>2</sub> sample in a 10 mmol·L<sup>-1</sup> NaCl in H<sub>2</sub>O solution. (a) The first area followed during the heating LP-TEM experiment. Magnified: an example of smaller particles growing more than the particle that was initially the largest in that area. The scale bar in each image corresponds to 50 nm. (b) The second area followed during the heating LP-TEM experiment, with the arrow showing the initially largest particle disappearing after the first 5 minutes. The scale bar corresponds to 100 nm in both images.



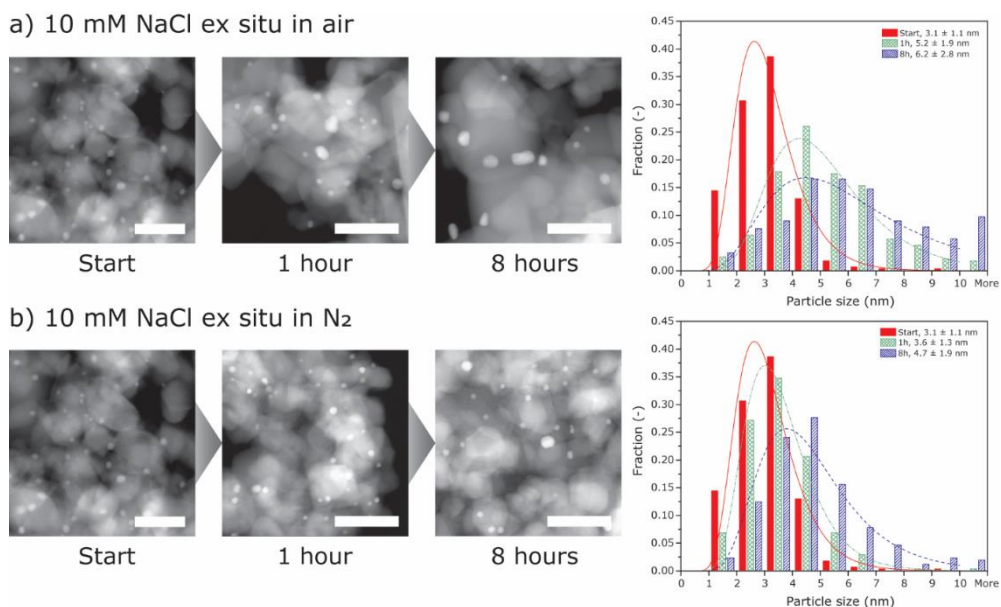


**Figure S4.9.** Ex situ experiments comparing the evolution of the particle size distributions for the Au/TiO<sub>2</sub> sample with a unimodal PSD over time in 10 mmol·L<sup>-1</sup> NaCl dissolved in H<sub>2</sub>O in contact with air (a) or pure N<sub>2</sub> (b) over a period of 8 hours. A representative scanning transmission electron microscopy image is shown for three different times, corresponding to the particle size distributions displayed in the graph to the right of the images. The scale bar in each image corresponds to 50 nm.

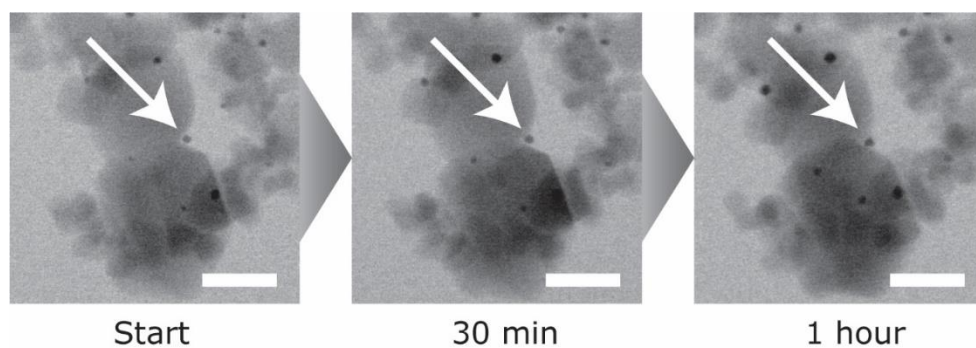


**Figure S4.10.** STEM images before, halfway and after of an individual particle in the center not changing in size during an in situ experiment with the unimodal PSD Au/TiO<sub>2</sub> sample in a 10 mmol·L<sup>-1</sup> NaCl in H<sub>2</sub>O solution. The scale bar in each image corresponds to 50 nm.

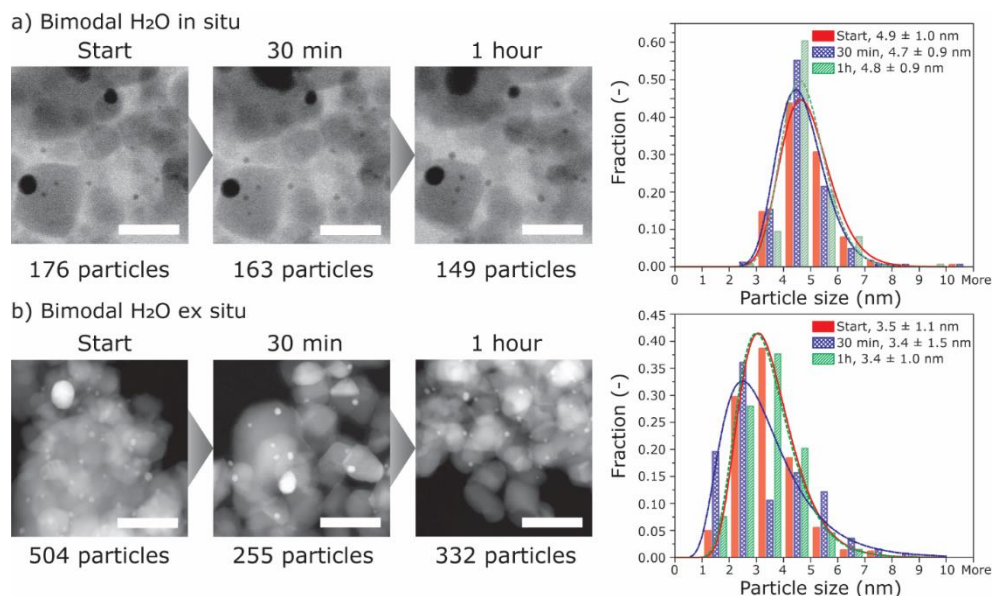


**Figure S4.11.** In situ and ex situ (a and b respectively) comparison of the evolution of the particle size distributions for the Au/TiO<sub>2</sub> sample with bimodal particle size distribution in water. A representative scanning transmission electron microscopy image in Bright Field (BF) (a) or High Angle Annular Dark Field (HAADF) (b) mode is shown for three different times, corresponding to the particle size distributions displayed in the graph to the right of the images. For the in situ experiments, each image is taken at the same position. The scale bar in each image corresponds to 50 nm.

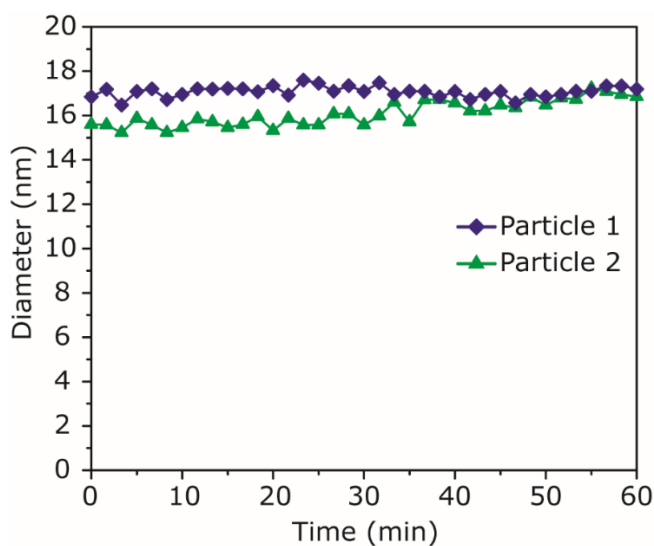


**Figure S4.12.** Diameter evolution over time of two large gold particles during in situ study of bimodal Au/TiO<sub>2</sub> in a solution of 10 mmol·L<sup>-1</sup> NaCl in H<sub>2</sub>O.

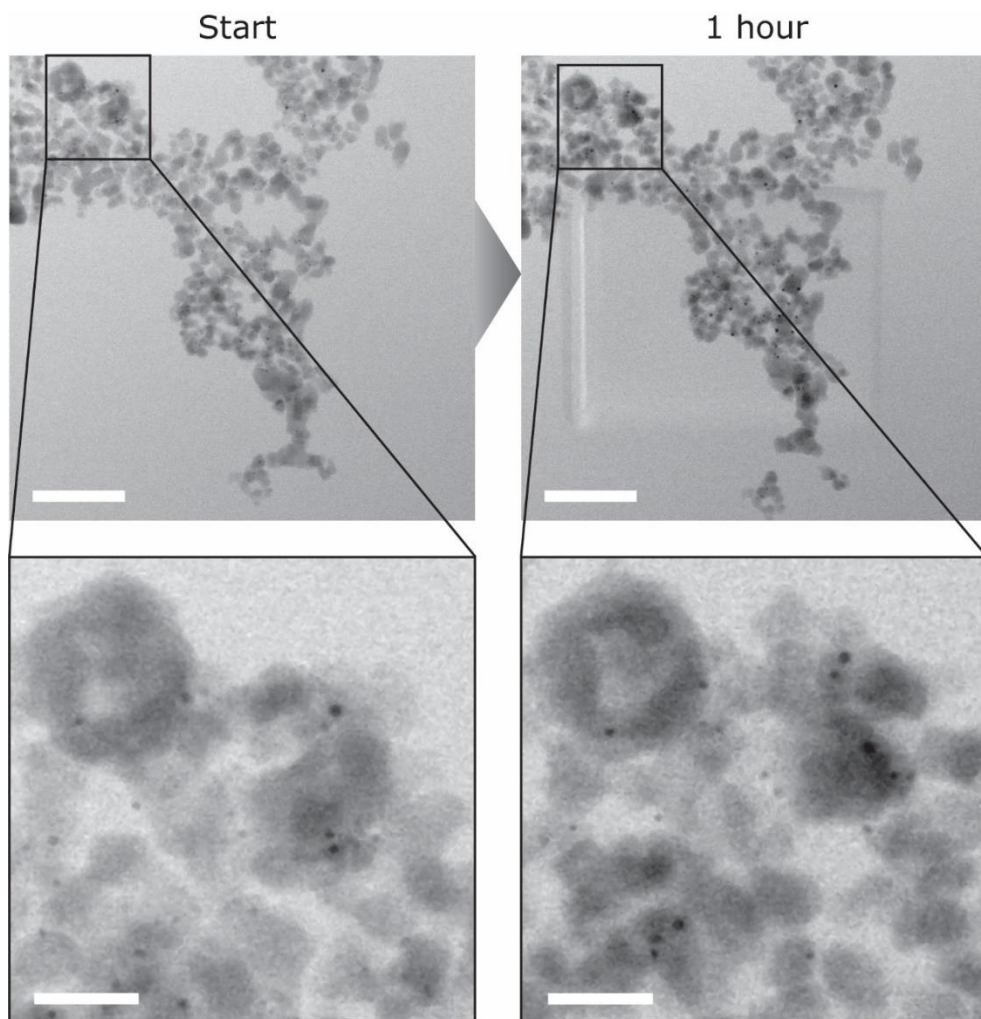


**Figure S4.13.** Overview STEM images before and after sintering of the unimodal PSD Au/TiO<sub>2</sub> catalyst for 60 minutes in 10 mmol·L<sup>-1</sup> NaCl dissolved in H<sub>2</sub>O, with the inset an area just outside of the irradiated area (the square in the middle of the image after one hour), showing the disappearance and change of a few of the gold particles. The irradiated area is the area inside the square visible in the center of the image after one hour. The scale bars in the top two images correspond to 200 nm and the scale bars in the bottom two images correspond to 50 nm.



## Chapter 5

# Advanced transmission electron microscopy study of structural changes in gold catalysts relevant for the oxidation of HMF

### Abstract

The production of 2,5-furandicarboxylic acid (FDCA) through liquid-phase oxidation of 5-hydroxymethylfurfural (HMF) is an important step in the production of bio-based polymers. Supported gold nanoparticles are highly promising catalysts for this reaction due to their high activity and selectivity but often suffer from rapid deactivation, likely originating from extensive structural changes of the catalyst. In this work, we combine in situ liquid phase transmission electron microscopy (LP-TEM) and TEM analysis of laboratory scale experiments to assess key parameters responsible for the structural changes of an Au/TiO<sub>2</sub> catalyst. We found that extensive gold particle (original size ~3 nm) detachment and subsequent particle coalescence and growth to 5.5 nm was present under conditions relevant to the aqueous-phase reaction, predominantly as a result of the high pH required. We propose that the origin of this detachment is the negative charge of both the gold nanoparticles and the TiO<sub>2</sub> support when the pH is higher than the point of zero charge (PZC) of TiO<sub>2</sub>. We also show that using a support (MgO) with a PZC close to the pH of the reaction mixture limits gold nanoparticle detachment. Identification and understanding of these nanoscale changes are critical to enhance knowledge of catalyst evolution and to increase catalyst stability.

## 5.1 Introduction

Solid heterogeneous catalysts play a key role in modern chemical industry and are crucial for high energy and atom efficiency in many chemical processes.<sup>1-2</sup> Despite the fact that a catalyst is by definition not consumed during the reaction, it does change slowly over time. In many cases, this change is detrimental to the performance of the catalyst and ultimately requires expensive catalyst replacement. This decrease in performance is usually referred to as deactivation and is a major consideration in industrial applications of catalysts.<sup>3</sup>

A challenge in preventing catalyst deactivation is that the underlying mechanisms are not always well-understood at a fundamental level. This is partially due to the fact that many heterogeneous catalysts consist of nanoparticles (often  $\leq 10$  nm)<sup>4</sup> anchored to a high surface area material, the support, to limit deactivation. Such small particles maximize available surface area per gram of material, which is advantageous because the chemical reactions only take place at the interface between the solid and fluid phase. As a result though, changes to the catalyst that result in deactivation are often also occurring at the nanoscale. It can therefore be very difficult to study these changes, as only a few techniques are able to image such small structural features.

An important technique that is often employed to study structural changes at the nanometer scale, is transmission electron microscopy (TEM). Although this is an indispensable tool for the investigation of catalysts, a high vacuum is required for this technique, resulting in limitations for the samples and environments that can be investigated.<sup>5</sup> For regular TEM, samples therefore need to be dry and no gas can be present and as a result, catalysts can only be investigated as-synthesized and post-mortem. Studying structural changes of catalytic materials and the mechanisms behind those changes is therefore quite difficult, as the catalyst cannot be observed during the reaction.

Developments in environmental TEM (ETEM)<sup>6-9</sup> and heating<sup>10</sup> holders provided a great leap forward in in situ TEM studies of catalysts in contact with a low pressure gas (typically  $< 5$  mbar). However, performing liquid phase TEM (LP-TEM) has only been possible since recently as a result of improved microfabrication techniques that allowed for cell-type holders.<sup>11-12</sup> Nevertheless, this powerful tool has already been used to study a wide variety of materials and processes in a liquid at the nanoscale, such as biomineralization,<sup>13</sup> electrochemical deposition and growth,<sup>14-15</sup> protein movement over a cell membrane,<sup>16</sup> metal nucleation and growth,<sup>17-19</sup> nanoparticle aggregation<sup>20</sup> and oxide stability.<sup>21-24</sup> In addition, recent work has investigated sintering behavior of

a supported gold catalyst,<sup>25</sup> showing that this technique holds great promise for the study of catalyst deactivation.

A catalytic system of particular interest is the liquid-phase oxidation of 5-hydroxymethylfurfural (HMF) to 2,5-furandicarboxylic acid (FDCA) in an aqueous environment using molecular oxygen. The heterogeneous catalyst is usually a supported noble metal catalyst such as Au, Pt, Pd and Ru or one of their bimetallics.<sup>26-34</sup> FDCA can be used as a building block in the synthesis of several polyesters, polyamides and polyurethanes<sup>35</sup> and HMF is a dehydration product readily produced from C6 sugars and other biomass,<sup>36-37</sup> which means this reaction is a key step in the production of bio-based polymers. The mechanisms involved and the influence of the reaction conditions have been studied extensively and indicate that although the incorporated oxygen originates from the H<sub>2</sub>O and the O<sub>2</sub> is only required for closing the redox cycle, the presence of hydroxide ions is important.<sup>38</sup> As a result, an alkaline environment is important for high catalyst activity,<sup>39</sup> along with the increased solubility of the conjugate base of FDCA,<sup>40-41</sup> which prevents catalyst deactivation through fouling by the reaction product.

Gold catalysts are particularly interesting for this reaction due to their very high activity and selectivity and resistance to poisoning. The latter is likely the result of the difficulty of oxide formation on gold nanoparticles, which is believed to be among the main causes of deactivation in other metal catalysts.<sup>42</sup> The catalyst support also has significant influence and a large variety of supports have been investigated, a few examples being TiO<sub>2</sub>,<sup>43</sup> CeO<sub>2</sub>,<sup>28, 44</sup> SiO<sub>2</sub>,<sup>45</sup> hydrotalcites<sup>46</sup> and various types of carbon.<sup>27, 31, 47</sup> Nevertheless, on many of the supports, irreversible catalyst deactivation is still often observed. Unfortunately, detailed investigations on the mechanisms behind this loss of activity are scarce and focus predominantly on carbon and silica supports,<sup>31, 45</sup> with only limited information of the underlying nanoscale structural changes and dynamics.

The aim of this work is therefore to employ LP-TEM in combination with TEM studies of laboratory experiments to gain new insights in the structural changes of one of the more promising Au catalysts, namely Au supported on TiO<sub>2</sub>, during the liquid-phase oxidation of HMF to FDCA. TEM studies and EDX mapping of samples acquired directly from the reaction mixture revealed extensive gold particle detachment and subsequent particle coalescence and growth under conditions relevant to the liquid phase oxidation of HMF. Through systematic variation of the reaction mixture chemistry, it was found that a high pH was likely the main cause of this detachment. LP-TEM subsequently provided direct evidence for this mechanism and the detrimental influence of a high pH on catalyst stability. We propose that the origin of

this detachment is the negative charge present on both the gold nanoparticles and the TiO<sub>2</sub> support when the pH is above the point of zero charge (PZC) of both components. In addition, we found that using an MgO support with a PZC similar to the pH of the reaction mixture does indeed limit the loss of gold, highlighting the power of in situ TEM to enhance our knowledge of catalyst evolution, thus limiting deactivation.

## **5.2 Results and discussion**

### **5.2.1 Au catalysts**

To study the structural changes of gold nanoparticles supported on TiO<sub>2</sub> during the liquid-phase oxidation of 5-(Hydroxymethyl)furfural (HMF), two different catalysts were prepared, one with gold supported on P25 TiO<sub>2</sub> and one with gold supported on commercially available MgO nanopowder. The TiO<sub>2</sub> supported catalyst was prepared by adapting the ion adsorption procedure developed by Zhu et al.<sup>48</sup> while the MgO supported catalyst was prepared by deposition-precipitation of dissolved AuCl<sub>3</sub> with urea, akin to previously reported procedures.<sup>49-50</sup>

Characterization of the resulting catalysts with scanning transmission electron microscopy (STEM), as shown in Figure 5.1, showed that both catalysts consist of small gold nanoparticles homogeneously distributed over the entire support. In the case of the MgO supported catalyst, the particle size distribution is quite broad, while in the TiO<sub>2</sub> supported catalyst, this distribution is narrow. Nevertheless, both samples largely contain Au nanoparticles smaller than 10 nm and as a result, should be catalytically active for the liquid-phase oxidation of HMF. Bulk gold loading was 0.99 wt% for the TiO<sub>2</sub> supported catalyst and 0.69 wt% for the MgO supported catalyst, as determined by Inductively Coupled Plasma Atomic Emission Spectrometry (ICP-AES).

X-ray diffraction (XRD) (Supporting Figure S5.1) showed that both samples predominantly contain the expected support crystal structures (a mixture of anatase and rutile in the case of the TiO<sub>2</sub> supported catalyst and periclase for the MgO supported catalyst, although in the latter some brucite (Mg(OH)<sub>2</sub>) was also observed). Due to the low loading and small particles, gold was not observed in XRD. N<sub>2</sub> physisorption shows that both catalysts have an IUPAC type IV isotherm (Supporting Figure S5.1), with an H<sub>3</sub> hysteresis, usually associated with non-rigid aggregates that are non-spherical. This is in agreement with TEM observations for the TiO<sub>2</sub> support, but not entirely for the MgO support. In the latter, many smaller pores were observed inside the larger MgO crystals after the synthesis procedure, which were not observed in the empty support (the MgO support investigated and characterized in Chapter 2).



As the overall crystals retain their shape and both the specific surface area and specific pore volume increased significantly after the catalyst synthesis procedure, we propose that this porosity likely originates from leaching of larger MgO crystals during the synthesis. In both cases, microporosity was negligible, while BET surface area and mesopore volume were significantly higher in the MgO supported catalyst ( $45 \text{ m}^2\cdot\text{g}^{-1}$  and  $0.16 \text{ cm}^3\cdot\text{g}^{-1}$  for  $\text{TiO}_2$  and  $244 \text{ m}^2\cdot\text{g}^{-1}$  and  $0.74 \text{ cm}^3\cdot\text{g}^{-1}$  for MgO respectively).

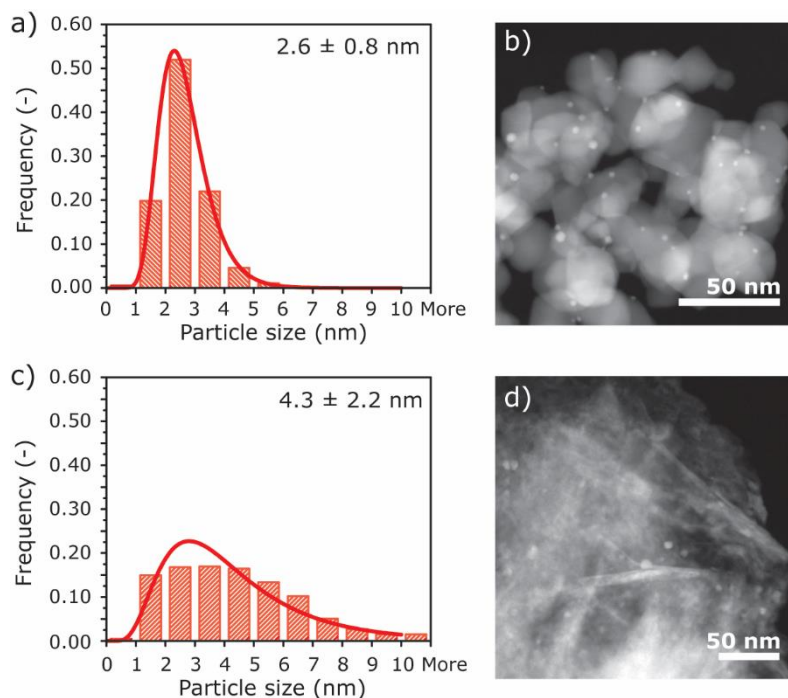


**Figure 5.1.** Particle size distributions (PSDs) with a lognormal fit and representative high-angle annular dark-field scanning transmission electron microscopy (HAADF-STEM) images of the 0.99 wt% Au/ $\text{TiO}_2$  catalyst (a and b) and the 0.69 wt% Au/MgO catalyst (c and d).

### 5.2.2 Structural changes during catalysis

The mechanisms underlying the structural changes of Au/ $\text{TiO}_2$  catalysts during the liquid-phase oxidation of HMF were first investigated using a laboratory setup at atmospheric pressure to allow for rapid and facile TEM sample acquisition. By omitting one of the three main reactants (HMF,  $\text{O}_2$  or  $\text{NaHCO}_3$ ), the effect of each individual reaction component on the catalyst evolution was investigated. Previous work exposing Au/ $\text{TiO}_2$  catalysts to water in contact with air at  $80 \text{ }^\circ\text{C}$  has already demonstrated that this catalyst does not change to any significant extent when both

HMF and  $\text{NaHCO}_3$  are absent in these experiments.<sup>25</sup> Therefore, any changes observed are most likely the result of the HMF and/or  $\text{NaHCO}_3$  present in the reaction mixture.

Representative STEM results of Au/ $\text{TiO}_2$  catalyst samples acquired after 24 hours of selective oxidation of HMF, using  $\text{NaHCO}_3$  as a base and under 1 bar of  $\text{O}_2$ , are shown in Figure 5.2. As can be observed in Figure 5.2a, significant amount of gold clustering is present, in which a large number of gold particles clump together and partially attach to each other. Such cluster formation without the formation of very large chunks of metal has been observed in very different catalytic systems as well, such as Co-based catalysts in the Fischer-Tropsch synthesis,<sup>51</sup> where it is also correlated with catalyst deactivation.

In addition to this gold cluster formation on the titania support, a large number of gold particles and several clusters of gold particles were found separate from the support on the TEM grid, as illustrated in Figure 5.2c. These particles were also found to be significantly larger than the particles remaining on the support, with an average size of 5.5 nm, while particles remaining on the support had an average nanoparticle size of 3.9 nm. To ensure that these particles were indeed gold nanoparticles, STEM-EDX mapping was performed (Figure 5.2d), which also confirmed that no support was present, as no Ti was detected. This is a strong indication that a part of the gold particles detaches from the  $\text{TiO}_2$  support during the reaction. This is also supported by the presence of  $\text{TiO}_2$  regions without any gold particles (Figure 5.2b) after reaction, as 'empty'  $\text{TiO}_2$  was not observed in the fresh catalyst.

When investigating the TEM results of the experiments in which one of the components was absent, several interesting differences were found, with TEM images provided in Supporting Figure S5.2. In the experiment where HMF and  $\text{O}_2$  were present, but the base was absent, only few particles were found separate from the  $\text{TiO}_2$  support and no  $\text{TiO}_2$  without gold particles was detected, indicating that particle detachment was limited. Cluster formation was still observed though, suggesting that HMF has some influence on the interaction between Au nanoparticles and support. In the experiment with  $\text{NaHCO}_3$  and  $\text{O}_2$ , but without HMF in the reaction mixture, a significant number of detached gold nanoparticles and empty or nearly empty  $\text{TiO}_2$  support was observed. In the presence of  $\text{NaHCO}_3$  and HMF, but the absence of  $\text{O}_2$ , the behavior observed was the same as the reaction with all components present, but significantly more severe, with more Au nanoparticles and clusters separate from the support. TEM results also showed that in all of the experiments, particle growth of particles remaining on the support was limited or nil, as can be seen from the particle size distributions in Supporting Figure S5.3. This indicates that the structural changes

observed in this system are primarily the result of gold nanoparticle detachment, which in turn causes particle coalescence and loss of gold specific surface area.

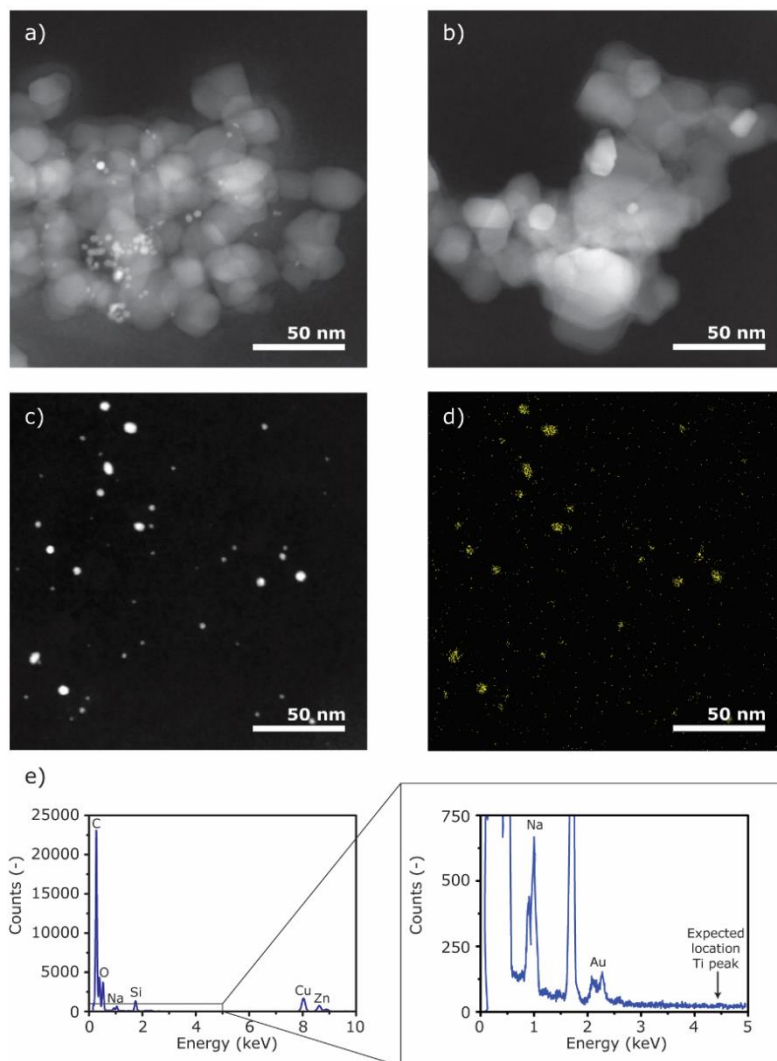


**Figure 5.2.** HAADF-STEM images and an EDX elemental map of several features observed in the used Au/TiO<sub>2</sub> catalyst after 24 hours in the reaction mixture containing HMF and NaHCO<sub>3</sub> at 80 °C under 1 bar of O<sub>2</sub>. (a) Example of Au nanoparticle clustering on the TiO<sub>2</sub> support. (b) Example of a TiO<sub>2</sub> support region without Au particles. (c) HAADF-STEM image of gold nanoparticles on the TEM grid without support present. (d) Au elemental map (in yellow) of the area in (c), confirming that the observed particles are indeed gold nanoparticles. (e) EDX spectrum integrated over the entire area shown in (c) and (d), showing Au peaks and the absence of Ti signal (with the expected location of the main Ti peak indicated by the arrow).

These observations are also in good agreement with the ICP-AES measurements of the used catalysts, shown in Table 5.1, with a lower weight percentage of gold present in all of the used catalysts than in the fresh catalyst. In addition, the used catalyst from the experiment without O<sub>2</sub> present, lost significantly more gold than the other used catalysts, as was also observed in TEM. Furthermore, in the absence of HMF, a significant amount of gold has been lost as well, again indicating that the base plays an important role in the decrease in gold loading during the reaction. Interestingly, the decrease in gold loading during the reaction itself (with all components present), is quite limited compared to the other experiments. When the base is indeed the main cause of gold loss, this is likely explained by the formation of the intermediate 5-hydroxymethyl-furancarboxylic acid (HMFCFA), which is an acid and therefore neutralizes the base during the experiment.

**Table 5.1.** Gold loading of the fresh and used Au/TiO<sub>2</sub> catalysts, comparing the absence of the individual components, as determined by ICP-AES.

Sample	Au content (wt%)
Fresh Au/TiO <sub>2</sub> catalyst	0.99
Used, regular reaction (HMF, NaHCO <sub>3</sub> and O <sub>2</sub> present)	0.92
Used, no base (HMF and O <sub>2</sub> present)	0.80
Used, no HMF (NaHCO <sub>3</sub> and O <sub>2</sub> present)	0.76
Used, no O <sub>2</sub> (NaHCO <sub>3</sub> and HMF present)	0.64

To follow the catalysis, High-Performance Liquid Chromatography (HPLC) was performed on the reaction mixture samples. The chromatograms (Supporting Figure S5.4) demonstrate that the catalyst is active for this oxidation, with almost full conversion of HMF after 8 hours. However, the main product detected was the intermediate HMFCFA, with only small amounts of the desired product 2,5-furandicarboxylic acid (FDCA) found. Based on our high pressure experiments and the work of Casanova,<sup>28</sup> we attribute this low FDCA yield to the low O<sub>2</sub> pressure during these experiments.

In the absence of base or catalyst, a slight increase in the HPLC peak area of HMF, likely originating from evaporation of H<sub>2</sub>O, was observed and no HMFCFA or FDCA was detected, indicating that both a base and a catalyst are required and that the reaction is indeed catalytic under these conditions. Surprisingly though, when the experiment is performed under inert atmosphere (absence of O<sub>2</sub>), the concentration of HMF does decrease significantly after longer periods of time (to ~10% of the initial peak area after 24 hours), but no HMFCFA or FDCA is detected. Based on the dark brown/black color of the suspension after reaction and the absence of any species

other than HMF in the HPLC analysis, this is likely the result of humin formation, which is known to be a possible side reaction in this system.<sup>52</sup>

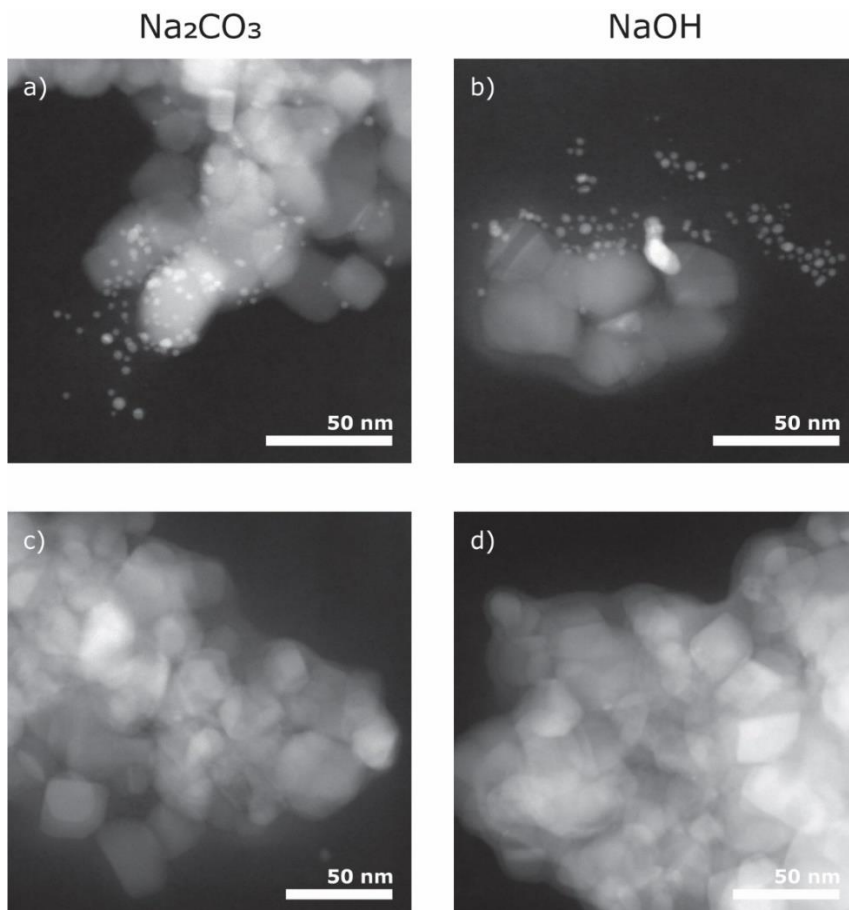


**Figure 5.3.** HAADF-STEM images of the used Au/TiO<sub>2</sub> catalysts after HMF oxidation, using Na<sub>2</sub>CO<sub>3</sub> (a and c) or NaOH (b and d) as the base. With (a) and (b) an example of a significant number of particles next to TiO<sub>2</sub> support when using Na<sub>2</sub>CO<sub>3</sub> and NaOH as a base respectively. (c) and (d) an example of empty regions of TiO<sub>2</sub> support after using Na<sub>2</sub>CO<sub>3</sub> and NaOH as a base respectively.

To further investigate the effect of the pH of the reaction mixture, additional experiments under 1 bar O<sub>2</sub> and at 80 °C were performed using different bases, namely Na<sub>2</sub>CO<sub>3</sub> and NaOH, but with the same molar concentration. This results in an initial pH of 11.7 for Na<sub>2</sub>CO<sub>3</sub> and 12.8 for NaOH, compared to a pH of 8.4 for NaHCO<sub>3</sub>. And although the higher pH is expected to accelerate the liquid phase oxidation of

HMF,<sup>28, 38</sup> it would likely also accelerate the detachment of gold nanoparticles from the support if a high pH is indeed the cause of particle detachment.

This is exactly what was also observed, with HPLC results showing a significantly faster consumption of HMF (Supporting Figure S5.4), but both TEM images (Figure 5.3) and the ICP results (Table 5.2) showing a significantly faster loss of gold nanoparticles. In both catalysts, TEM results show a large number of particles and clusters next to the support and only a limited number of particles remaining on the support. A large heterogeneity in the number of gold nanoparticles remaining on the support particles was observed though, as both a significant amount of empty TiO<sub>2</sub> particles and several TiO<sub>2</sub> particles that hardly lost any gold nanoparticles. ICP-AES results do also show that gold loadings of these used catalysts are significantly lower, compared to the experiments with NaHCO<sub>3</sub>.

**Table 5.2.** Gold loading of the fresh and used Au/TiO<sub>2</sub> catalysts (after 24h of reaction at 80 °C under 1 bar O<sub>2</sub>), comparing the use of different bases, as determined by ICP-AES.

Sample	Au content (wt%)
Fresh Au/TiO <sub>2</sub> catalyst	0.99
Used, NaHCO <sub>3</sub> as base (regular reaction)	0.92
Used, Na <sub>2</sub> CO <sub>3</sub> as base	0.62
Used, NaOH as base	0.58

To ensure the simplified low pressure experiments are representative for the processes occurring under typical reaction conditions, the HMF oxidation experiments with varying base were also performed in an autoclave with an O<sub>2</sub> pressure of 10 bar at 80 °C. Measurements of the used catalyst after 24 hours of reaction were performed. The TEM results were in good agreement with the results obtained at lower pressure. Again, many gold nanoparticles and clusters not attached to a support were observed and a significant fraction of the TiO<sub>2</sub> support was empty or nearly empty in these experiments (Figure 5.5). ICP-AES results (Table 5.3) do however show that gold loss was far more severe than during the low pressure experiments, to the extent that all bases caused a very significant loss of gold and that the trend in pH cannot be observed anymore. HPLC results showed that the FDCA yield was significantly higher (Supporting Figure S5.5), as is expected with higher O<sub>2</sub> partial pressures.

### 5.2.3 LP-TEM experiments

The behavior of the individual gold nanoparticles in an aqueous alkaline environment and the effect of pH was further investigated through the use of in situ TEM, using a specialized liquid phase (LP-) TEM holder (Poseidon Select, Protochips Inc.). In this

system, the sample and liquid are sandwiched between two silicon chips with thin, electron-transparent  $\text{Si}_x\text{N}_y$  windows. This allows imaging in the TEM and flowing liquid through the system, while separating the liquid from the high vacuum required for TEM.<sup>11</sup>

To investigate the influence of the pH, the sample was then brought in contact with  $\text{H}_2\text{O}$  with either  $57 \text{ mmol}\cdot\text{L}^{-1} \text{NaHCO}_3$  or  $57 \text{ mmol}\cdot\text{L}^{-1} \text{Na}_2\text{CO}_3$  dissolved in it (the same concentration as that of the lab-scale catalytic experiments). Due to the chemical interactions between NaOH solutions and silicon nitride and the resulting lack of membrane integrity, it was unfortunately not possible to perform this experiment with NaOH as the base. The particles were subsequently imaged continuously for 1 hour at room temperature, as the electron beam is known to be able to accelerate the processes involved,<sup>25</sup> mimicking the higher temperatures the sample is exposed to during the catalytic tests.

Because of this acceleration by the electron beam, the detachment outside of the imaged area is very slow. Since detachment did not occur in the absence of the beam, sufficient time was available to change the liquid composition at the sample, without altering the sample before starting the in situ experiment. This is because changing the composition of the liquid at the sample is a slow and gradual process, and therefore the concentration of the base increases slowly over time. This in turn means that the sample will be exposed to a  $\text{pH} > 7$  for a significant amount of time before the experiment can be started, but that the sample is not affected by this exposure.

M3 (soon available online, details in section 5.5 and the appendix) demonstrate that the pH is indeed a very important factor for gold particle detachment. As can be seen in Figure 5.4c, when using  $\text{NaHCO}_3$  as a base, almost half of the particles have detached from the support after 1 hour, while in the case of  $\text{Na}_2\text{CO}_3$ , almost all particles disappear ( $>95\%$ ) in the same time. From our control experiments (Supporting movie M1) and previous work,<sup>25</sup> in the absence of a base, very few particles detach for this system, indicating that the pH is indeed a crucial factor.

In addition, LP-TEM also allowed us to investigate the individual particle behavior, showing that particles have a significantly higher mobility when in contact with either  $\text{NaHCO}_3$  or  $\text{Na}_2\text{CO}_3$ , compared to  $\text{H}_2\text{O}$  only, as can be observed in the supporting movies. Particles predominantly detached, without shrinking, although a part of the Au nanoparticles did shrink during the experiments with  $\text{Na}_2\text{CO}_3$ . Because the imaging in LP-TEM only concerns a very small area and a significant liquid flow is present, particles are rapidly removed from the imaged area once detached and as a result, no cluster formation or reattachment could be observed in these experiments.

In addition, the influence of particle size on the likelihood of detachment was investigated, but no correlation between particle size and time of detachment could be found. This indicates that gold nanoparticle size does not play a major role in this system (Supporting Figure S5.6). This is also in agreement with the ex situ observation that particle size distributions of the particles remaining on the support do not change significantly during catalysis, while the detached particles found on the TEM grid tend to be significantly larger in size.

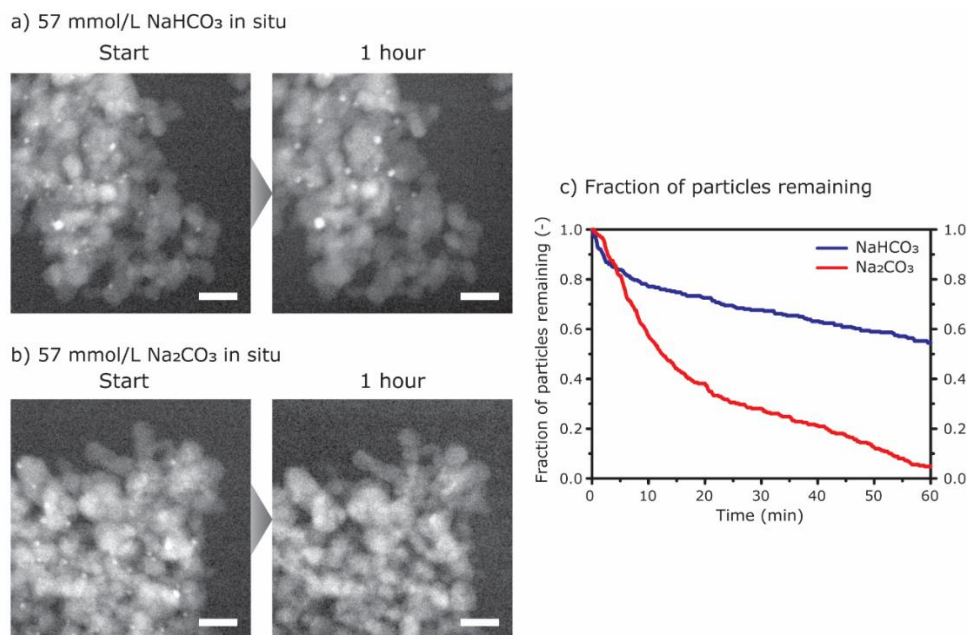


**Figure 5.4.** In situ HAADF-STEM images of the Au/TiO<sub>2</sub> catalyst before and after one hour of exposure to 57 mmol·L<sup>-1</sup> NaHCO<sub>3</sub> (a) and to 57 mmol·L<sup>-1</sup> Na<sub>2</sub>CO<sub>3</sub> (b) in LP-TEM respectively. The scale bar in each image corresponds to 50 nm. Some minor image processing has been performed to enhance particle visibility (see methods section). (c) Number of particles still remaining on the support over time during the in situ experiments in contact with either NaHCO<sub>3</sub> or Na<sub>2</sub>CO<sub>3</sub>. The number of particles is normalized with respect to the initial number of particles.

### 5.2.4 Origin of detachment

Based on the LP-TEM experiments and the lab-scale experiments, the origin of the observed structural changes of Au/TiO<sub>2</sub> catalysts during the liquid-phase oxidation of HMF is most likely the result of Au nanoparticle detachment. Following this detachment, subsequent particle coalescence and growth would be expected, ultimately resulting in a significant loss of gold. This in turn would likely cause catalyst deactivation, which is also in agreement with previous work by e.g. Casanova et al.<sup>28</sup>



and others, in which they found that catalyst deactivation in this system tends to be irreversible, even after washing. In their work, ICP-AES analysis of the reaction solution after catalyst separation did not show any gold in solution though. This might however be the result of the filtration method utilized to separate catalyst and solution, as gold nanoparticles would likely attach to the PTFE filter as well<sup>53</sup> and actual gold dissolution is likely very limited under these conditions. Because the catalyst itself was not measured with ICP-AES, only dissolved gold would likely be detected. This indicates that gold nanoparticle detachment in solution is an important factor in catalyst deactivation in liquid phase reactions.

The reason why particles detach and why this seems more severe at higher pH, is likely related to electrostatic interactions between particles and support. It is known that the point of zero charge (PZC) of TiO<sub>2</sub> is at a pH of 4-6, and therefore a pH above 6 would result in a negatively charged TiO<sub>2</sub> surface. Gold nanoparticles are known to be negatively charged in an aqueous solution<sup>54-56</sup> and based on electrochemical measurements, gold oxide has a point of zero charge around pH 4,<sup>57</sup> although as previously mentioned, these gold oxides are unlikely to form. It is however likely that gold nanoparticles will be negatively charged in this system as well, resulting in electrostatic repulsion at a pH above the PZC of TiO<sub>2</sub>. Due to the increase in negative surface charge with increasing pH, this repulsion is likely to become more severe at higher pH, i.e. when using the same concentration of a stronger base. This would then likely result in the observed faster detachment of Au nanoparticles when using a stronger base. Charging of the Au nanoparticle surface might also be able to explain the relatively slow growth and cluster formation of the detached particles, as colloidal gold nanoparticles without capping agents or charge to stabilize them, usually coagulate very rapidly.<sup>54</sup> This would then result in a balance between the attractive van der Waals interactions and the electrostatic repulsion of the negatively charged surface, which would slow down coagulation considerably.

**Table 3.** Gold loading of the fresh and used TiO<sub>2</sub> and MgO supported Au catalysts before and after the high pressure (10 bar O<sub>2</sub>) HMF selective oxidation experiments, as determined by ICP-AES.

Sample	Au content (wt%)
Fresh Au/TiO <sub>2</sub> catalyst	0.99
Used Au/TiO <sub>2</sub> , NaHCO <sub>3</sub> as base	0.25
Used Au/TiO <sub>2</sub> , Na <sub>2</sub> CO <sub>3</sub> as base	0.20
Used Au/TiO <sub>2</sub> , NaOH as base	0.24
Fresh Au/MgO catalyst	0.69
Used Au/MgO, Na <sub>2</sub> CO <sub>3</sub> as base	0.33

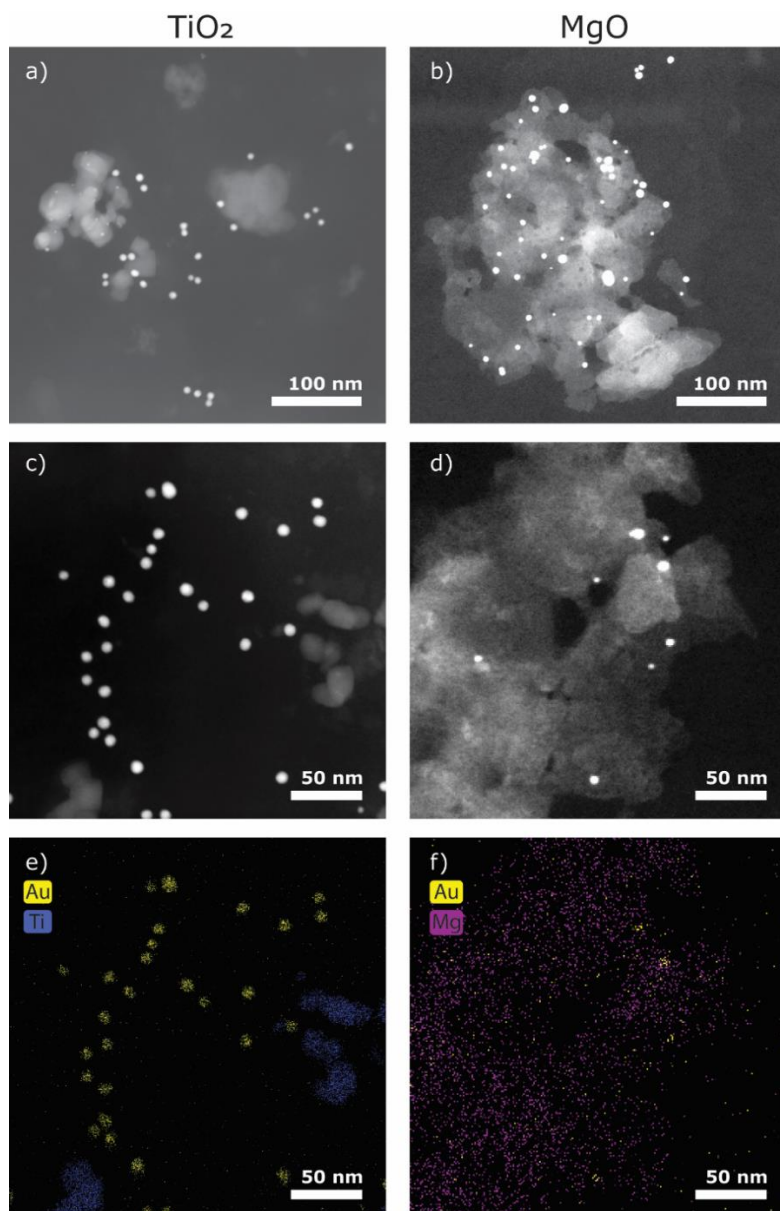


**Figure 5.5.** HAADF-STEM images and EDX elemental maps of the used Au/TiO<sub>2</sub> catalyst (a, c and e) and used Au/MgO catalyst (b, d and f) after an HMF oxidation experiment at high pressure (10 bar O<sub>2</sub>), using Na<sub>2</sub>CO<sub>3</sub> as the base. With (a) demonstrating that most particles are found next to the support when using TiO<sub>2</sub> as a support, although several smaller particles can still be observed on the leftmost TiO<sub>2</sub> particle; (b) shows that using MgO as a support results in a significantly higher fraction of Au particles remaining on the support, although several particles seem to have detached from the support as well.

To test this hypothesis, an additional experiment was performed, utilizing a support that has a significantly higher point of zero charge, namely MgO (PZC  $\sim 12$ <sup>58</sup>). The high pressure catalytic test with Na<sub>2</sub>CO<sub>3</sub> as base was carried out using an Au/MgO catalyst instead of the Au/TiO<sub>2</sub> catalyst. Although HPLC results (Supporting Figure S5.5) show the MgO supported catalyst had a lower overall conversion to FDCA with a similar amount of gold present, it is still a very active catalyst. TEM and EDX results (Figure 5.5) and ICP-AES results (Table 5.3) show that the loss of gold is lower than for the same experiment with Au/TiO<sub>2</sub>. It should be noted however that there is still a quite significant loss of gold and several large particles can be observed next to the MgO support, although not nearly as many as in the case of TiO<sub>2</sub>. This could be the result of the weaker metal-support interactions of Au with MgO<sup>59</sup> or the PZC of MgO not being sufficiently above the pH of the solution. Furthermore, the presence of HMF might also have some influence, as according to our low pressure experiments, some gold nanoparticle detachment was observed when HMF is present without base (Table 5.1). Although it would be very interesting to observe the processes involved with LP-TEM for the Au/MgO catalyst, these experiments could not be performed due to the instability of MgO under electron irradiation in the presence of water.<sup>21</sup>

### 5.3 Conclusions

In conclusion, this work presents new insights in the origin of the extensive nanoscale structural changes of Au/TiO<sub>2</sub> catalysts during the liquid-phase oxidation of 5-(Hydroxymethyl)furfural in an alkaline environment. Based on TEM studies and EDX mapping of samples acquired directly from reaction mixtures, we found that these structural changes likely originate from nanoparticle detachment and subsequent particle coalescence and growth during the reaction. Through variations in reaction mixture composition, it was also found that the presence of a base, i.e. a high pH, is likely the main cause for this detachment. LP-TEM confirmed that this detachment is indeed occurring in the presence of a base and additional experiments show that a higher pH also results in more gold loss, which in turn likely results in a faster catalyst deactivation.

We propose that the detachment of particles in an alkaline environment is the result of both the gold nanoparticles and the TiO<sub>2</sub> support attaining negative surface charges when the pH is higher than the point of zero charge of TiO<sub>2</sub> (pH 4-6). This weakens the particle-support interaction through electrostatic repulsion and allows gold nanoparticles to detach from the TiO<sub>2</sub> surface, resulting in both loss of gold and a decrease in specific surface area as a result of nanoparticle clustering and growth. This indicates that a method to limit the presence of a net negative surface charge on the support would result in less gold nanoparticle detachment. This was tested by using

magnesium oxide as a support, as its surface does not have a significant net negative charge under typical reaction conditions for HMF selective oxidation. Its use did indeed result in less gold nanoparticle detachment, despite MgO usually having a weaker interaction with supported nanoparticles than TiO<sub>2</sub>.

This demonstrates the power of detailed (in situ) TEM studies to investigate structural changes of catalysts and the underlying mechanisms at the nanoscale, and possibly presents a strategy to limit gold loss and associated catalyst deactivation during the liquid-phase oxidation of HMF. It also highlights the importance of the support choice in a liquid phase catalytic system, which should take into account the electrostatic charges that will be generated on the surface of the support and the metal nanoparticles under the specific reaction conditions, a consideration not usually necessary in gas phase catalysis. Ideally, to prevent particle detachment and associated catalyst deactivation, the support and particles having the same charge should be avoided.

## **5.4 Materials and Methods**

### **5.4.1 Catalyst synthesis**

The Au/TiO<sub>2</sub> catalyst was synthesized using a modified ion adsorption procedure developed by Zhu et al.<sup>48</sup> First, the required gold-ethylene diamine complex salt (Au(NH<sub>2</sub>-C<sub>2</sub>H<sub>4</sub>-NH<sub>2</sub>)<sub>2</sub>Cl<sub>3</sub>) was synthesized according to the method developed by Block and Bailar,<sup>60</sup> in which 0.25 g of HAuCl<sub>4</sub>·3H<sub>2</sub>O (≥99.9% pure, Sigma-Aldrich) was dissolved in 2.5 g of demineralized H<sub>2</sub>O in a glass beaker. To this solution, the corresponding amount of pure ethylene diamine (0.15 mL, 99.5% purity, Sigma-Aldrich) was added dropwise while stirring at 400 RPM. The solution was subsequently left for 30 minutes at room temperature to form the complex, after which it was precipitated out by adding 30 mL of ethanol (99.8% purity, Sigma-Aldrich). The resulting suspension was subsequently left overnight to settle, after which the liquid was removed. The complex was then dried for another 24 hours at room temperature to let the remaining ethanol evaporate and subsequently redissolved in 50 mL demineralized water, resulting in a 11 mmol·L<sup>-1</sup> solution of Au(NH<sub>2</sub>-C<sub>2</sub>H<sub>4</sub>-NH<sub>2</sub>)<sub>2</sub>Cl<sub>3</sub> in water.

The 1 wt% Au on TiO<sub>2</sub> catalyst was subsequently prepared by adding 12 mL of this 11 mmol·L<sup>-1</sup> solution to 18 mL demineralized water in a glass beaker, while stirring at 400 RPM. Then, 0.5 mL of a 1.0 mol·L<sup>-1</sup> NaOH (99% pure, Sigma-Aldrich) solution in water was added to increase the pH to approximately 12. After stirring for 5 minutes, 3.0g of commercial fumed TiO<sub>2</sub> powder (P25, Evonik Degussa) was dispersed in the solution and left for 2 hours to allow the gold precursor to adsorb on the TiO<sub>2</sub> surface,

while continuing stirring at 400 RPM to keep the powder suspended. The solid was subsequently separated by centrifugation (10 min, 4000 RPM) and washed three times with 40 mL of demineralized water.

The resulting powder was subsequently dried at 60 °C overnight, followed by an additional drying step in vacuum at room temperature for 24 hours. Finally, the powder was heated in a tube reactor to 300 °C for 2 hours in pure N<sub>2</sub>, followed by 2 hours at 400 °C in a 80%N<sub>2</sub>/20%O<sub>2</sub> mixture to reduce the ionic gold and remove any remaining ligands and other carbonaceous species, respectively. A flow of 150 mL·min<sup>-1</sup> was used in both steps and the heating and cooling rate was 5 °C·min<sup>-1</sup> throughout the entire reduction/oxidation procedure.

The Au/MgO catalyst was prepared using a modified deposition-precipitation procedure based on the work of Patil et al.<sup>50</sup> and Zanella et al.<sup>49</sup> in which urea is used as precursor for the ammonium hydroxide precipitation agent. In a typical procedure, 42 mg of AuCl<sub>3</sub>·3H<sub>2</sub>O was dissolved in 30 g demineralized H<sub>2</sub>O in a glass beaker. 0.75 g of pure urea was dissolved in 12 g of demineralized H<sub>2</sub>O in a separate vial, after which these two solutions were mixed while stirring at 400 RPM. 2.0 g of commercial MgO nanopowder (≤50 nm primary particle size, Sigma-Aldrich) was then dispersed in this solution, followed by heating to 80 °C. This temperature was maintained for 4 hours, which according to the previously mentioned references, should be sufficient to decompose the urea to increase the pH. After cooling the suspension to room temperature, the sample was separated by centrifugation (10 min, 4000 RPM) and washed with demineralized H<sub>2</sub>O 5 times.

The resulting powder was also dried at 60 °C overnight, followed by an additional drying step in vacuum at room temperature for 24 hours. This dry powder was subsequently heated to 400 °C, then subjected to a gas mixture of 80%N<sub>2</sub>/20%H<sub>2</sub> for 2 hours, followed by flushing with pure N<sub>2</sub> for 30 min and finally heated in a gas mixture of 80%N<sub>2</sub>/20%O<sub>2</sub> for another 2 hours to reduce the gold and remove any remaining (organic) contaminants, respectively. Throughout the entire treatment, the gas flow was 150 mL·min<sup>-1</sup> and the heating and cooling rate was 5 °C·min<sup>-1</sup>.

Throughout the entire synthesis of both catalysts, care was taken to cover the gold containing solutions with aluminum foil to prevent light from reaching the gold precursor. In addition, contact with any metal was prevented by using Teflon and glass equipment and by using parafilm to separate aluminum foil and solution where necessary. This was done to avoid partial reduction of the gold before the reduction/calcination procedure, which would typically result in larger gold particles and a broader particle size distribution, and can be induced by visible light or galvanic contact with metals less noble than gold.

### **5.4.2 Catalyst characterization**

The fresh catalysts were characterized by powder X-ray diffraction (XRD), using a Bruker D2 Phaser with a Co K $\alpha$  source. Samples were evaluated for  $2\theta$  between  $20^\circ$  and  $80^\circ$  for phase identification. Gold loading of both fresh and used catalysts was evaluated using Inductively Coupled Plasma Atomic Emission Spectrometry (ICP-AES). The used catalyst was isolated from the reaction mixture using centrifugation (10 min, 6000 RPM) and was calcined at  $300^\circ\text{C}$  in air before digestion to remove deposited carbonaceous species.

N<sub>2</sub> physisorption measurements of the fresh catalysts were performed at  $-196^\circ\text{C}$  (77K) using a Micromeritics Tristar 3000 instrument. Before the isotherm measurements, samples were dried at  $200^\circ\text{C}$  in air. Specific surface areas were calculated using the multipoint Brunauer-Emmett-Teller (BET) method ( $0.05 < P/P_0 < 0.25$ ). Microporosity was evaluated using the t-plot method, while pore volume was determined at  $p/p_0=0.998$  from the adsorption branches of the isotherms using the Barrett-Joyner-Halenda (BJH) method.

For both fresh and used catalyst, determination of gold particle size, catalyst morphology, particle dispersion and, in the case of the used catalyst also the presence of detached particles in the reaction mixture, was performed with Transmission Electron Microscopy (TEM). All TEM analyses were measured with a Talos F200X (Thermo Fischer Scientific), operated at 200 kV acceleration voltage. Depending on the catalyst, TEM, Bright-Field Scanning TEM (BF-STEM) and/or High-Angle Annular Dark-Field STEM (HAAFD-STEM) were used to evaluate the material. In addition, local chemical composition was determined using Energy-Dispersive X-ray Spectroscopy (EDX) mapping in STEM mode (STEM-EDX) where appropriate.

TEM samples of the fresh catalyst were prepared by dispersing the sample in isopropanol (Honeywell, Chromasolv™ 99.9%) and depositing a few droplets of this suspension on a 200 mesh copper-formvar TEM grid. Samples of the catalyst during and after the reaction were prepared by extracting a few droplets of the aqueous reaction mixture, using a stainless steel syringe, and depositing these droplets directly on the 200 mesh copper-formvar TEM grid. No filtering or other treatment was used to prevent alteration of the sample and loss of the detached nanoparticles as much as possible.

Gold particle sizes were subsequently determined from these (S)TEM images by measuring at least 200 particles using ImageJ. All averages presented are number averages, determined by summation of all individual diameters and dividing by the number of particles. Particle size distributions were determined from the diameter,

using a bin size of 1 nm and the accompanying lognormal fit was calculated using the lognfit function in Matlab.

### **5.4.3 Catalytic tests**

5-(Hydroxymethyl)furfural (HMF) liquid-phase oxidation tests with the Au/TiO<sub>2</sub> catalyst were performed in a laboratory setup consisting of a glass three-necked round-bottom flask with an oxygen supply line and connected to a water-cooled condenser. In a typical experiment, 90 mg (0.7 mmol) of HMF ( $\geq 99\%$  pure, Sigma-Aldrich) and 120 mg (1.4 mmol) NaHCO<sub>3</sub> ( $\geq 99\%$  pure, ACROS Organics) were dissolved in 25 mL demineralized H<sub>2</sub>O, followed by addition of 1.4  $\mu$ L of 1,4-dioxane (99.8%, Sigma-Aldrich) as an internal standard for the high-performance liquid chromatography (HPLC) analysis of the products. The system was subsequently mounted on a heater/stirrer plate with heating mantle, covered in aluminum foil and heated to 80 °C, while stirring at 400 RPM and bubbling O<sub>2</sub> at 1 bar through the solution continuously.

When the temperature reached 80 °C, 50 mg of the Au/TiO<sub>2</sub> catalyst was added to the system. Afterwards, HPLC and TEM samples were acquired at regular time intervals (0.5h, 1h, 1.5h, 2h, 3h, 4h, 6h, 8h and 24h for the HPLC samples and 0.5h, 1h, 2h, 4h, 8h and 24h for the TEM samples). After 24 hours, the heating and O<sub>2</sub> flow were stopped and the remaining catalyst was separated from the reaction mixture through centrifugation. The gold content of this separated catalyst was subsequently determined using ICP-AES.

For the HPLC samples, 0.1 mL of the reaction mixture was extracted, filtered with 0.45  $\mu$ m PTFE filters and diluted with 0.9 mL demineralized H<sub>2</sub>O (for a 1:10 dilution). These samples were subsequently analyzed using a Shimadzu LC-20AD equipped a Bio-Rad Aminex HPX-87H column, with 5 mmol·L<sup>-1</sup> H<sub>2</sub>SO<sub>4</sub> in H<sub>2</sub>O at 60 °C with a flow of 0.55 mL·min<sup>-1</sup> as the eluent. As mentioned previously, TEM samples were acquired by extracting a few droplets from the reaction mixture and depositing them directly onto a 200 mesh copper-formvar TEM grid, followed by drying the grid for several hours at room temperature.

To investigate the influence of the individual components on the structural changes of the Au/TiO<sub>2</sub> catalyst, a set of experiments was performed in which one of the components (either HMF, NaHCO<sub>3</sub> or O<sub>2</sub>) was absent. In the case of testing the absence of O<sub>2</sub>, nitrogen was bubbled through the system instead, taking care to allow for ample time to purge the system of any remaining oxygen before adding the catalyst. To investigate the influence of pH, the NaHCO<sub>3</sub> was replaced by the same molar concentration of a different base, either Na<sub>2</sub>CO<sub>3</sub> (99.5%, ACROS Organics) or

NaOH (99%, Sigma-Aldrich). Each of these experiments was performed twice to check reproducibility.

High pressure experiments were performed akin to previously reported procedures.<sup>45</sup> In a typical experiment, the Au/TiO<sub>2</sub> catalyst was suspended in 7 mL of a solution containing 0.2 mmol HMF (25 mg) and 0.4 mmol base (either NaHCO<sub>3</sub>, Na<sub>2</sub>CO<sub>3</sub> or NaOH) in H<sub>2</sub>O in a stainless steel autoclave. In addition, an experiment with the Au/MgO catalyst was performed under the same conditions using Na<sub>2</sub>CO<sub>3</sub> as a base. Each reactor was heated to 80 °C and pressurized to 10 bar of pure O<sub>2</sub> (Linde, 99.99%) while stirring at 900 RPM. After leaving the system for 24 hours to react, the autoclave was cooled down and depressurized, after which a TEM and an HPLC sample were acquired in the same way as the previous experiments. The remaining used catalyst was then separated by centrifugation and gold loading determined with ICP-AES.

### 5.4.4 Liquid Phase Transmission Electron Microscopy

In situ TEM experiments were performed to investigate the effect of the pH on particle detachment and whether particle size influences the extent of detachment. In such an experiment, the sample is brought in contact with a liquid enclosed between two thin silicon nitride (Si<sub>x</sub>N<sub>y</sub>) windows. These windows are sufficiently strong to withstand the pressure difference between the liquid and the high vacuum of the TEM, while keeping the liquid layer thickness thin enough for imaging with high resolution. The experiments themselves were performed using previously reported procedures.<sup>25</sup>

### 5.4.5 Liquid cell preparation

In a typical experiment, a small and large silicon chip with a nominally 50 nm thick silicon nitride (Si<sub>x</sub>N<sub>y</sub>) window of 20x550 μm (Protochips Inc., USA) were cleaned in acetone and methanol according to manufacturer instructions. Subsequently, compressed air was used to accelerate the evaporation of methanol from the chip surface and both chips were then plasma-cleaned in an 80%Ar/20%O<sub>2</sub> plasma for two minutes to render the chip surface hydrophilic.

A small amount of the Au/TiO<sub>2</sub> catalyst was then dispersed in 2 mL of high-purity isopropanol (Honeywell, Chromasolv™ 99.9%) and sonicated for at least 15 minutes to disperse agglomerates. A 0.5 μL droplet of this suspension was placed on the silicon nitride layer of the large silicon liquid cell chip and left to dry for 5 minutes to obtain a sufficient amount of catalyst particles on the window for imaging in the TEM.

The small silicon chip also containing a 20x550 μm Si<sub>x</sub>N<sub>y</sub> window and 150 nm gold spacers to separate the two chips, was then placed in the dedicated liquid cell TEM holder (Protochips Inc., USA). The longest edge of the window of the small chip was



oriented perpendicular to that of the large chip for optimal resolution.<sup>11</sup> A 1  $\mu\text{L}$  drop of water (sterile-filtered, Bioreagent,  $\leq 1$  Eu/mL,  $\leq 5$  ppm metal impurities, Sigma-Aldrich) was then added on top of the small chip and the cell was subsequently assembled by placing the large silicon chip containing the sample on top. In this configuration, the sample is dispersed on the top chip when the holder is inserted in the microscope for optimal spatial resolution in STEM mode.<sup>61</sup>

### 5.4.6 Imaging

Imaging was performed using a Talos F200X (Thermo Fischer Scientific), operated in Scanning Transmission mode (STEM) mode at 200 kV acceleration voltage and using both a bright field (BF) and high-angle annular dark field (HAADF) detector for imaging with a camera length of 125 mm. A beam current of 0.21 nA was used for imaging, as determined by the screen current without a holder present in the electron microscope. Images were collected with a pixel dwell time of 2.4  $\mu\text{s}$ , with 2048x2048 pixel images, for a total of 10 s/frame. All experiments were performed at a magnification of 225 kx, corresponding to a field of view of 500x500 nm, which results in an electron dose rate of  $5.2 \cdot 10^3 \text{ e}^- \cdot \text{nm}^{-2} \cdot \text{s}^{-1}$ .

Each liquid cell experiment was performed in flow mode using a flow of 4  $\mu\text{L} \cdot \text{min}^{-1}$  to prevent the buildup of gases and bubble formation due to electron beam induced water decomposition.<sup>62</sup> Before an in situ experiment was started,  $\text{H}_2\text{O}$  was flushed through the system for 30 minutes to remove any remaining bubbles. A small area within the sample was then continuously imaged in STEM mode with a total of 360 images being acquired, corresponding to exactly 1h of electron beam scanning. In this way the particles and their detachment can be followed in real time, while the beam was found to slightly accelerate detachment locally.

When scanning in water did not show any unusual behavior, a solution with the same concentration of either  $\text{NaHCO}_3$  or  $\text{Na}_2\text{CO}_3$  as the HMF oxidation experiments (57  $\text{mmol} \cdot \text{L}^{-1}$ ) was flushed through the holder. The experiment was started at least 45 minutes after starting the introduction of the base to ensure the liquid around the sample had the desired composition. Due to the chemical interactions between NaOH solutions and silicon nitride and the resulting lack of membrane integrity, it was unfortunately not possible to perform this experiment with NaOH. Experiments with the Au/MgO catalyst could not be performed in situ due to the instability of MgO under electron irradiation in the presence of water.<sup>21</sup>

For the in situ experiments, images were first processed with ImageJ to enhance particle visibility. First, images were processed by using a Gaussian blur filter with a sigma of 1.5, followed by using the despeckle function, which replaces each pixel with

the median value of the 3x3 grid of pixels around it. For each base, at least 200 particles were followed and their diameter was measured manually at the start using ImageJ. If the particle disappeared, the size just before disappearance was also measured and recorded along with the time of disappearance, which was subsequently used to construct Figure 5.4 and Supporting Figure S5.6.

## 5.5 Acknowledgements

The authors gratefully acknowledge R. Vogel for assistance with performing the high pressure experiments, R. Dalebout, L. Weber and P. Paalanen for performing the N<sub>2</sub> physisorption measurements, C. Vis and P. Wijten for assistance with HPLC analysis and J.D. Meeldijk for technical assistance with the transmission electron microscope. K.P. de Jong and M.J. Meijerink acknowledge funding from the European Research Council, an EU FP7 ERC Advanced Grant no. 338846. J. Zečević acknowledges financial support by Netherlands Organization for Scientific Research (NWO), Veni Grant no. 722.015.010.

## 5.6 References

- (1). De Jong, K. P., *Synthesis of Solid Catalysts*. John Wiley & Sons: 2013.
- (2). Chorkendorff, I.; Niemantsverdriet, J. W., *Concepts of Modern Catalysis and Kinetics*. John Wiley & Sons: 2017.
- (3). Moulijn, J. A.; Van Diepen, A.; Kapteijn, F., Catalyst Deactivation: Is It Predictable?: What to Do? *Appl. Catal., A* **2001**, *212* (1-2), 3-16.
- (4). Valden, M.; Lai, X.; Goodman, D. W., Onset of Catalytic Activity of Gold Clusters on Titania with the Appearance of Nonmetallic Properties. *Science* **1998**, *281* (5383), 1647-1650.
- (5). Carter, C. B.; Williams, D. B., *Transmission Electron Microscopy*. Springer-Verlag US: 2009.
- (6). Van den Berg, R.; Elkjaer, C. F.; Gommès, C. J.; Chorkendorff, I.; Sehested, J.; De Jongh, P. E.; De Jong, K. P.; Helveg, S., Revealing the Formation of Copper Nanoparticles from a Homogeneous Solid Precursor by Electron Microscopy. *J. Am. Chem. Soc.* **2016**, *138* (10), 3433-3442.
- (7). Simonsen, S. B.; Chorkendorff, I.; Dahl, S.; Skoglundh, M.; Sehested, J.; Helveg, S., Direct Observations of Oxygen-Induced Platinum Nanoparticle Ripening Studied by in Situ Tem. *J. Am. Chem. Soc.* **2010**, *132* (23), 7968-7975.
- (8). Challa, S. R.; Delariva, A. T.; Hansen, T. W.; Helveg, S.; Sehested, J.; Hansen, P. L.; Garzon, F.; Datye, A. K., Relating Rates of Catalyst Sintering to the Disappearance of Individual Nanoparticles During Ostwald Ripening. *J. Am. Chem. Soc.* **2011**, *133* (51), 20672-20675.
- (9). Liu, R.-J.; Crozier, P. A.; Smith, C. M.; Hucul, D. A.; Blackson, J.; Salaita, G., Metal Sintering Mechanisms and Regeneration of Palladium/Alumina Hydrogenation Catalysts. *Appl. Catal., A* **2005**, *282* (1-2), 111-121.

- (10). Saka, H.; Kamino, T.; Ara, S.; Sasaki, K., In Situ Heating Transmission Electron Microscopy. *MRS Bull.* **2008**, *33* (2), 93-100.
- (11). De Jonge, N.; Ross, F. M., Electron Microscopy of Specimens in Liquid. *Nat. Nanotechnol.* **2011**, *6* (11), 695-704.
- (12). Yuk, J. M.; Park, J.; Ercius, P.; Kim, K.; Hellebusch, D. J.; Crommie, M. F.; Lee, J. Y.; Zettl, A.; Alivisatos, A. P., High-Resolution Em of Colloidal Nanocrystal Growth Using Graphene Liquid Cells. *Science* **2012**, *336* (6077), 61-64.
- (13). Smeets, P. J. M.; Cho, K. R.; Kempen, R. G. E.; Sommerdijk, N. A. J. M.; De Yoreo, J. J., Calcium Carbonate Nucleation Driven by Ion Binding in a Biomimetic Matrix Revealed by in Situ Electron Microscopy. *Nat. Mater.* **2015**, *14* (4), 394-399.
- (14). Sacci, R. L.; Dudney, N. J.; More, K. L.; Parent, L. R.; Arslan, I.; Browning, N. D.; Unocic, R. R., Direct Visualization of Initial SEI Morphology and Growth Kinetics During Lithium Deposition by in Situ Electrochemical Transmission Electron Microscopy. *Chem. Commun.* **2014**, *50* (17), 2104-2107.
- (15). Radisic, A.; Vereecken, P. M.; Hannon, J. B.; Searson, P. C.; Ross, F. M., Quantifying Electrochemical Nucleation and Growth of Nanoscale Clusters Using Real-Time Kinetic Data. *Nano Lett.* **2006**, *6* (2), 238-242.
- (16). De Jonge, N.; Peckys, D. B.; Kremers, G. J.; Piston, D. W., Electron Microscopy of Whole Cells in Liquid with Nanometer Resolution. *Proc. Natl. Acad. Sci. U. S. A.* **2009**, *106* (7), 2159-2164.
- (17). Zheng, H.; Smith, R. K.; Jun, Y.-w.; Kisielowski, C.; Dahmen, U.; Alivisatos, A. P., Observation of Single Colloidal Platinum Nanocrystal Growth Trajectories. *Science* **2009**, *324* (5932), 1309-1312.
- (18). Alloyeau, D.; Dachraoui, W.; Javed, Y.; Belkahla, H.; Wang, G.; Lecoq, H.; Ammar, S.; Ersen, O.; Wisnet, A.; Gazeau, F.; Ricolleau, C., Unravelling Kinetic and Thermodynamic Effects on the Growth of Gold Nanoplates by Liquid Transmission Electron Microscopy. *Nano Lett.* **2015**, *15* (4), 2574-2581.
- (19). Hermannsdörfer, J.; de Jonge, N.; Verch, A., Electron Beam Induced Chemistry of Gold Nanoparticles in Saline Solution. *Chem. Commun.* **2015**, *51* (91), 16393-16396.
- (20). Woehl, T. J.; Park, C.; Evans, J. E.; Arslan, I.; Ristenpart, W. D.; Browning, N. D., Direct Observation of Aggregative Nanoparticle Growth: Kinetic Modeling of the Size Distribution and Growth Rate. *Nano Lett.* **2013**, *14* (1), 373-378.
- (21). Meijerink, M. J.; De Jong, K. P.; Zečević, J., Assessment of Oxide Nanoparticle Stability in Liquid Phase Transmission Electron Microscopy. *Nano Res.* **2019**, *12* (9), 2355-2363.
- (22). Meijerink, M. J.; Spiga, C.; Hansen, T. W.; Damsgaard, C. D.; De Jong, K. P.; Zečević, J., Nanoscale Imaging and Stabilization of Silica Nanospheres in Liquid Phase Transmission Electron Microscopy. *Part. Part. Syst. Charact.* **2019**, *36* (1), 1800374.
- (23). Lu, Y.; Geng, J.; Wang, K.; Zhang, W.; Ding, W.; Zhang, Z.; Xie, S.; Dai, H.; Chen, F.-R.; Sui, M., Modifying Surface Chemistry of Metal Oxides for Boosting Dissolution Kinetics in Water by Liquid Cell Electron Microscopy. *ACS Nano* **2017**, *11* (8), 8018-8025.
- (24). Zečević, J.; Hermannsdörfer, J.; Schuh, T.; De Jong, K. P.; De Jonge, N., Anisotropic Shape Changes of Silica Nanoparticles Induced in Liquid with Scanning Transmission Electron Microscopy. *Small* **2017**, *13* (1), 1602466.

- (25). Meijerink, M. J.; de Jong, K. P.; Zečević, J., Growth of Supported Gold Nanoparticles in Aqueous Phase Studied by in Situ Transmission Electron Microscopy. *J. Phys. Chem. C* **2020**, *124* (3), 2202-2212.
- (26). Gorbaney, Y. Y.; Kegnæs, S.; Riisager, A., Effect of Support in Heterogeneous Ruthenium Catalysts Used for the Selective Aerobic Oxidation of HMF in Water. *Top. Catal.* **2011**, *54* (16-18), 1318.
- (27). Davis, S. E.; Houk, L. R.; Tamargo, E. C.; Datye, A. K.; Davis, R. J., Oxidation of 5-Hydroxymethylfurfural over Supported Pt, Pd and Au Catalysts. *Catal. Today* **2011**, *160* (1), 55-60.
- (28). Casanova, O.; Iborra, S.; Corma, A., Biomass into Chemicals: Aerobic Oxidation of 5-Hydroxymethyl-2-Furfural into 2, 5-Furandicarboxylic Acid with Gold Nanoparticle Catalysts. *ChemSusChem: Chemistry & Sustainability Energy & Materials* **2009**, *2* (12), 1138-1144.
- (29). Davis, S. E.; Benavidez, A. D.; Gosselink, R. W.; Bitter, J. H.; De Jong, K. P.; Datye, A. K.; Davis, R. J., Kinetics and Mechanism of 5-Hydroxymethylfurfural Oxidation and Their Implications for Catalyst Development. *J. Mol. Catal. A: Chem.* **2014**, *388*, 123-132.
- (30). Ait Rass, H.; Essayem, N.; Besson, M., Selective Aerobic Oxidation of 5-HMF into 2, 5-Furandicarboxylic Acid with Pt Catalysts Supported on TiO<sub>2</sub>-and ZrO<sub>2</sub>-Based Supports. *ChemSusChem* **2015**, *8* (7), 1206-1217.
- (31). Donoeva, B.; Masoud, N.; De Jongh, P. E., Carbon Support Surface Effects in the Gold-Catalyzed Oxidation of 5-Hydroxymethylfurfural. *ACS Catal.* **2017**, *7* (7), 4581-4591.
- (32). Taarning, E.; Nielsen, I. S.; Egeblad, K.; Madsen, R.; Christensen, C. H., Chemicals from Renewables: Aerobic Oxidation of Furfural and Hydroxymethylfurfural over Gold Catalysts. *ChemSusChem: Chemistry & Sustainability Energy & Materials* **2008**, *1* (1-2), 75-78.
- (33). Pasini, T.; Piccinini, M.; Blosi, M.; Bonelli, R.; Albonetti, S.; Dimitratos, N.; Lopez-Sanchez, J. A.; Sankar, M.; He, Q.; Kiely, C. J., Selective Oxidation of 5-Hydroxymethyl-2-Furfural Using Supported Gold-Copper Nanoparticles. *Green Chem.* **2011**, *13* (8), 2091-2099.
- (34). Lolli, A.; Albonetti, S.; Utili, L.; Amadori, R.; Ospitali, F.; Lucarelli, C.; Cavani, F., Insights into the Reaction Mechanism for 5-Hydroxymethylfurfural Oxidation to FDCA on Bimetallic Pd-Au Nanoparticles. *Appl. Catal., A* **2015**, *504*, 408-419.
- (35). Gandini, A.; Belgacem, M. N., Furans in Polymer Chemistry. *Prog. Polym. Sci.* **1997**, *22* (6), 1203-1379.
- (36). Kazi, F. K.; Patel, A. D.; Serrano-Ruiz, J. C.; Dumesic, J. A.; Anex, R. P., Techno-Economic Analysis of Dimethylfuran (DMF) and Hydroxymethylfurfural (HMF) Production from Pure Fructose in Catalytic Processes. *Chem. Eng. J.* **2011**, *169* (1-3), 329-338.
- (37). Iris, K.; Tsang, D. C., Conversion of Biomass to Hydroxymethylfurfural: A Review of Catalytic Systems and Underlying Mechanisms. *Bioresour. Technol.* **2017**, *238*, 716-732.
- (38). Davis, S. E.; Zope, B. N.; Davis, R. J., On the Mechanism of Selective Oxidation of 5-Hydroxymethylfurfural to 2, 5-Furandicarboxylic Acid over Supported Pt and Au Catalysts. *Green Chem.* **2012**, *14* (1), 143-147.
- (39). Ide, M. S.; Davis, R. J., The Important Role of Hydroxyl on Oxidation Catalysis by Gold Nanoparticles. *Acc. Chem. Res.* **2014**, *47* (3), 825-833.

- (40). Lilga, M. A.; Hallen, R. T.; Gray, M., Production of Oxidized Derivatives of 5-Hydroxymethylfurfural (HMF). *Top. Catal.* **2010**, *53* (15-18), 1264-1269.
- (41). Payne, S. M.; Kerton, F. M., Solubility of Bio-Sourced Feedstocks in 'Green'solvents. *Green Chem.* **2010**, *12* (9), 1648-1653.
- (42). Zhang, Z.; Deng, K., Recent Advances in the Catalytic Synthesis of 2, 5-Furandicarboxylic Acid and Its Derivatives. *ACS Catal.* **2015**, *5* (11), 6529-6544.
- (43). Gorbanev, Y. Y.; Klitgaard, S. K.; Woodley, J. M.; Christensen, C. H.; Riisager, A., Gold-Catalyzed Aerobic Oxidation of 5-Hydroxymethylfurfural in Water at Ambient Temperature. *ChemSusChem: Chemistry & Sustainability Energy & Materials* **2009**, *2* (7), 672-675.
- (44). Albonetti, S.; Lolli, A.; Morandi, V.; Migliori, A.; Lucarelli, C.; Cavani, F., Conversion of 5-Hydroxymethylfurfural to 2, 5-Furandicarboxylic Acid over Au-Based Catalysts: Optimization of Active Phase and Metal-Support Interaction. *Applied Catalysis B: Environmental* **2015**, *163*, 520-530.
- (45). Masoud, N.; Donoeva, B.; de Jongh, P. E., Stability of Gold Nanocatalysts Supported on Mesoporous Silica for the Oxidation of 5-Hydroxymethyl Furfural to Furan-2, 5-Dicarboxylic Acid. *Appl. Catal., A* **2018**, *561*, 150-157.
- (46). Gupta, N. K.; Nishimura, S.; Takagaki, A.; Ebitani, K., Hydrotalcite-Supported Gold-Nanoparticle-Catalyzed Highly Efficient Base-Free Aqueous Oxidation of 5-Hydroxymethylfurfural into 2, 5-Furandicarboxylic Acid under Atmospheric Oxygen Pressure. *Green Chem.* **2011**, *13* (4), 824-827.
- (47). Villa, A.; Schiavoni, M.; Campisi, S.; Veith, G. M.; Prati, L., Pd-Modified Au on Carbon as an Effective and Durable Catalyst for the Direct Oxidation of HMF to 2, 5-Furandicarboxylic Acid. *ChemSusChem* **2013**, *6* (4), 609-612.
- (48). Zhu, H.; Ma, Z.; Clark, J. C.; Pan, Z.; Overbury, S. H.; Dai, S., Low-Temperature CO Oxidation on Au/Fumed SiO<sub>2</sub>-Based Catalysts Prepared from Au(en)<sub>2</sub>Cl<sub>3</sub> Precursor. *Appl. Catal., A* **2007**, *326* (1), 89-99.
- (49). Zanella, R.; Giorgio, S.; Henry, C. R.; Louis, C., Alternative Methods for the Preparation of Gold Nanoparticles Supported on TiO<sub>2</sub>. *The Journal of Physical Chemistry B* **2002**, *106* (31), 7634-7642.
- (50). Patil, N.; Uphade, B.; Jana, P.; Bharagava, S.; Choudhary, V., Epoxidation of Styrene by Anhydrous T-Butyl Hydroperoxide over Reusable Gold Supported on MgO and Other Alkaline Earth Oxides. *J. Catal.* **2004**, *223* (1), 236-239.
- (51). Munnik, P.; De Jongh, P. E.; De Jong, K. P., Control and Impact of the Nanoscale Distribution of Supported Cobalt Particles Used in Fischer-Tropsch Catalysis. *J. Am. Chem. Soc.* **2014**, *136* (20), 7333-7340.
- (52). Galkin, K. I.; Krivodaeva, E. A.; Romashov, L. V.; Zalesskiy, S. S.; Kachala, V. V.; Burykina, J. V.; Ananikov, V. P., Critical Influence of 5-Hydroxymethylfurfural Aging and Decomposition on the Utility of Biomass Conversion in Organic Synthesis. *Angew. Chem. Int. Ed.* **2016**, *55* (29), 8338-8342.
- (53). Penhoat, M.; Vanbésien, T.; Cocud, A.; Addad, A.; Vezin, H.; Rolando, C., PtFe Supported Gold Nanoparticles as Photocatalysts for Oxidative Esterification of Aldehydes. *New J. Chem.* **2016**, *40* (11), 9460-9470.
- (54). Palazzo, G.; Valenza, G.; Dell'Aglio, M.; De Giacomo, A., On the Stability of Gold Nanoparticles Synthesized by Laser Ablation in Liquids. *J. Colloid Interface Sci.* **2017**, *489*, 47-56.

- (55). Geoghegan, W. D.; Ackerman, G. A., Adsorption of Horseradish Peroxidase, Ovomuroid and Anti-Immunoglobulin to Colloidal Gold for the Indirect Detection of Concanavalin a, Wheat Germ Agglutinin and Goat Anti-Human Immunoglobulin G on Cell Surfaces at the Electron Microscopic Level: A New Method, Theory and Application. *Journal of Histochemistry & Cytochemistry* **1977**, *25* (11), 1187-1200.
- (56). Sylvestre, J.-P.; Poulin, S.; Kabashin, A. V.; Sacher, E.; Meunier, M.; Luong, J. H., Surface Chemistry of Gold Nanoparticles Produced by Laser Ablation in Aqueous Media. *The Journal of Physical Chemistry B* **2004**, *108* (43), 16864-16869.
- (57). Duval, J. F.; Huijs, G. K.; Threels, W. F.; Lyklema, J.; van Leeuwen, H. P., Faradaic Depolarization in the Electrokinetics of the Metal–Electrolyte Solution Interface. *J. Colloid Interface Sci.* **2003**, *260* (1), 95-106.
- (58). Parks, G. A., The Isoelectric Points of Solid Oxides, Solid Hydroxides, and Aqueous Hydroxo Complex Systems. *Chem. Rev.* **1965**, *65* (2), 177-198.
- (59). Liu, X. Y.; Wang, A.; Zhang, T.; Mou, C.-Y., Catalysis by Gold: New Insights into the Support Effect. *Nano Today* **2013**, *8* (4), 403-416.
- (60). Block, B. P.; Bailar Jr, J. C., The Reaction of Gold (III) with Some Bidentate Coördinating Groups. *J. Am. Chem. Soc.* **1951**, *73* (10), 4722-4725.
- (61). De Jonge, N., Theory of the Spatial Resolution of (Scanning) Transmission Electron Microscopy in Liquid Water or Ice Layers. *Ultramicroscopy* **2018**, *187*, 113-125.
- (62). Woehl, T.; Abellan, P., Defining the Radiation Chemistry During Liquid Cell Electron Microscopy to Enable Visualization of Nanomaterial Growth and Degradation Dynamics. *Journal of microscopy* **2017**, *265* (2), 135-147.

## Supporting Information

### Supporting Movies description

**Movie M1:** (M1\_Au\_TiO2\_H2O): The Au/TiO<sub>2</sub> catalyst being scanned for 1 hour in H<sub>2</sub>O, with only a limited number of particles disappearing and displaying some mobility. During the movie, some very dark spots appear, seem to grow to quite large proportions (typically >25 nm) and then disappear quickly. These are likely partially the result of some form of TiO<sub>2</sub> charging from the electron beam and partially from overlapping TiO<sub>2</sub> crystals, but not Au particles since they also appear in pristine TiO<sub>2</sub>.

**Movie M2:** (M2\_Au\_TiO2\_NaHCO3): The Au/TiO<sub>2</sub> catalyst being scanned for 1 hour in 57 mmol·L<sup>-1</sup> NaHCO<sub>3</sub> in H<sub>2</sub>O. As can be seen, quite a few particles (approximately 45%) disappear instantly, far more than in Movie M1. Mobility is also significantly higher, with particles changing position on the support significantly more often.

**Movie M3:** (M3\_Au\_TiO2\_Na2CO3): The Au/TiO<sub>2</sub> catalyst sample being scanned for 1 hour in 57 mmol·L<sup>-1</sup> Na<sub>2</sub>CO<sub>3</sub> in H<sub>2</sub>O. In this case, almost all particles disappeared after one hour. And again, mobility is significantly higher than in water, with particles changing position on the support significantly more often. Some particles can be seen to shrink before disappearing, indicating some dissolution might take place as well.

Movies can be transferred by the author of this thesis upon request (m.j.meijerink@uu.nl).

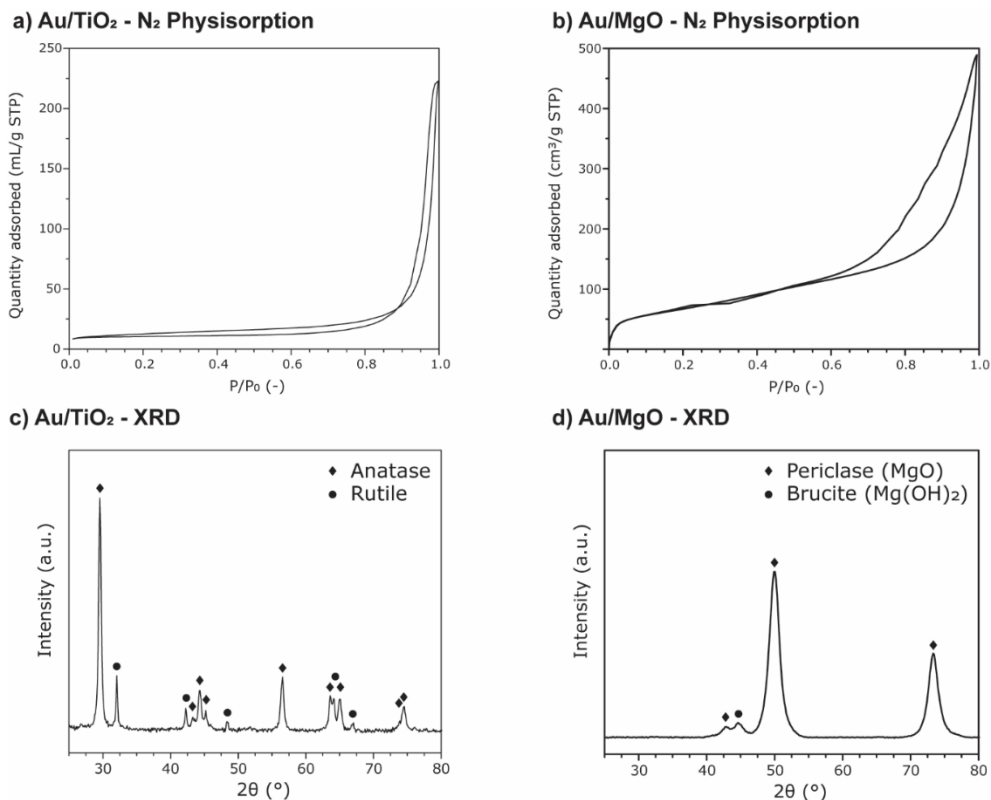
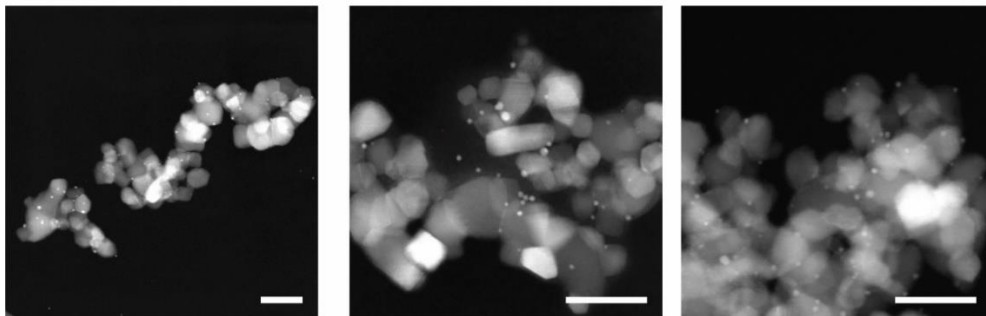


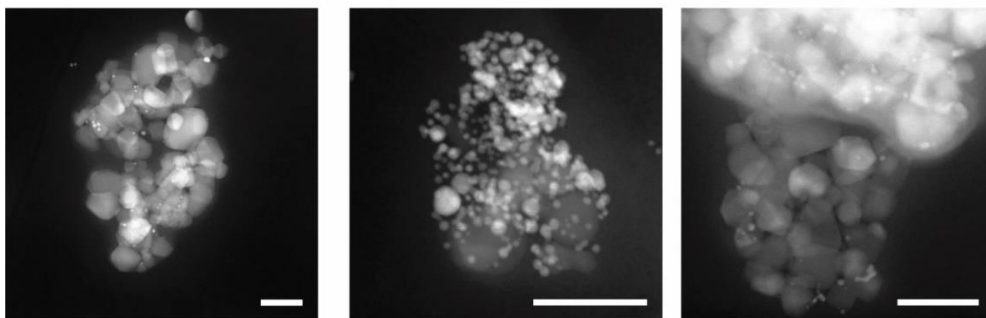
**Figure S5.1.** Nitrogen physisorption isotherms and X-ray diffraction patterns of the Au/TiO<sub>2</sub> (a and c respectively) and the Au/MgO catalyst (b and d respectively). Both catalysts contain the expected crystalline phases, namely anatase and rutile in an approximately 3:1 ratio in the case of the Au/TiO<sub>2</sub> catalyst and periclase in the case of the Au/MgO catalyst. The Au/MgO catalyst also contains some brucite (Mg(OH)<sub>2</sub>), which originates from the reaction of MgO with water during the deposition-precipitation. With our laboratory XRD equipment Au crystalline phases were not observed, predominantly due to the low loading (<1 wt%) and small particle size.



a) Used sample, no base



b) Used sample, no HMF



c) Used sample, no O<sub>2</sub>

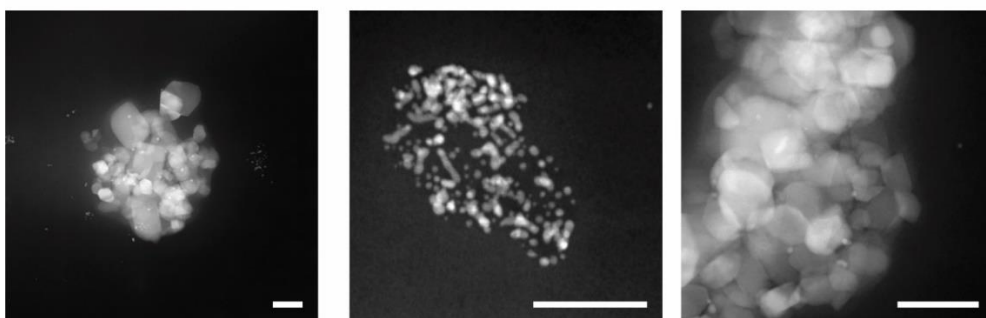


**Figure S5.2.** HAADF-STEM images of each of the used Au/TiO<sub>2</sub> samples (after 24 hours of reaction) of the experiments at 1 bar with one of the main reactant components missing, with (a) the absence of base (but O<sub>2</sub> and HMF still present), (b) the absence of HMF (O<sub>2</sub> and NaHCO<sub>3</sub> present) and (c) the absence of O<sub>2</sub> (NaHCO<sub>3</sub> and HMF present).

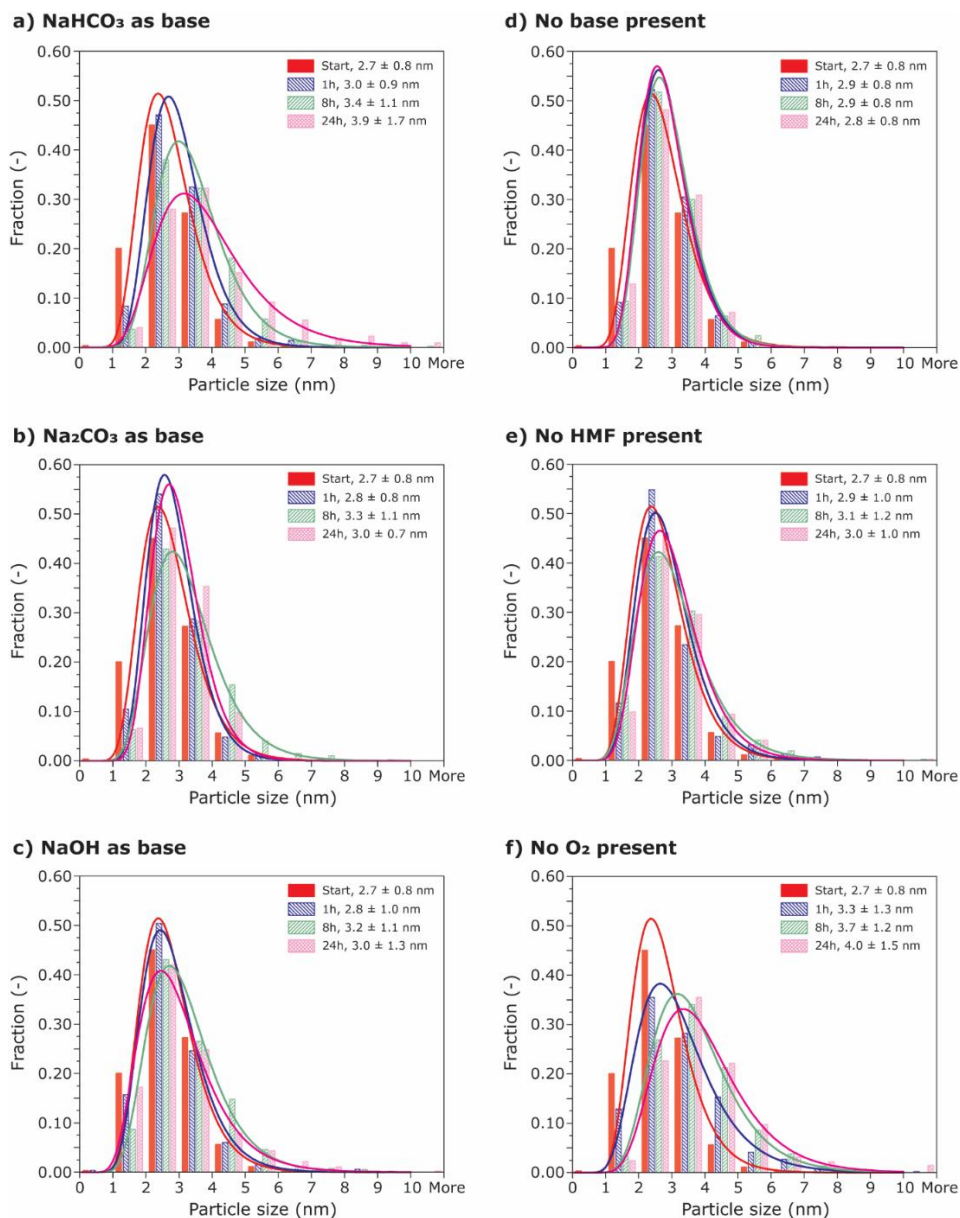


**Figure S5.3.** Comparison of the evolution of the particle size distributions (PSDs) for the Au/TiO<sub>2</sub> catalyst in different experiments at the start and after 1h, 8h and 24h. (a-c) Complete catalytic experiments comparing the use of three different bases, with (a) NaHCO<sub>3</sub>, (b) Na<sub>2</sub>CO<sub>3</sub> and (c) NaOH with the same concentration of base. (d-f) comparison of the PSD evolution when one of the main reactant components is missing, with (d) the absence of base (but O<sub>2</sub> and HMF still present), (e) the absence of HMF (O<sub>2</sub> and NaHCO<sub>3</sub> present) and (f) the absence of O<sub>2</sub> (NaHCO<sub>3</sub> and HMF present).

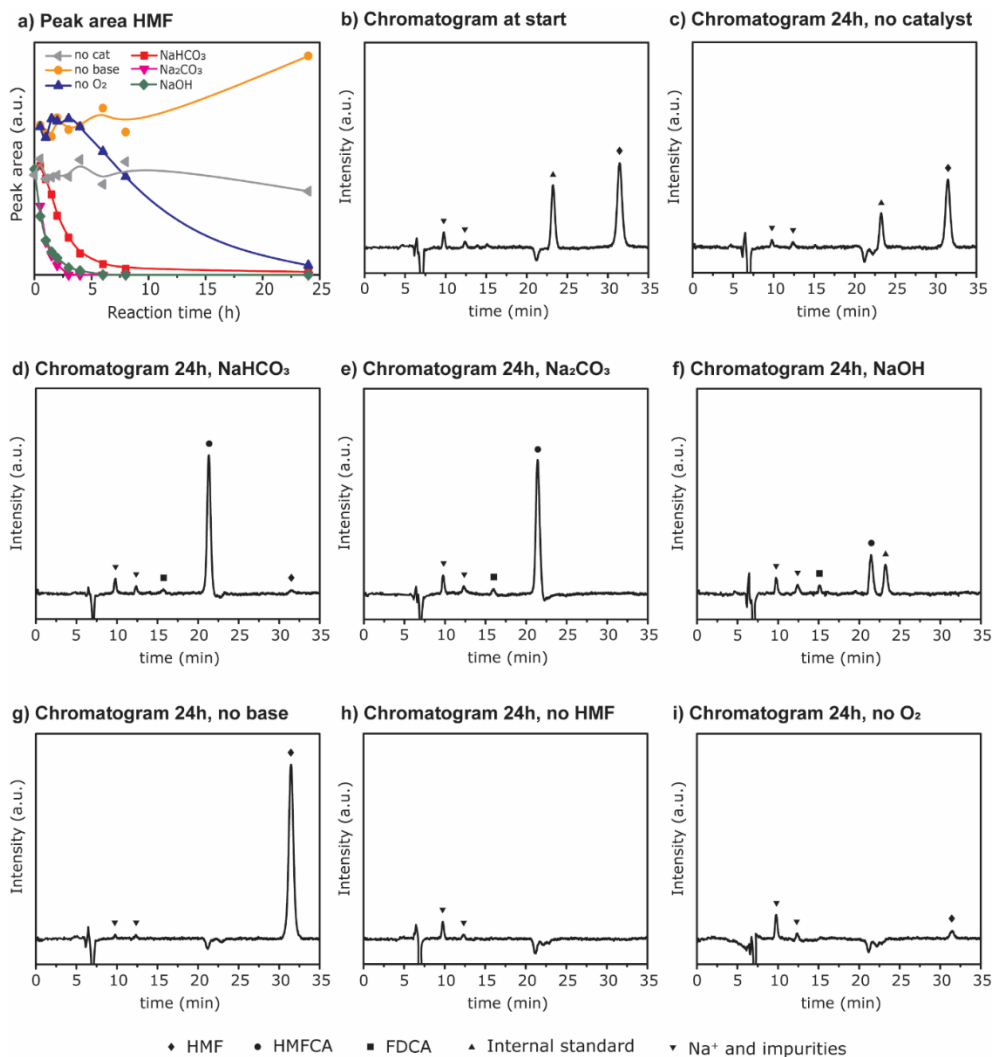


**Figure S5.4.** High pressure liquid chromatography data for the experiments performed at low pressure (1 bar) O<sub>2</sub>, or N<sub>2</sub> in (i), with (a) the peak area of the HMF peak at 32 minutes over time for all experiments with HMF present. Due to problems with the internal standard, the exact concentration could not be determined. (b) Typical chromatogram of the reaction mixture at the start of an experiment. (c-i) Chromatograms of reaction mixtures after 24 hours for all of the different mixtures tested, with (c) the blank experiment without catalyst. (d-f) Complete catalytic experiments comparing the use of three different bases, with (d) NaHCO<sub>3</sub>, (e) Na<sub>2</sub>CO<sub>3</sub> and (f) NaOH with the same concentration of base. (g-i) Comparison of the experiments with one of the main reactant components missing, with (g) the absence of base (but O<sub>2</sub> and HMF still present), (h) the absence of HMF (O<sub>2</sub> and NaHCO<sub>3</sub> present) and (i) the absence of O<sub>2</sub> (NaHCO<sub>3</sub> and HMF present).

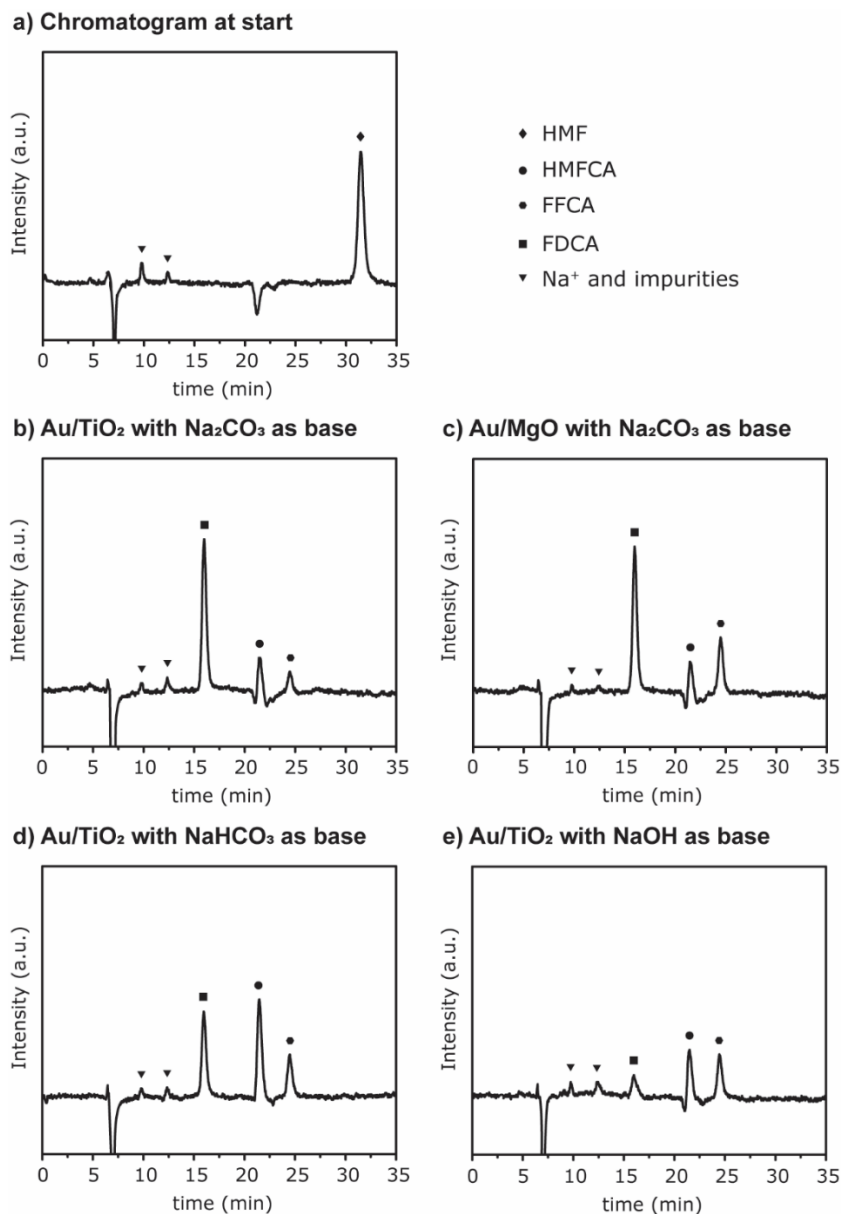


**Figure S5.5.** High pressure liquid chromatography data for the experiments performed at high pressure O<sub>2</sub> (10 bar) with (a) a typical chromatogram of the reaction mixture at the start of an experiment. (b-e) Chromatograms of the reaction mixtures after 24 hours for the different mixtures tested, with a pressure of 10 bar O<sub>2</sub> and a temperature of 80 °C, with (b) and (c) comparing the Au/TiO<sub>2</sub> and Au/MgO catalyst, using Na<sub>2</sub>CO<sub>3</sub> as a base. (d) and (e) present the HPLC where the Au/TiO<sub>2</sub> catalyst was used with the other two bases used in this work, with (d) NaHCO<sub>3</sub> and (e) NaOH as a base respectively.

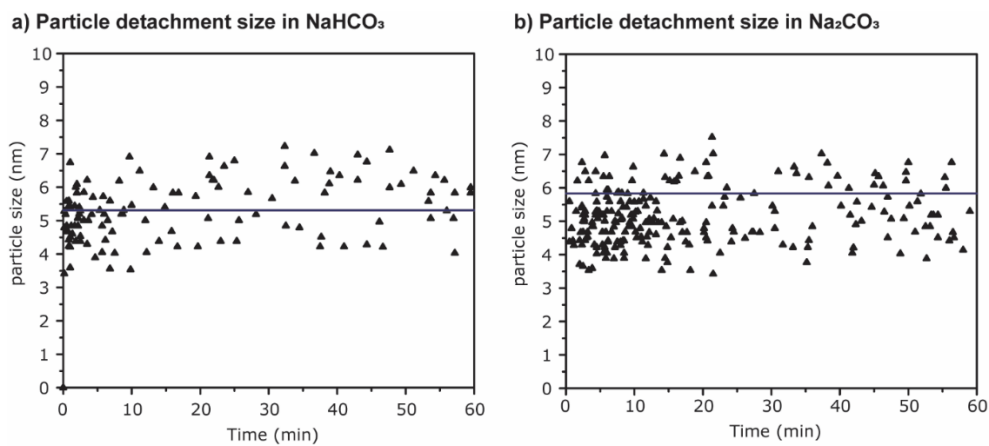


**Figure S5.6.** Overview of the diameter of each measured particle during the LP-TEM experiments at the moment it detaches, along with the corresponding time of disappearance. With (a) the in situ experiment in  $57 \text{ mmol}\cdot\text{L}^{-1} \text{ NaHCO}_3$  and (b)  $57 \text{ mmol}\cdot\text{L}^{-1} \text{ Na}_2\text{CO}_3$ , dissolved in  $\text{H}_2\text{O}$ . Each point in the graph corresponds to a single particle detaching. The solid line corresponds to the median particle diameter at the start.



## **Chapter 6**

### **Summary and Outlook**

## 6.1 Summary

Solid heterogeneous catalysts are materials of high importance for the chemical industry and enable our modern way of life. Obtaining a detailed understanding of these complex materials requires visualization of their structure at many length scales. Due to the resolution limitations of visible light microscopes, electron microscopy is a key technique in visualizing the nanostructures of these catalysts.

Although catalysts are defined as materials that increase the rate of a chemical reaction without being consumed, this does not mean they do not change over long periods of time. In fact, heterogeneous catalysts are typically very dynamic materials and investigating how they change during their synthesis and during their use is of great scientific and technological interest. Transmission electron microscopes (TEMs) have allowed us to study these catalysts in great detail, however, the high vacuum conditions of the instruments prevent the observation of catalysts in contact with liquid or gas. As both the synthesis and use of these materials requires the presence of a liquid and/or gas, investigation of the dynamic processes involved in heterogeneous catalysis has remained a challenge.

Recent advances in microfabrication and MEMS technology have provided ways to overcome these limitations, in particular through enclosing liquids or gases in specialized microscope holders and separating them from the vacuum of the TEM. This strategy introduces new challenges though, as the high-intensity, high-energy electron irradiation now interacts with both the solid sample and the fluid, introducing new electron beam effects and sample damage mechanisms, especially in liquid phase TEM (LP-TEM). As many catalyst synthesis procedures have at least one step involving a liquid and many chemical processes take place in liquid, LP-TEM is potentially a very valuable technique in the field of heterogeneous catalysis.

In this thesis, we have therefore explored the use of LP-TEM in the field of heterogeneous catalysis, first by thoroughly investigating how the electron beam affects catalyst supports in a liquid. This knowledge was subsequently used to study Au/TiO<sub>2</sub> catalyst evolution and deactivation in various aqueous environments.

First, **Chapter 1** provides a general introduction to the field of heterogeneous catalysis and its importance, with gold catalysts and catalyst deactivation being discussed in detail. Furthermore, many aspects of electron microscopy and the main techniques used are explained, along with a detailed discussion of current in situ TEM techniques and the main damage mechanisms.



In **Chapter 2**, the stability of six commonly used oxide catalyst supports in LP-TEM was evaluated, through subjecting the oxides to a controlled electron dose when in contact with water and observing the resulting structural changes. It was found that a correlation exists between the Gibbs free energy of oxide hydration and the extent of structural change and damage observed. Other physio-chemical properties, such as porosity, specific surface area, crystallinity and solubility were shown to be of limited importance. The correlation was also able to rationalize LP-TEM observations of other oxides in literature and allowed for a facile approach to estimate oxide stability in LP-TEM. In addition, it was found that several oxides for which the hydration reaction of both the oxide and the main suboxides was thermodynamically unfavorable, namely  $\text{TiO}_2$ ,  $\text{ZrO}_2$  and  $\text{Nb}_2\text{O}_5$ , were extremely stable. This stability was such that these oxides did not show any structural changes at all during the experiments performed in this study, making them excellent candidates for further LP-TEM experiments.

**Chapter 3** reports the origin of the degradation of one of the less stable oxides studied in Chapter 2, namely  $\text{SiO}_2$ , in more detail. To this end, Stöber silicas with varying degrees of hydroxylation were exposed to a controlled electron dose in water and the change in projected surface area was tracked as a measure of stability. One of the silicas was subsequently also exposed to an aqueous environment with various solutes and to octane and toluene, while again tracking the projected surface area. It was found that the formation of reducing radicals, such as  $\cdot\text{H}$  and  $e^-_{(\text{aq})}$ , through interaction of the electron beam with the liquid, was likely responsible for opening Si-O-Si bonds and the subsequent silica hydroxylation and dissolution. In addition, environmental TEM (ETEM) demonstrated that the presence of even small amounts of water vapor has a significant detrimental effect on silica stability during in situ TEM. Scavenging these reducing radicals in the liquid did however stabilize the silica significantly, providing an approach to study  $\text{SiO}_2$  in LP-TEM.

**Chapter 4** focuses on nanoscale processes involved in Ostwald ripening (OR) of supported metal catalysts in a liquid phase. Through the use of LP-TEM it was possible to image this process in real time at the individual nanoparticle level. Having identified  $\text{TiO}_2$  as a very stable oxide in Chapter 2, this material was used as a support for gold nanoparticles as a model system. Because this catalyst is quite stable in water, but sinters rapidly in the presence of  $\text{Cl}^-$  ions, the sintering behavior was compared in water with and without dissolved NaCl. In situ LP-TEM clearly showed that the growth of Au nanoparticles occurred through a form of OR, whereby particles grew or disappeared, probably via monomer transfer. However, although particle ensemble behavior matched ex situ results and OR predictions very well, at the individual nanoparticle level, the process was found to differ significantly. Most importantly, no clear correlation between the particle size and growth or shrinkage behavior could be

found, in contrast to predictions of classical Ostwald ripening models. In addition, the existence of a significant fraction of inert particles that neither grew, nor shrank, was observed. LP-TEM also showed that particle shrinkage was sudden and seemed to be a stochastic process while particle growth by monomer attachment was slow and likely the rate-determining step for sintering in this system.

**Chapter 5** investigates structural changes of Au/TiO<sub>2</sub> catalysts relevant to the selective oxidation of 5-(hydroxymethyl)furfural (HMF) to 2,5-furandicarboxylic acid (FDCA). This was done by combining in situ liquid phase transmission electron microscopy (LP-TEM) and TEM analysis of laboratory scale experiments to assess the key parameters responsible for the structural changes of an Au/TiO<sub>2</sub> catalyst. These experiments demonstrated that extensive gold particle detachment and subsequent particle coalescence and growth occurred under typical reaction conditions, predominantly as a result of the high pH required in this reaction. It was proposed that the origin of this detachment is the negative charge present on both the gold nanoparticles and the TiO<sub>2</sub> support when the pH is higher than the point of zero charge (PZC) of TiO<sub>2</sub>. It was also shown that using a support with a PZC close to the pH of the reaction mixture (MgO in this work) limited gold nanoparticle detachment. Identification and understanding of these nanoscale changes are critical for improving our knowledge of catalyst evolution and deactivation during liquid phase catalysis and this work demonstrates that LP-TEM can deliver a significant contribution to this effort.

In conclusion, the work in this thesis explores the use of liquid phase transmission electron microscopy for studying dynamic processes taking place in solid heterogeneous catalysts in liquids at the nanoscale. It was clear that the main challenge for successfully studying these materials in LP-TEM is the effect of the electron beam interacting with the liquid and solid, causing degradation of several important oxides, such as SiO<sub>2</sub>, Al<sub>2</sub>O<sub>3</sub> and MgO. Possible strategies to mitigate this were found and include the use of lower electron dose rates, the use of more stable oxides (TiO<sub>2</sub>, ZrO<sub>2</sub> and Nb<sub>2</sub>O<sub>5</sub> in this work) and in the case of SiO<sub>2</sub>, the use of radical scavengers to lower the concentration of reducing radicals the oxide is exposed to. Despite great challenges, using gold nanoparticles supported on TiO<sub>2</sub> as a model catalyst proved successful to study liquid phase Ostwald ripening and to study the structural changes of this catalyst relevant for the selective oxidation of HMF. Through the use of LP-TEM combined with laboratory experiments, novel insights in both of these processes was obtained. In addition, this work also provides new strategies and clues for other studies on synthesis and evolution of solid heterogeneous catalysts in liquid phase.

## 6.2 Outlook

Of particular interest for future study is the use of LP-TEM for following catalyst synthesis in a liquid phase. The synthesis of almost all heterogeneous catalysts involves at least one liquid phase step. This holds in particular for the catalyst synthesis methods most commonly used in industry, namely coprecipitation, deposition-precipitation, impregnation and hydrothermal synthesis. These processes are not always well-understood at the nanoscale and LP-TEM can yield very useful information to improve these processes. An interesting example would be the coprecipitation/deposition-precipitation of nickel (hydr)oxide on silica, which forms nickel phyllosilicate platelets with a structure that is very different from the original silica. It is currently believed that the silica dissolves and then precipitates again together with nickel as a phyllosilicate, but many details are still unknown. In situ observations could improve our knowledge of how these platelets exactly form and could aid in more precise control over the synthesis procedure to prepare better catalysts.

This in situ investigation work could of course also be extended to many other coprecipitation and deposition-precipitation processes. A group of examples could be the synthesis of supported noble metal catalysts, in particular gold based catalysts, which are very often prepared through (reductive) deposition-precipitation. Ion adsorption processes in combination with liquid phase reduction, especially of noble metals, is another area that could benefit from LP-TEM investigations to optimize the synthesis and minimize the required amount of expensive precious metal. Here it is even more important to consider the electron beam effects, as noble metal ions are very easily reduced by the electron beam, possibly altering the synthesis mechanism.

Possible solutions to these challenges with electron beam effects could also be the rapid development of new technologies in the EM field. Recent advances in aberration correction and (direct detection) cameras already allowed for major improvements in image resolution and faster image acquisition. Utilization of this technology for LP-TEM experiments could already lower the required electron dose significantly and/or increase the attainable resolution (both spatial and temporal) and new developments in EM technology would likely allow for even lower doses/higher resolution. In addition, development and use of rapid Electron Energy Loss Spectroscopy and EDX in LP-TEM could yield very valuable chemical information, allowing for example information on the composition of solid phases being formed during catalyst synthesis, among many other very interesting applications. Another promising line of investigation could be to follow up on the work described in chapter 5 on the catalyst evolution/deactivation relevant to the selective oxidation of HMF. The same

techniques are relatively easy to apply to other biomass processing systems taking place in an aqueous phase and could yield valuable insights on catalyst evolution during these reactions. Several other types of reactions taking place in a slurry-type reactor could also be mimicked in an LP-TEM environment and the catalyst investigated. Here it might be more challenging to translate the results well to large-scale applications though, especially considering the pressure limitations of the current LP-TEM systems ( $\leq 1.5$  bar).

The recent availability of new electrochemical liquid cell holders also allows for investigating many electrochemical reactions and observing how nanomaterials behave in such an environment. This is very promising for investigation of electrocatalysts and how their evolution depends on both the chemical environment and electrical parameters, such as the effect of the current density. In addition, this system had been used to study the electrochemical deposition of lithium metal for Li-ion batteries. Extending this work to other types of electrochemical deposition and investigation of various battery materials is also very promising. Obtaining more insight in these processes might allow for significant improvements in battery design, currently an important topic with many practical applications.

Related to the study of materials other than catalysts, although electron beam damage is generally to be avoided, in some cases it could be very useful. One field where this could be the case is the study of materials for nuclear applications. The extremely high radiation doses encountered in LP-TEM are able to mimic several years of nuclear reactor ionizing radiation exposure in mere hours. In addition, nanoscale information on material evolution is readily available, making it a very promising tool for the study of material degradation in many applications where materials are exposed to ionizing radiation while in contact with a liquid.

Finally, the availability of holders to perform gas phase TEM (GP-TEM) in a similar system is also an area of research that can answer many fundamental questions regarding catalyst synthesis, activation and catalysis. Following the reduction and/or particle formation of many supported metal catalysts during the gas phase treatment that often follows liquid phase steps, is also an important step in determining the final structure of many catalysts. Again, information at the nanoscale is limited in many cases and using GP-TEM to follow these steps can aid in improving thermal treatments to prepare better catalysts. In addition, observing the structure of catalysts during gas phase reactions and how they change can yield a lot of information on the active phase of the catalyst and the reaction mechanisms of a catalytic reaction. In short, the use of various types of in situ TEM can greatly benefit the field of heterogeneous catalysis and materials science in general.

## Nederlandse samenvatting

De meeste mensen kennen een katalysator vooral als een (vrij prijzig) onderdeel van een auto, maar er bestaan verschillende soorten katalysatoren die allen zeer belangrijk zijn voor de moderne maatschappij. Een katalysator is, volgens een klassieke definitie, een stof die een chemische reactie sneller en efficiënter laat verlopen zonder zelf verbruikt te worden. Het meest gebruikte type katalysator is de zogenaamde heterogene katalysator. Dit is meestal een heel fijn verdeelde vaste stof; moleculen in een vloeistof of gas kunnen zich hechten aan het oppervlak van dit materiaal, daar reageren tot andere moleculen en daarna weer loslaten. Dit soort katalysatoren hebben veel verschillende toepassingen en worden daarom op veel verschillende plekken gebruikt. Bijvoorbeeld in een auto om schadelijke gassen uit de motor, zoals koolstofmonoxide, stikstofoxiden en onverbrande benzine, om te zetten in veel minder schadelijke stoffen. Maar ze worden ook gebruikt in de chemische industrie om producten zoals medicijnen, kunstmest, plastic, waterstof, verf en vele andere chemicaliën te produceren.

Heterogene katalysatoren zijn vaak bijzonder ingewikkelde materialen. De belangrijkste reden hiervoor is dat de reactie alleen op het oppervlak van de katalysator plaats kan vinden en daarom is het belangrijk om het beschikbare oppervlak zo groot mogelijk te maken. De meest gebruikelijke manier om dat te doen is door de katalysatordeeltjes zo klein mogelijk te maken. De grootte van deze deeltjes ligt over het algemeen tussen de 1 en 20 nanometer en ze heten daarom ook nanodeeltjes. Eén nanometer is één miljardste van een meter, ongeveer 100 000 keer dunner dan een menselijke haar of ongeveer 5 atomen op een rij. Zulke kleine deeltjes zijn beweeglijk en lastig te scheiden van de vloeistoffen of gassen met reactanten en producten. Om dit op te lossen worden de nanodeeltjes vastgezet op een dragermateriaal, zoals silica ( $\text{SiO}_2$ ), alumina ( $\text{Al}_2\text{O}_3$ ), titania ( $\text{TiO}_2$ , voor zover we weten zijn er geen feeënkoninkinnen betrokken bij katalyse) of koolstof/actieve kool (C).

Ondanks het feit dat een katalysator niet snel verbruikt wordt tijdens een chemische reactie, verandert het materiaal wel na verloop van tijd, meestal op een manier waardoor de katalysator slechter gaat werken. Om beter te begrijpen hoe dit werkt, is het belangrijk om de katalysator en het proces zichtbaar te maken. Dit is alleen niet zo makkelijk, want de resolutie die een lichtmicroscop kan halen is bij lange na niet genoeg om zulke kleine deeltjes zichtbaar te maken. Daarom moeten we een speciale microscoop gebruiken, namelijk een elektronenmicroscop. Dit apparaat gebruikt een bundel van elektronen in plaats van licht om een preparaat te “zien” en de beste elektronenmicroscopen zijn zelfs in staat om individuele atomen zichtbaar te maken.

De interacties van elektronen met materialen zijn alleen wel iets anders en vooral veel sterker dan de interacties van licht met materialen. Om te zorgen dat de elektronen niet afgebogen worden door gasmoleculen tussen de elektronenbron, het preparaat en de elektronendetector, moeten de metingen in hoog vacuüm gedaan worden met hele dunne preparaten. Omdat er ook een gas of een (verdampende) vloeistof aanwezig moet zijn voor katalyse, is het daardoor normaal gesproken niet mogelijk om een katalysator te bekijken terwijl de reactie verloopt, ook wel *in situ* observatie genoemd. Dat maakt het erg lastig om te zien hoe de katalysator verandert tijdens de reactie en is het moeilijk om erachter te komen wat er precies voor zorgt dat de katalysator minder goed gaat werken.

Gelukkig bieden de recente technologische ontwikkelingen op het gebied van microfabricage nieuwe mogelijkheden om katalysatoren wel *in situ* te bekijken. De belangrijkste ontwikkeling is die van een speciale preparaathouder die volledig afgesloten kan worden van het vacuüm van de elektronenmicroscopie. Daardoor is het alsnog mogelijk om kleine hoeveelheden katalysator te bekijken in de aanwezigheid van een vloeistof of gas. Omdat deze techniek relatief nieuw is, zijn er nog veel vragen over een aantal praktische aspecten. De belangrijkste vragen gaan over wat het effect van de elektronenbundel is op de processen die bekeken worden en hoe de bundel de katalysator kan beschadigen. Deze vragen zijn in het bijzonder belangrijk voor katalysatoren in contact met een vloeistof, waarbij de elektronenbundel ook veel interactie heeft met de vloeistof. Hierdoor worden in de vloeistof ook veel reactieve moleculen gevormd, die de katalysator aan kunnen tasten.

Dit proefschrift gaat daarom over het gebruik van vloeistoffase (*in situ*) elektronenmicroscopie, ook wel: 'liquid phase transmission electron microscopy' (LP-TEM) genoemd, om katalytische materialen te onderzoeken. Eerst hebben we gekeken naar de effecten van de elektronenbundel op verschillende belangrijke dragermaterialen in contact met waterige oplossingen. Deze kennis is daarna gebruikt om de veranderingen van een katalysator, namelijk goud nanodeeltjes afgezet op titania als dragermateriaal, te onderzoeken in verschillende waterige oplossingen. Dit is als volgt beschreven in de verschillende hoofdstukken van dit proefschrift:

In **hoofdstuk 1** geven we een inleiding van de verschillende onderwerpen in dit proefschrift, waaronder een introductie van de twee belangrijkste aspecten in dit proefschrift, namelijk heterogene katalyse en elektronenmicroscopie. Verder wordt er beschreven hoe een heterogene katalysator kan veranderen en is er een gedetailleerd overzicht van op goud gebaseerde katalysatoren. Bij de elektronenmicroscopie wordt er vooral ingegaan op de verschillende vormen en technieken die beschikbaar zijn en

worden de verschillende typen in situ elektronenmicroscopie besproken, gevolgd door een overzicht van de belangrijkste beschadigingsmechanismen.

In **Hoofdstuk 2** wordt de stabiliteit van verschillende dragermaterialen vergeleken tijdens LP-TEM in water. Hierbij zijn de dragers  $\text{SiO}_2$ ,  $\text{TiO}_2$ ,  $\text{Al}_2\text{O}_3$ ,  $\text{MgO}$ ,  $\text{ZrO}_2$  en  $\text{Nb}_2\text{O}_5$  blootgesteld aan een grote hoeveelheid elektronen gedurende 1 uur en werd er gekeken naar hoe de materialen veranderden en welk deel van het materiaal oploste. We konden laten zien dat er een groot verschil was in stabiliteit van de verschillende dragers en dat  $\text{TiO}_2$ ,  $\text{ZrO}_2$  en  $\text{Nb}_2\text{O}_5$  geen zichtbare beschadigingen opliepen gedurende het hele experiment. De andere 3 oxides waren niet zo stabiel en losten op, maar er was een groot verschil in de snelheid waarmee ze oplosten. Die oplossnelheid heeft ook een correlatie met de mate waarin het oxide met water kan reageren tot een hydroxide. Verrassend genoeg bleken materiaaleigenschappen zoals porositeit, kristalstructuur en oplosbaarheid geen invloed te hebben op de oplossnelheid.

In **Hoofdstuk 3** kijken we in detail naar waar de beschadigingen van  $\text{SiO}_2$  in LP-TEM precies vandaan komen. Omdat de invloed van de meeste materiaaleigenschappen beperkt was, hebben we kleine silicaballetjes blootgesteld aan de elektronenbundel in verschillende oplossingen en opnieuw de oplossnelheid gevolgd. Hier konden we de invloed van de interactie van de elektronenbundel met de oplossing uit afleiden en bepalen welke reactieve moleculen mogelijk verantwoordelijk zijn voor aantasting van  $\text{SiO}_2$ . Dit bleken zogenoemde reducerende radicalen te zijn, zoals losse waterstofatomen en opgeloste elektronen. Waarschijnlijk zijn deze radicalen verantwoordelijk omdat ze in staat zijn om de sterke silicium-zuurstof bindingen open te breken, waardoor het oxide oplost in de vloeistof. Dit onderzoek laat ook zien dat  $\text{SiO}_2$  te stabiliseren is door het toevoegen van 'radical scavengers', moleculen die deze radicalen kunnen afvangen voordat de radicalen met  $\text{SiO}_2$  reageren.

In **Hoofdstuk 4** gebruiken we een van de stabiele dragermaterialen die we in Hoofdstuk 2 gevonden hebben, namelijk  $\text{TiO}_2$ , als drager voor goud nanodeeltjes. Deze katalysator hebben we gebruikt als modelsysteem om een van de belangrijkste processen waardoor een katalysator minder actief wordt, te volgen. Dit proces heet Ostwaldvergroving en zorgt ervoor dat de deeltjes langzaam groter worden doordat sommige deeltjes oplossen en de goudatomen weer neerslaan op andere deeltjes. Voor goudkatalysatoren gaat dit vrij langzaam in water en daarom is er ook natriumchloride (keukenzout) toegevoegd, omdat chloride-ionen het groeiproces flink versnellen. Met behulp van LP-TEM konden we zien dat de nanodeeltjes drie verschillende typen gedrag konden vertonen, namelijk groeien, krimpen of niet van grootte veranderen. Dat laatste is erg onverwacht, want er werd aangenomen dat een deeltje altijd van grootte verandert tijdens Ostwaldvergroving. Verder zagen we dat het groeien een

heel langzaam proces was, maar dat deeltjes heel snel krimpen en verdwijnen op het moment dat ze beginnen met krimpen. Wat ook verrassend is, is dat de grootte van de deeltjes niet uit lijkt te maken voor het bepalen van het gedrag dat ze vertonen, terwijl er altijd aangenomen werd dat alleen de kleinere deeltjes krimpen en alleen de grotere deeltjes groeien.

In **Hoofdstuk 5** bestuderen we de veranderingen van de katalysator in Hoofdstuk 4 die relevant zijn voor de katalyse van een chemische reactie, namelijk de selectieve oxidatie van 5-(hydroxymethyl)furfural (HMF) naar 2,5-furaandicarbonzuur (FDCA). Met behulp van een combinatie van LP-TEM met TEM-analyse van monsters uit het reactiemengsel konden we zien dat een groot deel van de goud nanodeeltjes loslaten van de drager en daarna samenklonteren. De belangrijkste oorzaak hiervan was de aanwezigheid van een base, die er vermoedelijk voor zorgt dat zowel de gouddeeltjes als het  $\text{TiO}_2$  dragermateriaal een negatieve elektrische lading krijgen. Doordat negatieve ladingen elkaar afstoten, laten de nanodeeltjes los en krijgen ze de kans om in de vloeistof samen te klonteren. Bij het gebruik van een andere drager die minder snel een negatieve elektrische lading krijgt, namelijk  $\text{MgO}$ , laten minder deeltjes los. Dit laat ook goed zien dat LP-TEM veel potentie heeft voor het onderzoeken van katalysatoren in een vloeistoffase.

**Hoofdstuk 6** bevat een korte Engelse samenvatting en bespreekt enkele mogelijke richtingen voor vervolgonderzoek waarbij in situ elektronenmicroscopie en in het bijzonder LP-TEM een belangrijke bijdrage kunnen leveren aan het veld van heterogene katalyse.



## List of Abbreviations

BF	Bright Field
DF	Dark Field
EDX	Energy-Dispersive X-ray spectroscopy
EELS	Electron Energy Loss Spectroscopy
EM	Electron Microscopy/Microscope
ETEM	Environmental Transmission Electron Microscopy/Microscope
FCC	Fluid Catalytic Cracking
FDCA	2,5-furandicarboxylic acid
FFCA	5-Formyl-2-furancarboxylic acid
HAADF	High Angle Annular Dark Field
HMF	5-(hydroxymethyl)furfural
HMFA	5-hydroxymethyl-2-furancarboxylic acid
HPLC	High Performance Liquid Chromatography
ICP-AES	Inductively Coupled Plasma Atomic Emission Spectroscopy
LP(-TEM)	Liquid Phase (Transmission Electron Microscopy)
LSW	Lifshitz-Slyozov-Wagner (model)
MCS	MicroSuperCapacitor
MEMS	MicroElectroMechanical System
OR	Ostwald Ripening
PDC	Particle Diffusion and Coalescence

## **Chapter 6**

---

PSD	Particle Size Distribution
PZC	Point of Zero Charge
SEM	Scanning Electron Microscopy/Microscope
SMSI	Strong Metal-Support Interaction
STEM	Scanning Transmission Electron Microscopy
TEM	Transmission Electron Microscopy/Microscope
TGA	Thermogravimetric Analysis
XRD	X-ray Diffraction

## List of Publications and Presentations

### Publications

This thesis is based on the following publications:

Meijerink, M. J.; De Jong, K. P.; Zečević, J. Assessment of Oxide Nanoparticle Stability in Liquid Phase Transmission Electron Microscopy. *Nano Res.* **2019**, *12*, 2355-2363.

Meijerink, M. J.; Spiga, C.; Hansen, T. W.; Damsgaard, C. D.; De Jong, K. P.; Zečević, J. Nanoscale Imaging and Stabilization of Silica Nanospheres in Liquid Phase Transmission Electron Microscopy. *Part. Part. Syst. Charact.* **2019**, *36*, 1800374.

Meijerink, M. J.; de Jong, K. P.; Zečević, J. Growth of Supported Gold Nanoparticles in Aqueous Phase Studied by in Situ Transmission Electron Microscopy. *J. Phys. Chem. C* **2020**, *124*, 2202-2212.

Meijerink, M. J.; Lan, Z. Z.; Donoeva, B.; de Jong, K. P.; Zečević, J. Advanced transmission electron microscopy study of structural changes in gold catalysts relevant for the oxidation of HMF. *In preparation*

### Other Publications by the Author

Sartipi, S.; Alberts, M.; Meijerink, M. J.; Keller, T. C.; Pérez-Ramírez, J.; Gascon, J.; Kapteijn, F. Towards Liquid Fuels from Biosyngas: Effect of Zeolite Structure in Hierarchical-Zeolite-Supported Cobalt Catalysts. *ChemSusChem* **2013**, *6*, 1646-1650.

Sun, X.; Suarez, A. I. O.; Meijerink, M.; Van Deelen, T.; Ould-Chikh, S.; Zečević, J.; De Jong, K. P.; Kapteijn, F.; Gascon, J. Manufacture of Highly Loaded Silica-Supported Cobalt Fischer-Tropsch Catalysts from a Metal Organic Framework. *Nature Communications* **2017**, *8*, 1-8.

Carabat, A.; Meijerink, M.; Brouwer, J.; Kelder, E.; van Ommen, J.; van der Zwaag, S.; Sloof, W. Protecting the MoSi<sub>2</sub> Healing Particles for Thermal Barrier Coatings Using a Sol-Gel Produced Al<sub>2</sub>O<sub>3</sub> Coating. *J. Eur. Ceram. Soc.* **2018**, *38*, 2728-2734.

## Presentations

### Oral Presentations

Stability of catalyst supports in liquid phase TEM. Meijerink, M. J.; de Jong, K. P.; Zečević, J., 18<sup>th</sup> Netherlands' Catalysis and Chemistry Conference (NCCC), Noordwijkerhout, the Netherlands, 2017.

Stability of Silicon Dioxide in Liquid Phase TEM. Meijerink, M. J.; de Jong, K. P.; Zečević, J., Microscopy and Microanalysis 2017 (M&M 2017), St. Louis, Missouri, USA, 2017.

Nanoscale Transmission Electron Microscopy Imaging of Oxides in Liquid. Meijerink, M. J.; de Jong, K. P.; Zečević, J., Chemistry of Innovating Science (CHAINS), Veldhoven, the Netherlands, 2017.

Ostwald Ripening at the Individual Nanoparticle Level: In Situ TEM of TiO<sub>2</sub> Supported Gold Nanoparticle Growth. Meijerink, M. J.; de Jong, K. P.; Zečević, J., 20<sup>th</sup> Netherlands' Catalysis and Chemistry Conference (NCCC), Noordwijkerhout, the Netherlands, 2019.

Catalyst Particle Growth at the Nanoscale: In Situ TEM of TiO<sub>2</sub> Supported Gold Nanoparticle Growth. Meijerink, M. J.; de Jong, K. P.; Zečević, J., 26<sup>th</sup> North American Catalysis Society Meeting (NAM2019), Chicago, Illinois, USA, 2019.

Catalyst Particle Growth at the Nanoscale: In Situ TEM of TiO<sub>2</sub> Supported Gold Nanoparticle Growth. Meijerink, M. J.; de Jong, K. P.; Zečević, J., 14<sup>th</sup> European Congress on Catalysis (EuropaCat 2019), Aachen, Germany, 2019.

### Poster Presentations

Catalyst Support Stability in Liquid Phase TEM. Meijerink, M. J.; de Jong, K. P.; Zečević, J., 19<sup>th</sup> Netherlands' Catalysis and Chemistry Conference (NCCC), Noordwijkerhout, the Netherlands, 2018.

Assessment of Oxide Nanoparticle Stability in Liquid Phase TEM. Meijerink, M. J.; de Jong, K. P.; Zečević, J., 4<sup>th</sup> International Conference on In Situ and Correlative Electron Microscopy (CISCeM), Saarbrücken, Germany, 2018.

## Acknowledgements

Exploring the universe and contributing even a little to understanding how it works is a great pleasure and I am very grateful that I had the opportunity to do so in the Inorganic Chemistry and Catalysis group during the past four years. Of course, doing research and writing a PhD thesis is a challenging task that cannot be done without the support and inspiration of many people and I would like to thank all of them here.

Allereerst wil ik graag mijn promotor Krijn en copromotor Jovana hartelijk bedanken voor de mogelijkheid om mijn onderzoek bij ICC te doen. Heel erg bedankt ook voor alle ondersteuning, ideeën en ook de vrijheid om te onderzoeken wat mij het interessantste leek. Maar ook heel erg bedankt voor jullie hulp bij en begrip voor de moeilijke persoonlijke omstandigheden waar ik mee te maken kreeg in de afgelopen jaren.

Beste Krijn, hartelijk bedankt voor de mogelijkheid om bij jou te promoveren en voor het begeleiden van mijn project. Jouw goede input (en ook tegengas op de juiste momenten) hebben er mede voor gezorgd dat ik dit project tot een goed einde heb weten te brengen. Ik heb heel veel van je geleerd, onder andere tijdens het (werk)college geven en onze overlegmomenten (die regelmatig enigszins off-topic gingen) en ook vanwege alle kansen die je me gegeven hebt om mijn werk te presenteren op conferenties en te publiceren. Hartelijk bedankt voor de fijne samenwerking!

Dear Jovana, I would also like to thank you a lot for giving me the opportunity to work on this project and all your support, guidance and knowledge! Your door was always open for a short (coffee/tea) meeting and your wealth of knowledge about electron microscopy that you shared has helped me tremendously. You were also always very careful with your PhD students to make sure we didn't do too many stupid things (no, I am not cold, despite me having left my coat at my desk while standing outside in midwinter...) Just like your co-promotor was a great "catalyst" for you during your PhD research, so were you for me during my PhD research. Thank you again and it was a pleasure working with you!

Zonder de grote inzet van de technici zou zo'n beetje elk PhD onderzoek in het honderd lopen en mijn onderzoek is daar geen uitzondering op. Ik wil in het bijzonder Hans en Chris bedanken voor al hun hulp met de elektronenmicroscopie en voor het vrijdelen van al mijn pogingen de Talos (per ongeluk!) te slopen. Hans, je staat al in de acknowledgements van alle experimentele hoofdstukken in dit proefschrift, maar nogmaals bedankt voor zowel alle technische hulp als voor de gezelligheid! Een "kort"

gesprekje/kopje koffie halen met jou en Chris was altijd leuk, ook al ging het regelmatig iets langer door dan gepland.

Uiteraard wil ik ook graag de andere technici bedanken voor hun hulp. Pascal, hartelijk bedankt voor alle hulp met de HPLC, bestellen van spullen en de gezellige gesprekken (en de heerlijke sarcastische opmerkingen af en toe). Ad van der Eerden, bedankt voor de hulp met de autoclaven en zorgen voor de veiligheid in de laboratoria. En natuurlijk ook AdM, Dennie, Fouad, Herrick, Jan-Willem, Marjan, Oscar en Ramon hartelijk bedankt voor jullie hulp en gezellige (lunch)gesprekken. Ook de ondersteuning van het secretariaat is onmisbaar en daarom wil ik ook Dymph, Ilonka, Iris, Monique en alle anderen bedanken voor hun hulp (en flexibiliteit als ik weer eens last minute een laser pointer nodig had).

Vloeistoffase TEM kan op zijn tijd ook erg moeilijk en frustrerend zijn en daarom ben ik heel blij dat ik daar niet alleen in stond. Nynke in het bijzonder hartelijk bedankt voor al jouw hulp, inclusief het mij (af en toe letterlijk) opvegen van de grond. Ik weet dat dat niet makkelijk voor je was en ben je heel erg dankbaar daarvoor, maar ook voor al jouw vrolijkheid, gezelligheid en zorgzaamheid! Lars, jij ook enorm bedankt voor al jouw hulp, samenwerking, gezelligheid en helpen met het verzinnen van backupplannen voor als mijn PhD zou mislukken, die ik zonder jou en Nynke waarschijnlijk hard nodig gehad zou hebben.

Voor de vloeistoffase TEM wil ik ook graag de LP-TEM onderzoekers van Soft Condensed Matter bedanken voor hun hulp, vragen, discussies en adviezen. Alfons en Marijn, hartelijk bedankt voor jullie vragen en ideeën en dat jullie onderdeel willen zijn van mijn promotiecommissie. Albert, Tom, Sina, Wiebke and Wessel, thank you for your ideas, questions and practical help with (heating) LP-TEM.

I would also like to thank the other members of the TEM team of the ICC group, Giorgio, Haissam, Johan, Lisette, Nienke, Oscar, Petra, Savannah, Tom and Wouter for both the scientific discussions and enjoyable company. Savannah, also thanks for your great organizational skills and your delicious cookie bribery to make us join the TEM meetings. And Giorgio, thank you for being Giorgio :p

Tijdens mijn onderzoek heb ik ook studenten mogen begeleiden, die ik ook graag wil bedanken voor hun bijdrage aan dit proefschrift. Sanne, bedankt voor jouw harde werk en doorzettingsvermogen met een project dat achteraf veel pittiger bleek dan dat het in de eerste instantie leek. Desondanks heb je dat onderzoek toch tot een succesvol einde weten te brengen. Zhou Zhou, jij ook heel erg bedankt voor je harde werk en succesvolle project, dat uiteindelijk een belangrijke bijdrage heeft geleverd

aan het laatste experimentele hoofdstuk van dit proefschrift. Het was erg leuk om jullie beiden te begeleiden en nogmaals bedankt voor de inzet en gezelligheid.

During the last few years, I also had the opportunity to work together with several people from other research groups. I would therefore also like to thank Jorge, Freek, Xiaohui, Alma and Samy from Delft University of Technology for the very nice collaboration investigating Co/SiO<sub>2</sub> catalysts prepared from metal-organic frameworks. And I would like to thank Cristiano, Thomas and Christian from the Technical University of Denmark for the very nice work on Stöber silica stability in the presence of an electron beam that we did together.

I would also like to thank the other scientific staff of ICC for their nice discussions and help. Petra, thank you for all your help and ideas and I enjoyed working, teaching and talking with you a lot. Florian, thank you for the nice talks we had and not getting crazy (and even giving some ideas/suggestions) when Jovana and I were discussing for a long time after I came into the office with what I thought was a short question. Baira, thank you for the very nice collaboration and your support and ideas. Peter, thank you for your support and ideas and the nice company during borrels and lunches. Also thanks to Bert, Eelco, Frank, Freddy, Gareth, Pieter, Robin and Wart for their advice and contributions.

In addition to all the science, I would also like to thank all the people that made my time at the ICC group so enjoyable. First of all, thanks to my open office neighbors Jogchum, Jochem, Nynke, Marisol, Nikos, Haissam and Daan. Second, thanks to my fellow BorrelCie buddy Jochem for all the nice borrels that we prepared and had together and thanks to our BorrelCie predecessors Jelle and Ramon and our successors Francesco, Johan and Max. Furthermore, I would like to thank my fellow teaching assistants for the enjoyable times during the teaching we did together, especially Tom, who I'm sure will definitely be missing drinking all those delicious chococino's together, and Savannah, but also Nynke, Wouter, Marisol, Remco and Laura.

I would also like to thank the people for the great times I've had with all the lunches, broodjes Tricolore (thanks to Fouad, Ramon and Wouter for organizing them!), conferences, barbecues, borrels, coffee breaks, courses, dinners, labuitjes and parties with everyone, so thank you Ana, Anne-Eva, Baira, Bas, Beatriz L, Beatriz S, Carlos, Carolien, Caroline, Charlotte, Christa, Christia, Donglong, Egor, Erik, Federica, Fouad, Francesco, Giorgio, Guusje, Haissam, Hideto, Ilse, Ioannes, Iris, Ivan, Jelle, Jeroen, Jessi, Jochem D, Jochem W, Joel, Jogchum, Johan, Joris, Justine, JX, Kang, Katarina, Katinka, Koen, Lars, Laura B, Laura K, Laurens, Lee, Lennart, Lisette, Luc, Luke, Maarten, Manuel, Marianna, Marisol, Marjolein, Matteo, Max, Miguel, Nazila, Nienke, Nikos, Nynke, Oscar BC, Oscar K, Pascal, Peter B, Peter N, Petra J, Petra K, Ramon,

Remco, Rolf, Romy, Roozbeh, Roxana, Roy, Sam, Sander, Savannah, Silvia, Sophie, Stanislav, Stijn, Suzan, Suzanne, Thomas, Tom Daley, Tom van Deelen, Wirawan, Wouter, Yannick and anyone else that I might unintentionally have missed.

Verder wil ik ook graag Mara, Nicolette, Mickey, Anton, Kiki en Stella heel erg bedanken voor jullie vriendschap en alle leuke momenten samen. Het was altijd gezellig en jullie hebben mij heel erg gemotiveerd om door te gaan met mijn PhD en veel steun geboden tijdens de moeilijke periodes.

Tot slot wil ik graag mijn familie heel erg bedanken voor al hun steun. Dank jullie voor alle ondersteuning, vertrouwen en gezelligheid, zowel tijdens mijn promotie als de rest van mijn leven. Lieve papa, ik had gehoopt dat je dit moment nog mee had kunnen maken, maar het heeft helaas niet zo mogen zijn. Bedankt voor alles en ik hoop dat je trots op me zou zijn. Lieve mama, Laurens, Robert en Inge (samen met Tim), jullie ook enorm bedankt voor alles wat jullie mij gegeven hebben!



## Curriculum Vitae

Mark Meijerink was born on the 18<sup>th</sup> of May, 1991 in Amstelveen, the Netherlands. After graduating high school (gymnasium, Hermann Wesselink College, Amstelveen) in 2009, he started studying Molecular Science & Technology at Leiden University and Delft University of Technology. He specialized in chemical engineering, and followed a 6 month minor in materials science at the Politecnico di Milano. He graduated in 2012 after finishing his bachelor thesis on *the effect of the zeolite support in zeolite-supported cobalt catalysts on the liquid composition of the Fischer-Tropsch synthesis* with dr. S. Sartipi in the Catalysis Engineering group of Prof. dr. Freek Kapteijn and Prof. dr. Jorge Gascon.

The same year, he started his double degree, a master in Chemical Engineering and a master in Materials Science & Engineering, at Delft University of Technology. He specialized in process engineering for the master Chemical Engineering and in metals science and high temperature materials for the master Materials Science & Engineering. The master thesis was a project on *synthesizing an Al<sub>2</sub>O<sub>3</sub> anti-oxidation coating for MoSi<sub>2</sub> healing particles used in self-healing thermal barrier coatings* with dr. A.L. Carabat and in the groups of dr. ir. W. G. Sloof, Prof. dr. ir. J. R. van Ommen and dr. E. M. Kelder. During his internship in the research group of Prof. dr. W. Nakao at Yokohama National University, Japan, he worked on *investigating the self-healing mechanism of Al<sub>2</sub>O<sub>3</sub>/TiC ceramic composites using FIB-SEM*.

In 2015, he started his PhD under supervision of Prof. dr. ir. K. P. de Jong and dr. J. Zečević on *the use of advanced electron microscopy techniques to study supported metal catalysts*. The main results thereof are presented in this thesis and have been published (or are pending publication) in peer-reviewed journals and presented at national and international conferences.

